Forced Response System Identification of Gas Turbine Fan Flutter

by

Andras Laszlo Andor Kiss
S.B., Massachusetts Institute of Technology (2013)
S.M., Massachusetts Institute of Technology (2015)

Submitted to the Department of Aeronautics and Astronautics
in partial fulfillment of the requirements for the degree of
Doctor of Philosophy in Aerospace Engineering
at the
MASSACHUSETTS INSTITUTE OF TECHNOLOGY
February 2021

© Massachusetts Institute of Technology 2021. All rights reserved.

Author .....
Department of Aeronautics and Astronautics
December 28, 2020

Certified by .....
Zoltán S. Spakovszky
Professor of Aeronautics and Astronautics
Thesis Supervisor

Certified by .....
Edward M. Greitzer
H.N. Slater Professor of Aeronautics and Astronautics
Committee Member

Certified by .....
Jayant Sabnis
Senior Lecturer
Committee Member

Accepted by .....
Zoltán S. Spakovszky
Professor of Aeronautics and Astronautics
Chair, Graduate Program Committee

Forced Response System Identification of Gas Turbine Fan Flutter

by

Andras Laszlo Andor Kiss

Submitted to the Department of Aeronautics and Astronautics
on December 28, 2020, in partial fulfillment of the
requirements for the degree of
Doctor of Philosophy in Aerospace Engineering

Abstract

Flutter in aero-engine fans continues to present major safety concerns and cost millions of dollars in maintenance from high-cycle fatigue. New technologies to improve safety and reduce cost require knowledge of damping levels, but determining the in-situ flutter damping of an installed fan remains challenging.

This thesis introduces a first-of-its kind forced response system identification approach to measure fan flutter damping in a full gas turbine aero-engine. A reduced order modeling framework that captures the effect of actuator dynamics, flutter and stall dynamics, and sensor dynamics on forced response was developed for rigorous design of the experiment. A statistical analysis demonstrates that the experiment is capable of measuring flutter damping within 15% for most flutter modes throughout the entire operating range of the Pratt & Whitney 615 turbofan engine. The least damped, and therefore most limiting, flutter modes yield the least error with flutter margin estimated within 1.5 points or 14%.

A key enabling technology for this experiment is a high power zero-net mass flux actuator capable of exciting the flutter modes. Experimental characterization of the actuator dynamics at this thus far un-explored scale demonstrates the limitations of current reduced order models in predicting actuator performance. This thesis establishes the need for experimental characterization of such actuators for future forced response experiments.

Virtual forced response system identification experiments demonstrate robustness of the approach to noise sources, with damping measurements succeeding even with noise levels above those typical in engine testing. Fans with different performance characteristics were simulated demonstrating that flutter damping can be measured with similar levels of error as compared with the PW615 engine. Guidelines on system identification, data processing, and experimental setup are developed for future forced response experiments. Finally, detailed design demonstrates the experiment can be conducted safely and with no impact on the engine steady state performance.

The thesis contributions are (1) a new approach to measuring fan flutter damping in aero-engines that enables the development of flutter mitigation technologies

and advanced prognostics, and (2) a forced response reduced order modeling framework that provides new capability for experimental design and coupled engine system dynamic modeling that can identify detrimental engine conditions.

Thesis Supervisor: Zoltán S. Spakovszky
Title: Professor of Aeronautics and Astronautics

per aspera ad astra...

Acknowledgments

First and foremost I would like to express my sincerest thanks to my advisor and mentor Professor Spakovszky. It seems hard to believe that we began working together over ten years ago, but all through that time he has supported, encouraged, and guided me as I grew, both as a researcher and as a person. He was always willing to make time to talk, tackle the difficult problems we faced, and keep me going with his positivity. Professor, I owe you a debt of gratitude, if not some beigli as well!

I would also like to thank my committee members, Professor Greitzer and Dr. Sabnis, for their invaluable insight and (sometimes lengthy) comments that helped improved this thesis. Thanks also to the readers, Dr. Tan and Dr. Strazisar for their help and willingness to take on this role, even from halfway across the world.

In an eleven year career at MIT and the GTL, I have met more wonderful people here than I could list in twenty pages, if not only a few. In Young, my brother in Jet-A, concrete dust, and hákarl, working on the PW615 with you and becoming your friend has been one of the highlights of my time at GTL. We did it!! Alex, thanks for endless enjoyable conversations and an amazing friendship; I cannot wait to visit you in Bavaria and get some of this "proper" German beer i've heard so much about. Thanks to my work husband, Vaishnavi, for simply being there for a rant and putting up with my incessant teasing and eye rolling. Thanks to the rest of the GTL gaming gang, Yuan Kang and Jonas, for all the laughs and late night games of skittles. Special thanks to Jinwook who got me through quals, classes, and helped me with all the computer admin work.

One cannot imagine the GTL without our former lab manager, Jimmy Letendre, who was always willing to give a helping hand and whose down-to-Earth knowledge saved many an experiment from its grad student designer, or our admin Robin Courchesne-Sato, who handled last second orders and requests with aplomb. Thanks also to Dave Robertson and Todd Billings, who were always willing to help with some crazy electrical problem, loan me a tool, or help me build a part. A very special thanks to the whole Pratt & Whitney Canada A-team: Ed, Adrian, Kevin, Rick, and

David who made every day Christmas and spent late nights in the test cell with us to get the engine running! I am also deeply grateful for the technical and financial support of Pratt & Whitney America throughout my entire time at the GTL.

Outside of the GTL I would like to thank my friends Matt, Stephen, and Andrew for all the laughs, always keeping me grounded, and reminding me of life outside of MIT. Special thanks to Karen who always was there with a "how you?" or a walk along the river. Cressica, my climbing partner in arms, I loved all the years we got to spend and climb together; I promise we will get that 12a one day! To Larry, Terry, and the rest of the MacGregor house team, the four years I spent at MacGregor working with you and becoming your friends was one of the most amazing experiences I have had. To my MacG students, especially Megan, Bobby, and Yiran: I am so privileged to know you and to have watched you develop through your undergraduate career. I cannot wait to see how you change the world.

Finally, I would like to thank, with all the love in the world, my family. To my Mom and Dad, Eva and Gabor, you always encouraged me to do what I love and never wavered in your faith in me, even when I lacked it in myself. To my grandmother, Klara, you always told me to shoot for the stars and I could never have done this without you. To my sister, Katica, and aunt, Agi, you were always there to be counted on and support me. Lastly, to my partner Jeff, whose unconditional love and support reminded me that I could in fact keep going, even in my worst moments. I love you with all my heart and cannot wait to embark on a new chapter in our lives together. And yes, we can finally get a dog!

Contents

1 Introduction **31**

1.1 Motivation 31

1.2 A Brief Introduction to Flutter 33

1.3 Previous Work and Limitations 35

1.3.1 High Fidelity Numerical Modeling 36

1.3.2 Reduced Order Modeling 38

1.3.3 Flutter Stability Experiments 38

1.4 Research Objectives 42

1.5 Technical Approach 43

1.6 Contributions 46

1.7 Organization of Thesis 47

2 Development of the Forced Response Experiment Modeling Framework **49**

2.1 Overview of the Forced Response System Identification Experiment . 49

2.2 Reduced Order Modeling of Fan Flutter 51

2.2.1 Inputs to Flutter Reduced Order Model 54

2.2.2 System Modes from Fan Flutter Model 55

2.3 Forced Response Actuation 62

2.3.1 Actuator Functional Requirements & Selection 62

2.3.2 ZNMF Actuator Dynamics & Reduced Order Modeling 64

2.3.3 Design Implications 67

2.3.4 Fan Flutter Reduced Order Model with Actuation 69

2.4 Blade Vibration Sensing 72
2.4.1 Effective Sampling Rate 74
2.4.2 Requirements on Sensor Count 75
2.5 System Identification 76
2.5.1 Transfer Function Estimation 78
2.5.2 Eigenvalue Inference from Estimated Transfer Function 79
2.6 Summary of Modeling Framework Development 81

3 Experimental Characterization of ZNMF Actuator Performance 83
3.1 Motivation for Experimental Characterization 84
3.2 Technical Approach 85
3.3 Experimental Setup 86
3.3.1 Hotwire Calibration 88
3.3.2 Hotwire Data Processing 90
3.4 Impact of Actuator Geometry on Frequency Response 96
3.5 Assessment of Actuator Reduced Order Model 102
3.6 Incorporating Actuator Transfer Function into Flutter Modeling Framework 104
3.7 Summary of Actuator Experimental Characterization 108

4 Virtual Experiments for Assessing Experimental Error 109
4.1 Virtual Experiments in Absence of Noise 110
4.2 Impact of Actuator Dynamics on System Identification 113
4.3 Incorporating Noise into Virtual Experiments 116
4.3.1 Sources of Noise 116
4.3.2 Statistical Framework for Error Estimation 118
4.4 Results at Design Point with Noise 124
4.5 Effect of Operating Point on System Identification 129
4.5.1 Flow Coefficient Variation 129
4.5.2 Fan Speed Variation 134
4.5.3 New Capability: Quantification of Damping Across Fan Map . 141

4.6 General Limitations of Experimental Design 143
4.7 Summary of Virtual Experiment Results 144

5 Error Sensitivity Studies **147**
5.1 Signal Processing 148
5.1.1 Windowing Function 149
5.1.2 Window Overlap 153
5.1.3 Window Length 155
5.2 Experimental Conditions 158
5.2.1 Noise Magnitude 158
5.2.2 Ensemble Averaging 160
5.2.3 Forcing Magnitude 162
5.3 Fan Design 165
5.3.1 Applicability of Experimental Design to Larger Engines 168
5.4 General Recommendations and Guidelines 169
5.5 Summary of Error Sensitivity Studies 170

6 Detailed Experimental Design **173**
6.1 Functional Requirements of Experimental Design 173
6.2 Inlet Duct Acoustic Flutter Model 174
6.3 Actuator Detailed Design 181
6.4 Blade Stress Analysis 186
6.5 Summary of Detailed Design 189

7 Summary, Conclusions, & Future Work **191**
7.1 Summary 191
7.2 Conclusions 193
7.2.1 General Conclusions 193
7.2.2 PW615 Specific Conclusions 194
7.3 Recommendations for Future Work 195
7.3.1 Flutter Reduced Order Modeling 195

7.3.2 Signal Processing & System Identification 196
7.3.3 PW615 Experiment 196

A Flutter Reduced Order Model Inputs **199**

B Actuator Volume Flow Estimation from Centerline Velocity **201**

C Fan Design Sensitivity Studies **205**

D Reduced Order Modeling in Test Cell Design **209**

List of Figures

1-1 Flutter instability from feedback loop of body vibration and fluid pressure forces with insufficient damping ζ. 31

1-2 Schematic representation of *work per unit cycle* (WPUC), which governs stability, and *interblade phase angle* (IBPA), which defines a family of flutter modes. 34

1-3 Multiple flutter regimes throughout fan map motivate unified methodology to characterize flutter damping (reproduced from [9]). 36

1-4 Measurement of flutter mode damping with forcing from upstream distortion limited to discrete shaft speeds at Campbell diagram crossings. Figure reproduced from [39]. 42

1-5 Key aim is the experimental characterization of flutter damping for multiple fan flutter modes in Pratt & Whitney 615 turbofan engine. . 44

1-6 Integrated approach for characterization of flutter damping with forced response system identification. 45

2-1 Control theoretic representation of individual dynamics of actuator, flutter, and sensor systems which govern measured flutter response and estimated damping in forced response experiment. 50

2-2 Semi-actuator disk representation with flexible rotor capture flutter dynamics in reduced order model. 51

2-3 Comparison of Rotor 67 (left) and the PW615 fan (right). Both feature wide-chord rotors with a pressure ratio approximately 1.6 and tip Mach number approximately 1.2. 55

2-4 Eigenvalues of reduced order model capture bending and torsion flutter modes and rotating stall modes. 56

2-5 Eigenvectors define mode shape for corresponding eigenvalue, e.g. 1^{st} forward nodal diameter bending mode dominated by bending perturbations (arbitrary scale). 57

2-6 Bending mode eigenvalues with nodal diameters labeled. Mode frequencies are separated by multiples of shaft frequency in the absolute frame. 57

2-7 Higher nodal diameter backward traveling modes can appear forward traveling in absolute frame and are excited by forward traveling wave excitation. 60

2-8 Model captures switching of mode propagation direction in absolute frame as demonstrated by bending perturbations of 1^{st} and 3^{rd} backwards nodal diameters. 60

2-9 Flutter mode damping ratio as function of interblade phase angle. Bending modes are less stable than torsion modes for PW615. 61

2-10 Schematic overview of acoustic speaker driven ZNMF actuator. Actuator design space defined by neck and cavity geometries and speaker properties. 65

2-11 Equivalent circuit representation of ZNMF actuator (reproduced from [48]). Neck flow $\dot{V}_{neck}$ maximized when cavity volume is minimized, reducing design space to neck radius and length for a given speaker. . 66

2-12 Reduced order model based ZNMF actuator for multiple neck lengths. Increase in actuator bandwidth and flow drives design to short necks. 68

2-13 Reduced order model based ZNMF actuator performance for multiple orifice radii. High sensitivity of actuator flow to orifice radius(due to inverse quartic scaling of viscous resistance term) drives design to large orifice radius. 68

2-14 Control volume analysis to incorporate upstream air injection into flutter model. Injection angle not significant to first order for zero mean injection flow. 69

2-15 Forced response simulation with 1st nodal diameter forcing. Forward and backward traveling wave excitation excite flutter modes with response an order of magnitude greater than the sensor resolution. . . . 71

2-16 Forced response simulation with 3rd nodal diameter forcing. Forward traveling wave excitation excites both forward and backward flutter modes with response an order of magnitude greater than the sensor resolution. 72

2-17 Measurement of blade bending from blade tip time-of-arrival. Bending resolution set by sensor sampling rate (smallest measurable Δt). . . . 73

2-18 Impact of stagger on sensor resolution. Increasing stagger decreases bending resolution. 74

2-19 Effective sampling rate of blade bending versus time limited to blade passing frequency in tip-timing systems. 75

2-20 System identification process to estimate flutter damping from experiment data. Methodology assessed with virtual experiments. 77

2-21 Example sensor-to-forcing transfer function from virtual experiment with process noise. Resonant peak due to 1st forward nodal diameter flutter mode. 79

2-22 Example identification of 1st forward nodal diameter flutter mode, blue, with damping ratio estimated within 1%. 81

3-1 Hotwire traverses used to determine actuator performance across design space 86

3-2 ZNMF actuator characterization experiment setup. Hotwire traverses of interchangeable orifices used to characterize frequency response across design space 87

3-3 Data acquisition process to ensure measurements at separate radial positions are phase-locked as needed for accurate transfer function phase estimation. 88
3-4 Hotwire calibration curves with error bars. High error motivates refined calibration technique for future work. 89
3-5 Low-speed calibration data fit to King's law trend from literature, providing evidence calibration is meaningful. 90
3-6 Measured centerline velocity periodic for single frequency excitation. Development of transfer function estimation procedure required as hotwire only measures velocity magnitude. 91
3-7 Comparison of analytical and estimated transfer functions of model system. Transfer function well estimated by reconstruction procedure in absence of noise. 95
3-8 Estimation of model system transfer function with -2dB noise. Alternative coherence definition captures impact of noise on transfer function estimation. 95
3-9 Measured frequency responses for multiple orifice radii. Actuator bandwidth and peak flow are essentially independent of orifice radius producing no preferred orifice radius for experiment. 97
3-10 Measured frequency responses for multiple neck lengths. Trade-off between peak flow and bandwidth with neck length for larger orifice radius. 98
3-11 Assessment of impact of mechanical clamping of speaker diaphragm by neck mounting plate with spacer ring. Left side: with clamping, right side: without clamping 99
3-12 Measured frequency responses with and without spacer ring. Frequency of both modes decreases and peak volume flow increases with reduction in mechanical clamping, introducing another design degree-of-freedom. 101
3-13 Actuator flow at flutter mode frequencies increased up to 500% by tailoring actuator response to nodal diameter. 101

3-14 Actuator model fails to capture impact of orifice radius on actuator bandwidth and peak volume flow in comparison to measured performance in Figure 3-9. 103

3-15 Actuator model captures reduction in cavity mode frequency with neck length but fails to capture peak volume flow trends in comparison to measured performance in Figure 3-10. 103

3-16 Linearity of volume flow to voltage transfer function demonstrated as curves for multiple voltage levels collapse. Average transfer function defined in red. 105

3-17 Spatial Fourier transform of actuator flow field for ND1 and ND3 forcing. Spatial aliasing permits excitation of higher nodal diameter modes 106

3-18 Spatial Fourier transform of actuator flow field for two orifice radii. Reducing orifice radius reduces effective forcing magnitude and drives design to large orifice radius. 107

4-1 Resonance from 1^{st} forward nodal diameter mode in bending-to-actuator-flow transfer functions $T_{y\Phi_f}(f)$ for 1^{st} forward nodal diameter forcing for PW615 fan. Near unity coherence achieved due to the absence of noise. 111

4-2 Resonance from 2^{nd} and 6^{th} backward, as well as 2^{nd} forward, nodal diameters in bending-to-actuator-flow transfer function $T_{y\Phi_f}(f)$ with 2^{nd} forward nodal diameters forcing. due to propagation direction switching and forcing spatial aliasing. 112

4-3 Analytical and identified eigenvalues for 1^{st} and 2^{nd} forward forcing. Error in damping ratio is entirely from system identification procedure and minimal due to the absence of noise. 113

4-4 Actuator frequency response function with less damped cavity mode. Actuator dynamics expected to have largest effect on 0^{th} nodal diameter mode due to proximity of actuator cavity mode. 114

4-5 Comparison of measured transfer functions with and without actuator dynamics characterization. Actuator characterization needed to isolate flutter dynamics in transfer function. 115
4-6 Systematic bias and confidence in a single damping measurement characterized by expected value and percentile statistics of damping ratio error probability density function. 119
4-7 Estimated error PDF from 1000 virtual experiments and best-fit normal distribution. Error distribution is non-normal, preventing use of parametric methods to form confidence interval of percentile points. . 120
4-8 Estimation of error mean and percentile point distributions with bootstrapping, permitting confidence intervals on percentile points to be derived. 121
4-9 Dependence of 80% - 95% single-sample confidence intervals on number of virtual experiments performed. 300 and 1000 experiments needed for 80% and 95% single-sample confidence intervals to converge respectively. 123
4-10 Transfer function from 1st forward nodal diameter forcing with expected noise levels. Coherence values around resonance used to guide system identification frequency limits. 124
4-11 Error metrics from statistical analysis for operation at design point and expected noise levels. Mean error less than 2% and 95% single-sample confidence interval magnitude less than 15% except for 2nd and 6th backward nodal diameters. 125
4-12 Mean damping ratio with 95% single-sample confidence interval error bars as a function of interblade phase angle. Mean error and confidence intervals are small relative to changes in analytical damping ratio with interblade phase angle. 126
4-13 Low coherence and proximity of 6th backward nodal diameter mode to 2nd forward nodal diameter results in greater error than other modes. 127
4-14 2nd backwards nodal diameter mode near low frequency limit of actuator rendering it un-identifiable with noise. 128

4-15 Approaching stall on total-to-static characteristic reduces damping for forward nodal diameters and increases damping for backward nodal diameters 130
4-16 Mean damping ratios and 95% single-sample confidence intervals for multiple steady flow coefficients. Error metrics improve for modes with reduced damping. 131
4-17 Multiple damping measurements along fan characteristic enables flutter margin estimate. Flutter margin estimated within 1.5 points or 14% for critical flutter mode of PW615, the 1st forward nodal diameter. 134
4-18 Reducing fan speed increases mode non-dimensional frequency and effective stiffness, reducing the variation of damping ratio with interblade phase angle. 135
4-19 Mean estimated damping ratio and 95% single-sample confidence intervals for $\frac{N}{N_{TO}} = 1.0, 0.9$. Mean damping ratio follows trend except for 6th backward and 2nd forward nodal diameters. 136
4-20 Merging of 2nd forward and 6th backward nodal diameter modes in transfer function due to equal absolute frame frequency results in identified eigenvalues at intermediate growth rate. 137
4-21 Mean estimated damping ratio and 95% single-sample confidence intervals for $\frac{N}{N_{TO}} = 0.7, 0.5, 0.3$. Analytical trends captured but 3rd and 5th backward nodal diameters becomes un-identifiable for certain speeds. 138
4-22 Transfer functions for 3rd forward nodal diameter forcing at $\frac{N}{N_{TO}} = 0.3$. 3rd and 5th forward nodal diameter modes excitable by actuator but un-observable due to limited sampling rate from tip-timing. 139
4-23 Fan map with contours of constant 1st forward nodal diameter damping ratio produced from virtual experiment data. Experiment provides new capability to identify regions of low damping or instability. 141
4-24 Example fan map with flutter instability limiting fan operation and regions of low damping in operating range. Experiment enables identification of problematic operating points. 142

5-1 Example result of window function choice: increased side-lobes of Rectangular window manifests as ringing in transfer function as compared to Hann window. 150

5-2 Impact of window function on error metrics. Hann and Hamming windows perform best overall except for 2^{nd} backward nodal diameter with Rectangular window. 152

5-3 Rectangular window preserves low-frequency information discarded by tapered windows due to input signal non-stationarity. 152

5-4 Impact of window overlap fraction on error metrics. Little impact on error metrics with 50% overlap or greater. 153

5-5 Low overlap fraction corrupts estimated transfer function with regions of high noise. 154

5-6 Reduction in cross-power spectral density and power spectral density at discrete frequencies due to non-overlaping, tapered windows 155

5-7 Decreasing window length/increasing number of window reduces noise in estimated transfer function making dynamics more recognizable. . 156

5-8 Impact of window length on error metrics. Error insensitive to window length in 8-32 window range but increases above 32 windows, with damping over-predicted. 157

5-9 Estimated 1^{st} forward nodal diameter transfer function with 8 and 256 windows. Increased averaging from high window counts excessively smooths transfer function, erroneously increasing apparent damping. . 158

5-10 Error metrics increase with turbulence intensity and 6^{th} backward nodal diameter un-identifiable above 3%. 159

5-11 No change in error metrics for sensor noise below 10x sensor resolution with error growing rapidly above 50x sensor resolution. 160

5-12 Ensemble averaging effective in reducing error from noise, but has diminishing returns above 30 trial averaging. 161

5-13 Schematic representation of reducing actuator flow. Margin in actuator flow equivalent to margin in sensor resolution for low noise environments, but not in high noise environments where noise level dominates. 164

5-14 Error increases with reduced forcing magnitude due to reduced signal-to-noise ratio, but least damped modes identifiable with up to 85% reduction in actuator flow. 164

5-15 Sensitivity of 1^{st} forward nodal diameter damping ratio to fan parameters (reproduced from [22]). Studies performed for parameters with high sensitivity and that are likely to vary between Rotor 67 and the PW615 fan. 165

5-16 Varying mechanical damping demonstrates improved error metrics for fan designs that reduce mode damping. 167

5-17 Transfer functions with varying mechanical damping. Decreased damping improves 6^{th} backward nodal diameter coherence, improving identification. 167

5-18 Changes in damping ratio due to center of pressure location captured with same dependence of error metrics on mode damping ratio. . . . 168

6-1 Actuator mounting duct to be placed between engine inlet duct and bellmouth. Ability to set total inlet length provides opportunity to influence inlet duct acoustics. 175

6-2 Acoustic model for determining pressure wave phase difference at fan face which drives acoustic flutter (reproduced from [72]) 175

6-3 Flutter index as a function of fan speed and inlet length for PW615 for 0^{th} to 3^{rd} forward nodal diameters. At constant inlet length, flutter index varies more rapidly with speed for higher nodal diameters, reducing speed-averaged flutter index. 178

6-4 Fan speed averaged flutter index $\beta_{\bar{N}}$ as a function of inlet length. No inlet length produces $\beta_{\bar{N}} = 0$ for all nodal diameters, L/D = 2.35 chosen as compromise between 0^{th} and 1^{st} forward nodal diameters. . 179

6-5 Sinusoidal dependence of flutter index on inlet length at constant fan speed. 180

6-6 Estimation of flutter aerodamping dependence on inlet length using flutter damping measurements for inlet lengths marked by red dashed lines.[1] 181

6-7 Mounting duct with eight circumferential actuators to be installed between bellmouth and engine inlet duct. 182

6-8 Modular actuator mounting system which allows multiple neck lengths to be used to tailor actuator performance to the flutter mode of interest. 182

6-9 Static pressure in sealed back cavity equalized with bellmouth throat to eliminate steady force on speaker diaphragm. 183

6-10 Mesh lining of actuator duct to reduce lip-separation from actuator neck cavity prevents additional process noise and changes in fan steady performance. 184

6-11 Traverse system modified with mesh screen sample to assess impact of mesh on actuator volume flow frequency response. 185

6-12 Volume flow frequency response with and without mesh screen present. Mesh screen has negligible impact on actuator performance 185

6-13 Experimentally measured alternating stress for PW615 from first bending mode Campbell diagram crossing provides comparison dataset for blade stress analysis of Rotor 67 blade geometry (measurements by manufacturer). 187

6-14 Comparison of Rotor 67 first bending stress distribution to measured PW615 fan stress. Rotor 67 analysis representative of PW615 with good agreement in modeshape and stress magnitude 188

6-15 Blade stress limitations not exceeded as estimated peak alternating stress from forced response experiment below Goodman line for all speeds to be tested. 189

B-1 Measured velocity profile is in qualitative agreement with analytical results. 202

B-2 Ratio of average velocity to centerline velocity for unsteady flow expected to be near unity for actuator operation, enabling volume flow estimation from centerline velocity. 203

B-3 Good agreement of volume flow frequency responses from traverse measurement and centerline velocity methods with centerline velocity method producing a conservative estimate. 203

C-1 Error metrics for variation of elastic axis and center of gravity location. Change in damping ratio well captured by experimental design. . . . 206

C-2 Rotor loss functions with modified steepness parameter and resultant total-to-static pressure rise characteristics. Damping measured off-design to increase impact of loss function. 207

C-3 Experiment captures changes in flutter damping with loss function steepness parameter. 208

C-4 Experiment capture variation of flutter damping ratio with blade mass. 208

D-1 Typical engine test cell design with large diameter augmentor tube and exhaust stack not feasible for MIT test cell (reproduced from [82]) . . 210

D-2 Exhaust system reduced order model consisting of linked compressible flow and control volume analyses enabled assessment of design concepts and design space exploration. 210

D-3 Structural design of exhaust system enabled by insight into relationship of design parameters A_1/A_2 and A_4/A_3 and system pressure levels provided by model. 213

D-4 Model provides estimates of quantities of interest across design space and identified trade-offs that informed final design configuration. . . . 214

D-5 Noise impact on surrounding buildings deemed acceptable due to estimates from reduced order model. 214

D-6 Reduced order model provided insight to diagnose observed system behavior as incomplete diffusion. Experimentally measured data in good agreement with model when corrected for incomplete diffusion. . 216

List of Tables

4.1 Dependence of damping ratio error on transfer function and system identification model degrees-of-freedom. Higher degrees-of-freedom permit identification of flutter mode, even without actuator characterization. 116

4.2 Mean error generally ±3% and maximum 95% single-sample confidence interval magnitude ±15% across multiple operating points at takeoff speed.[2] 132

4.3 Mean error generally ±3% and maximum 95% single-sample confidence interval magnitude ±15% across fan speed range. 140

5.1 Parameters for sensitivity study from most controllable (signal processing) to least controllable (fan design). *means at nominal noise levels and/or experimental setup. 147

5.2 Survey of mechanical damping values across literature. Assessed range $\zeta_b = 0.30 \pm 50\%$ covers values from literature. 166

A.1 Required fan system inputs to flutter reduced order model 199

Nomenclature

Roman

$\dot{m}$	Mass flow
$\dot{V}$	Volume flow
$\hat{e}$	Damping ratio error percentile point
A	Area
b_b, b_t	Mechanical damping dashpot coefficients in bending, torsion
C	Acoustic capacitance
c_0	Acoustic propagation speed
C_{yx}	Coherence function from x to y
D	Diameter
e	Damping ratio error
E, U	Voltage, free-stream velocity in King's law
F	Net force
f	Frequency
i, j	Imaginary unit
k_b, k_t	Blade stiffness in bending, torsion

L Length

L_r, L_s Stagnation pressure loss coefficients of rotor, stator

M Blade mass, acoustic mass, or Mach number

N Shaft speed (RPM)

n Nodal diameter index, King's law fitting coefficient

p Static pressure

P_t Stagnation pressure

P_{xx} Power spectral density of x

P_{xy} Cross power spectral density between x and y

Q Net blade displacement

q Blade bending displacement

Q_b, Q_t Non-dimensional blade stiffness in bending, torsion

R Acoustic resistance

r, R Radius

s Laplace parameter $\sigma + \mathrm{i}\omega$

T Temporal period

t Time coordinate

T_t, T_s Stagnation, static temperature

T_{yx} Frequency domain transfer function from x to y

u Axial velocity component

U_{tip} Fan tip speed

V Volume, voltage

Greek

α Blade torsional displacement, percentile parameter

β Confidence interval parameter, flutter index

γ Blade stagger angle

λ Acoustic wavelength

ν Kinematic viscosity

Ω Shaft angular frequency

ω Angular frequency, imaginary component of eigenvalue

ω_b, ω_t Angular frequency of blade bending, torsion modes

Φ, ϕ Flow coefficient

Ψ_p Flutter model plenum pressure coefficient

Ψ_{ts} Total-to-static pressure rise coefficient

ρ Fluid density

σ Real component of eigenvalue

θ Circumferential coordinate

ζ Damping ratio

Operators

$\bar{a}$ Time averaged value of a

$\ddot{a}$ Second time derivative of a

$\dot{a}$ First time derivative of a

$\hat{a}$ Temporal Fourier coefficient of a

$\vec{a}$ Vector quantity a

a' Unsteady perturbation to time averaged value $\bar{a}$

$E[a]$ Expected value of a

Acronyms

BND Backward nodal diameter

E,EO Engine order

FND Forward nodal diameter

IBPA Interblade phase angle

L/D Length to diameter ratio

ND Nodal diameter

PW615 Pratt & Whitney 615 (turbofan engine)

SFC Spatial Fourier coefficient

WPUC Work per unit cycle

ZNMF Zero-net mass flux

Chapter 1

Introduction

1.1 Motivation

Flutter is a self-excited instability formed by a feedback loop of the aerodynamics surrounding a body and the structural mechanics that govern the body vibration. As in Figure 1-1, when flutter modes have negative damping, $\zeta < 0$, energy from the fluid flow around a body is transferred into the body structure, manifesting itself as vibrations of growing amplitude until either the operating condition is altered, a limit cycle is established, or the body fails. Even if flutter modes are positively damped, and thus do not result in exponentially growing vibration amplitudes, the amount of damping present impacts the amplitude of vibrations during normal operation and has a strong impact on part life due to high-cycle fatigue. Flutter is thus a critical issue in high performance turbomachinary such as fans, compressors, and turbines.

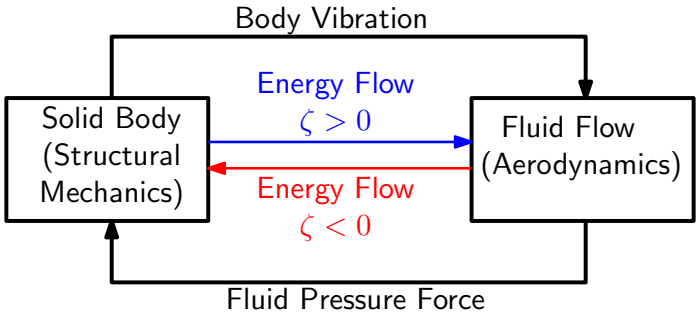


Figure 1-1: Flutter instability from feedback loop of body vibration and fluid pressure forces with insufficient damping ζ.

Early work on turbomachine flutter began in the 1950s in two-dimensional cascades (e.g. [1]) and it is a problem that continues to present major challenges, with implications on safety and cost because failure of gas turbine components due to fatigue still occurs. A recent example is Southwest 1380, which experienced a fan blade failure in-flight resulting in a passenger death. The National Transportation Safety Board concluded in its accident report that "...the probable cause of this accident was a low-cycle fatigue[1] crack in the dovetail of fan blade no. 13, which resulted in the fan blade separating in flight..." [3]. Flutter and forced response related high cycle fatigue can have high financial costs. An Air Force study found that "... between 1982 and 1996, high cycle fatigue accounted for 56% of Class A engine-related failures... required an expenditure of 850,000 maintenance man-hours... [and] over $400 million per year..." [4]. The same study outlined a science and technology program with the goal of determining alternating stress within 20% and damping resonance stress by 60% for gas turbine fans to address the high costs associated with high cycle fatigue.

These examples demonstrate the need to identify flutter damping levels such that existing mitigation strategies can be implemented if needed. Identification of damping levels also enables the development and assessment of new technologies for flutter mitigation. Measuring the flutter damping of an installed fan, however, remains challenging and there is not yet an experimental methodology capable of measuring in-situ flutter damping for an engine-scale test in the public literature. This work develops and assesses such a methodology.

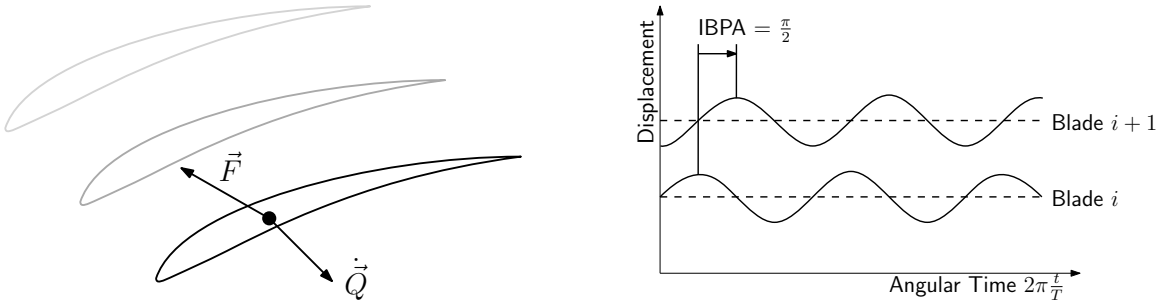
To be effective, considerations of gas turbine flutter must begin early in the design cycle. Preliminary design tools for flutter are often rooted in empirical models based on previous engine designs, and their applicability is unknown as the industry moves to new design regimes with larger, lower pressure ratio fans and integrated propulsors. Reduced order models (ROMs) present an opportunity to introduce a methodology grounded in fundamental principles, rather than empiricism, early in the design pro-

[1]Flutter is typically associated with high-cycle fatigue, but can reduce overall fatigue life due to the interaction of high and low-cycle fatigue [2].

cess when they are most effective. ROMs also present an opportunity for so-called "smart engines" with intelligent control systems that capture coupled system dynamics to improve reliability and safety. The validity of existing reduced order models for flutter, however, have yet to be assessed with data from engine testing. Flutter damping measurements from engine tests could also provide the needed data to define modeling requirements to improve these models. Active testing of flutter damping also presents an opportunity for intelligent prognostics to improve lifeing models and reduce the reliance on statistical models. Active health monitoring can determine problematic engine conditions earlier, improving safety and extending the useful life of an engine. Ultimately, the development of reduced order modeling, flutter mitigation strategies, and active health monitoring requires the development of a robust and well characterized experimental methodology to measure flutter damping within an engine.

1.2 A Brief Introduction to Flutter

We will now briefly review the core concepts of flutter in gas turbine fans. Consider a fan blade vibrating; this vibration can be decomposed into bending, the displacement of a spanwise section normal to the chordline, and torsion, the rotation of the section around an axis within the section. In the absence of vibration, there is a steady pressure distribution on the suction and pressure sides of the blade which defines the net force on the blade. For a vibrating blade, however, an unsteady pressure distribution arises on the blade, and thus also an unsteady net force. If the instantaneous blade velocity and net force have a component in phase (the dot product of the velocity vector $\dot{\vec{Q}}$ and the instantaneous force vector $\vec{F}$ in Figure 1-2a is greater than zero), work is done *by* the fluid *on* the blade and energy is put into the blade vibration. If the instantaneous velocity and net force have a component out of phase, work is done *by* the blade *on* the fluid, with energy dissipation from the blade vibration into the fluid. If the vibration is periodic with period T, we can define a "work per unit cycle" (WPUC), Equation 1.1, which is the net energy transferred between the fluid



(a) Work per unit cycle quantities

(b) Interblade phase angle

Figure 1-2: Schematic representation of *work per unit cycle* (WPUC), which governs stability, and *interblade phase angle* (IBPA), which defines a family of flutter modes.

and the blade vibration during a cycle.

$$\text{WPUC} = \int_0^T \dot{\vec{Q}} \cdot \vec{F} dt \tag{1.1}$$

If the work per unit cycle is positive, the damping is negative and vice versa. This form of damping, called "aerodynamic damping" or "aerodamping," can be positive or negative. Material and mechanical damping, however, is purely dissipative and thus can only be positive. Material damping arises from dissipation within the material of the blade itself due to displacement, although this effect is typically negligible in turbomachinery blades [5]. Mechanical damping refers to energy dissipation due to friction between mechanical components in the fan assembly. This may be incidental, such as friction in the attachment between the blade and the fan disk, or intentionally added via design elements such as snubbers or platform dampers [6]. The net damping is the combination of aerodamping and mechanical damping and determines whether the system is stable.

Each vibratory mode of the rotor blade gives rise to a family of flutter modes. In each mode of this family, any individual blade is vibrating at the same frequency and with the same mode shape, but the phasing between adjacent blades varies between each mode in the family, giving rise to the "interblade phase angle" (IBPA) as in Figure 1-2b. Circular symmetry restricts the possible values of the interblade phase angle to a finite set of values. Flutter modes are often labeled by the number of blades

around the disk that are in-phase with each other, i.e. the number of *nodal diameters* (a term borrowed from disk mechanics). For a given blade vibratory frequency, any non-zero interblade phase angle gives rise to traveling waves. In the rotating frame, a given interblade phase angle produces two modes: one forward traveling (in the direction of rotor rotation) and one backward traveling (against the direction of rotor rotation).

A short clarification on terminology is useful here. The term "flutter" is typically associated with stability, the situation where negative aerodamping overcomes the positive mechanical damping and the mode grows unstable. "Forced response," however, refers to the vibratory motion of a stable mode due to some form of excitation such as upstream distortion. The forced response problem focuses on predicting the magnitude of the vibratory motion while the flutter problem focuses on predicting the stability boundary. These two problems are linked through the mode damping and it has been shown that damping measurements can be used to address these separate problems in a single approach [7, 8]. The term "flutter mode damping" will be used to refer to the damping value of one of the modes described above, regardless if the mode is stable or not.

1.3 Previous Work and Limitations

Flutter can manifest throughout the fan or compressor map, as indicated in Figure 1-3 and current experiments can assess damping for only small portions of the fan map. What will be developed in this thesis is a unified way to characterize flutter damping throughout the fan operating map in a representative engine environment.

A comprehensive review of numerical techniques for predicting flutter was provided by Marshall and Imregun [10]. They review a variety of numerical techniques, from actuator disk methods to high-fidelity, unsteady 3D CFD. Most salient, however, is their identification of a lack of reliable and well-documented experimental data for assessment of these numerical methods. This was echoed by Baretels and Sayma [11] in a later review article which identified that the computational expense for

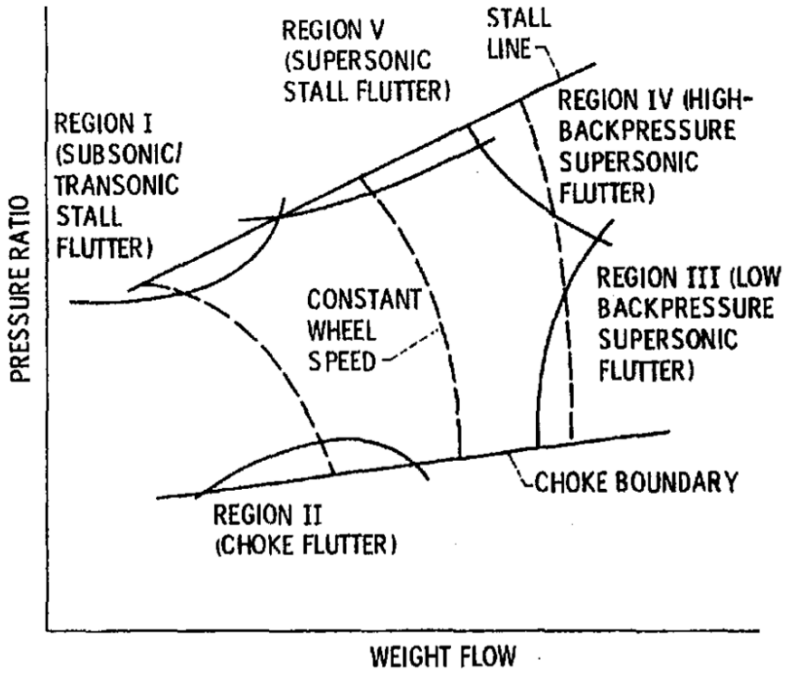


Figure 1-3: Multiple flutter regimes throughout fan map motivate unified methodology to characterize flutter damping (reproduced from [9]).

aeroelastic predictions is still excessively large and that there is a major opportunity for improvements with additional experimental data.

1.3.1 High Fidelity Numerical Modeling

Numerical methods have proven invaluable for investigating the fundamental mechanisms of the different flutter regimes in Figure 1-3. Vahdati et al. [12] determined that stall flutter was driven by a suction side separation resulting in an unsteady pressure field behind the leading-edge shock which is in-phase with the blade displacement. Vahdati and Cumpsty [13] found that a cut-on upstream, but cut-off downstream acoustic field is a prerequisite for transonic stall flutter. They identified that the plunge-to-twist ratio[2] of the first bending mode is a critical parameter, with increased torsional content reducing the damping. Lee et al. [14] determined that

[2]the ratio of the blade bending and torsional displacements for a single mode, sometimes called twist-to-flap

"flutter bite" is driven by a reflected pressure wave from the fan intake when it is in-phase with the upstream propagating pressure wave from the fan. Finally, Stapelfeldt and Vahdati [15] demonstrated that modifications of the steady radial loading distribution could improve flutter margin and that bleeds at the fan tip trailing edge could attenuate the upstream traveling pressure wave to reduce acoustic flutter. This latter work demonstrates how characterization of flutter mechanisms from high-fidelity computations can drive improved flutter control strategies during the design process.

High-fidelity computations, however, have struggled to accurately predict the installed flutter damping and stability boundary due to uncertainties associated with the full engine environment. Stapelfeldt and Vahdati [16] showed that the typical assumption of a hard wall intake and uniform blades resulted in the computations over-estimating the flutter margin as compared to rig tests. It was only after incorporating both the acoustic liner and realistic structural and aerodynamic blade mistuning that the computations agreed with the measured flutter boundary. This indicates that flutter damping estimates from high-fidelity computations are dependent on capturing engine specific geometries and mistuning which may not be known a-priori. The move towards integrated bladed rotors (IBRs) makes capturing the effects of mistuning even more difficult as the blade-to-blade coupling through the disk makes IBRs highly sensitive to mistuning and promotes mode localization [17]. High-fidelity computations also ignore potentially relevant dynamics which impact flutter damping. Crawley et al. [18] demonstrated both numerically and experimentally that coupling flexible blades and a flexible shaft through a rigid disk (such as in a fan section) results in a coupled system with different natural frequencies and system modeshapes for the first nodal diameter flutter mode. Their analytical coupling parameter implies that the coupling between blade and shaft dynamics increases as shaft mass, moment of inertia, and stiffness decreases, as is the case with the current trend towards small core compressors and high bypass ratio fans. Current practices for high-fidelity flutter computations rely on finite element models of the blades in isolation [15, 19] or, at most, the blade-disk system to derive system modeshapes and do not capture potential rotordynamic interactions with flutter dynamics. Such cou-

pled dynamics can only be captured via full engine experiments, as designed in this work, or modeling the entire fan and rotordynamic system.

1.3.2 Reduced Order Modeling

On the opposite end of the fidelity spectrum, reduced order models have gained attention as a means to reduce computational cost. Gysling and Myers [20] coupled an incompressible semi-actuator disk representation of the fan rotor and stator with a two degree of freedom structural model to capture bending and torsion. Wong [21] later extended this model to relax the assumption of a linear dependence on interblade phase angle to capture higher nodal diameter flutter modes. While actuator disks assume the wavelength of perturbations is much longer than the blade pitch, a condition violated by high interblade phase angles, the extended model showed reasonable agreement with experimental cascade data at high interblade phase angle. Copeland and Rey [22] further extended the model to capture the effects of the rotor-stator gap. In a first-of-its-kind forced response system identification experiment, Copeland et al. [23, 24] demonstrated that this model did remarkably well at estimating the flutter damping ratio for a fan rig. While this is a positive indicator for the potential utility of this class of models, their limitations have yet to be fully established. Specifically, effects of compressibility and the accuracy of such ROMs outside the mid-subsonic regime, as well as their applicability to a real engine environment, have yet to be characterized. In summary, both high-fidelity and reduced order numerical methods require high quality engine data for validation and point to the need for experiments such as the one developed in this thesis.

1.3.3 Flutter Stability Experiments

Much of the experimental investigation into flutter has focused on cascade flows. In such experiments, blades are typically externally oscillated while varying aerodynamic parameters such as incidence, inlet Mach and Reynolds numbers, interblade phase angle, and reduced frequency. Cordwise and spanwise unsteady pressure distri-

butions are measured and spatially and temporally integrated to determine the work per unit cycle and mode aerodamping (e.g. [25–31]). Cascade testing also permits measurements at conditions that may be difficult or impossible to achieve in rotating experiments, such as heavily separated flow at high incidence angle [30].

Bölcs and Fransson [32] provided a de-facto standard set of data for nine cascade configurations, ranging from flat plates to highly cambered airfoils, which continues to be utilized as a benchmark for numerical flutter methods today (e.g. [33,34]). Cascade testing offers a highly controllable and accessible environment for detailed measurements, but its limitations reduce the representativeness to real turbomachinery flows. Cascades are inherently two dimension, or quasi-two dimensional, and fail to capture three dimensional steady loading distributions, and radially varying shock structures and associated shock-boundary layer interaction [35]. Furthermore, cascade blades are rigid and externally oscillated in bending or torsion and do not capture realistic modeshapes for modern, highly three dimensional blades. Finally, simulating representative Mach numbers, Reynolds numbers, and reduced frequencies simultaneously in cascades is challenging due to the need for precise blade-to-blade external excitation at high frequencies [31]. The extent to which the simplifying assumptions of cascade flows are valid can best be assessed with data from engine testing.

Flutter stability experiments on rotating hardware are much more limited than those in cascades owing to the unique challenges presented by the rotating environment for blade excitation and response measurement. Rotating experiments can be divided into two categories: those with frequency controlled excitation and those without. The former use an actuator (pneumatic or piezoelectric) for which frequency content can be controlled independently of shaft speed. Crawley [8] performed the first flutter damping measurement in a transonic compressor by utilizing a fast shut-off pneumatic injector installed in two upstream vanes to measure the step response from all nodal diameters simultaneously. To determine the damping of individual flutter modes, fast response strain gauge data for each blade was required to separate the responses from each nodal diameter. The measured flutter damping was in reasonable agreement with a 2D, weak shock analysis, with the analytical result

under-predicting the damping by 50%. Jeffers et al. [36] developed a technique to measure damping where excitation and blade response measurement were performed simultaneously via piezoelectric actuators and strain gauges installed in select modified blades. A new data processing methodology was developed to eliminate the typical issue of cross-talk in slip-rings between high voltage actuation signals for piezoelectrics and sensitive strain gauge signals. It was shown that the mechanical and aerodamping could be derived from the net flutter damping by performing the experiment both in vacuum and in air. Kielb et al. [37] later used this technique to independently measure structural and aerodynamic damping in a turbine rig at representative Mach numbers, concluding that aerodynamic damping constituted as much as 85% of the total damping. Rey et al. [24] implemented pneumatic actuation using synthetic jet actuators circumferentially mounted in the rotor-stator gap of a subsonic fan rig and blade response was measured using a single eddy current sensor for damping estimation. A 450% increase in flutter damping was demonstrated with active flutter control via the synthetic jet actuators.

Crawley [8], Jeffers et al. [36], and Kielb et al. [37], however, all utilized intrusive forcing and measurement techniques not amenable to engine-scale fan testing. In the latter case especially, it is unclear that piezoelectric actuators would have sufficient authority to sufficiently excite fan blades, whose mass is several times greater than that of turbine blades. Furthermore, Jeffers et al. reported poor reliability of strain gauge and piezoelectric actuator wiring above tip speed speeds of 300 m/s, well below that of transonic fans. It was also shown that the presence of the piezoelectric actuator increased the measured damping by up to 50%. Both of these factors motivate the development of a measurement technique that does not utilize actuators installed within the blade.

Measuring blade response in the rotating frame also presented challenges as there is little frequency separation of different nodal diameter flutter modes in the rotating frame, resulting in poor accuracy from the single degree-of-freedom curve fitting technique typically used to derive damping from forced response data. An uncertainty analysis revealed that the largest source of error was due to the curve fitting tech-

nique, especially in the presence of random noise, demonstrating the need for a means to rigorously evaluate damping estimation techniques with representative dynamics and noise levels.

In all these experiments it is unknown to what extent actuator dynamics were considered when inferring damping; assuming actuator dynamics are negligible could introduce errors in estimated damping levels, but it is unclear under what conditions such errors can occur and how large they may be. This work addresses the question of when actuator dynamics must be characterized for accurate damping estimation and demonstrates the need for non-intrusive actuators whose performance and dynamics are well characterized.

Rotating experiments without frequency controlled excitation generally rely on aerodynamic excitation from distortion upstream of the rotor, resulting in an excitation frequency that is a harmonic of shaft frequency. The flutter mode is excited when the machine is at a shaft speed such that the excitation frequency is equal to the flutter mode frequency, i.e. Campbell diagram crossings as in Figure 1-4. Murray and Key [38] measured flutter mode damping of an embedded rotor in high-speed compressor rig utilizing blade response data from a non-intrusive stress measurement system (tip-timing) with excitation from upstream stator wakes as the compressor was accelerated through the Campbell diagram crossing. They demonstrated that blade damping did not change with an increase in steady loading of the rotor and that casing mounted pressure transducers can be used to quantify forced response.

Kammerer and Abhari [39] utilized distortion screens upstream of a turbocharger impeller to excite flutter modes and measured the response using strain gauges. Two screens with different number of lobes were used to measure the damping at two separate speeds. They concluded that aerodynamic damping dominated structural damping, with it comprising 90% of the total damping, in agreement with Kielb et al. Unlike Murray and Key, however, they found that damping depended on the steady loading of the impeller, with the damping increasing with loading at one speed and decreasing with loading at the other. A fundamental limitation for this category of experiments is that damping measurements can only be performed for select shaft

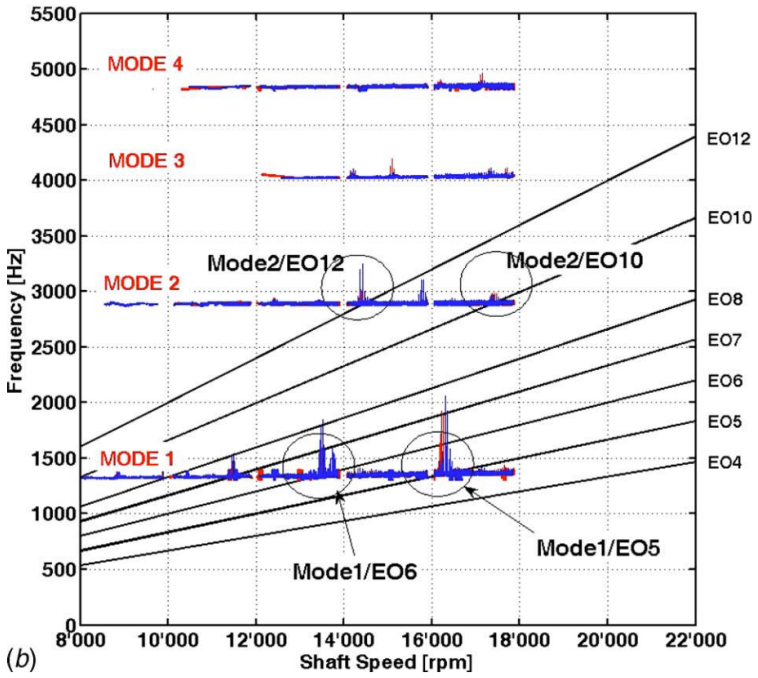


Figure 1-4: Measurement of flutter mode damping with forcing from upstream distortion limited to discrete shaft speeds at Campbell diagram crossings. Figure reproduced from [39].

speeds, that of the Campbell diagram crossing, and cannot characterize damping throughout the fan operating map as will be achieved in this work. Such experiments cannot assess which, if any, operating speeds are limited by flutter instability.

1.4 Research Objectives

The works discussed sought a difficult goal: characterize the flutter damping, or at minimum the flutter boundary, in a realistic and relevant environment. The ability to measure flutter damping at these realistic conditions, however, is still limited. Within the public literature, flutter damping measurements have not yet been demonstrated in engine testing. To address this challenge, the objectives of this work are to:

1. Develop an experimental methodology to measure fan flutter damping in a turbofan environment

2. Assess the limitations of the experimental methodology and quantify the un-

certainty in the flutter damping measurement

3. Assess extensibility of the methodology to other fan designs

4. Develop best practices and experimental guidelines for flutter damping experiments

The primary goal is to demonstrate the feasibility of an engine scale experiment to measure flutter damping within typical margins for engine operability.

1.5 Technical Approach

The Pratt & Whitney 615 (PW615) turbofan engine installed in the MIT test cell, shown in Figure 1-5, serves as a platform for experimental development. It features a modern, wide-chord fan design with a bladed disk. The fan has a pressure ratio of approximately 1.6 and a bypass ratio of 2.2. A key aim of this work would be the measurement of flutter damping for the PW615 for multiple modes.

The central idea behind the experimental approach is forced response system identification. A system with unknown dynamics is excited with a known forcing and the dynamical properties and modes of the system are estimated by measuring the response to this forcing. Such testing requires the integration of actuators, sensors, and the dynamical system of interest. Figure 1-6 outlines how the forced response experiment fits into the overall objective of flutter damping characterization as well as the approach to meet the research objectives with associated outcomes.

A flutter reduced order modeling framework utilizing the model from Ref. [21] is developed to estimate the fan flutter behavior of the PW615 with inputs for the model partially derived from high fidelity computations and engine performance testing. The reduced order modeling framework is extended to incorporate reduced order models of a variety of actuation methodologies in order to assess which actuation methods are most effective. To assess the predictions of the actuator reduced order model and ensure sufficient actuation for a measurable and useful flutter response, the actuator performance and dynamics are experimentally characterized.

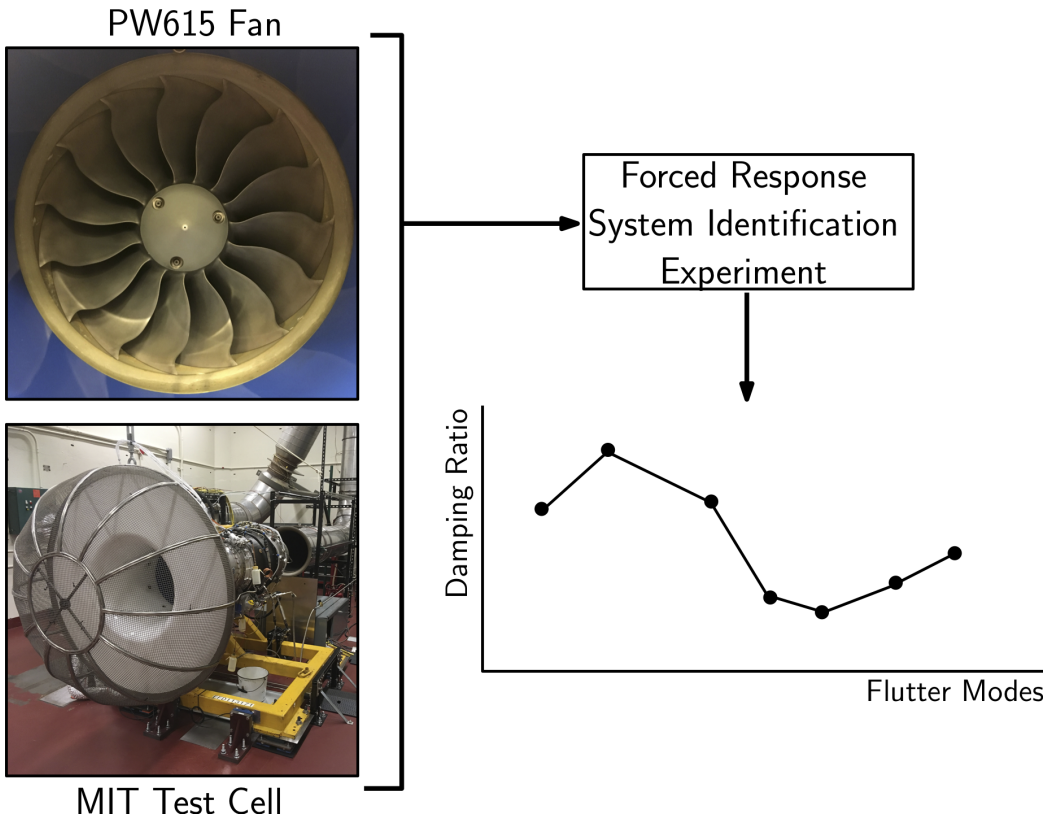


Figure 1-5: Key aim is the experimental characterization of flutter damping for multiple fan flutter modes in Pratt & Whitney 615 turbofan engine.

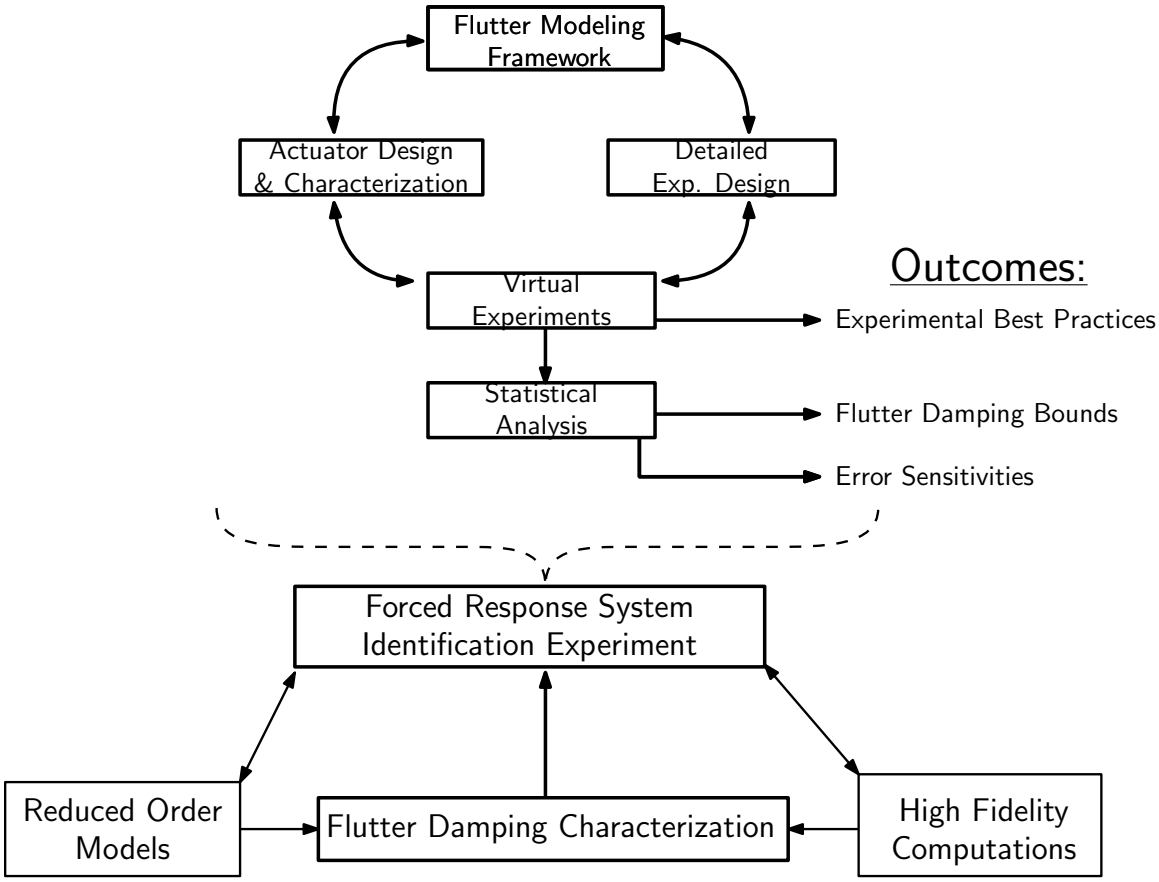


Figure 1-6: Integrated approach for characterization of flutter damping with forced response system identification.

"Virtual experiments" are then performed that simulate the entire flutter experiment. The actuators are represented by the experimentally characterized actuator dynamics and the engine's response is represented by the flutter modeling framework. This virtual experiment simulates the entire physical experimental chain, starting from the input signal to the actuator and finishing with the measured fan vibratory response. As the true flutter damping for the virtual experiment is known *a-priori* (analytically from the flutter reduced order model dynamics), the estimated flutter damping error is quantified. By incorporating noise sources to simulate a realistic environment, experimental error and bounds on the flutter damping are estimated with a statistical analysis. The flutter model inputs that represent the fan performance and geometry are varied to assess the sensitivity of the flutter damping error metrics to fan performance and determine how extensible the methodology is to other fan designs. The virtual experiments and statistical analysis are also used to develop best practices and produce guidelines for future forced response system identification experiments. A detailed experimental design is performed to determine how the experimental methodology would be implemented for a full engine test.

1.6 Contributions

The specific contributions of this work are as follows:

1. Design of a first-of-its-kind engine scale experiment capable of measuring flutter damping within 15%, equivalent to 1.5 points of flutter margin, for the least damped flutter modes throughout the engine operating range. Such an experiment could enable the development of flutter mitigation technologies, numerical design tools, and advanced prognostics by providing a means of assessing their efficacy and accuracy.

2. A coupled forced response reduced order modeling framework providing new capability for experimental design and larger system dynamics modeling. This new framework has future utility in fully coupled engine dynamical models that

seek to identify detrimental engine conditions due to the dynamical coupling of multiple engine systems.

3. Characterization of zero-net mass flux actuator dynamics at a thus far unexplored scale demonstrating limitations and shortcomings of current reduced order models in predicting actuator performance, establishing the need for experimental characterization of zero-net mass flux actuators in future forced response experiments.

4. Best practices for flutter forced response system identification experiments and an experimental design that is robust to noise sources and generalizable to other engine fans.

5. Development of a rigorous approach to the design of forced response system identification experiments which can be used to design experiments that characterize dynamics of other engine systems and identify possible dynamical instabilities.

1.7 Organization of Thesis

Chapter 2 introduces a reduced order modeling framework capable of capturing the essential physics to perform complete virtual experiments and experimental design. The flutter modeling framework is developed and adapted to include the effects of forcing. An actuator reduced order model is also developed and utilized for preliminary design of the actuator. Finally, a system identification framework to derive flutter damping from fan vibration measurements is described.

Chapter 3 experimentally characterizes the actuator design space and demonstrates the design of a capable actuator for the forced response experiment. A novel data processing methodology for measuring zero net mass flux actuator performance from the characterization experiment is derived, resulting in a variety of actuator designs with different trade-offs. It is shown that the actuator reduced order model can

capture some trends in the actuator dynamics, but it is in poor agreement with measured actuator performance metrics. This demonstrates the need for experimental characterization of actuator performance during experimental design of future forced response experiments.

Chapter 4 rigorously assesses the forced response experiment using virtual experiments. The experimental design is shown to be capable of flutter damping measurements for multiple flutter modes throughout the engine operating range. A statistical framework for assessing experimental error is developed and it is demonstrated that the experimental error is a function of the specific flutter mode, but the damping values associated with the least damped modes are measured within 15%.

Chapter 5 utilizes the statistical framework to assess how the error depends on different elements of the experimental design and operating environment. The experiment is shown to be robust to expected noise sources and best practices with respect to experimental design and data post-processing are established for future PW615 engine tests and general forced response system identification experiments. Simulating a range of fans with varying performance within the flutter modeling framework demonstrates the experimental methodology is extensible to other fan designs.

Chapter 6 takes the learnings from the virtual experiments and develops a detailed implementation of the experimental design. Actuator detailed design is performed to allow multiple configurations from those tested in Chapter 3 to be utilized, tailoring the actuator performance to the flutter mode of interest. A simple model of acoustic flutter from literature is used to guide engine inlet design. Finally, a dynamic blade stress analysis is performed, demonstrating the experiment does not induce excessive levels of stress on the blade.

Finally, Chapter 7 summarizes the thesis, provides conclusions, and offers recommendations for future work. Appendix D describes the role of reduced order modeling in the design of the MIT PW615 turbofan test cell. It is included as a demonstration for future researchers of the utility of reduced order modeling in the development of experiments.

Chapter 2

Development of the Forced Response Experiment Modeling Framework

2.1 Overview of the Forced Response System Identification Experiment

The forced response system identification experiment can be broken down into three components as in Figure 2-1: actuators which provide excitation to the plant system, the plant system itself whose dynamics are to be characterized (the rotating fan), and sensors which measure the plant system response. It is clear that the plant system has associated dynamics, but both the actuators and sensors can also have associated dynamics (or a transfer function in the frequency domain). For example, servo motors exhibit non-uniform response in power output and displacement when driven at different frequencies [40] and measuring unsteady pressure through tubing can damp high frequencies due to viscous resistance [30].

The experiment proceeds as follows: a command signal $i(t)$ is provided to the actuator, with the signal having sufficient frequency content to excite the frequencies of the flutter modes of interest. The actuator converts this input signal into a physical perturbation $u_f(t)$ to the fan. For example, it could apply an unsteady force to the fan blade root or vary the fan blade incidence angle. In the ideal case of no actuator

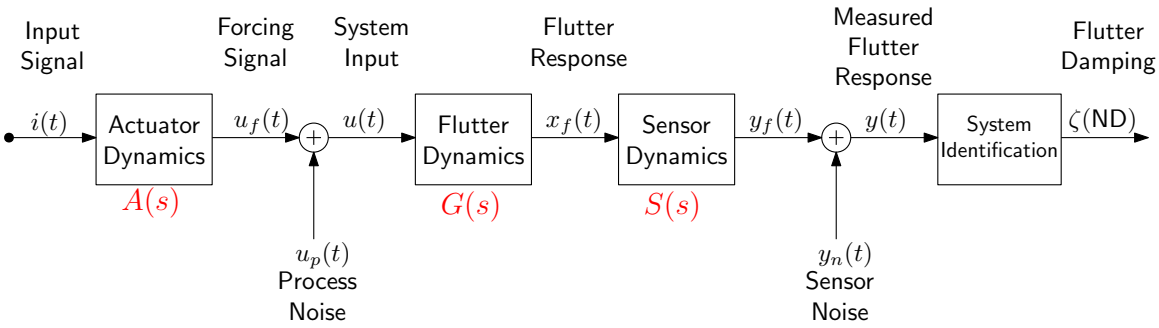


Figure 2-1: Control theoretic representation of individual dynamics of actuator, flutter, and sensor systems which govern measured flutter response and estimated damping in forced response experiment.

dynamics, $A(s) = \text{const}$, $i(t)$ and $u_f(t)$ are identical[1]. For an actuator with dynamics, $u_f(t)$ is a modulated version of $i(t)$. A critical aspect of actuator design is to ensure it has sufficient bandwidth to excite the highest frequency modes of interest and sufficient power to create measurable levels of response, such as vibration at the fan tip. In the presence of process noise $u_p(t)$, such as inlet turbulence, the actuator forcing signal is corrupted, producing the final, but unknown, input to the fan $u(t)$.

The fan blades vibrate in response to the input forcing, producing the flutter system response $x_f(t)$. This can be thought of as the entire system response, which is the true vibratory motion of each point of each blade. The sensors measure some portion of the full system response, for example the motion of the mid-chord point of the tip, to produce $y_f(t)$, which is again modulated by any associated sensor dynamics. Noise, $y_n(t)$, can corrupt the sensor output, producing $y(t)$. Going from $i(t)$ to $y(t)$ represents the complete physical experiment. System identification techniques utilize the measured flutter response and input signal to estimate the damping for the flutter mode excited in the experiment.

The goal of the experiment is to estimate the flutter dynamics $G(s)$ from which flutter damping can be derived. With non-zero actuator and sensor dynamics, $A(s) \neq \text{const} \neq S(s)$, the measured flutter response is dependent on those dynamics: $Y(s) = A(s)G(s)S(s)I(s)$.[2] Thus characterizing these dynamics can be critical for accurately

[1] except for a constant scaling factor, or gain, and a change of physical units, e.g. volts to Newtons

[2] $Y(s)$ and $I(s)$ are the Fourier transforms of the sensor output signal $y(t)$ and the actuator input signal $i(t)$ in Figure 2-1

estimating the flutter damping. In the "virtual experiments" performed in this work, each of these physical systems are replaced with reduced order models of their dynamics, or experimentally measured transfer functions, such that the entire experiment can be simulated and its accuracy assessed.

2.2 Reduced Order Modeling of Fan Flutter

The flutter reduced order model is based on the the work of Wong [21]. The model is an improvement of an earlier analysis of Gysling et al. [20] and is not limited to low interblade angles and can capture higher order flutter modes. While a nonlinear model can capture the dynamics of the rotor-stator gap [22], and these dynamics may seem especially relevant for a fan where the rotor-stator gap is large compared to that of core compressors and turbines, it was shown that flutter damping is insensitive to the rotor-stator gap length [22] and these dynamics were not included. A brief overview of the flutter model is provided below (further details can be found in [21]).

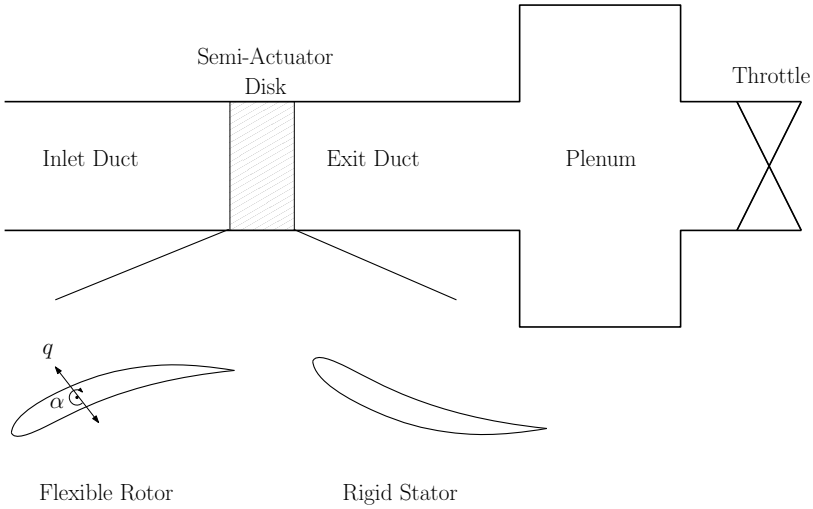


Figure 2-2: Semi-actuator disk representation with flexible rotor capture flutter dynamics in reduced order model.

Figure 2-2 presents a schematic overview of the flutter reduced order model. The flow is assumed to be incompressible[3], two dimensional (axial and circumferential), and inviscid. The turbomachinery is replaced by a semi-actuator disk which represents

[3]the role of compressibility and the utility of a compressible model is discussed in Section 7.3.1

the turbomachinery as a discontinuous rise in the static pressure and is matched to the flow in the exit duct. The overall pressure rise from the semi-actuator disk is set by the individual contributions of each blade row. The model consists of the following elements:

- Blade row performance is captured using total pressure loss and trailing edge flow angle deviation as a function of blade incidence. The performance in each blade row is estimated as in a mean-line analysis, with velocity, flow angle, and static pressure determined at the inlet and exit of the blade row.

- Unsteady total pressure loss is captured using a first order lag equation.

- A structural model is coupled with the semi-actuator disk where the rotor is considered flexible but the stator is rigid. The flexible rotor has two degrees-of-freedom: torsion around a specified elastic axis along the blade chord and bending normal to the chordline.

- Blade stiffness is captured through the non-dimensional bending and torsional frequency parameters $Q_b = \frac{\omega_b R}{U_{tip}}$ and $Q_t = \frac{\omega_t R}{U_{tip}}$ where $\omega_b = \sqrt{\frac{k_b}{M}}$ and $\omega_t = \sqrt{\frac{k_t}{I}}$ are the dimensional frequencies of the first bending and torsion mode of the rotor blade respectively.

- Mechanical damping is similarly captured through the non-dimensional damping parameters $\zeta_b = \frac{b_b}{2M\omega_b}$ and $\zeta_t = \frac{b_t}{2M\omega_t}$ where b_b and b_t are the bending and torsion mechanical damping "dashpot" coefficients of a damped harmonic oscillator.

The non-uniform, unsteady flow is cast as a perturbation to a uniform, steady background flow as in Equation 2.1 for the flow coefficient Φ. The perturbation is further projected onto N pairs of spatial Fourier coefficients as in Equation 2.2. Each of these spatial harmonics corresponds to a nodal diameter and thus unique interblade

phase angle.

$$\Phi(\theta, t) = \bar{\Phi} + \Phi'(\theta, t) \tag{2.1}$$

$$\Phi'(\theta, t) = \sum_{n=0}^{N} \hat{\Phi}_{nc}(t) \cos n\theta + \hat{\Phi}_{ns}(t) \sin n\theta \tag{2.2}$$

The steady, uniform background flow[4] is solved for a given throttle coefficient using a non-linear, iterative solver. The unsteady plenum pressure Ψ_p and the unsteady spatial Fourier coefficients for the inlet flow coefficient Φ, rotor and stator loss coefficients L_r, L_s, rotor bending q and torsion α are cast as state variables, producing $10N + 6$ state variables. All other perturbation quantities are derived as linear combinations of these states. The unsteady continuity, momentum, loss-lag, and structural dynamic equations are linearized about the steady operating point, keeping only terms that are first-order in perturbation quantities. This forms a set of second order differential equations of the form:

$$\mathbf{a}\ddot{\vec{x}} + \mathbf{b}\dot{\vec{x}} + \mathbf{c}\vec{x} = \vec{f}(t), \tag{2.3}$$

where $\vec{x}$ is the state vector

$$\vec{x} = [\hat{\Phi}_0, \hat{\Phi}_{1,c}\hat{\Phi}_{1,s}, \cdots, \hat{\Phi}_{N,s}, \hat{L}_{r,0}, \cdots, \hat{L}_{s,0}, \cdots, \hat{q}_0, \cdots, \hat{\alpha}_0, \cdots, \hat{\alpha}_{N,s}, \Psi_p]^T.$$

$\mathbf{a}, \mathbf{b}, \mathbf{c}$ are matrices of real values derived from the linearization of the governing equations and $\vec{f}(t)$ is the unsteady, external forcing to the system. This system can be re-cast in state-space form $\dot{\vec{X}} = \mathbf{A}\vec{X}$ which is used for dynamic simulation and system identification methods.

For the case without forcing, $\vec{f}(t) = 0$, the homogenous solution of the ordinary differential equations is found by assuming a solution of the form $\vec{x}(t) = \vec{x}e^{\lambda t}$ forming the quadratic eigenvalue problem

$$(\mathbf{a}\lambda^2 + \mathbf{b}\lambda + \mathbf{c})\vec{x} = 0.$$

[4]consisting of the flow coefficient, rotor and stator loss, and rotor bending and torsion, from which all other flow quantities can be determined

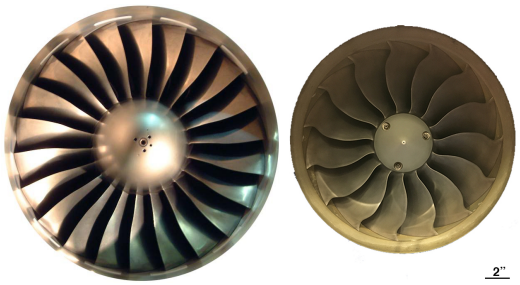
Each spatial harmonic is represented using two real-valued spatial Fourier coefficients (one each for a cosine and sine term of a given spatial harmonic, $\hat{\Phi}_{nc}$ and $\hat{\Phi}_{ns}$ respectively in Equation 2.2), and thus the $\mathbf{a}, \mathbf{b}, \mathbf{c}$ matrices are real-valued[5]. The eigenvalues are consequently either real-valued, representing modes that are purely exponential decay or growth, or complex conjugate pairs, modes that are oscillatory and possibly grow or decay depending on the real part of the eigenvalue. Modifications to the model to incorporate forcing and the solution procedure for the forced case are discussed in Section 2.3.4.

2.2.1 Inputs to Flutter Reduced Order Model

Multiple inputs are needed to characterize the aerodynamic, structural, and geometric properties of the fan to be modeled and a full listing of these inputs is provided in Appendix A. The most critical inputs are the natural frequencies of the rotor blade first bending and torsion modes which set the required actuator bandwidth. The frequencies for the PW615 were derived from finite element analyses and experiments by the manufacturer for rotational speeds throughout the engine operating range. Detailed performance and geometrical parameters, however, are not publicly available for the PW615 fan rotor and inputs were derived for a similar rotor, Rotor 67, instead.

Rotor 67 is a wide-chord, transonic fan, developed by NASA. that has performance similar to that of the PW615 fan. Figure 2-3 shows a comparison of the two fans. Rotor 67 has been extensively studied and aerodynamic, aero-elastic, and structural data are publicly available (e.g. [19, 42, 43]). Utilizing these data assumes the aerodynamic performance of Rotor 67 is similar to that of the PW615 fan. Within the fidelity of reduced order modeling, however, the limiting factor is not expected be the precision of the model inputs. What is more important is to ensure the inputs are representative of the regime in question, rather than capturing the exact numerical values. For example, both fans are transonic, with supersonic blading at the tip, and

[5]the spatial Fourier coefficients can also be cast as a single, complex coefficient $\hat{\Phi}_n = \hat{\Phi}_{nc} + \mathrm{i}\hat{\Phi}_{ns}$, in which case the matrices $\mathbf{a}, \mathbf{b}, \mathbf{c}$ are complex and the complex eigenvalues need not come in complex-conjugate pairs [41].



	R67	PW615
Design PR	1.59	≈1.6
Tip Mach	1.25	≈1.2
Mass Flow (kg/s)	33.3	≈20
Diameter (in)	20.1	17
Blade Count	22	15
Aspect Ratio	1.56	1.4

Figure 2-3: Comparison of Rotor 67 (left) and the PW615 fan (right). Both feature wide-chord rotors with a pressure ratio approximately 1.6 and tip Mach number approximately 1.2.

of similar aspect ratio and blade natural frequencies. To assess the importance of this assumption, a sensitivity study for the most critical model input quantities (as determined in [22]) derived from Rotor 67 is performed in Section 5.3, where it is shown that the experiment is feasible for a wide range of these input parameters.

2.2.2 System Modes from Fan Flutter Model

Solving Equation 2.3 results in a set of eigenvalues that define the natural modes of the system, as plotted on the complex plane in Figure 2-4 for the PW615 operating at takeoff power. The PW615 fan has 15 blades, and thus a maximum of $N = 7$ nodal diameters or spatial harmonics are modeled, producing 76 states and 152 eigenvalues (the complex conjugates are not plotted in Figure 2-4 for clarity). The corresponding eigenvectors describe the "mode shape" of that mode, namely the relative magnitudes of the different state variables.

An example of mode shape in which flow quantities are reconstructed in time and space around the casing circumference is shown in Figure 2-5. The mode behavior is dominated by bending displacement, contains only the first spatial harmonic, and propagates in the direction of rotor rotation (positive theta). Hence it is categorized as the 1^{st} forward nodal diameter bending mode. The absolute magnitude of the perturbations in Figure 2-5 is not significant, as eigenvectors can be multiplied by any factor, and only the relative magnitude of the eigenvector entries are relevant. Other modes are categorized by whether they are dominated by perturbations in

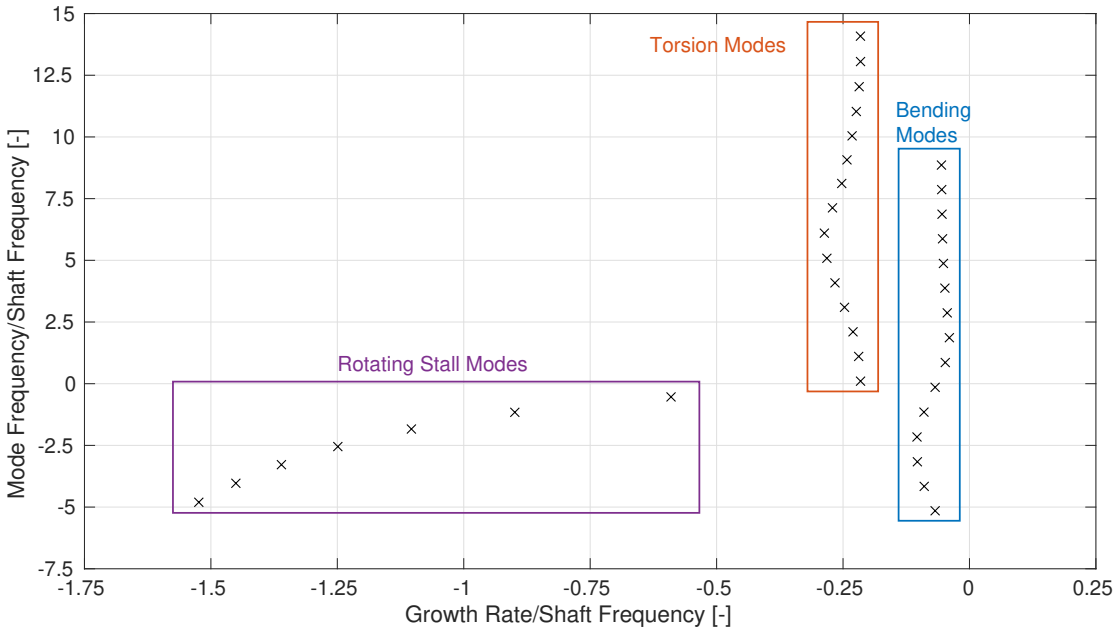


Figure 2-4: Eigenvalues of reduced order model capture bending and torsion flutter modes and rotating stall modes.

torsional displacement (torsional flutter modes), inlet flow coefficient (rotating stall or surge modes), or rotor and stator loss coefficients[6] (loss-lag modes) as labeled in Figure 2-4.

The bending eigenvalues are labeled with the corresponding nodal diameter of the eigenvalue in Figure 2-6. The frequency of the 0^{th} nodal diameter, for which all blades vibrate in unison and there is no wave propagation about the circumference, is close to the blade natural frequency of 1.9E[7] as is typical. The frequency of each nodal diameter is close to the blade natural frequency in the rotating frame, but in the absolute frame, the frame of the model, the frequency is shifted by a multiple of rotor frequency $\omega_{abs} = \omega_b + n\Omega$ where n is the nodal diameter (positive and negative for forward and backwards respectively). Correspondingly, Figure 2-6 shows the 1^{st} forward nodal diameter at a frequency of approximately 2.9E and the 1^{st} backward nodal diameter at a frequency of approximately 0.9E.

[6] not shown in Figures 2-4 and 2-5

[7] E here representing "engine order" or shaft frequency

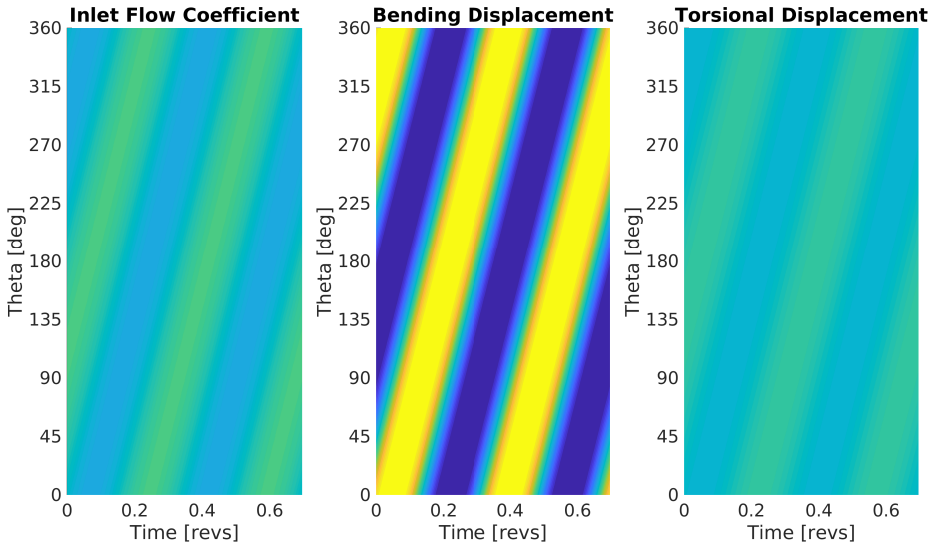


Figure 2-5: Eigenvectors define mode shape for corresponding eigenvalue, e.g. 1st forward nodal diameter bending mode dominated by bending perturbations (arbitrary scale).

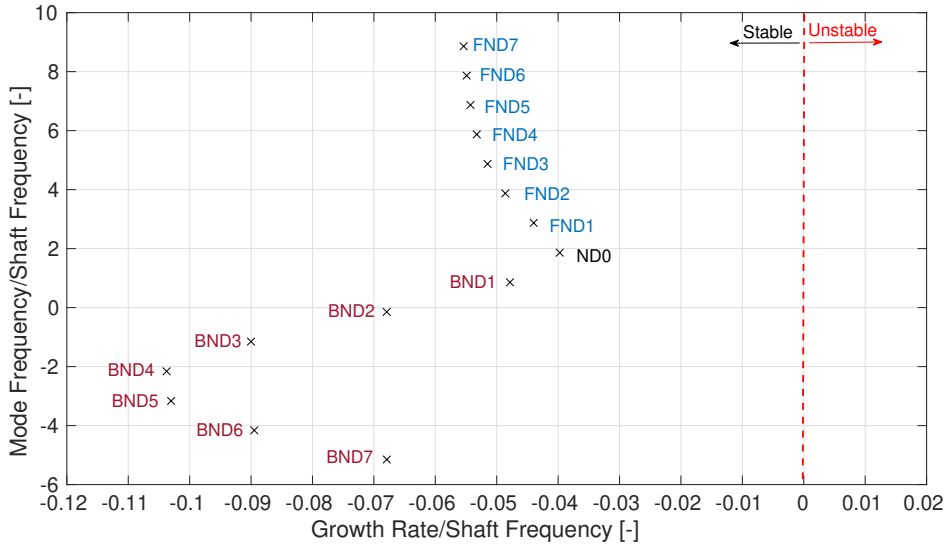


Figure 2-6: Bending mode eigenvalues with nodal diameters labeled. Mode frequencies are separated by multiples of shaft frequency in the absolute frame.

Behavior of Flutter Modes in the Absolute Frame

A benefit of measuring blade vibrations in the absolute frame is that different flutter modes are easily distinguished by frequency, rather than grouped together at nearly the same frequency [24]. This improves recognition of the flutter modes, as well as curve-fitting to estimate damping, as response levels can be more easily attributed to a single flutter mode. Conversely, this effect is detrimental if actuators operate in the absolute frame as the required actuator bandwidth is increased to excite higher nodal diameter, forward traveling modes.

Observing the flutter modes in the absolute frame also means that higher nodal diameter, backward traveling modes can appear forward traveling in the absolute frame, as depicted in Figure 2-7. In the relative frame, the blade is vibrating near its natural frequency, regardless of interblade phase angle or nodal diameter, as for the bending $q(\theta_{rel}, t) = \cos(\omega_b t - n\theta_{rel})$, where $n > 0$ is a forward traveling wave and $n < 0$ is a backward traveling wave in the relative frame. The speed of the wave propagation, or the phase velocity, in the relative frame is thus $\omega_{phase,rel} = \frac{\omega_b}{n}$. As ω_b is nearly constant with n, the wave slows down with increasing magnitude of n in the relative frame. The phase velocity in the absolute frame, however, is shifted by the rotor speed Ω:

$$\omega_{phase,abs} = \omega_{phase,rel} + \Omega = \frac{\omega_b}{n} + \Omega.$$

If $\omega_b > \Omega$, as is typical for turbomachinery blades, then for small $n < 0$ the wave is backward traveling in the absolute frame as $\omega_{phase,abs} < 0$. For higher backward nodal diameters, however, the term $\frac{\omega_b}{n}$ is negative but smaller in magnitude than Ω. $\omega_{phase,abs}$ thus becomes positive and the backward nodal diameter mode appears forward traveling in the absolute frame, as shown for the 3$^{\text{rd}}$ nodal diameter in Figure 2-7.

This phenomena is observed in the model results, as shown by the mode shapes for the backwards 1$^{\text{st}}$ and 3$^{\text{rd}}$ nodal diameters in Figure 2-8 ($\omega_{phase,abs} \approx -0.9$ and $\omega_{phase,abs} \approx 0.4$ respectively). Modes that feature this behavior are denoted as having negative frequency in Figures 2-4 and 2-6 as is the case for the 2$^{\text{nd}}$ to 7$^{\text{th}}$ backward

nodal diameters for the PW615 at takeoff speed.

Recognizing this phenomena is important for the experiment because traveling wave excitation by actuators operating in the absolute frame must travel in the correct direction to excite non-zero nodal diameter flutter modes. When the backward nodal diameter mode's frequency is negative, forward traveling wave excitation can excite both the backward and forward modes. There will be two peaks in the frequency response of the blade vibration, one each from the forward and backward nodal diameter modes at frequencies separated by $2\omega_b$, as shown graphically for the 3^{rd} nodal diameter in Figure 2-7.

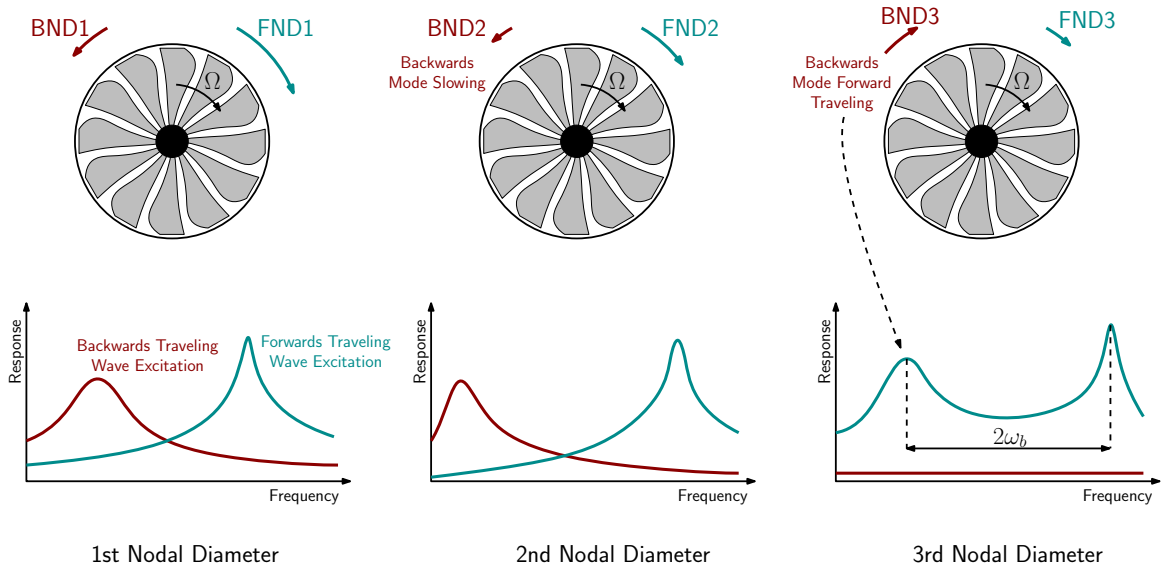


Figure 2-7: Higher nodal diameter backward traveling modes can appear forward traveling in absolute frame and are excited by forward traveling wave excitation.

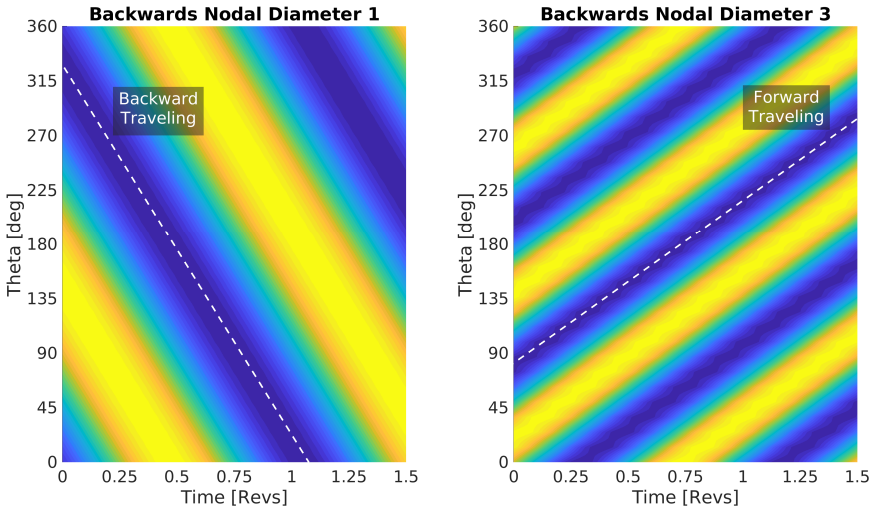


Figure 2-8: Model captures switching of mode propagation direction in absolute frame as demonstrated by bending perturbations of 1st and 3rd backwards nodal diameters.

Flutter Mode Stability

The stability of each mode is described by its damping ratio ζ, where $\zeta < 0$ for an unstable mode and $\zeta > 0$ for a stable mode. Given a flutter mode eigenvalue $\lambda = \sigma + \mathrm{i}\omega_{abs}$ in the absolute frame, the damping ratio is defined by

$$\zeta = -\frac{\sigma}{\sqrt{\sigma^2 + \omega_{rel}^2}} = -\frac{\sigma}{\sqrt{\sigma + (\omega_{abs} - n)^2}} \tag{2.4}$$

Damping ratios for bending and torsion flutter modes are plotted as a function of interblade phase angle in Figure 2-9. For the PW615 at takeoff, the least stable mode is the 0^{th} nodal diameter bending mode and *the bending modes are less stable than the torsion modes*. The focus in this thesis will thus be to measure the damping of the bending modes. Focusing on bending modes also reduces the required bandwidth of the forcing actuator because the natural frequency of the first torsion mode is nearly four times that of the first bending mode for the PW615 fan blade.

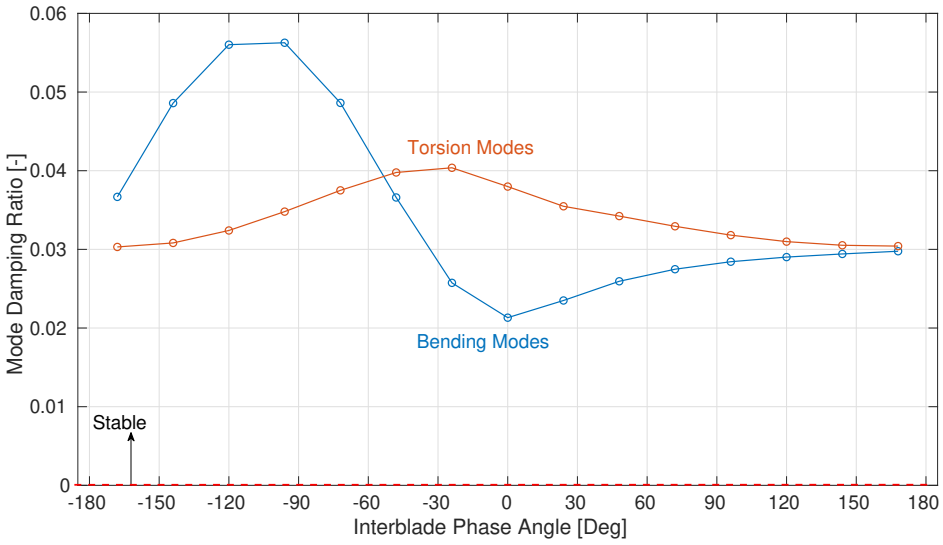


Figure 2-9: Flutter mode damping ratio as function of interblade phase angle. Bending modes are less stable than torsion modes for PW615.

2.3 Forced Response Actuation

2.3.1 Actuator Functional Requirements & Selection

In this section we will discuss the types of actuators available and their strengths and limitations as related to the forced response experiment. The actuators for the experiment are required to meet several functional requirements:

1. **Bandwidth:** The actuator must have sufficient bandwidth or frequency response as to excite the flutter modes. The first bending mode is roughly 500-600 Hz and, as seen in Section 2.2, the apparent frequency in the absolute frame is increased for higher nodal diameters.

2. **Authority:** The actuator must have sufficient power across its frequency range to produce a measurable response. An actuator capable of operating at high frequencies is not useful if the system response is so small as to be unmeasurable (what constitutes measurable is set by the sensors, see Section 2.4).

3. **Spatial Excitation:** The actuator must be capable of exciting multiple nodal diameters. It is unknown *a-priori* which nodal diameter is the least stable, so restricting the experiment to a single nodal diameter greatly reduces the utility of the damping measurement. The modes of interest, however, are typically within an interblade phase angle of $\pm 60^\circ$ [44], corresponding to the 0^{th} to the 3^{rd} nodal diameter for the PW615.

4. **Non-intrusiveness:** A primary motivation of this work is the development of intelligent diagnostics that are minimally invasive to the engine system and thus applicable to flight engines. A brief overview of the forcing methodologies considered and their applicability to this forced response experiment is provided below.

There are two forms of actuation: structural and aerodynamic. In structural actuation, the blade is excited into vibration by directly applying force to a portion of the blade, typically through the use of piezoelectric actuators embedded into a

modified blade or applied to the surface (e.g. [36]). Direct structural excitation must operate in the rotating frame, mandating the use of an electrical or pneumatic slip ring or wireless telemetry. Both of these require extensive modifications to the fan rotor system which does not satisfy the goal of a non-intrusive methodology. Furthermore, modifications of the blade needed to incorporate the actuators alter the blade vibratory modes [36], introducing a new source of error.

Aerodynamic forcing perturbs the aerodynamic conditions of the blade in a controlled way and much work in aerodynamic forcing has been done in the interest of active stall control. Paduano [41] utilized torsional stepper motors to rotate inlet guide vanes to produce an unsteady swirl into a low-speed compressor but commercial engine fans do not have inlet guide vanes and major modifications of the engine would be required to allow the fan exit guide vanes to rotate. Spakovszky [45] demonstrated active rotor shaft whirling with magnetic bearings to produce unsteady, non-uniform tip clearances thereby perturbing the pressure field and blade loading. Rotor whirl could be introduced by off-engine shakers, but this technique can only excite the first nodal diameter.

The most common aerodynamic actuation is via unsteady air injection, perturbing the incidence or backpressure, and therefore loading, of the blade. Berndt [46] developed a motor driven high-speed valve to modulate injected flow into a compressor inlet duct. Motor limitations constrained the bandwidth of the actuator to 400Hz and motors capable of operating at the speeds required to excite flutter modes (the first bending mode corresponds to approximately 35,000RPM) are typically limited in their power capabilities, limiting their utility for this work.

Rey et al. [24] used audio-speaker based zero net mass flux (ZNMF)[8] actuators to great effect in demonstrating active flutter control and ZNMF actuators with bandwidths as high as 2kHz have been demonstrated [47]. They are compact, allowing multiple actuators to be mounted circumferentially on the inlet duct to excite multiple nodal diameters and do not require any modifications to the engine because they can be mounted upstream in the inlet duct. ZNMF actuators were selected for the

[8]also known as synthetic jets

forced response experiment but the primary concern with these actuators is power. A significant portion of this work is therefore dedicated to the design of a ZNMF actuator with sufficient authority.

2.3.2 ZNMF Actuator Dynamics & Reduced Order Modeling

A schematic overview of ZNMF actuator is shown in Figure 2-10. The actuator consists of an oscillating diaphragm within a cavity and an orifice exposed to the primary flow. As the diaphragm oscillates, it cyclically ingests and expels fluid from the primary flow. The oscillating diaphragm can be driven by piezoelectrics, a mechanical piston, or, as in Figure 2-10, an acoustic speaker. The dynamics of the actuator are characterized by its frequency response $\dot{V}_{inj}(f_d)$ the volume of air that is ingested and expelled when the diaphragm is driven at a single frequency f_d. As will be derived in Section 2.3.4, the unsteady volume flow perturbation $\dot{V}_{inj}$ is the figure of merit for the ZNMF actuator.

We now introduce a lumped element model of the actuator dynamics [48] to determine whether an adequate design is feasible. As will be shown in Section 3.1, the actuator required for the experiment is of a physical scale that violates several of the model assumption. The actuator model was thus considered a tool to assess trends in the actuator design, provide an order-of-magnitude estimate of its performance, and assist in understanding the mechanisms that govern the actuator dynamics. Chapter 3 is dedicated to experimentally characterizing the actuator performance to determine if the actuator performance is sufficient for the forced response experiment and to assess the applicability of the model for actuators in this operating regime.

The actuator dynamics are described using an equivalent circuit representation as in Figure 2-11. The electric current through the speaker voice coil due to an applied AC voltage is estimated with the coil electrical resistance R_{coil} and inductance L_{coil}. A gyrator[9] parameter, based on the coil inductance, the permanent magnet strength

[9]a circuit element that converts energy from one physical domain to another where the effort variable of one domain is proportional to the flow variable of the other (acoustic pressure and electric current respectively in Figure 2-11).

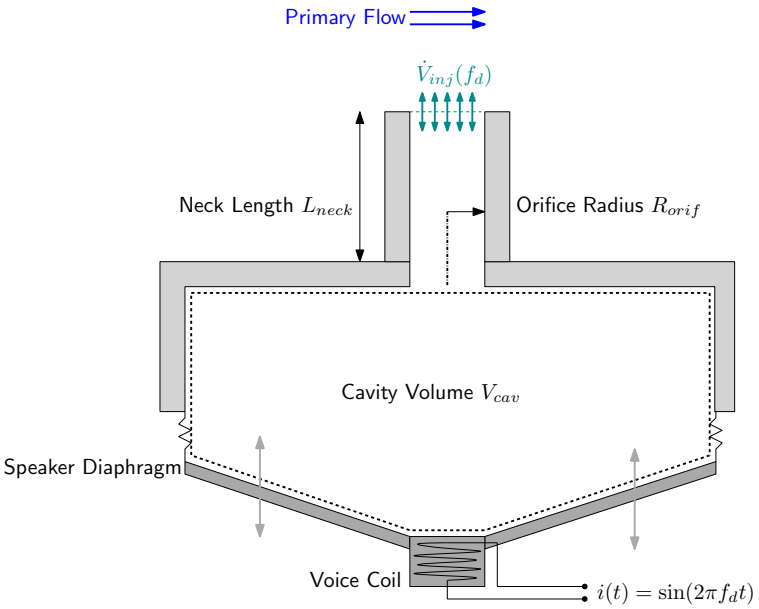


Figure 2-10: Schematic overview of acoustic speaker driven ZNMF actuator. Actuator design space defined by neck and cavity geometries and speaker properties.

B, and the diaphragm surface area S converts the electrical current into an equivalent acoustic pressure.

The diaphragm dynamics are captured with an acoustic capacitance C_{diaph}, resistance R_{diaph}, and mass M_{diaph}. Combined with the acoustic pressure, these determine the net fluid volume flow $\dot{V}_{net}$ the diaphragm can produce. A portion of the net volume flow goes into the compression of the cavity fluid $\dot{V}_{cav}$ while the remainder goes through the neck and orifice $\dot{V}_{neck} = \dot{V}_{inj}$. The neck acoustic impedance consists of an equivalent acoustic mass M_{neck}, due to the oscillating fluid mass in the neck, and resistance R_{neck}. The flow in the neck is assumed to be fully developed, producing a viscous resistance that is linear with volume flow. Loss from the sudden expansion of the jet from the neck contributes to R_{neck} with a term that is non-linear with volume flow $\sim \dot{V}_{neck}^2$. The additional resistance R_{rad} and acoustic mass M_{rad} associated with acoustic radiation from a jet into a quiescent fluid is also included.

The design space for the ZNMF actuator contains many degrees of freedom, but the majority of them correspond to the acoustic speaker. These parameters are modifiable for custom speaker designs, but are fixed for a given off-the-shelf speaker design, in which case, the primary design variables become the cavity volume, neck

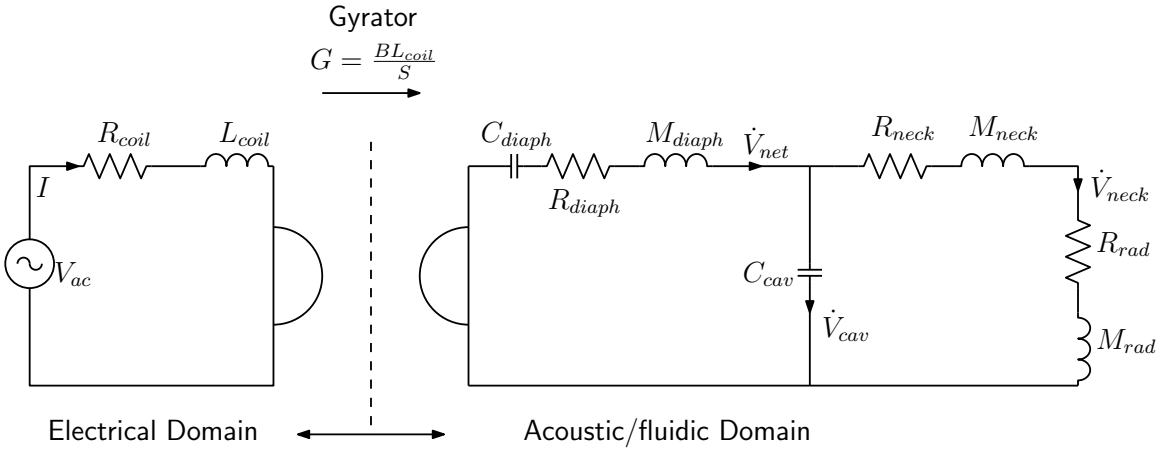


Figure 2-11: Equivalent circuit representation of ZNMF actuator (reproduced from [48]). Neck flow $\dot{V}_{neck}$ maximized when cavity volume is minimized, reducing design space to neck radius and length for a given speaker.

length, and orifice length as defined in Figure 2-10. From Figure 2-11, however, it is clear that if the speaker design variables are fixed, volume flow through the neck is maximized when the volume flow through the cavity is minimized. This occurs when the acoustic impedance of the cavity is much greater than the impedance of the neck, corresponding to minimizing the cavity capacitance, and thus volume. For any neck design, the actuator performance is improved by minimizing the cavity volume, reducing the design variables to the neck length and the orifice radius.

Acoustic speaker selection was driven by considering the maximum rated power, the physical size of the speaker, and intended frequency range of the speaker. As the primary concern is producing sufficient volume flow, the goal was to maximize the rated electrical power of the speaker. Increasing speaker maximum power, however, inevitably came with an increased speaker diameter and packing constraints around the inlet duct circumference limits the maximum size of of the speaker. The number of excitable nodal diameters ND_{max} is directly related to the number of actuators N_{act} via the Nyquist sampling theorem[10]: $N_{act} = 2\mathrm{ND}_{max} + 1$. To excite up to the third nodal diameter requires at minimum seven actuators. With the tip radius of approximately 8.5", the speaker diameter is limited to $D \leq \frac{2\pi r_{tip}}{N_{act}} \approx 7''$. Larger

[10]although higher nodal diameters can be excited with reduced power through spatial aliasing, see Section 3.6

speakers are favored because they have higher power ratings and are optimized for lower frequencies which better correspond to the 1.5kHz bandwidth the experiment needs.

The 6" audio speaker model 6MB500FT from PRV Audio was selected as it offered the highest rated power (250W continuous, 500W intermittent) for this size class of speaker.[11] The ZNMF actuator model requires multiple inputs describing the speaker's electromagnetic characteristics and the mechanical behavior of the diaphragm. Such inputs were either published by the manufacturer [49] or were derivable from the published "Small parameters", a set of standard parameters that characterize the speaker's mechanical and acoustic attributes [50].

2.3.3 Design Implications

Typical reduced order model based ZNMF actuator frequency responses for multiple neck lengths are presented in Figure 2-12 and for multiple orifice radii in Figure 2-13. The frequency response contains two modes: one associated with a diaphragm resonance and the second associated with an acoustic resonance within the cavity and neck. The frequency of the diaphragm mode is unchanged with the actuator design, but the cavity mode frequency increases with orifice radius and decreases with neck length because the neck and cavity form a Helmholtz resonator. The cavity mode's frequency dependence is consistent with the Helmholtz frequency $f_h = \frac{c_0}{2\pi}\sqrt{\frac{A_{orifice}}{L_{neck}V_{cav}}}$.

The peak mass flow of the cavity mode also increases for shorter necks due to the viscous resistance in the neck. From the assumption of fully-developed flow in the neck, the viscous resistance scales linearly with neck length $R_{visc} \sim L_{neck}$ and with orifice radius to the fourth power $R_{visc} \sim 1/r_{orif}^4$. Accordingly, the peak mass flow is more sensitive to orifice radius than neck length, as demonstrated in comparing Figure 2-13 and Figure 2-12.

The reduced order model results suggest both peak mass flow and bandwidth are achieved with large orifice radius and short neck length. The peak mass flow of 2.4% engine mass flow for this design occurs at frequency 2.4E, decreasing to 0.02% of

[11] Standard audio speakers sizes in the range of interest are 4", 5", 6", and 8"

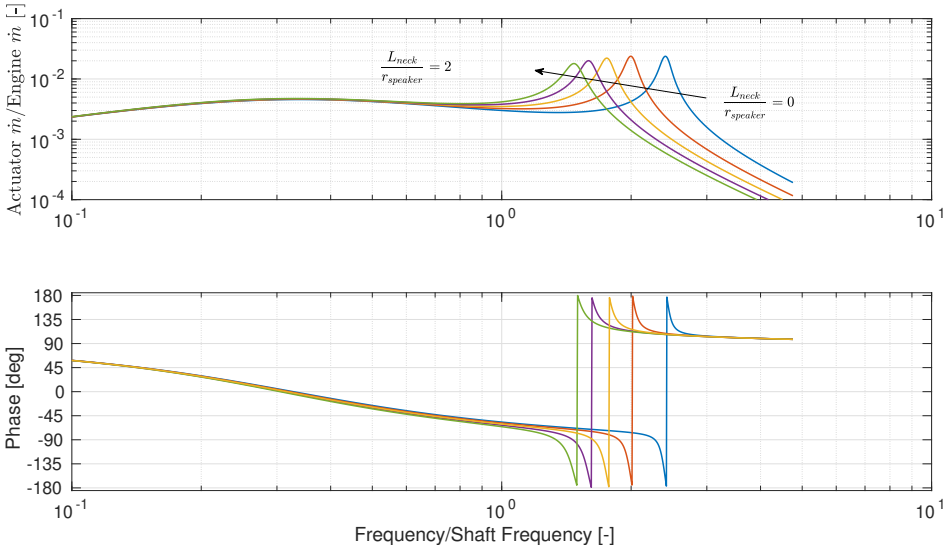


Figure 2-12: Reduced order model based ZNMF actuator for multiple neck lengths. Increase in actuator bandwidth and flow drives design to short necks.

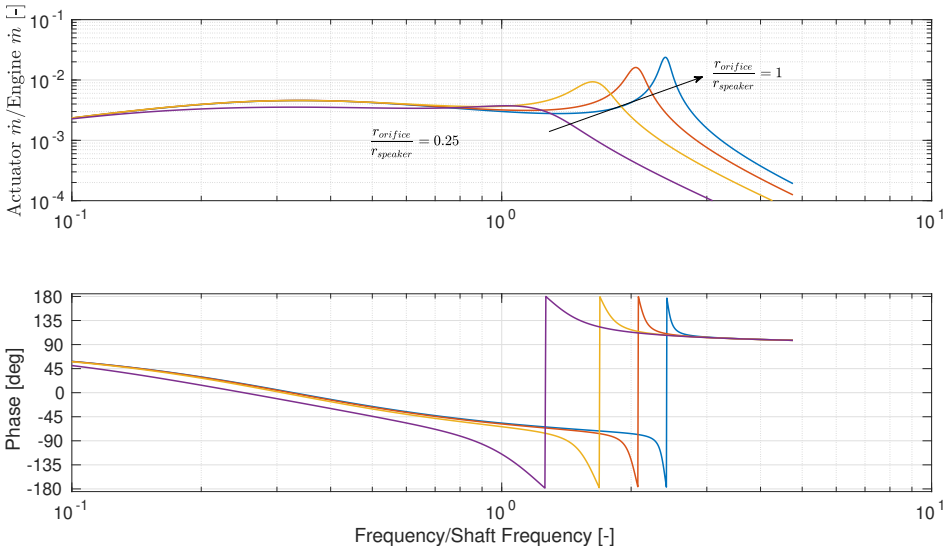


Figure 2-13: Reduced order model based ZNMF actuator performance for multiple orifice radii. High sensitivity of actuator flow to orifice radius(due to inverse quartic scaling of viscous resistance term) drives design to large orifice radius.

engine mass flow at 5E. The parameters $\frac{r_{orifice}}{r_{speaker}} = 1$ and $\frac{L_{neck}}{r_{speaker}} = 0$ are selected for the candidate actuator design.

2.3.4 Fan Flutter Reduced Order Model with Actuation

The flutter reduced order model was modified to incorporate the effects of unsteady air injection upstream of the fan to estimate the fan blade forced response. The control volume analysis in Figure 2-14 is used to include the effects of unsteady air injection in the flutter model.

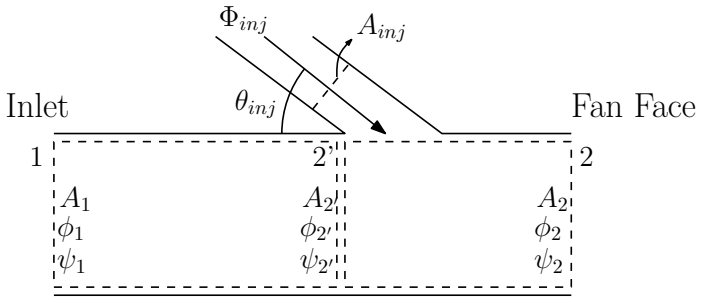


Figure 2-14: Control volume analysis to incorporate upstream air injection into flutter model. Injection angle not significant to first order for zero mean injection flow.

The flow is assumed to be incompressible[12] inviscid from stations 1 to 2', uniform and axial at station 2, and the injected air is assumed to have zero swirl ($v_{inj} = 0$). Expanding the unsteady continuity equation, subtracting the steady continuity equation, and non-dimensionalizing by the blade speed U_{tip} yields the non-dimensional axial velocity perturbation ϕ_2' at station 2.

$$\rho u_2 A_2 = \rho u_{2'} A_{2'} + \rho w_{inj} A_{inj}$$

$$\phi_2' = \phi_{2'}' + \underbrace{\Phi_{inj}' A_{inj}}_{\dot{V}_{inj}} \frac{1}{A_2}$$

We carry out the same procedure the axial momentum equation, non-dimensionalizing

[12]the assumption of incompressible flow is used for consistency with the flutter model, but is reasonable given the axial Mach number in the PW615 inlet duct is at most 0.4 at takeoff conditions.

instead by the rotor dynamic head ρU_{tip}^2, and discarding second order perturbation terms to determine the pressure perturbation ψ_2' at station 2.

$$\rho u_{2'}^2 A_{2'} + \underbrace{(\rho w_{inj} A_{inj})}_{\dot{m}_{inj}} \underbrace{(w_{inj}\cos(\theta_{inj}))}_{\text{injection axial vel.}} - \rho u_2^2 A_2 = (p_2 - p_{2'})A_2$$

$$2\bar{u}_{2'}u_{2'}' + 2\bar{w}_{inj}w_{inj}'\cos(\theta_{inj})\frac{A_{inj}}{A_2} - 2\bar{u}_2 u_2' = \frac{p_2' - p_{2'}'}{\rho}$$

$$\psi_{2'}' + 2\bar{\phi}_{2'}\phi_{2'}' + 2\bar{\Phi}_{inj}\Phi_{inj}'\cos(\theta_{inj})\frac{A_{inj}}{A_2} - 2\bar{\phi}_2\phi_2' = \psi_2'$$

To first order, and in the case of a ZNMF actuator with zero mean injection velocity $\bar{\Phi}_{inj} = 0$, the injection axial momentum (and thus injection angle) is irrelevant and the only effect is the mass flow perturbation. The figure of merit for the actuator thus becomes the magnitude of the mass perturbation[13], rather than the momentum perturbation, it can produce. This is important in the design of the actuator; the design that produces the maximum momentum perturbation does not necessarily produce the maximum mass perturbation.

We now write the model as a non-homogenous second order differential equation,

$$\mathbf{a}\ddot{\vec{x}} + \mathbf{b}\dot{\vec{x}} + \mathbf{c}\vec{x} = \mathbf{f}\vec{\Phi}_{inj}(t),$$

where $\vec{\Phi}_{inj}$ is a vector containing the unsteady spatial Fourier coefficients of the ZNMF actuator injection velocity. Both cosine and sine coefficients are included in $\vec{\Phi}_{inj}$ allowing both standing and traveling wave excitation to be simulated. As with the homogenous case, we transform this into state-space form $\dot{\vec{X}} = \mathbf{A}\vec{X} + \mathbf{F}\vec{\Phi}_{inj}$ with an arbitrary unsteady forcing distribution $\phi_{inj}'(\theta, t)$ Fourier projected to obtain $\vec{\Phi}_{inj}(t)$. The time history of the system state vector $\vec{X}$ to this forcing signal is computed to determine the bending response.

For a 1st nodal diameter forcing pattern, resonant peaks in the bending response, shown in Figure 2-15, are at frequencies of approximately 2.9E and 0.9E with forward

[13]In the incompressible framework of the model, the mass flow perturbation is equivalent to the volume flow perturbation $\dot{V}_{inj}$

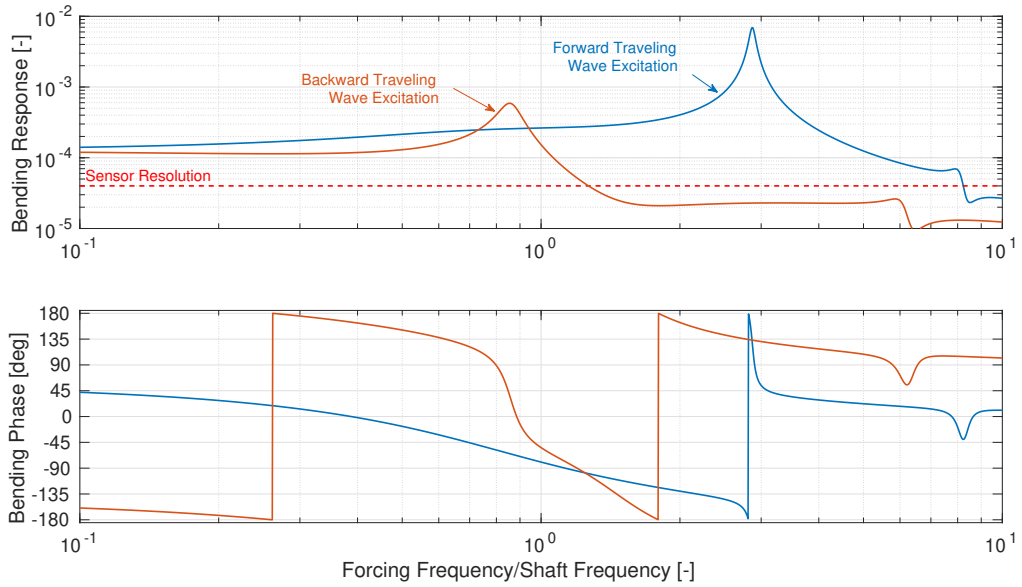


Figure 2-15: Forced response simulation with 1st nodal diameter forcing. Forward and backward traveling wave excitation excite flutter modes with response an order of magnitude greater than the sensor resolution.

traveling and backward traveling wave excitation respectively. This is consistent with the 1st nodal diameter forward and backward flutter modes in Figure 2-6. For a 3rd nodal diameter forcing pattern, two resonant peaks are observed in Figure 2-16 with forward traveling wave excitation, at frequencies of approximately 1.1E and 4.9E. Backward traveling wave excitation produces no response. This is a consequence of actuators operating in the absolute frame as discussed in Section 2.2.2. The first resonant peak in Figure 2-16 is due to to the 3rd backward nodal diameter flutter mode and the second is due to the 3rd forward nodal diameter flutter mode. The peaks are separated in frequency by twice the blade natural frequency $2\omega_b \approx 3.8$E as in Figure 2-7.

The applied forcing in Figures 2-15 and 2-16 was of the level predicted by the actuator reduced order model in Figure 2-12 for the candidate actuator design, i.e. 0.02% engine mass flow for 3rd forward nodal diameter forcing and 0.1% engine mass flow for 1st nodal diameter. All flutter resonances are seen to be an order of magnitude or more greater than the sensor resolution (discussed in Section 2.4) indicating that the candidate actuator design's performance is sufficient. Actuator performance

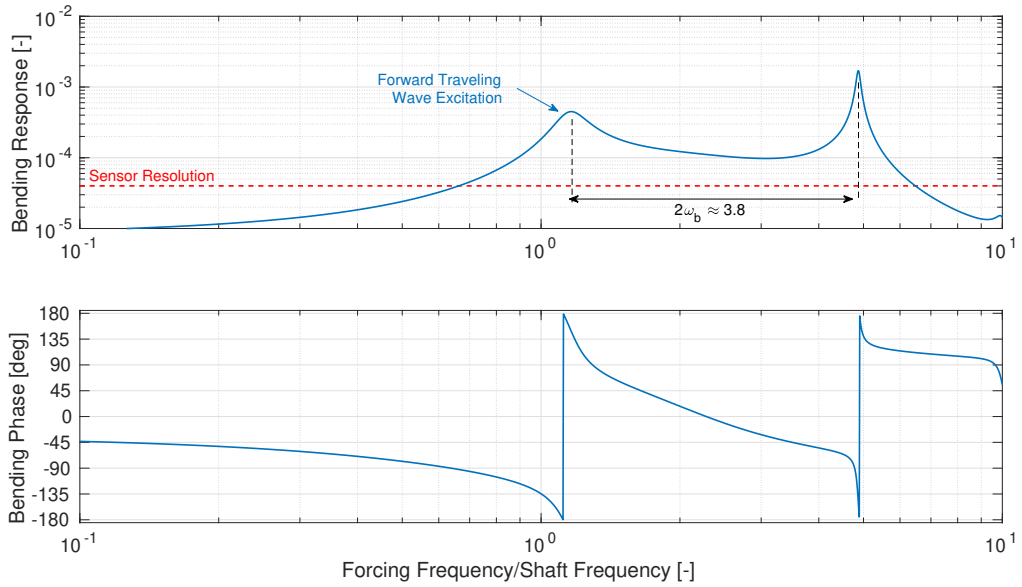


Figure 2-16: Forced response simulation with 3rd nodal diameter forcing. Forward traveling wave excitation excites both forward and backward flutter modes with response an order of magnitude greater than the sensor resolution.

across the design space is experimentally characterized in Section 3.5 to assess the reduced order model's prediction.

2.4 Blade Vibration Sensing

Blade deflections due to forcing are measured using a non-intrusive stress measurement system or "tip-timing" system, consisting of a small probe installed into the fan outer casing which contains two fiber optic filaments. Laser light is transmitted through one filament and the amount of reflected light is measured by the other. When the blade arrives at the probe, the amount of light reflected increases and the time-of-arrival (TOA) of the blade can be determined. As shown schematically in Figure 2-17, the discrepancy between the measured TOA and the expected TOA for a perfectly rigid blade (based on shaft speed and the number of blades) is a direct measure of the displacement of the blade at the location of the probe. While the displacement measured at any point of the blade is due to a combination of torsion and bending, locating the sensor at the axial position of the blade's elastic axis means

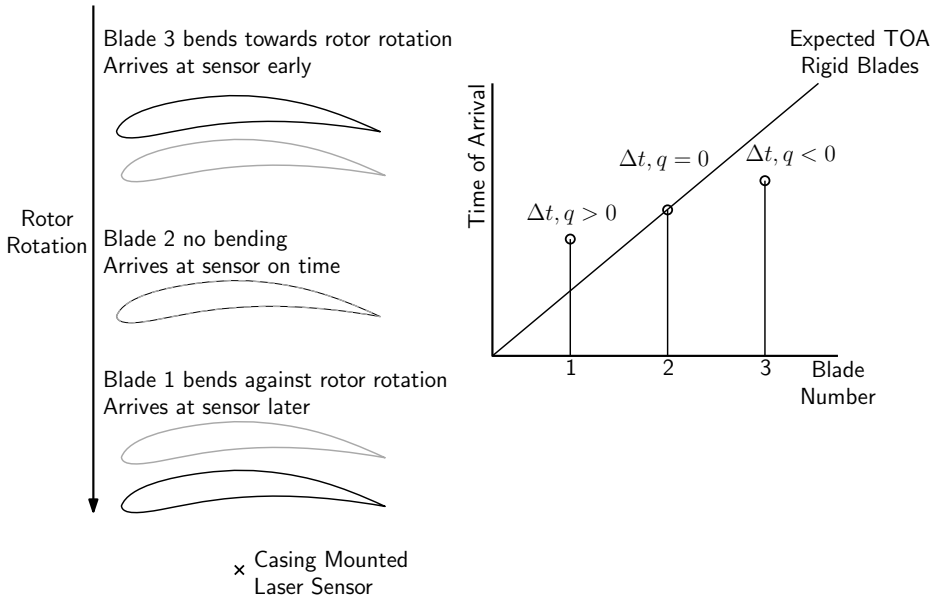


Figure 2-17: Measurement of blade bending from blade tip time-of-arrival. Bending resolution set by sensor sampling rate (smallest measurable Δt).

that only the bending component is measured.

The primary constraint imposed by the measurement system is its resolution: how small a displacement can be measured. The higher the sensor resolution, the less actuator power is required to excite a measurable response. The minimum measurable non-dimensional displacement, y_{min}, is a function of how small a discrepancy in TOA can be detected, which is in turn related to the sampling rate of the reflected light intensity. This relation is described in Equation 2.5. The minimum detectable displacement is the distance the blade tip travels in-between samples of the light intensity, which represent a binary "blade present" or "blade not present" signal.

$$y_{min} = \frac{U_{tip} t_{samp}}{r_{tip}} = \frac{(2\pi f_{shaft} r_{tip}) t_{samp}}{r_{tip}} = \frac{2\pi f_{shaft}}{f_{samp}} \tag{2.5}$$

The tip-timing system measures displacement in the circumferential direction, but bending is defined as the linear translation of a section normal to the chord line. For non-zero stagger γ, the component of bending displacement in the circumferential direction is reduced, as shown in Figure 2-18. The effective bending resolution thus decreases with stagger as $q_{min} = \frac{y_{min}}{\cos(\gamma)}$. This effect is important in high-speed fans

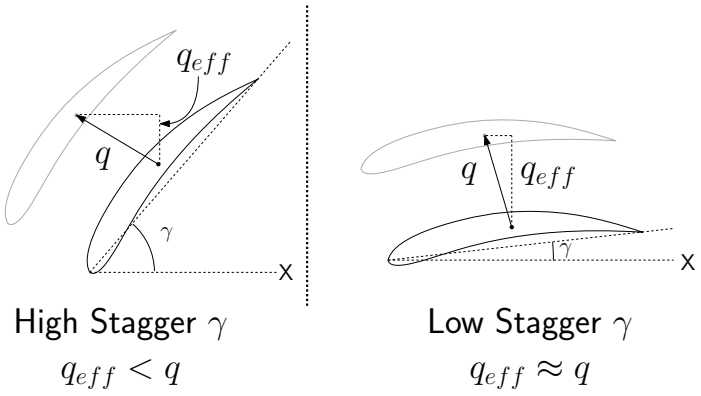


Figure 2-18: Impact of stagger on sensor resolution. Increasing stagger decreases bending resolution.

which are highly staggered at the tip. A Prime Photonics FOCIS system is considered for this experiment, offering a 100MHz sampling rate of its laser receivers [51] and results in an effective non-dimensional bending resolution of approximately 4×10^{-5} ($\approx 8\mu$m) for the PW615 at takeoff power, improving to approximately 1.3×10^{-5} ($\approx 2.5\mu$m) at idle.

2.4.1 Effective Sampling Rate

The sampling rate of the tip-timing system sets the effective resolution in blade displacement, but it does not set the rate at which bending measurements are taken (i.e. the sampling rate of bending displacement versus time). As shown in Figure 2-19, at any moment of time t_0 each of the N_b blades has an instantaneous bending displacement $q(\theta_i(t_0), t_0)$ where $\theta_i(t_0)$ is the absolute frame location of the i^{th} blade at moment t_0. A tip-timing sensor at a fixed absolute frame location θ_{sensor}, however, can only produce a measurement with the passing of a blade and the sampling rate of bending displacement versus time is thus fixed at the blade passing frequency $f_{BPF} = N_b\text{E}$, where N_b is the number of blades.

As a result, flutter modes above the Nyquist frequency, $\frac{N_b}{2}\text{E}$ in the absolute frame, become unobservable, regardless if the actuator has sufficient bandwidth to excite them. The PW615 has 15 blades and thus a Nyquist frequency of 7.5E. The absolute frame frequencies of the 6^{th} and 7^{th} forward nodal diameter bending modes are above

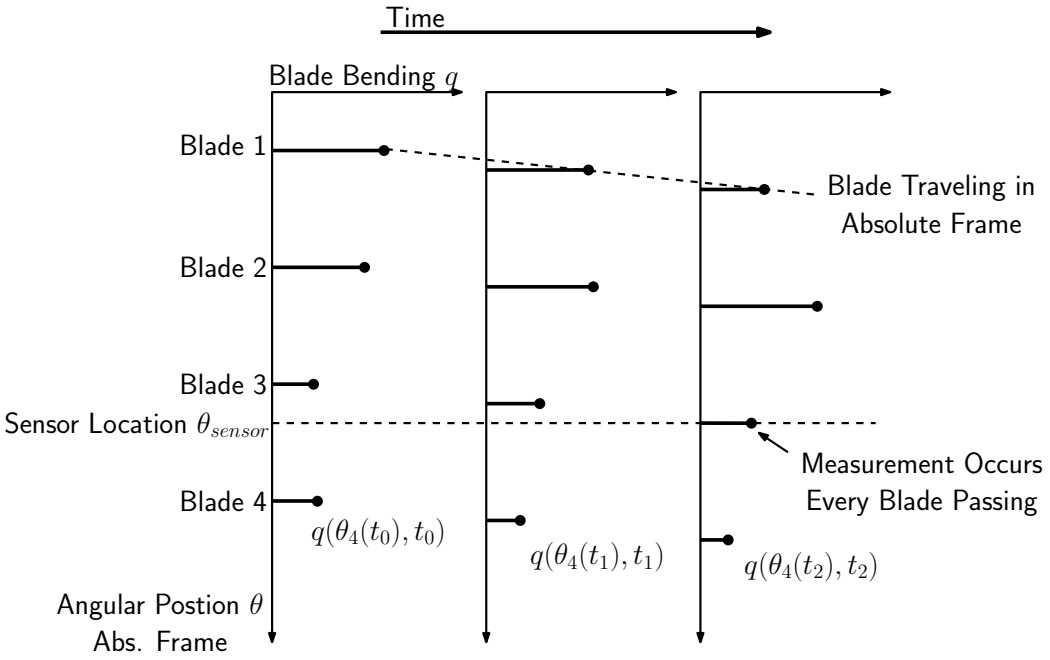


Figure 2-19: Effective sampling rate of blade bending versus time limited to blade passing frequency in tip-timing systems.

7.5 (see Figure 2-6), rendering these modes unobservable. This limitation becomes more restrictive at lower shaft speeds as the non-dimensional frequency increases, rendering modes of interest potentially unobservable.[14]. For example, the first blade bending frequency for the PW615 is 1.9E at take-off and increases to 5.5E at idle, making the 3$^{\text{rd}}$ forward nodal diameter and higher unobservable at idle. If flutter modes at frequencies higher than blade passing are of interest, tip-timing sensors are insufficient and on-blade sensors must be used.

2.4.2 Requirements on Sensor Count

Finally, there is the question of sensor count. Because the different flutter mode frequencies are close to the blade natural frequency in the relative frame, on-blade sensing requires high sensor counts to distinguish the flutter modes via a spatial Fourier transform. The sensor requirement for on-blade sensing is thus determined by the Nyquist criterion $N_{sensor} = 2\text{ND}_{max} + 1$. The spectral separation achieved

[14]The blade natural frequency decreases with shaft speed due to reduced gyroscopic stiffening, but the decrease in shaft speed dominates

by sensing in the absolute frame reduces the required sensor count as modes are distinguishable by their observed frequency (identification and active control of flutter modes has been demonstrated with a single sensor [24]).

An exception is when two modes with similar frequencies are excitable with the same forcing pattern. For example, the 2$^{\text{nd}}$ forward and 6$^{\text{th}}$ backward nodal diameter modes[15] in Figure 2-6 are both near a frequency of 4E. In such cases it may be necessary to increase sensor counts so the appropriate spatial Fourier transform can be performed to distinguish the signals from each mode. As will be shown, however, this is not required for the PW615.[16]

2.5 System Identification

The goal of system identification in this context is to estimate the flutter eigenvalues, and thus the mode damping, from the measured bending response to a given input signal. An overview of the system identification process is provided in Figure 2-20.

The process begins with the simulation of a bending response time signal in the "virtual experiment", the top dashed box in Figure 2-20. A dynamic simulation is performed with the actuator input signal $v(t)$s (a swept sinusoid or "chirp" across the frequencies of interest), the known actuator dynamics, and the flutter model to produce a time sequence of the flutter model state vector $X(t)$. The spatial Fourier coefficients of the bending mode are used to reconstruct the time sequence of a tip-timing sensor output at a given circumferential location, $y(t)$ in Figure 2-20.

The sensor resolution from Section 2.4 is incorporated by setting samples with magnitude less than the sensor resolution to zero. When noise sources are modeled, this process can be repeated multiple times and ensemble averaged to assess the improvements from averaging. The virtual experiment simulates an engine test with actuators and tip-timing sensors installed, denoted as the "physical" experiment in

[15]The 6$^{\text{th}}$ backward nodal diameter mode is excitable with 2$^{\text{nd}}$ forward nodal diameter forcing forcing due to appearing forward traveling in the absolute frame and spatial aliasing of the air injection pattern of the ZNMF actuators, see Section 3.6

[16]the exception being for two modes at 90% of take-off speed

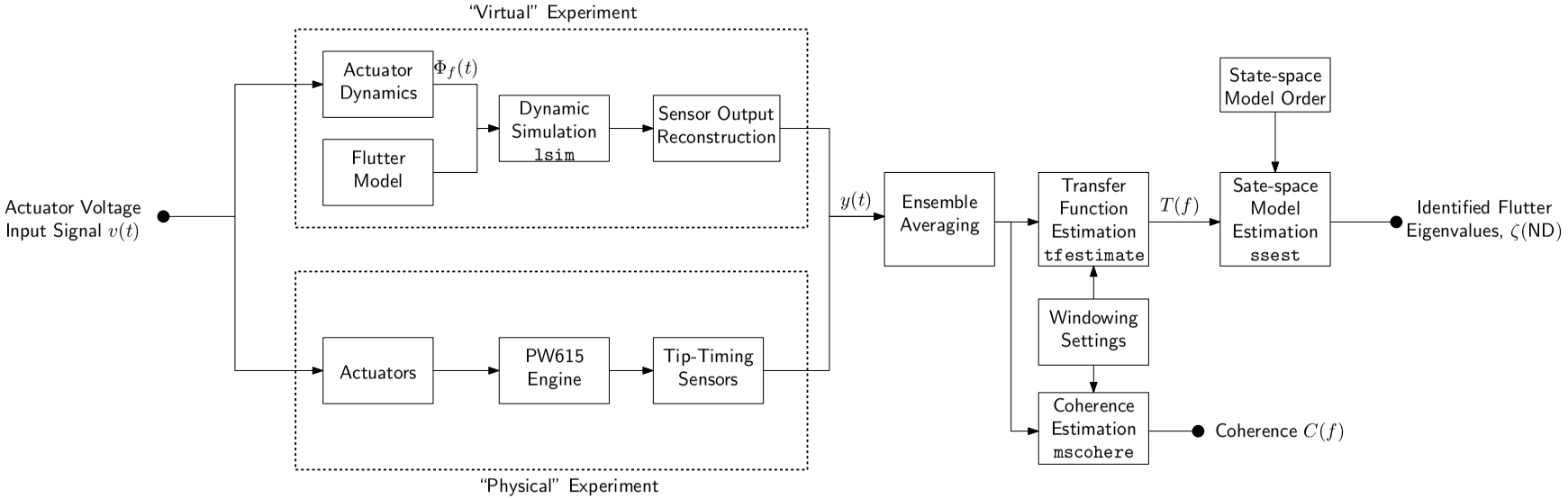


Figure 2-20: System identification process to estimate flutter damping from experiment data. Methodology assessed with virtual experiments.

Figure 2-20. We then estimate the frequency domain transfer function, $T(f)$ that represents the flutter dynamics from the time signal of the tip-timing sensor and the input signal. A state-space model is fit to the transfer function, from which we can infer the flutter eigenvalues and damping for each nodal diameter, ζ(ND). Transfer function estimation and eigenvalue inference are discussed in the next two sections.

2.5.1 Transfer Function Estimation

We now derive a frequency domain transfer function from the flutter response time signal. The transfer function $T_{yx}(f)$ is estimated as

$$T_{yx}(f) = \frac{P_{yx}(f)}{P_{xx}(f)} \tag{2.6}$$

where $P_{yx}(f)$ is the cross power spectral density between the output and input signals y and x and $P_{xx}(f)$ is the power spectral density of the input signal. The magnitude squared coherence is also estimated as

$$C_{yx}(f) = \frac{|P_{yx}(f)|^2}{P_{xx}(f)P_{yy}(f)}$$

and is a measure of how much of the output signal power at a given frequency is correlated to the input signal. Coherence values near unity indicate a high correlation between the input and output signals and coherence values near zero indicate low correlation, i.e. the output power at that frequency is primarily from noise. It is used in this context to identify the portion of the total transfer function estimate that is useful for system identification.

Power spectral densities are estimated using Welch's averaged periodigram method to reduce the variance in the transfer function and coherence estimates. Welch's method uses spectral windowing, and requires window functions, length, and overlap to be specified. Improper windowing can increase error in the damping estimate and this effect is quantified in Section 5.1. The sensor-output-to-actuator-voltage-input transfer function represents the joint transfer function $T_{yv}(f) = A(j\omega)G(j\omega)|_{\omega=2\pi f}$,

containing both the actuator dynamics $A(s)$ and the flutter dynamics $G(s)$ in Fig. 2-1. In this joint transfer function there is no discrimination between resonances due to flutter modes and those due to actuator modes. With an a-priori characterization of the actuator dynamics, however, the forcing function $\Phi_f(t)$ can be determined from the input signal $v(t)$, and therefore the sensor output to forcing transfer function $T_{y\Phi_f}(f)$ can be estimated which contains only the flutter dynamics. The impact of actuator dynamics on damping estimation is assessed later in Section 4.2.

Figure 2-21 shows an example of an estimated sensor output to forcing transfer function. A single resonant peak occurs at a frequency of 2.9E due to the 1st forward nodal diameter flutter mode. The frequencies of low coherence in Figure 2-21 are due to the presence of simulated inlet turbulence (process noise).

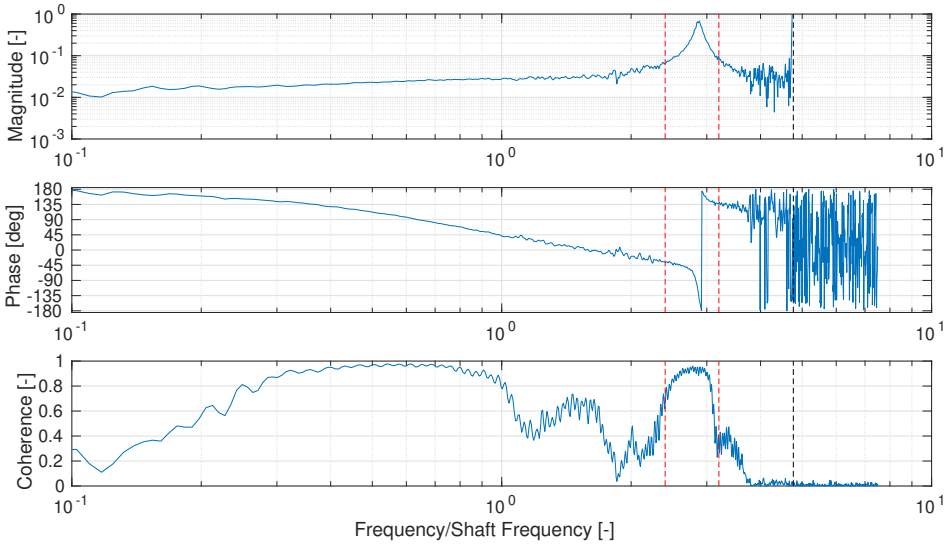


Figure 2-21: Example sensor-to-forcing transfer function from virtual experiment with process noise. Resonant peak due to 1st forward nodal diameter flutter mode.

2.5.2 Eigenvalue Inference from Estimated Transfer Function

With the sensor output to forcing transfer function, parametric system identification is used to estimate the eigenvalues, and thus damping, of the flutter modes excited by the forcing. A "black-box" approach is taken where no mathematical structure is imposed on the identified model and a state-space model is estimated using a

prediction error minimization algorithm to fit a state-space model to the estimated transfer function [52][17].

An additional input to the system identification function is the model order which determines the number of states in the state-space model. Increasing the model order substantially above the number of modes excited from a particular forcing pattern did not generally improve accuracy (with accuracy being limited to the quality of the estimated transfer function) and can obfuscate which of the identified eigenvalues represents the flutter mode. A heuristic was to limit model order to $2(i+1)$ where i is the number of modes excited,[18]. For example, a model order of four for 1^{st} forward nodal diameter forcing and eight for 3^{rd} forward nodal diameter forcing.

From the eigenvalues of the identified state-space model, we can find the flutter damping ratio using Equation 2.4 with the growth rate σ and absolute frame frequency ω_{abs} are given from the identified state-space model eigenvalues. Vertical dashed red lines in the transfer function, Figure 2-21, mark the region of high coherence surrounding the 1^{st} forward nodal diameter flutter mode response which was used for system identification. The identified eigenvalue, shown in Figure 2-22 on the complex plane, is nearly coincident with the analytical eigenvalue from the flutter model. The error in frequency ω, growth rate σ, and damping ratio ζ are all below 1% for this specific case. Quantification of experimental error in the face of random noise is discussed in Chapter 4.

[17] as implemented in the MATLAB system identification toolbox function `ssest`

[18] The factor of 2 is present as each identified mode is described with a pair of complex conjugate eigenvalues.

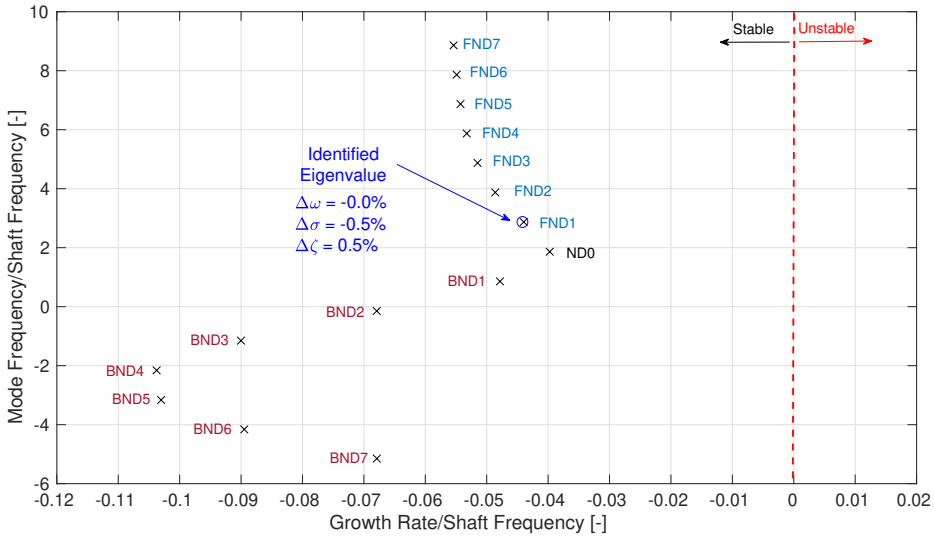


Figure 2-22: Example identification of 1st forward nodal diameter flutter mode, blue, with damping ratio estimated within 1%.

2.6 Summary of Modeling Framework Development

A reduced order model of a flutter forced response experiment has been implemented. The model captures the flutter dynamics for the PW615 fan and the effect of actuation with upstream air injection with zero-net massflux (ZNMF) actuators. A reduced order model of the actuator was used to estimate performance trends with actuator design parameters. A forced response simulation with the actuator performance predictions indicated that the actuator can sufficiently excite the flutter modes of interest to be measured. A tip-timing system has been specified to measure the blade bending response. While the system imposes limitations, in terms of bending resolution and sampling rate, it is demonstrated that these limitations do not prevent the measurement of the flutter modes of interest. Finally, a system identification framework has been established to infer the flutter damping from the measured (or simulated) unsteady bending response measurements.

Chapter 3

Experimental Characterization of ZNMF Actuator Performance

In this chapter we answer the question "what is the performance of the candidate ZNMF actuator and how does this performance depend on the actuator design?" We describe the development of a novel methodology to experimentally characterize the actuator frequency response in order to measure the actuator performance across the design space. These measured frequency responses are implemented in the flutter modeling framework and are used to assess if the actuator can sufficiently excite the flutter modes in Chapters 4 and 5.

The experimental results in this chapter will show that, in contrast to the predictions of the actuator reduced order model, there is no single best geometry for the forced response experiment, and a range of geometries may be required, depending on the flutter mode of interest. Further, it will be shown that, while the actuator reduced order model accurately predicts some aspects of the actuator dynamics, it does not capture the dependence of key performance metrics (bandwidth and peak flow) on the actuator geometry. This demonstrates the need for experimental characterization of actuators at this scale for future forced response experiments.

3.1 Motivation for Experimental Characterization

Although the reduced order model in Section 2.3 has been shown to capture ZNMF actuator performance [47, 48, 53], actuators in the literature and the current actuator design differ in physical scale. The current design has two to five times the diameter of those found in the literature, and this disparity violates three assumptions made in the model.

1. Inherent to lumped element modeling is the assumption that the characteristic length scale is much less than the wavelength of the phenomena of interest [48]. The characteristic length scale is the speaker diameter $D_{speaker}$ and the wavelength is that of the acoustic waves $\lambda_{acoustic}$ at the driven frequency f_{driven}. At some frequencies desired for this experiment, the speaker diameter is more than half the acoustic wavelength.

$D_{speaker}/\lambda_{acoustic}$	f_{driven}
0.013 - 0.65	0.1E - 5E

2. The model assumes fully developed flow in the neck. This assumption is only valid if the thickness of the neck boundary layer is equal to or greater than the orifice radius. For an infinite oscillating flat plate, the viscous length scale is of the order $\sqrt{\frac{2\nu}{\omega}}$ where ν is the kinematic viscosity and ω the angular frequency of the oscillation [54]. The criteria for fully developed flow is therefore $R_{orifice}\sqrt{\frac{\omega_{acoustic}}{2\nu}} \ll 1$. This criterion is violated by several orders of magnitude for even the smallest orifice considered.

$R_{orifice}\sqrt{\frac{\omega_{acoustic}}{2\nu}}$	f_{driven}
45 - 330	0.1E - 5E

3. Inherent in assuming Poiseuille flow is that the flow in the neck is incompressible. An unsteady flow can only be considered incompressible if it is acoustically compact, i.e. when $\left(\frac{\omega L}{c_0}\right)^2 \ll 1$ where ω is the angular frequency, L is the characteristic length scale of the flow, and c_0 is the speed of sound of the medium

[54]. The validity of this criterion is strongly dependent on the specific neck length of the actuator as shown below:

$\left(\frac{\omega_{acoustic} L_{neck}}{c}\right)^2$	$\frac{L_{neck}}{r_{speak}}$	f_{driven}
0.0002 - 0.50	0.33	0.1E - 5E
0.007 - 17.5	2.0	0.1E - 5E

For the shortest neck length, the assumption of acoustic compactness is valid throughout the frequency range of interest. For the longest neck, however, the assumption becomes invalid at a frequency of 1E.

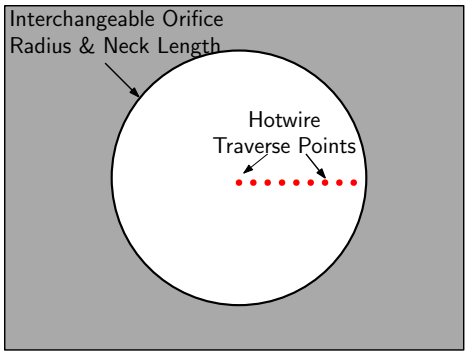
Because the assumptions of the actuator reduced order model have limited applicability for the present experiment, an experimental assessment of the ZNMF actuator performance is thus required.

3.2 Technical Approach

The goal of the experimental characterization is to determine whether the actuator has sufficient authority at the frequencies of interest by measuring the volume flow of the actuator as a function of the driven frequency. A constant temperature hotwire anemometer is used to measure the unsteady axial velocity when the speaker is driven a single frequency. The hotwire is traversed radially, as in Figure 3-1a, and the measurement repeated at each radial location. The separate measurements are phase-locked to derive the instantaneous axial velocity distribution $v_x(t, r)$ for the driven frequency. Assuming axisymmetry, the volume flow is found by spatially integrating the axial velocity.

$$\dot{V}(t) = \int_0^{r_{orifice}} 2\pi r v_x(t, r) dr$$

The temporal Fourier coefficient of $\dot{V}(t)$ at the driven frequency f_d is computed to determine the volume flow response magnitude and phase at the driven frequency. The process is repeated over the frequency range to derive the volume flow frequency



(a) Hotwire traverse - front view

$\frac{L_{neck}}{r_{speaker}}$ \ $\frac{r_{orifice}}{r_{speaker}}$	0.33	0.5	0.75	1
0.33	0.50	0.33	0.22	0.17
0.50	0.75	0.50	0.33	0.25
0.67	1.13	0.75	N/A	N/A
1.0	N/A	N/A	0.67	0.50

(b) Design space - values of $L_{neck}/D_{orifice}$

Figure 3-1: Hotwire traverses used to determine actuator performance across design space

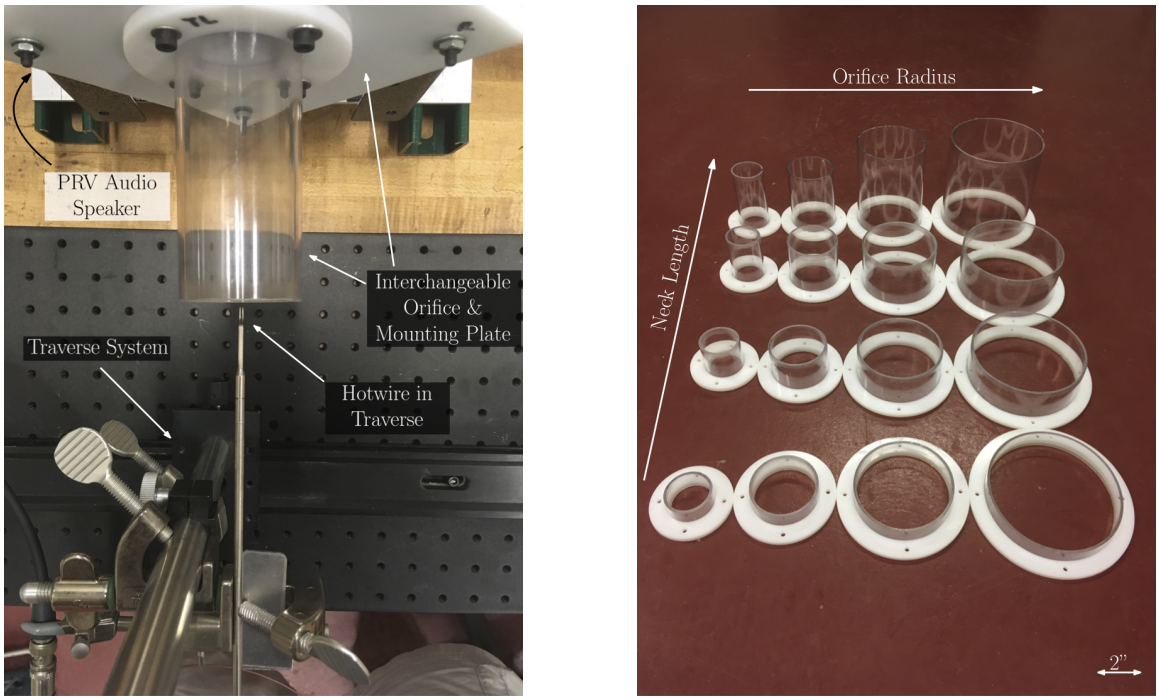
response function for actuator geometries across the design space in Figure 3-1b.[1]

3.3 Experimental Setup

The actuator consists of a PRV Audio 6MB500FT speaker mounted vertically and flush to a polycarbonate plate to form the cavity, as in Figure 3-2a. A separate plate was manufactured for each orifice radius and polycarbonate tubes of varying length, shown in Figure 3-2b, were attached concentrically to the plate orifice to form the neck. A Dantec 55P11 miniature hotwire probe is mounted within the traverse system so the probe is flush with the orifice face and at the centerline height. The traverse system consists of a rail mounted to an optical table with a lockable carriage and, the hotwire was traversed increments of the probe width (1.5mm). The hotwire probe was driven by a Dantec 56C17 constant temperature anemometer bridge with an overheat ratio of 0.5.

The hotwire was calibrated in a free jet with adjustable upstream pressure. A pitot-static probe was mounted approximately 3 hotwire widths adjacent and a Scanivalve DSA3217 1PSID pressure scanner was used to measure the dynamic pressure. The total temperature in the free jet settling chamber was continuously monitored and did not deviate more than 0.1°C throughout a calibration. After changing the

[1]Tests were not conducted for entries marked N/A due to lack of appropriate length circular tubing in the required radius



(a) Hotwire and actuator

(b) Orifices sweep design space

Figure 3-2: ZNMF actuator characterization experiment setup. Hotwire traverses of interchangeable orifices used to characterize frequency response across design space

free jet velocity, data collection was delayed a minimum of 20 flow-through times of the settling chamber to ensure flow uniformity. Pressure data was sampled at 20Hz and the hotwire voltage at 5kHz, with both time averaged over 5 seconds. A data point was obtained in the absence of flow to measure the zero velocity voltage and a fourth-order polynomial fit is used to form the calibration curve.

The need for phase-locking time sequences at separate radial positions, meant that particular attention needed to be paid to the data acquisition process, described schematically in Figure 3-3, to ensure data coherency. A waveform consisting of a series of single frequency sinusoids covering the desired frequency range (0.1E - 5E) was first generated. Each sinusoid was repeated for between 150 and 600 periods to ensure the actuator flow starting transient decayed and periodic flow was achieved. A National Instruments NI-9263 digital-to-analog voltage output module produced the voltage signal to the audio amplifier which in turn drove the actuator speaker. The output waveform was produced at an update rate of 100kHz (the maximum possible

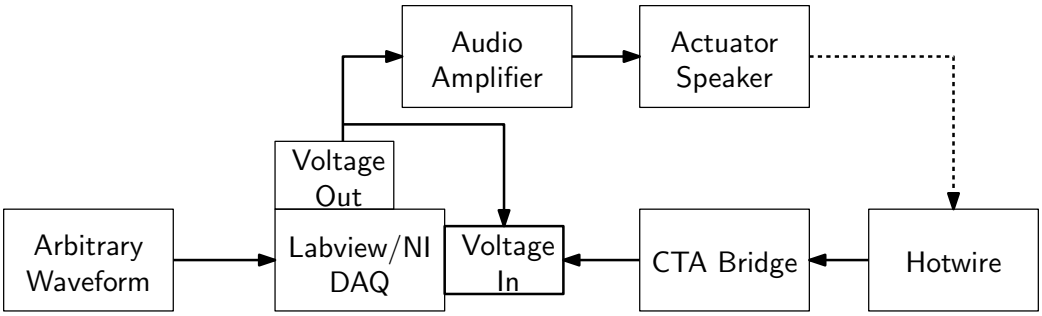
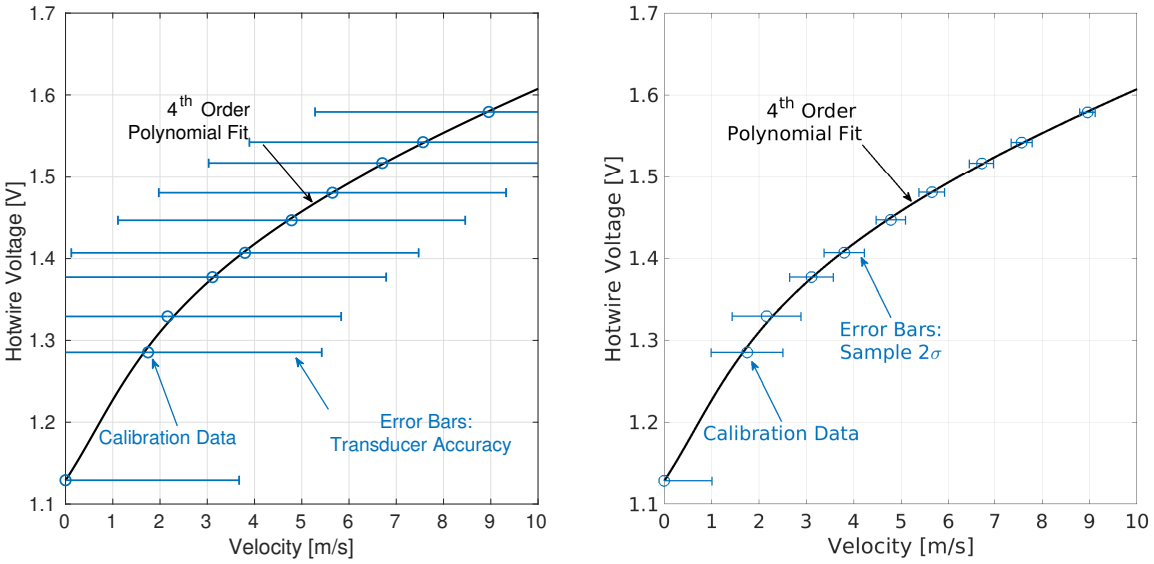


Figure 3-3: Data acquisition process to ensure measurements at separate radial positions are phase-locked as needed for accurate transfer function phase estimation.

from the output module) to minimize spectral leakage due to discretization of the desired waveform. The analog voltage output signal of the CTA bridge was sampled at 20kHz using a NI-9215 voltage input module. An integer divisor of the voltage output rate was used to ensure the input was a fixed sub-sampling of the output. Amplifier voltage output and hotwire voltage sampling were driven by the same clock to ensure synchronization (e.g. the 4^{th} hotwire voltage sample always corresponded to the same moment in time as the 20^{th} amplifier output sample). Strict temporal synchronization between the signals is needed to properly capture the phase of the actuator transfer function.

3.3.1 Hotwire Calibration

The 1PSID DSA3217 pressure transducer was the lowest range, highest accuracy, transducer available for calibration purposes. With its quoted accuracy of $\pm 0.12\%$ of full scale, implying a maximum dynamic pressure error of 8.3 Pascals, 3.7 m/s at standard conditions. Peak velocities for the smallest orifice reached 25 m/s, corresponding to 12% error, although, velocities in the larger orifices were typically in the range of 3-8 m/s. As in Figure 3-4a, this results in excessively large error for the calibration. The resolution of the scanner, however, exceeds the accuracy as in Figure 3-4b shows the same calibration with error bars representing two standard deviations of the 100 samples taken for time averaging. A higher accuracy calibration is desirable and an area for future work is thus to assess these results with an



(a) Error bars: quoted pressure transducer accuracy

(b) Error bars: 2 sample standard deviations

Figure 3-4: Hotwire calibration curves with error bars. High error motivates refined calibration technique for future work.

improved hotwire calibration via low-speed methods found in the literature [55–57] or a specialized calibrator capable of calibrating to velocities as low as 0.02 m/s (such as the Dantec Streamline Pro).

The low-speed calibration data show the expected behavior with regard to King's law. King's law, derived from convective heat transfer around a circular cylinder, states the hotwire voltage and free-stream velocity are related by $E^2 = A + BU^n$ where E is the voltage, U the free-stream velocity, and A, B, n are fitting coefficients. While n is typically in the range of 0.4-0.5 for velocities of interest, it is expected to increase to unity as the velocity (and thus wire Reynolds number) approaches zero [56]. Values of n as high as 0.75 have been observed in the literature for velocities in the 0-2 m/s range [57]. The calibration data in Figure 3-4 was fit with King's law with multiple exponents as well as the conventional 4^{th} order polynomial [58] in Figure 3-5. The lowest velocity data is best represented with a higher exponent of 0.75, with the fit improving with lower exponents at higher velocities; the 4^{th} order polynomial captures the changing exponent behavior.

Even with the uncertainty in magnitude of the volume flow, the high amount of

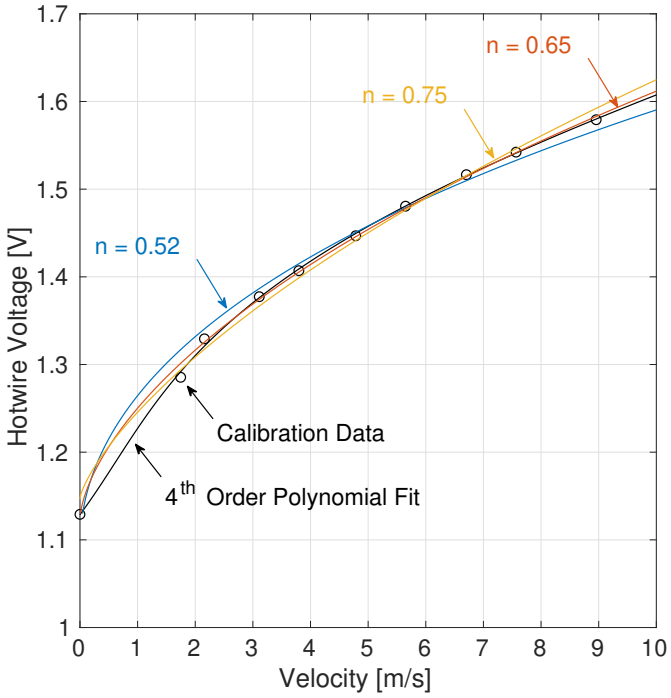


Figure 3-5: Low-speed calibration data fit to King's law trend from literature, providing evidence calibration is meaningful.

actuator flow margin to be discussed in Section 5.2.3 suggest the final actuator design is still sufficient to conduct the experiment. Further, there is much less uncertainty in the observed bandwidth, shape of the frequency response, and in comparisons between frequency responses. For a given calibration curve, these differences are purely due to differences in hotwire voltage which has a much lower error of 0.7%. As the calibration procedure described represented the best capable within the resources available and the low-speed calibration data matched expected trends from King's law, it was deemed sufficient to proceed with the analysis and design of experiment.

3.3.2 Hotwire Data Processing

A typical centerline velocity trace for single frequency voltage excitation is shown in Figure 3-6. The flow is closely periodic with only a 3% variation in peak velocity between cycle periods. A single hotwire anemometer only measures velocity magnitude of a directional one-dimensional flow and cannot distinguish reverse flow. The

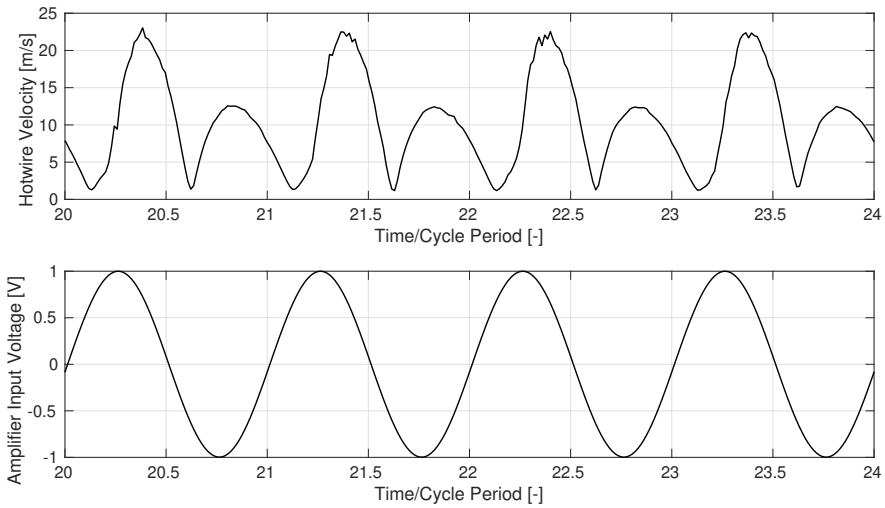


Figure 3-6: Measured centerline velocity periodic for single frequency excitation. Development of transfer function estimation procedure required as hotwire only measures velocity magnitude.

hotwire velocity of the top plot thus represents the absolute value of the directional velocity response[2]. The transfer function estimation process of Section 2.5 is inapplicable here as the power from a frequency f of the input signal appears at frequency $2f$ and higher harmonics in the output power, which is not captured in the cross power spectral density.

We thus wish to reconstruct the output of the system[3] using the a-priori information that the output is due to excitation by a single frequency sinusoidal input and by employing the discrete Fourier transform coefficients of the measured absolute value signal and the known Fourier series expansion of the absolute value of a sinusoid. Let us define a sinusoid $y(t)$ of arbitrary magnitude A, phase ϕ, angular frequency ω, and its absolute value $y_a(t)$:

$$y(t) = A\sin(\omega t + \phi)$$
$$y_a(t) = |y(t)| = |A\sin(\omega t + \phi)|.$$

[2]the directional velocity would have negative values indicating reverse flow
[3]specifically the Fourier coefficient of the system output at the driven frequency

The function $y_a(t)$ is periodic with period $t = 0.5$. Let $f(t) = y_a(t)$ over this domain

$$f(t) = |\sin(\omega t)|, 0 \leq t \leq 0.5$$
$$f(x) = |\sin(x)|, x = \omega t, 0 \leq x \leq \pi.$$

The Fourier series expansion of $f(x)$ is

$$f(x) = \frac{a_0}{2} + \sum_{k=1}^{k=\infty} a_k \cos(2kx)$$
$$a_0 = \frac{\pi}{4},\ a_k = \frac{-4}{\pi(4k^2 - 1)}.$$

We define the following coefficients from the Fourier transform Y_a of the absolute value signal $y_a(t)$:

$$Y_{a,0} = Y_a(0) = \frac{1}{T}\int_0^T y_a(t)dt$$
$$Y_{a,k} = Y_a(e^{j2\omega}).$$

The original magnitude A can be derived from the Fourier transform coefficients, using linearity, as

$$A = \frac{\pi}{2}Y_{a,0} = |Y_{a,k}|\frac{\pi(4k^2 - 1)}{4}. \tag{3.1}$$

To derive the phase of the signed sinusoid, the time shifting property of Fourier series is first used to re-write the coefficients a_k:

$$f(\omega t) \longrightarrow f(\omega t + \phi)$$
$$a_n \longrightarrow a_n e^{jn\phi}, n = 2k$$
$$a_k \longrightarrow a_k e^{j2k\phi}.$$

Writing the coefficient a_k in polar form we obtain,

$$a_k = -\frac{4}{\pi(4k^2-1)} = e^{j\pi}\frac{4}{\pi(4k^2-1)} = e^{j\pi}|a_k|.$$

The original sinusoid's phase ϕ can be found from $\angle Y_{a,k}$, the argument of the Fourier coefficient $Y_{a,k}$ as

$$\begin{aligned} e^{j\angle Y_{a,k}} &= e^{j\pi}e^{j2k\phi} \\ \phi &= \frac{\angle Y_{a,k} - \pi}{2k}. \end{aligned} \tag{3.2}$$

Equations 3.1 and 3.2 show the relation between the original magnitude A and phase ϕ and the Fourier coefficients of the measured absolute value signal. The reconstructed phase is limited to the domain $[-\pi, 0]$ rather than $[-\pi, \pi]$ and is thus accurate only to $\phi \pm \pi$ because the absolute value of $\sin(\omega t)$ is identical to that of $\sin(\omega t + \pi)$. The process described is repeated for each driven frequency to estimate the full transfer function $T_{vy}(f)$, and the same procedure is performed on the unsteady volume flow $\dot{V}(t)$.

The traditional definition of coherence below between the amplifier voltage $V_{amplifier}(t)$ and the reconstructed velocity signal $U_{recon}(t)$ results in unity coherence values, eliminating its utility, because noise power is not captured in the reconstructed signal which is a pure sinusoid at the driven frequency.

$$\begin{aligned} C_{yx}(f_{driven}) &= \frac{|P_{yx}(f_{driven})|^2}{P_{xx}(f_{driven})P_{yy}(f_{driven})} \\ x(t) &= V_{amplifier}(t) \\ y(t) &= U_{recon}(t). \end{aligned}$$

We can derive an alternative definition using the absolute value of the amplifier voltage, and comparing it to the measured velocity from the hotwire $U_{hotwire}(t)$. The goal of this new coherence definition is not to estimate precisely the value of the coherence were the directional velocity signal available, but rather to provide a metric for the

signal-to-noise ratio that assesses the quality of the data and provide guidance in the characterization experiment.

$$C_{yx}(f_{driven}) = \frac{|P_{yx}(2f_{driven})|^2}{P_{xx}(2f_{driven})P_{yy}(2f_{driven})} \tag{3.3}$$
$$x(t) = |V_{amplifier}(t)|$$
$$y(t) = U_{hotwire}(t).$$

The reconstruction procedure was tested using an example transfer function in Equation 3.4 designed to have similar dynamic behavior to that expected from the actuator. A sinusoidal input signal was constructed as described in 3.3 and the system output produced through a dynamical simulation. Taking the absolute value of the system output mimicked the effect of the hotwire. The reconstruction procedure was applied and Welch's method used to estimate the transfer function value at the driven frequency.

$$G(s) = 10^5 \frac{s - 2\pi(-40 + 100j)}{(s - 2\pi(-20 + 60j))(s - 2\pi(-10 + 200j))} \tag{3.4}$$

The transfer function estimate using the reconstruction procedure is in good agreement with the analytical transfer function as in Figure 3-7, which compares the analytical transfer function and the estimate from the procedure. The limitation of estimating the phase, however, is apparent at approximately 250Hz where the analytical phase decreases and wraps from $-\pi$ to π but the estimated phase wraps from $-\pi$ to 0. The reconstruction procedure, however, is easily corrupted by noise as shown Figure 3-8, in which -2dB noise was added to the system output prior to estimating the transfer function. The estimate from the reconstruction procedure, is poorer than that if the directional system output is used. The alternate coherence definition, however, correctly indicates where noise has corrupted the transfer function estimate, proving its utility.

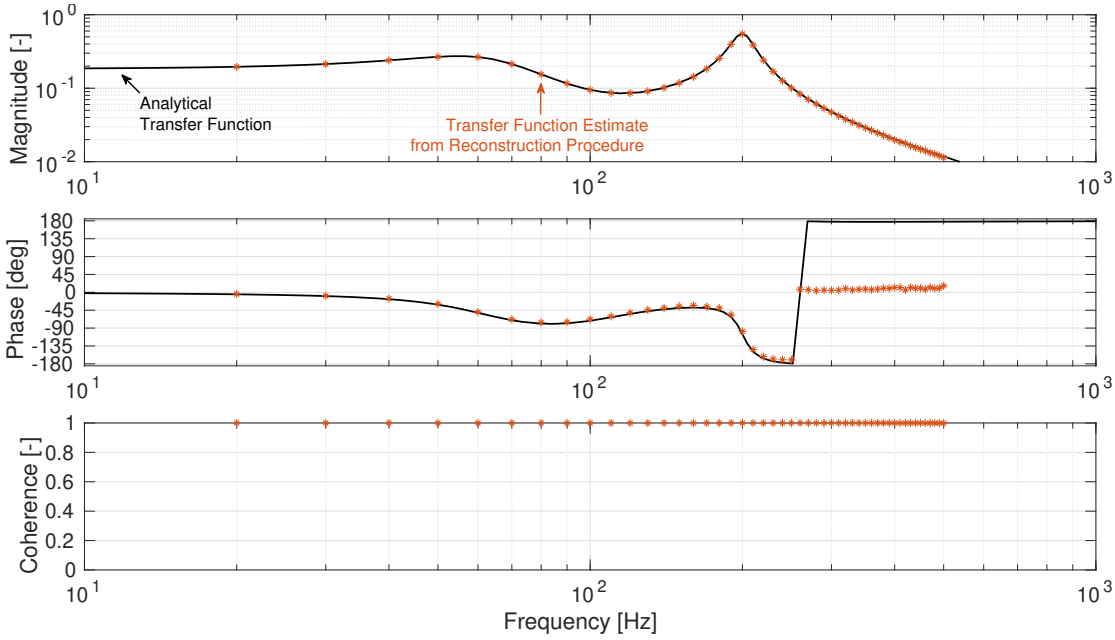


Figure 3-7: Comparison of analytical and estimated transfer functions of model system. Transfer function well estimated by reconstruction procedure in absence of noise.

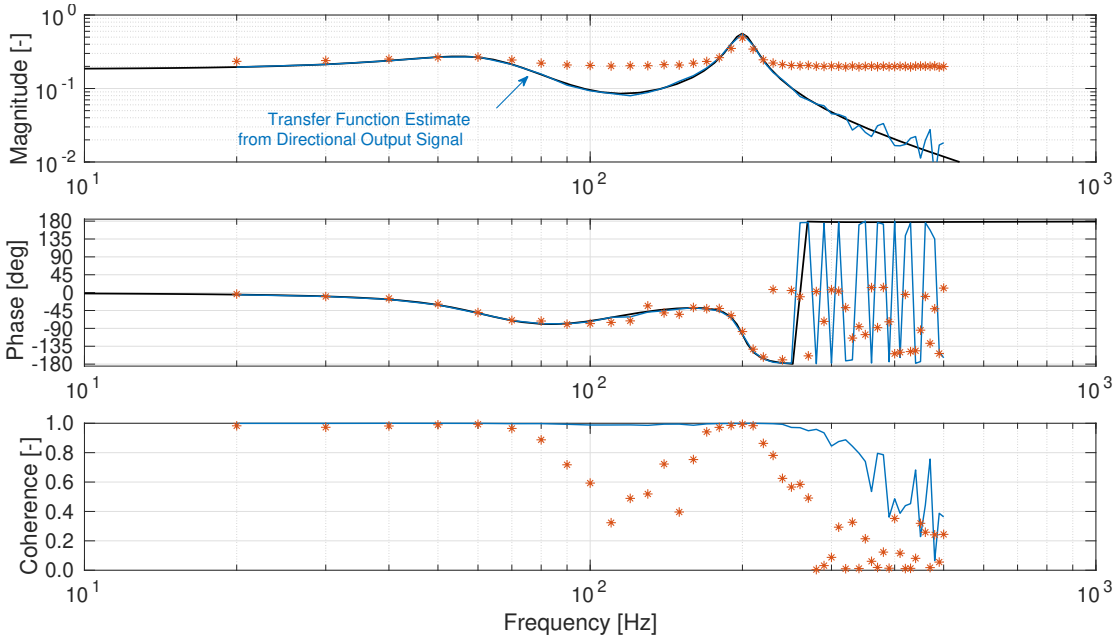


Figure 3-8: Estimation of model system transfer function with -2dB noise. Alternative coherence definition captures impact of noise on transfer function estimation.

3.4 Impact of Actuator Geometry on Frequency Response

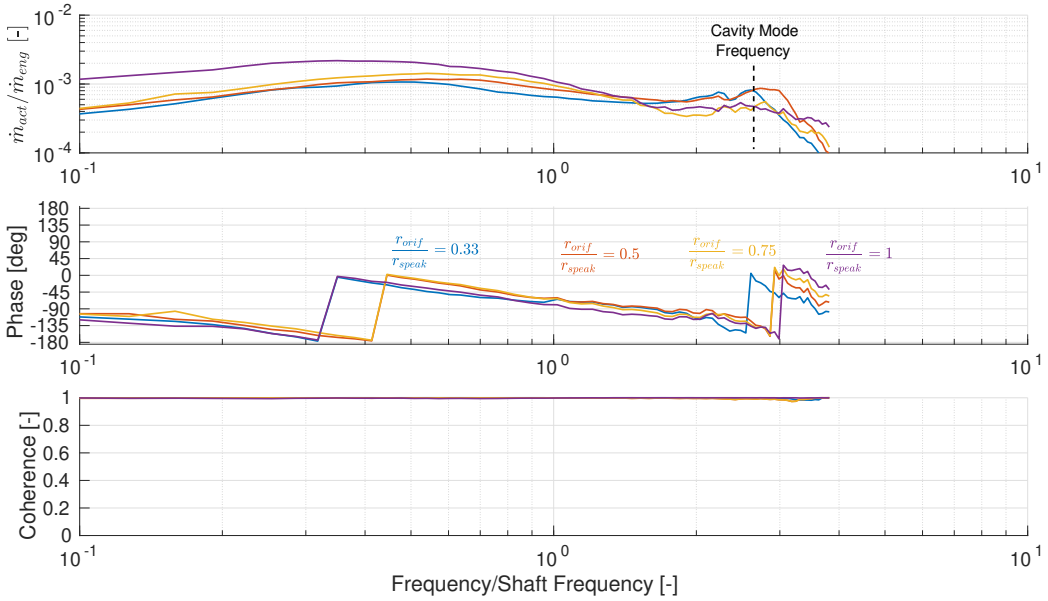
To determine the impact of neck length and orifice radius on actuator performance, volume flow frequency response functions were measured[4] across the design space of Figure 3-1b. No measurable response was produced by the actuator above a frequency of 4E, rendering the 3$^{\text{rd}}$ forward nodal diameter, with frequency $\approx$ 4.9E at take-off power, un-excitable.

Frequency responses for different orifice radii and of two different neck lengths are shown in Figure 3-9. The two modes predicted by the reduced order model, a low-frequency diaphragm mode and a high-frequency cavity mode, are both observed in the magnitude plot, with associated phase roll-off. The measured cavity mode frequency, and thus actuator bandwidth, however, does not change with the orifice radius. Figure 3-9 also does not show clear trends between peak volume flow for the cavity mode and the orifice radius; $\frac{r_{orif}}{r_{speak}} = 0.5$ produces the maximum for the shorter neck in Figure 3-9a while $\frac{r_{orif}}{r_{speak}} = 1.0$ produces the maximum for the longer neck in Figure 3-9b. The low-frequency behavior of the actuator is similar across all orifice radii with the exception of $\frac{r_{orif}}{r_{speak}} = 1.0$, which is associated with a change in diaphragm stiffness through mechanical clamping rather than orifice and neck dynamics. The implication for experiment design is that there *is not a strong preference for a specific orifice radius.*

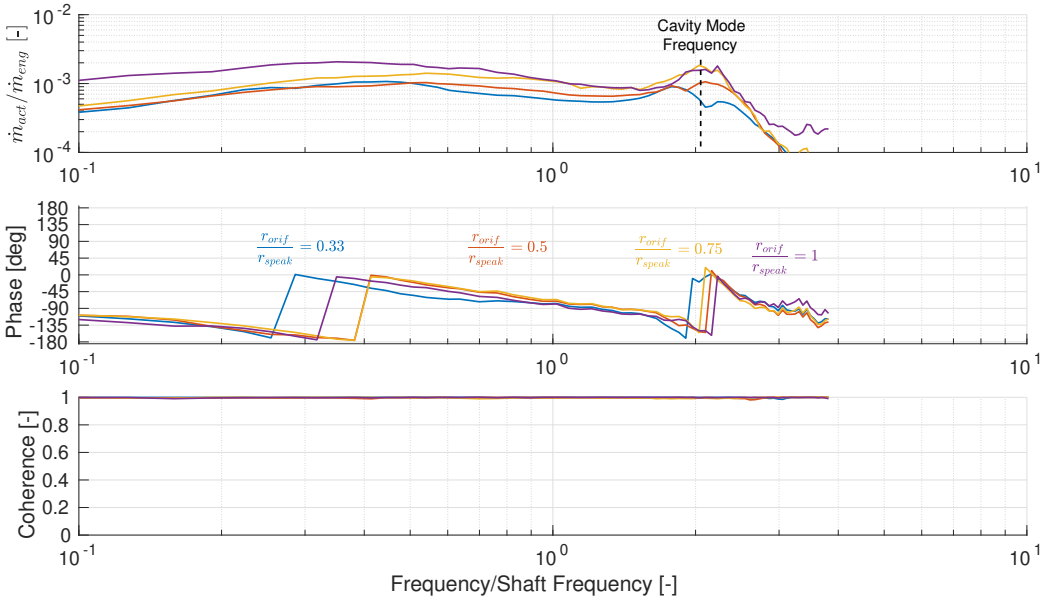
The neck length has a strong impact on both the cavity mode frequency and peak volume flow, as in Figure 3-10. For all orifice radii, the cavity mode frequency decreases as the neck length is increased. While the peak volume flow from the cavity mode is equivalent for all neck lengths for $\frac{r_{orif}}{r_{speak}} = 0.33$, it increases by nearly an order of magnitude for $\frac{r_{orif}}{r_{speak}} = 0.75$ over the range of neck lengths tested.

Of particular interest was the cause of the increased low frequency response for the largest orifice radius $\frac{r_{orif}}{r_{speak}} = 1.0$ in Figure 3-9. This was the only orifice radius tested for which the orifice in the neck mounting plate (the white plate in Figure 3-2a)

[4]see Appendix B for estimating volume flow from centerline velocity measurements.

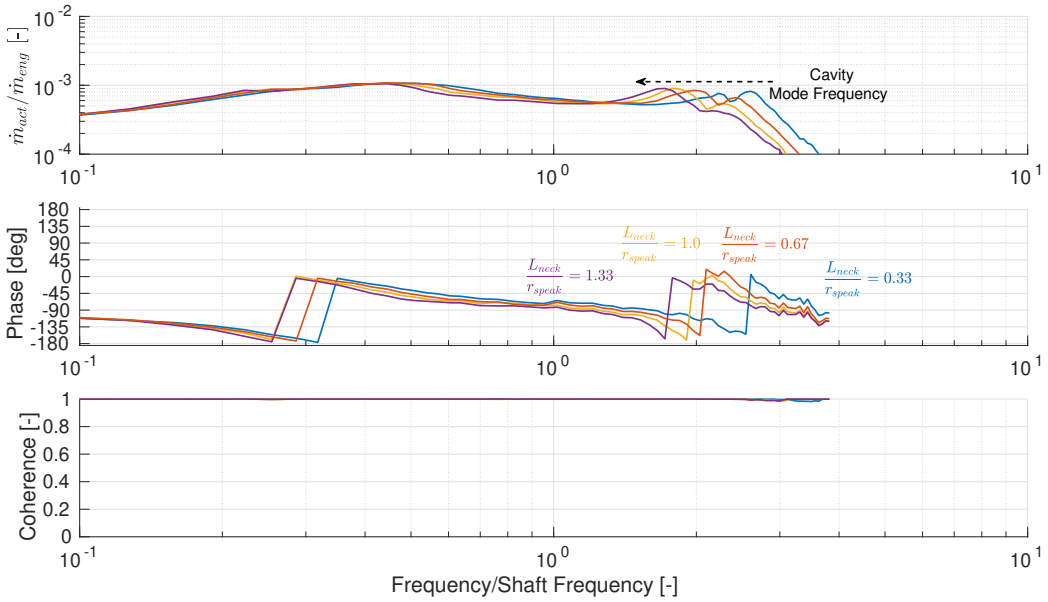


(a) $\frac{L_{neck}}{r_{speak}} = 0.33$

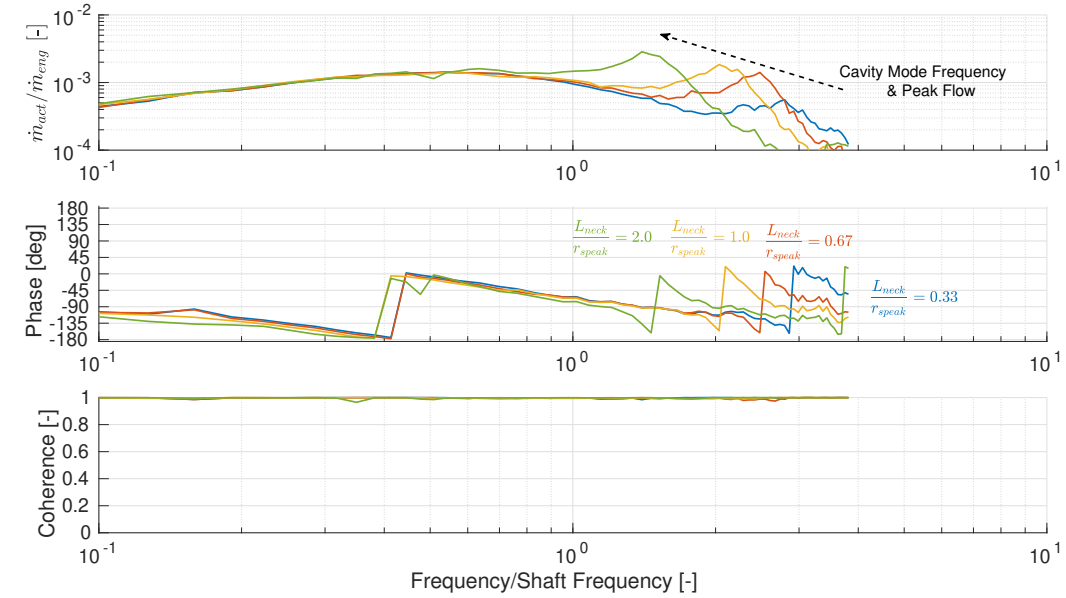


(b) $\frac{L_{neck}}{r_{speak}} = 1.0$

Figure 3-9: Measured frequency responses for multiple orifice radii. Actuator bandwidth and peak flow are essentially independent of orifice radius producing no preferred orifice radius for experiment.



(a) $\frac{r_{orif}}{r_{speak}} = 0.33$



(b) $\frac{r_{orif}}{r_{speak}} = 0.75$

Figure 3-10: Measured frequency responses for multiple neck lengths. Trade-off between peak flow and bandwidth with neck length for larger orifice radius.

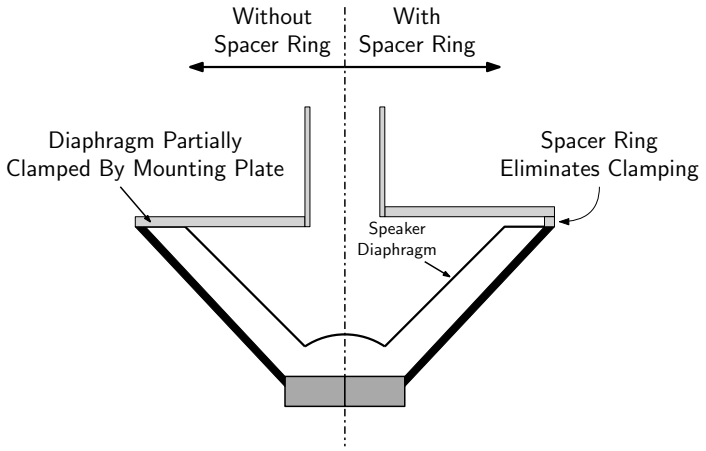


Figure 3-11: Assessment of impact of mechanical clamping of speaker diaphragm by neck mounting plate with spacer ring. Left side: with clamping, right side: without clamping

did not partially cover the speaker diaphragm. It was hypothesized that the clamping force from the mounting plate partially restricted the diaphragm movement thereby increasing the effective stiffness. This hypothesis was assessed by inserting a spacer ring between the speaker and the mounting plate for the $\frac{r_{orif}}{r_{speak}} = 0.75$, eliminating any contact between the speaker diaphragm and the mounting plate as in Figure 3-11.

The resultant frequency responses in Figure 3-12 show the frequency of the diaphragm mode decreases with spacer ring installed, as consistent with the scaling of the natural frequency with stiffness $f_n \sim \sqrt{k}$. The spacer also increases the cavity volume by approximately 10%, which further decreases the cavity mode natural frequency. Peak volume flow for both modes increases as a greater portion of the diaphragm is free to move and displace air. The spacer thus introduces another degree-of-freedom to tailor the actuator response without modifying the speaker construction or design.

The conclusion from the design space exploration is that there is a trade-off between peak volume flow (actuation authority) and cavity mode frequency (actuator bandwidth), *and there is no single geometry which maximizes both of these quantities*. The characterization experiment has provided a range of possible geometries and frequency responses that can be tailored to the nodal diameter of interest. Figure 3-13 pairs several nodal diameters of interest with actuator designs that maximizes the

actuator flow at the flutter mode frequency. By tailoring the actuator geometry to the mode of interest, the actuation authority can be improved by a factor of 2 to 5 at the flutter mode frequency. A requirement for the detailed design is thus to permit the neck length to be changed.

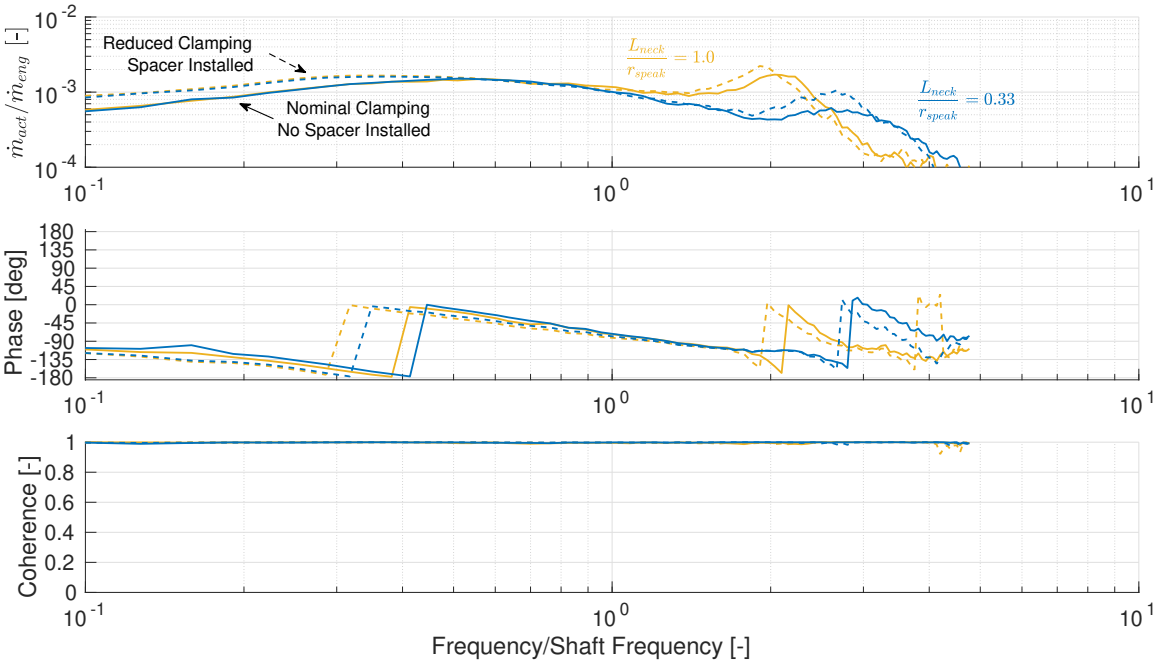


Figure 3-12: Measured frequency responses with and without spacer ring. Frequency of both modes decreases and peak volume flow increases with reduction in mechanical clamping, introducing another design degree-of-freedom.

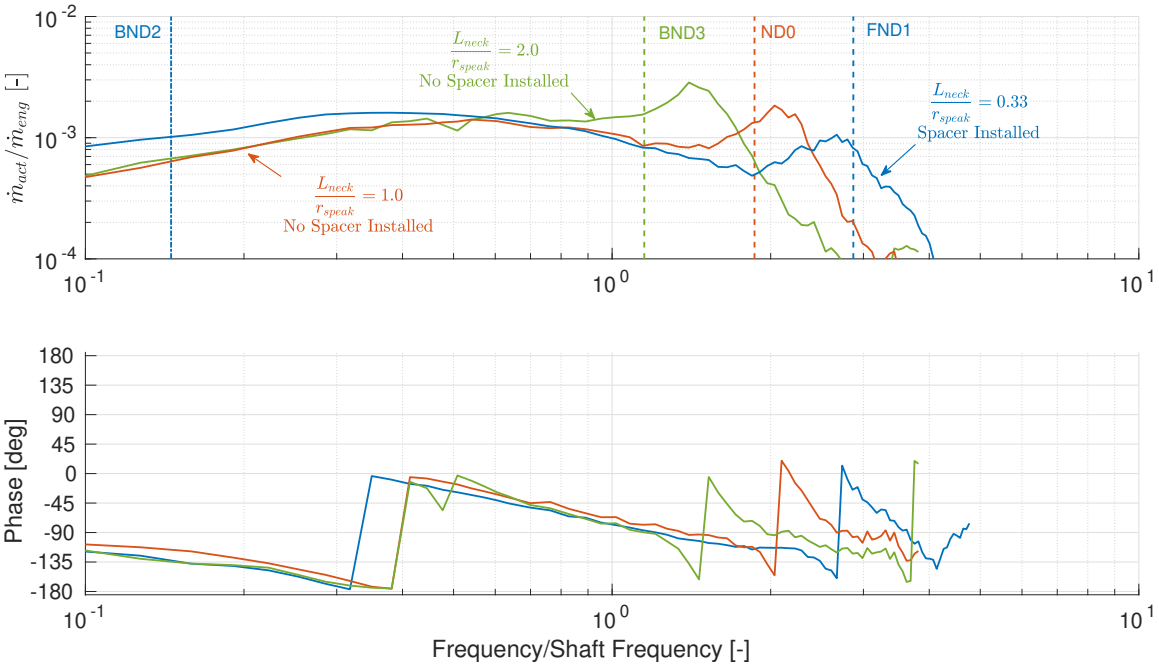


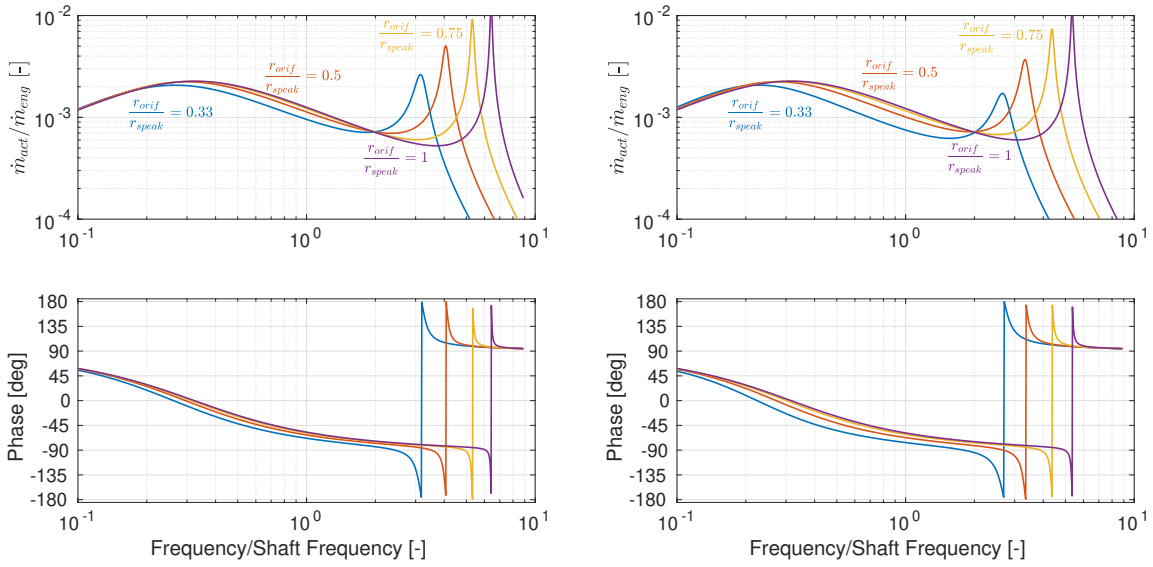
Figure 3-13: Actuator flow at flutter mode frequencies increased up to 500% by tailoring actuator response to nodal diameter.

3.5 Assessment of Actuator Reduced Order Model

We now compare measured actuator frequency responses to the estimates from the actuator model in order to determine its utility in designing actuators at this physical scale for other forced response experiments. Figure 3-14 shows the model results with varying orifice radii for the same actuator geometries and power as those in Figure 3-9. The reduced order model captures the general dynamics of the actuator, namely the existence of both the diaphragm and cavity mode and the overall magnitude of the response. The model captures the frequency and magnitude of the diaphragm mode response well, especially for the $\frac{r_{orif}}{r_{speak}} = 1$ case where the mechanical properties of the diaphragm are closest to the published speaker performance parameters due to the absence of mechanical clamping. The model fails to capture the measured invariance of the cavity mode frequency with orifice radius, predicting a monotonic increase in cavity mode frequency with orifice radius. It also predicts a decrease in cavity mode damping, and thus a large increase in the volume flow response, with increasing orifice radius. The measured performance, however, shows no clear trend in cavity mode damping and peak response with orifice radius. The observed disparity between the model predictions and the measured performance suggests the viscous resistance of the neck is not well predicted by Poiseulle flow.

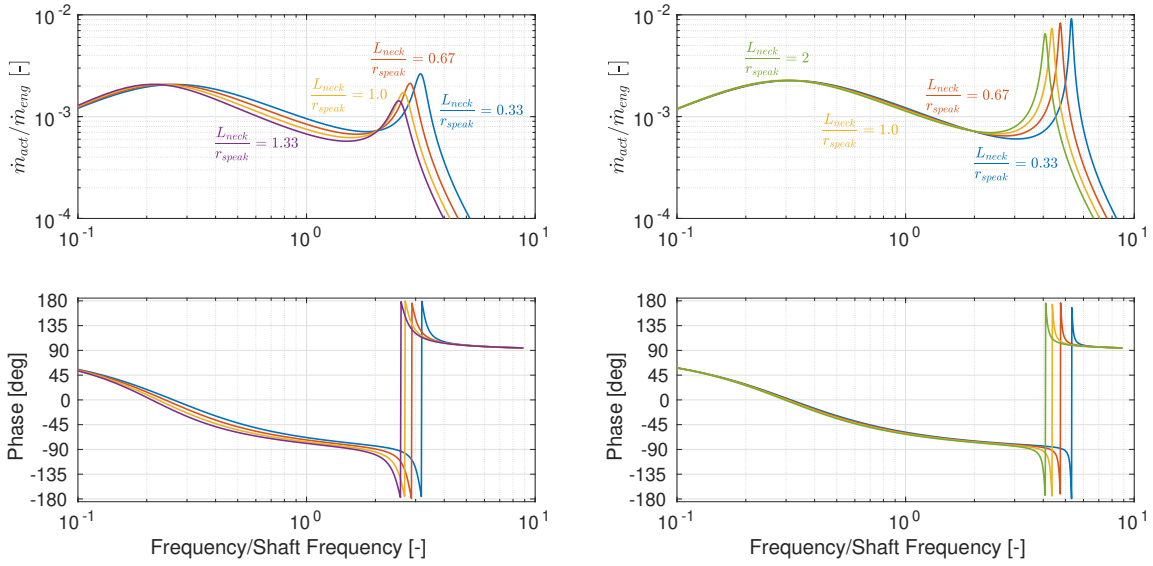
Figure 3-15 shows the model results when multiple neck lengths for the same geometries and actuator power as in Figure 3-10. The model captures the trend of decreasing cavity mode frequency with increased neck length. The impact of neck length on cavity mode damping, however, is not captured. The model predicts a monotonic decrease in damping with neck length but the measured cavity mode damping is *inversely* proportional to neck length. The measured effect of neck length on cavity mode damping, however, is not consistent across orifice size with negligible differences in peak volume flow across all neck lengths for $\frac{r_{orif}}{r_{speak}} = 0.33$ in Figure 3-10a and nearly an order of magnitude difference in peak volume flow for $\frac{r_{orif}}{r_{speak}} = 0.75$ in Figure 3-10b.

While the actuator reduced order model has some utility for predicting the re-



(a) $\frac{L_{neck}}{r_{speak}} = 0.33$ (b) $\frac{L_{neck}}{r_{speak}} = 1.0$

Figure 3-14: Actuator model fails to capture impact of orifice radius on actuator bandwidth and peak volume flow in comparison to measured performance in Figure 3-9.



(a) $\frac{r_{orif}}{r_{speak}} = 0.33$ (b) $\frac{r_{orif}}{r_{speak}} = 0.75$

Figure 3-15: Actuator model captures reduction in cavity mode frequency with neck length but fails to capture peak volume flow trends in comparison to measured performance in Figure 3-10.

sponse of actuators in this operating regime, it is clear that it does not capture some of the relevant trends and more detailed performance metrics. In general, the reduced order model for this actuator has over-predicted both the response magnitude (especially the peak response from the cavity mode) and bandwidth. Furthermore, it has not captured the impact of changing neck geometry on the frequency response. While this is perhaps unsurprising given the violation of the model assumptions, it demonstrates the need for experimental characterization of ZNMF actuators at this scale for future forced response experiments. Furthermore, it motivates the development of reduced order models that can better capture actuator performance and design trends at this physical scale for use in future experiment design.

3.6 Incorporating Actuator Transfer Function into Flutter Modeling Framework

To simulate the fan forced response, we now implement the measured actuator performance into the flutter reduced order modeling framework. To permit multiple actuator power levels, we derive volume flow transfer functions (dimensionally volume flow per volt) for amplifier voltages across the power range, as shown in black lines in Figure 3-16 for two different actuator geometries. These functions largely collapse except at near the high frequency limit of the actuator, where it produces its minimum response, implying the volume flow is linear with actuator voltage. We define an average transfer function, shown in red in Figure 3-16, to characterize the performance of that actuator geometry. The red curve in Figure 3-16 is multiplied by the ratio of the applied voltage to the maximum allowable voltage to determine the volume flow for that power level, so the amplifier voltage can be adjusted in the model as it could be done in the physical experiment.

We have thus far considered the performance of a single actuator, but the flutter modes respond to the level of forcing for a given spatial harmonic or nodal diameter. Therefore we must consider the entire flow pattern around the annulus to derive the

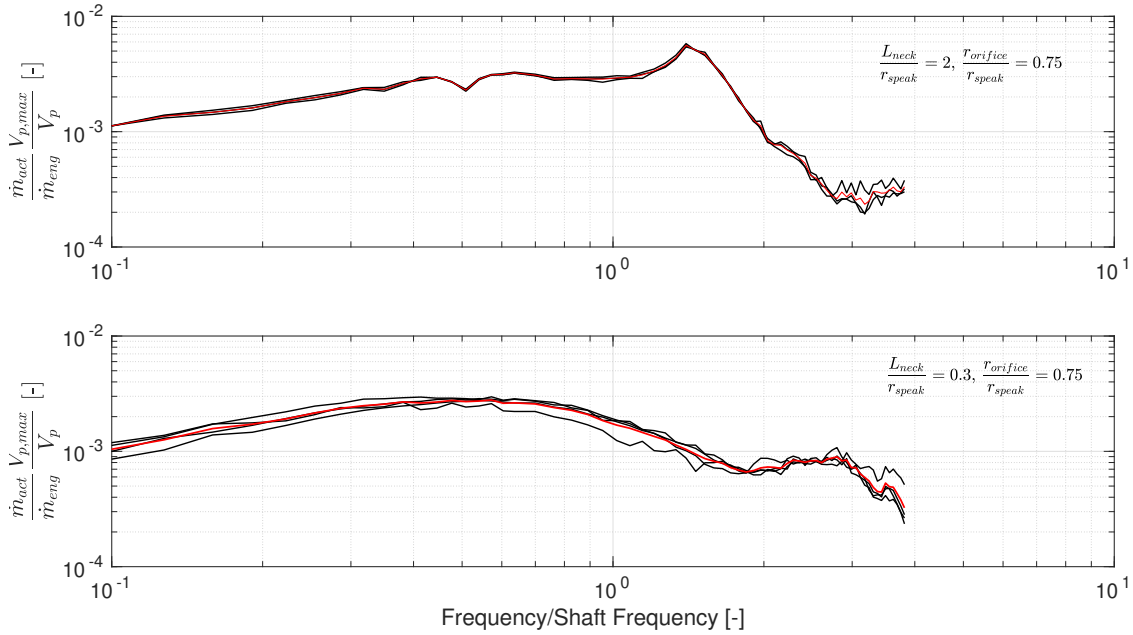


Figure 3-16: Linearity of volume flow to voltage transfer function demonstrated as curves for multiple voltage levels collapse. Average transfer function defined in red.

input to the flutter model, which are the magnitudes of the spatial Fourier coefficients of $\Phi_{inj} = \frac{u_{avg}}{U_{tip}}$. Because the velocity is approximately uniform across the orifice, the flow pattern downstream of the actuator is approximated with a square wave, as shown in Figure 3-17. The traveling wave command signal for nodal diameter ND $= n$,

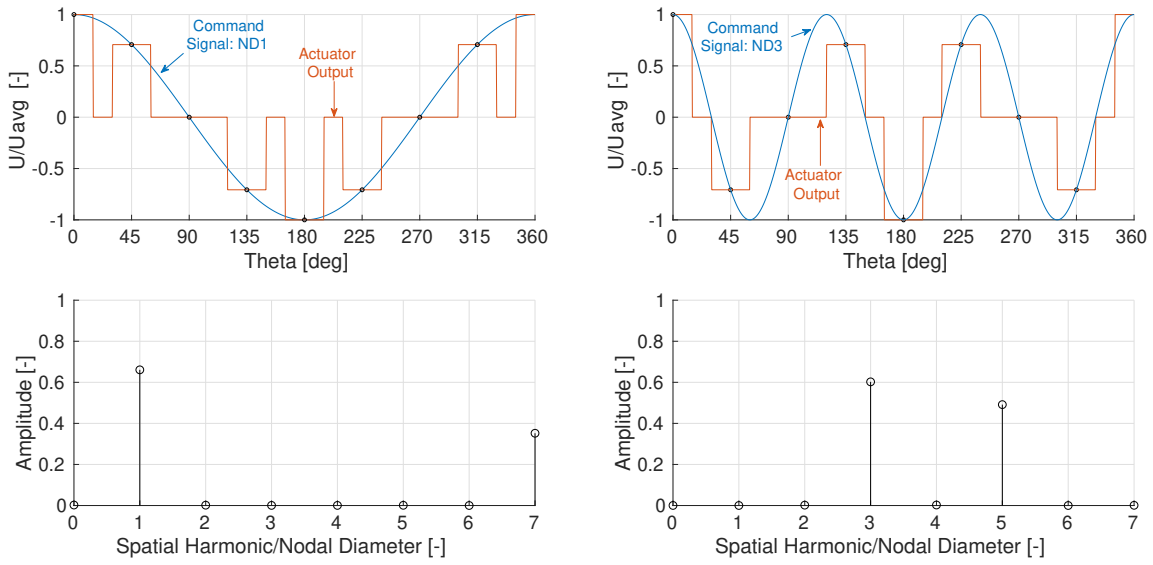
$$V_{command}(t, \theta) = \cos(\omega_f t \pm n\theta),$$

shown in blue of the top plot in Figure 3-17 for $t = 0$, is spatially discretized for the locations of the eight discrete actuators,

$$V_{command}(t, m) = \cos(\omega_f t \pm n\frac{2\pi}{8}m),\ m = 0 \ldots 7.$$

resulting in the square wave flow pattern in orange. The angular width of each actuator is determined by the ratio of orifice diameter to casing circumference (the $\frac{r_{orif}}{r_{speak}} = 0.75$ geometry is used in Figure 3-17). The magnitude of the spatial Fourier coefficients of the resulting flow pattern are given in the lower plots of Figure 3-17.[5]

[5]Spatial Fourier coefficients above the maximum nodal diameter of the PW615 are not shown.



(a) ND1 Forcing

(b) ND3 Forcing

Figure 3-17: Spatial Fourier transform of actuator flow field for ND1 and ND3 forcing. Spatial aliasing permits excitation of higher nodal diameter modes

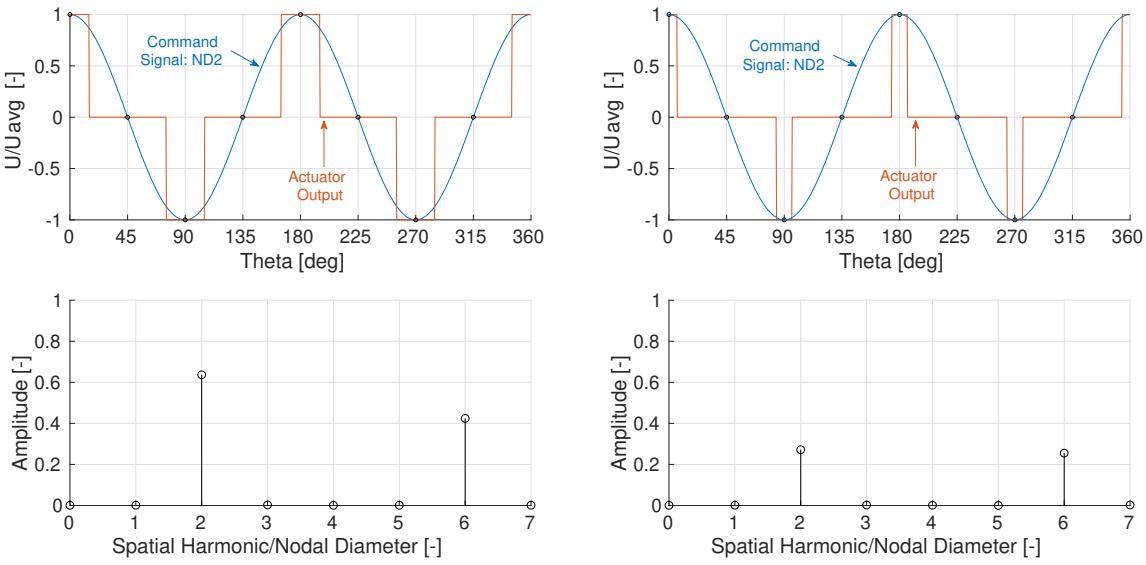
The dominant spatial Fourier coefficient is that of the commanded nodal diameter, but higher spatial Fourier coefficients are also non-zero due to spatial aliasing about the 4^{th} spatial harmonic (which is necessarily zero with eight actuators due to the Nyquist criterion). 1^{st} nodal diameter forcing aliases into the 7^{th}, 2^{nd} nodal diameter forcing into the 6^{th} and so on. Higher nodal diameter modes above the third can thus be excited with only eight actuators, albeit with reduced actuation power. The spatial Fourier coefficients of the actuator flow coefficient Φ_{inj} for a given forcing frequency f, amplifier voltage V_p, and forcing nodal diameter ND are given by

$$\hat{\Phi}_{inj,n}(\text{ND}, V_p, f) = \frac{V_p}{V_{p,max}} \cdot \tilde{u}_{avg}(f) \cdot \text{SFC}_n(\text{ND}),\ n = 0 \ldots 7. \tag{3.5}$$

In Equation 3.5 $\tilde{u}_{avg}(f)$ is the average velocity to voltage transfer function, as in Figure 3-16[6], and $\text{SFC}_n(\text{ND})$ is the magnitude of the n^{th} spatial Fourier coefficient for ND nodal diameter forcing.

The orifice radius impacts the effective actuation power by via the magnitude of

[6]the average velocity u_{avg} to voltage transfer function is identical to that in Figure 3-16 but scaled by the inverse of the orifice area.



(a) $\frac{r_{orif}}{r_{speak}} = 0.75$ (b) $\frac{r_{orif}}{r_{speak}} = 0.3$

Figure 3-18: Spatial Fourier transform of actuator flow field for two orifice radii. Reducing orifice radius reduces effective forcing magnitude and drives design to large orifice radius.

the spatial Fourier coefficient of the commanded nodal diameter. As in Figure 3-18, which shows the flow pattern and magnitude of the spatial Fourier coefficients for two orifice radii, reducing orifice radius reduces the angular width and the actuator flow field approaches a series of delta functions. The spatial Fourier coefficient of the commanded nodal diameter decreases as more energy is transferred to higher harmonics, reducing the effective actuation power for the commanded nodal diameter and driving the actuator design towards a large radius orifice.

Although the effect of the actuator on the fan is due to a mass perturbation rather than an axial momentum perturbation, as discussed in Section 2.3.4, the axial velocity distribution downstream of the actuators is relevant because it determines the magnitude of the forcing spatial Fourier coefficients. It is a significant assumption that the flow pattern downstream of the actuator is a square wave as the actuators are to be mounted radially in the inlet duct, implying the flow must turn axially. The associated viscous dissipation will inevitably smooth out the velocity distribution and result in dispersion of energy into multiple spatial Fourier coefficients. This will reduce the effective forcing and response of the commanded mode and excite

other flutter modes. Assessing actuator performance and the consequent downstream velocity distribution in cross-flow conditions representative of that in the PW615 inlet duct is therefore a potentially fruitful area for future work prior to performing the experiment.

3.7 Summary of Actuator Experimental Characterization

The volume flow frequency response for a ZNMF actuator with the candidate audio speaker has been experimentally measured across the design space of orifice radius and neck length. It was found that the actuator bandwidth decreased and the peak volume flow increased with neck length for a fixed orifice radius, introducing a trade-off between these quantities in the experimental design. The neck length is thus kept variable in the experiment so the actuator performance can be tailored to the flutter mode of interest. The bandwidth and peak volume flow was found to be essentially independent of the orifice radius for all neck lengths, producing no preferred orifice size for the experiment on the basis of a single actuator's performance alone. Incorporating multiple actuators into the experiment, however, drives the design to a larger orifice radius to increase the effective forcing of the commanded nodal diameter. The actuator reduced order model captured bulk features of the frequency response, but did not capture the measured dependence of bandwidth and peak volume flow on actuator geometry, demonstrating the need for experimental characterization of ZNMF actuators for future forced response experiments.

Two areas of future work have been identified for improved characterization of the actuator for the forced response experiment. One is improving the calibration procedure of the hotwire anemometer to reduce the error in the low velocity range where the actuator operates. A second is characterizing actuator performance in a cross-flow at conditions representative of that in the PW615 inlet duct during operation.

Chapter 4

Virtual Experiments for Assessing Experimental Error

With the experimentally characterized actuator frequency response function implemented in the flutter modeling framework, we can fully simulate the experimental chain in Figure 2-1. As the underlying flutter dynamics for the virtual experiment are known analytically, we can quantify the error in the identified flutter mode damping ratio. Furthermore, we can use the virtual experiments to assess the sensitivity of the experimental error to un-controllable factors and assess the strengths and limitations of the experimental design. Specifically, virtual experiments will be used to answer the following questions.

1. How relevant are actuator dynamics to identification of flutter dynamics? Is it necessary to characterize actuator dynamics prior to performing the experiment?

2. What is the expected error for operation with realistic noise levels? Can flutter damping ratio be measured throughout the fan operating range?

3. How robust is the experiment to noise sources; how does the damping ratio error depend on noise levels?

4. How much sensitive is the experiment to actuator and sensor performance or to

modeling errors that impact the magnitude of the forced response?

5. How sensitive is the experimental design and error to fan characteristics? To what extent is the experimental design extensible to other fan designs?

This chapter introduces the virtual experiment methodology, first in the absence of noise. Utilizing the noise-free results, we will quantify the impact of actuator dynamics on error and show it to be negligible, addressing the first question. A statistical approach is then developed to estimate error bounds in the presence of stochastic noise sources and we will use this framework to show flutter damping is measurable throughout the fan operating range, addressing the second question. The remaining questions are addressed in Chapter 5.

4.1 Virtual Experiments in Absence of Noise

The virtual experiment begins with the construction of the actuator voltage input signal $V_{in}(t)$, in this case a sinusoidal sweep or "chirp" across the bandwidth of the actuator,

$$\begin{aligned} V_{in}(t) &= V_p \sin(2\pi f_{inst} t) \\ f_{inst} &= f_{min} + \frac{f_{max} - f_{min}}{\tau} t = f_{min} + \dot{f} t. \end{aligned}$$

The chirp ramp rate $\dot{f}$ was chosen using the criterion of Hackenberg et al. [59] who showed that ramp rates violating this criterion resulted in over-estimation of the damping ratio. The ramp rate is bounded as below,

$$\dot{f} < \zeta^2 f_n^2,$$

where ζ is the flutter mode damping ratio of the least damped mode (the most restrictive condition) and f_n is the blade natural frequency. This results in an approximately 20 second chirp at take-off conditions.

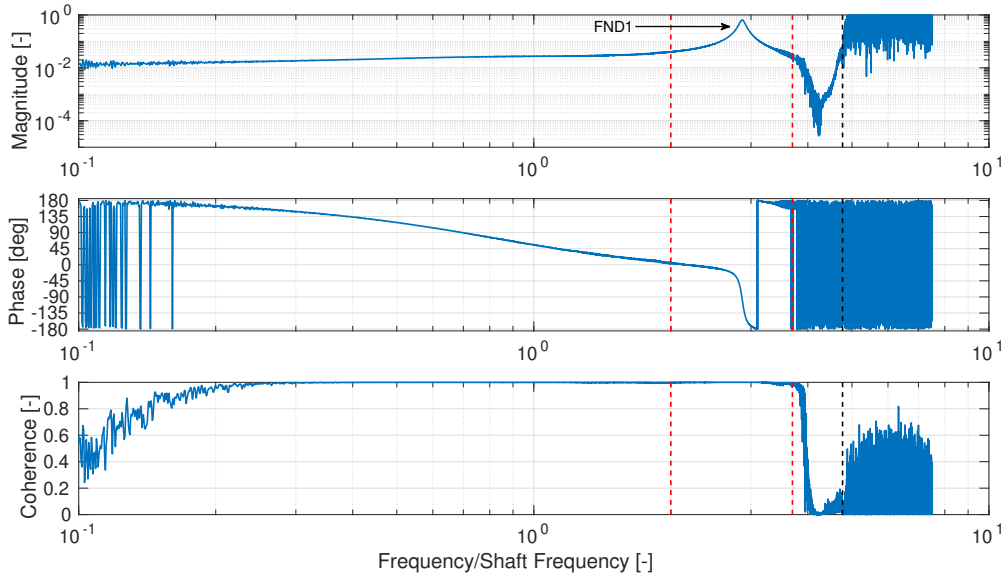


Figure 4-1: Resonance from 1st forward nodal diameter mode in bending-to-actuator-flow transfer functions $T_{y\Phi_f}(f)$ for 1st forward nodal diameter forcing for PW615 fan. Near unity coherence achieved due to the absence of noise.

The virtual experiment proceeds as described in Section 2.5 and Figure 2-20. The outputs are the two transfer functions of bending-to-actuator-input-voltage $T_{yv}(f)$ and, because the actuator dynamics are known, bending-to-actuator-flow $T_{y\Phi_f}(f)$. The actuator flow transfer function for a 1st forward nodal diameter forcing pattern is given in Figure 4-1 which shows the transfer function magnitude, phase, and coherence as a function of forcing frequency. The red dashed lines bound the portion of the transfer function used by the system identification algorithm and the black dashed line is the maximum frequency of the chirp f_{max}. A single resonance is observed from the 1st forward nodal diameter flutter mode at a frequency of 2E with associated phase roll-off of 180°. The coherence is near unity due to the absence of noise with a sharp drop to zero at a frequency of 4E as the bending response falls below the sensor resolution.

For 2nd forward nodal diameter forcing, three total resonances are expected in the transfer function:

- First from the 2nd forward nodal diameter flutter mode.

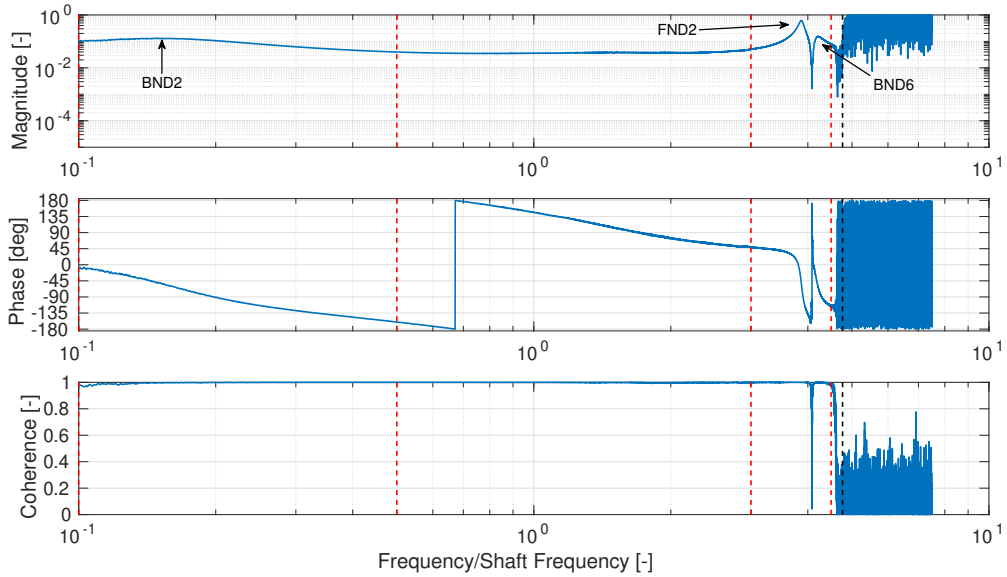


Figure 4-2: Resonance from 2nd and 6th backward, as well as 2nd forward, nodal diameters in bending-to-actuator-flow transfer function $T_{y\Phi_f}(f)$ with 2nd forward nodal diameters forcing. due to propagation direction switching and forcing spatial aliasing.

- Second from the 2nd backward nodal diameter flutter mode which has an absolute frame frequency of -0.1E, and thus presents as forward traveling in the absolute frame.

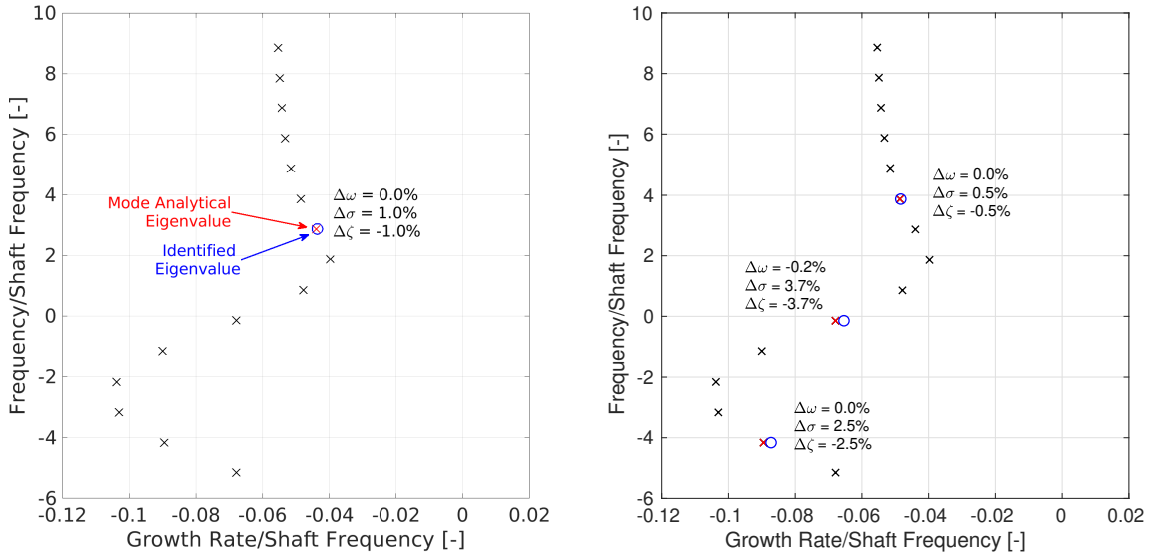
- Third from the 6th backward nodal diameter which has a frequency of -4E and is excited through spatial aliasing as described in Section 3.6.

All three of these resonances are seen in the transfer function with 2nd forward nodal diameter forcing[1], Figure 4-2.

The eigenvalues from the system identification are plotted in Figure 4-3 along with their analytical counterparts and the percent error in frequency ω, growth rate σ, and damping ratio[2] ζ. In the absence of noise, the errors are entirely due to the system identification process.

[1]The sharp dip in coherence and transfer function magnitude between the peaks of the 2nd forward and 6th backward nodal diameters is attributed to a lightly damped zero which reduces the bending response to below the sensor resolution.

[2]As the definition of damping ratio includes both the mode frequency and growth rate, the error in damping ratio ζ is not always equal to that in the growth rate σ.



(a) FND1 Forcing

(b) FND2 Forcing

Figure 4-3: Analytical and identified eigenvalues for 1st and 2nd forward forcing. Error in damping ratio is entirely from system identification procedure and minimal due to the absence of noise.

4.2 Impact of Actuator Dynamics on System Identification

Prior to implementing noise sources, we examine the impact of actuator dynamics on the system identification process and the damping ratio error to assess how important it is to characterize these dynamics prior to performing a forced response experiment. To maximize the effect of actuator dynamics, we use an actuator geometry with a less damped cavity mode, the volume flow frequency response function of which is shown in Figure 4-4. Overlaid are the frequencies of three modes for which this actuator geometry could be used. The 0th nodal diameter mode is at nearly the same frequency as the peak volume flow response due to the actuator cavity mode and is thus expected to be the most heavily impacted.

Figure 4-5 compares the bending-to-actuator-flow and bending-to-input-voltage transfer functions for the 0th and 3rd backward nodal diameter modes, demonstrating the effect of the actuator dynamics on the measured transfer function.[3] For the 0th

[3]The transfer function magnitudes have been scaled by the magnitude at the mode frequency to

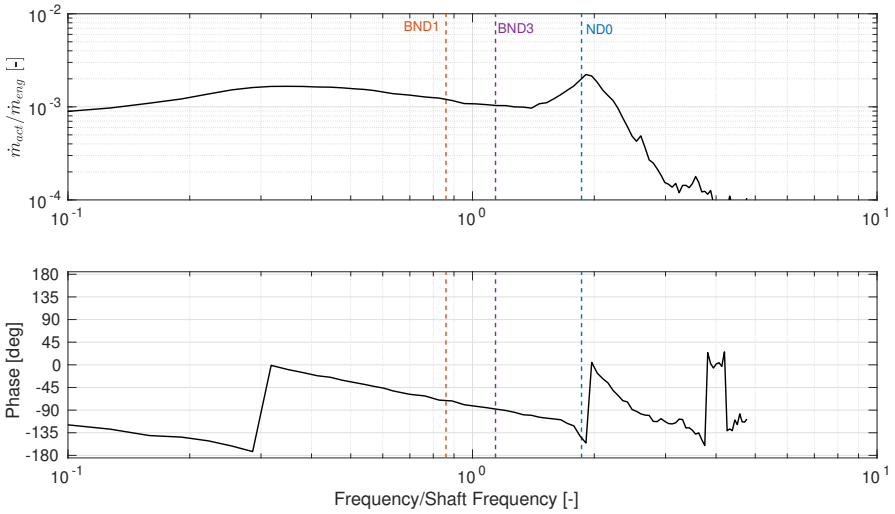
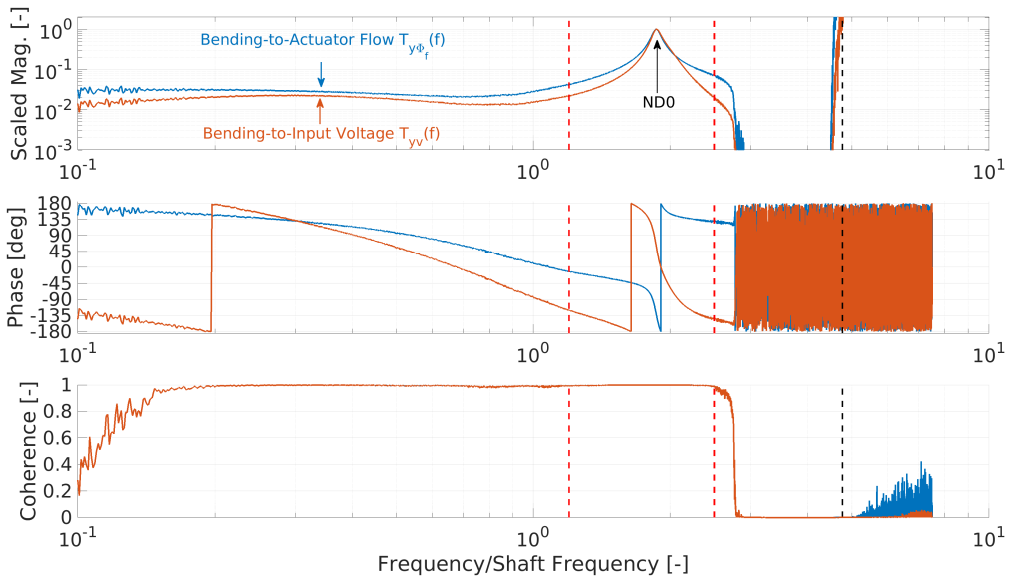


Figure 4-4: Actuator frequency response function with less damped cavity mode. Actuator dynamics expected to have largest effect on 0^{th} nodal diameter mode due to proximity of actuator cavity mode.

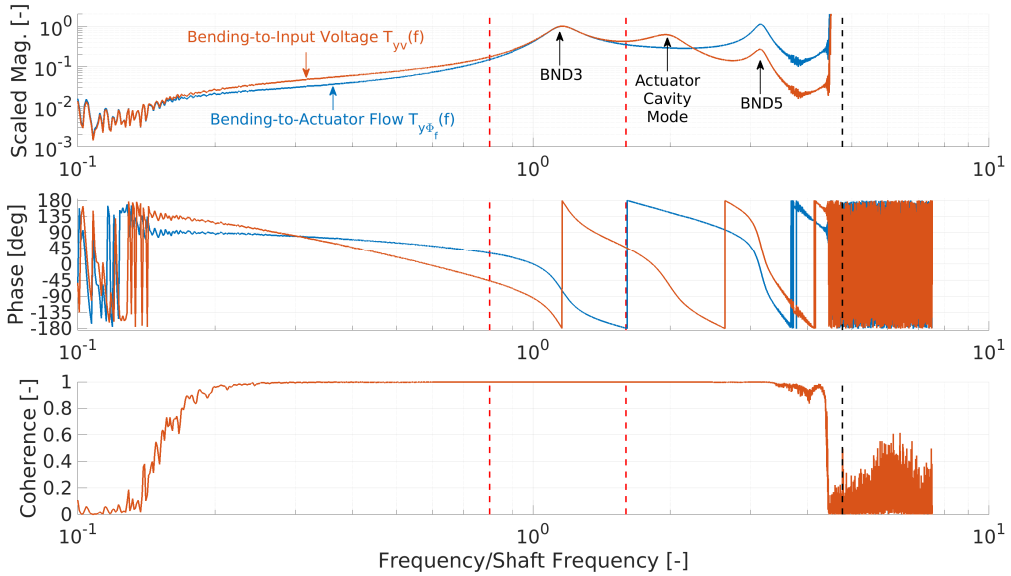
nodal diameter, Figure 4-5a, the actuator cavity mode and the flutter mode have merged into a single peak, but they are distinguishable from the phase which rolls off by 360° rather than the 180° expected for a single mode. The actuator dynamics cause the peak in the bending-to-input-voltage transfer function to appear steeper and less damped than that from the flutter dynamics alone. For the 3^{rd} backwards nodal diameter, Figure 4-5b, an extraneous peak appears in the bending-to-input-voltage transfer function from the actuator cavity mode. The two transfer functions agree well, however, in the vicinity of the resonance where the response is dominated by the flutter dynamics.

Table 4.1 compares the percent error in damping ratio for these three modes when the two transfer functions are used in the system identification algorithm. When a model with greater than two degrees of freedom is used (i.e. more than one pair of conjugate eigenvalues can be modeled) the error is less than 3.5% and is comparable between the two transfer functions. When only two degrees of freedom are used, however, the error for the transfer function with actuator dynamics is 100% to 1,500% greater than that for the flutter dynamics only transfer function, with the largest

ease comparison



(a) ND0 Mode (ND0 Forcing)



(b) BND3 Mode (FND3 Forcing)

Figure 4-5: Comparison of measured transfer functions with and without actuator dynamics characterization. Actuator characterization needed to isolate flutter dynamics in transfer function.

	>2DOF $T_{y\Phi_f}(f)$	>2DOF $T_{yv}(f)$	2DOF $T_{y\Phi_f}(f)$	2DOF $T_{yv}(f)$
BND3	-1.3%	-1.1%	-11.8%	-23.8%
BND1	-1.2%	-1.6%	-14.1%	-23.7%
ND0	0.7%	3.1%	-1.9%	-31.6%

Table 4.1: Dependence of damping ratio error on transfer function and system identification model degrees-of-freedom. Higher degrees-of-freedom permit identification of flutter mode, even without actuator characterization.

increase in error for the 0^{th} nodal diameter mode.

With the extra degrees of freedom, the system identification algorithm was able to determine the underlying flutter dynamics and use the extra degrees of freedom to "compensate" for the contribution of other modes. For the transfer function with actuator dynamics, the extra identified eigenvalues approached those of the actuator, essentially negating its contribution to the transfer function. These findings mean that with proper system identification configuration, characterization of the actuator dynamics is not necessary to accurately identify the underlying flutter dynamics. This will likely not hold, however, for actuators whose frequency response is non-linear. In such cases, the contribution from the actuator dynamics could not be removed by a combination of the extra linear modes in the identified state-space model. In this example, the actuator frequency response in Figure 4-5 was well described by a 6^{th} order state-space model. For the remainder of this work, the bending-to-actuator-flow output $T_{y\Phi_f}(f)$ is used for system identification.

4.3 Incorporating Noise into Virtual Experiments

4.3.1 Sources of Noise

We now incorporate noise sources into the virtual experiment to estimate realistic error metrics and assess how robust the experimental design is to noise. As summarized in Figure 2-1, noise sources can be broken into two categories: sensor noise and process noise.

Sensor noise is noise imposed on the underlying measured response and can be

thought of as the ideal measurement plus some disturbance. In this case, the true response is the time series of the measured bending at the sensor location $y_f(t, \theta_{sensor})$ corrupted by a disturbance time series $y_n(t)$. For the tip-timing system, noise can be electrical, such as background EM radiation levels, or optical, such as stray reflections. Shielding and grounding of the measurement system, however, typically can remove tonal noise sources (e.g. building AC mains frequency) resulting in a broadband noise spectrum. Consequently, sensor noise was implemented into the virtual experiment as white noise with an amplitude of a multiple of the sensor resolution. For ensemble averaging of multiple trials, a single dynamical simulation of the flutter dynamics was performed to produce the underlying response, $y_f(t)$ in Figure 2-1, and separate instantiations of sensor noise were added to produce the n time series, $y(t)$ in Figure 2-1, for ensemble averaging.

Process noise is due to a physical and un-controlled disturbance which acts as an input to the dynamical system of interest. Examples of process noise for the flutter experiment may include upstream vortex shedding, inlet distortion, and inlet turbulence. Geometry upstream of the blade row of interest, such as struts or other blade rows, can shed vortices which then convect downstream and impinge on the downstream blade row. This acts as a source of excitation at the vortex shedding frequency. For the PW615 fan, however, there is no upstream geometry, eliminating vortex shedding. Inlet distortion is a steady total pressure or temperature non-uniformity in the absolute frame resulting in a non-axisymmetric inlet velocity to the fan. While not traditionally thought as a source of noise as it is a steady phenomena in the absolute frame, in the relative frame it produces unsteady forcing at harmonics of the shaft frequency depending on the spatial frequency content of the non-uniformity. Introducing a non-axisymmetric mean flow, however, breaks the linear independence of the separate spatial harmonics and introduces coupling between the flutter modes which cannot be captured with the current flutter modeling framework because the modes are no longer separate sinusoidal spatial harmonics [60]. Reduced order models for compressor stall have been expanded to incorporate non-axisymmetric mean flows (e.g. [60, 61]) and doing so for the current flutter model is a fruitful area for future

work. Furthermore, system identification techniques have been developed to filter the effect of periodic disturbances [62], potentially enabling system identification even in the presence of inlet distortion.

Inlet turbulence represents a broadband disturbance that is difficult to filter. It was introduced to the model as a zero-mean unsteady disturbance in the inlet flow coefficient. To better represent the inverse scaling of turbulent kinetic energy with frequency, the time series of the inlet flow coefficient disturbance was produced with pink, rather than white, noise. The magnitude of the disturbance time series representing turbulence was set to a percentage of the mean flow coefficient based on the turbulence intensity. A separate disturbance time series of equal amplitude was added to each spatial harmonic to reflect homogeneous turbulence. For n trial ensemble averaging, n separate dynamical simulations were performed with separate instantiations of the turbulence for each simulation and the resultant n measurement time series were then averaged.

4.3.2 Statistical Framework for Error Estimation

The estimated damping ratio from system identification $\hat{\zeta}$ (in Section 4.1) was a single, deterministic value, but the introduction of random noise sources makes the estimated damping ratio, and thus the damping ratio error e, a random variable with an unknown probability density function $f(e)$,

$$e = \frac{\hat{\zeta} - \zeta}{\zeta}.$$

The error must thus be described in terms of statistical metrics rather than a single value. Two metrics of the experiment valuable to the user are that of *bias* and *confidence*. The first answers the question, to what extent would the average damping ratio of multiple measurements converge to the true value, i.e. to what extent does the expected value of $\hat{\zeta}$ deviate from the true value ζ? The second answers the question if only a single experiment is performed, how close to the true value is that measurement within some desired confidence?

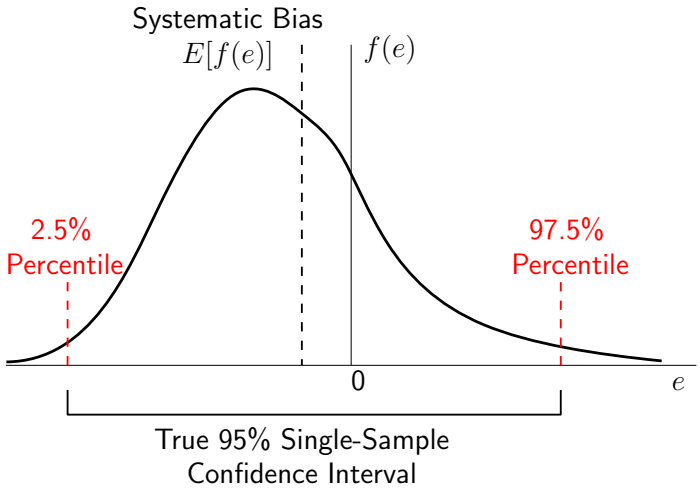


Figure 4-6: Systematic bias and confidence in a single damping measurement characterized by expected value and percentile statistics of damping ratio error probability density function.

These two questions are answered with the expected value and percentile statistics of the error probability density function, as in Figure 4-6 which graphically shows these statistics on an example error probability distribution. If $E[\hat{\zeta}] = \zeta$, the expected value of the error PDF $E[f(e)]$ is zero and, conversely, the expected value of the error PDF is a measure of the extent to which the expected value of $\hat{\zeta}$ deviates from the true value ζ. The interval of the PDF defined by the $100\alpha^{\text{th}}$ and $100(1-\alpha)^{\text{th}}$ percentiles, denoted e^{α} and $e^{1-\alpha}$ respectively where $\alpha \in (0, 1)$, represents the interval that a single sample, i.e. a single measurement, will fall in $100(1-2\alpha)\%$ of the time. This interval is henceforth referred to as the "$100(1-2\alpha)\%$ single-sample confidence interval," with $\alpha = 0.025$ in Figure 4-6. The "true" single-sample confidence interval $[e^{\alpha}, e^{1-\alpha}]$ is that based on the percentile statistics of the underlying, but unknown, error distribution. The goal is to construct an estimate of this interval $[\hat{e}^{\alpha}, \hat{e}^{1-\alpha}]$ with some confidence level.

If the damping ratio error distribution was known to be normal a-priori, we could readily construct percentile statistics based on the sample variance, and its associated confidence interval from the chi-square distribution. The error, however, is found to *not* be normally distributed. Figure 4-7 compares the estimated probability density from a histogram of 1,000 virtual experiments with noise to the best-fit normal dis-

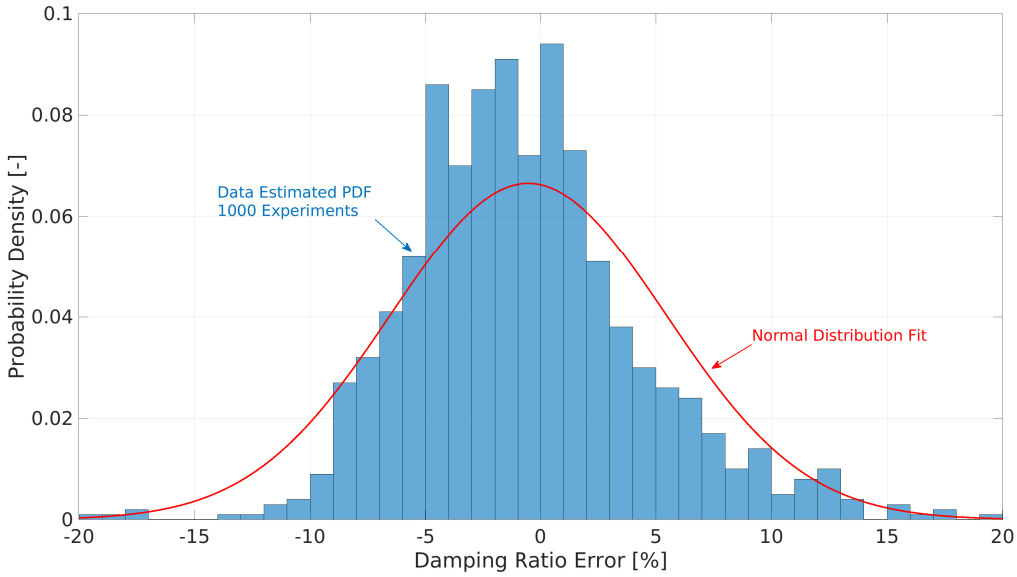


Figure 4-7: Estimated error PDF from 1000 virtual experiments and best-fit normal distribution. Error distribution is non-normal, preventing use of parametric methods to form confidence interval of percentile points.

tribution and demonstrates that the underlying error data is skewed and not well described by a normal distribution. This was confirmed with the Anderson-Darling and Shapiro-Wilk normality tests, both of which rejected the null hypothesis that the data in Figure 4-7 is normally distributed with a significance level of 0.05.

Percentile points can be determined directly from the sampled error distribution to form an estimated single-sample confidence interval, but a means of quantifying the confidence in the percentile statistics is needed. Non-parametric bootstrapping is used to form confidence intervals on the percentile statistics of the error distribution. Bootstrapping consists of re-sampling, with replacement, the original n-point sample distribution ($n = 1000$ in Figure 4-7) B times to form B new n-point distributions. The desired statistic, in this case percentile points, is computed for each of the B distributions to form a B-point bootstrap sampling distribution of the statistic. Figure 4-8 shows histograms of the bootstrap sampling distributions of mean error and the 2.5% and 97.5% percentile point statistics.[4] The bootstrap sampling distribution of the mean is normally distributed, as expected from the central limit theorem and was

[4] $B = 10,000$ bootstrap replications were used for all bootstrapping in this work. No change in the bootstrap distributions or statistic confidence intervals was observed for $B > 10,000$.

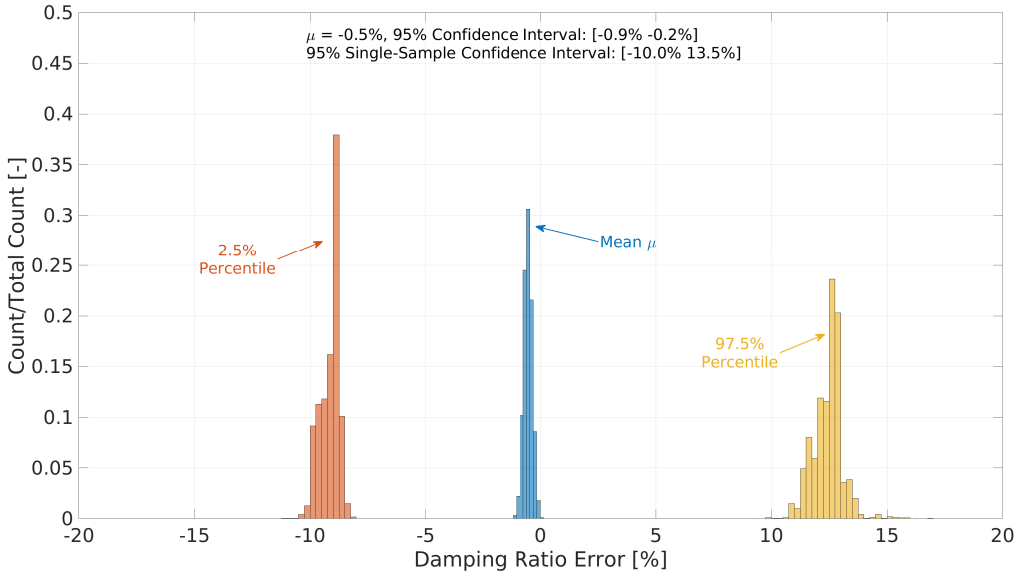


Figure 4-8: Estimation of error mean and percentile point distributions with bootstrapping, permitting confidence intervals on percentile points to be derived.

confirmed with normality tests. The distributions of the percentile points are regular and continuous, suggesting the resultant distributions well represent the underlying sampling distribution of the statistics.

From these distributions, we can form confidence intervals for the statistic. Because the mean error bootstrap sampling distribution is necessarily normal, a $100\beta\%$ confidence interval, where $\beta \in (0, 1)$, for the mean error can be constructed using the bootstrap sampling distribution variance. For the example error data, the mean error is -0.5% with a 95% confidence interval of [-0.9%, -0.2%], indicating the experiment has a low bias for this specific case.

Using the percentile method from Ref. [63], which consists of finding the $100(1 - \beta/2)^{\text{th}}$ and $100(\beta/2)^{\text{th}}$ percentiles of the bootstrap replications of the statistic, a $100\beta\%$ confidence interval was formed for each of the two percentile points. These are denoted $[\hat{e}_-^\alpha, \hat{e}_+^\alpha]$ and $[\hat{e}_-^{1-\alpha}, \hat{e}_+^{1-\alpha}]$ and the estimated $100(1 - 2\alpha)\%$ single-sample confidence interval is constructed as $[\hat{e}_-^\alpha, \hat{e}_+^{1-\alpha}]$, where the true interval $[e^\alpha, e^{1-\alpha}]$ will fall in the interval $[\hat{e}_-^\alpha, \hat{e}_+^{1-\alpha}]$ at least $100\beta\%$ of the time.[5] β is thus a measure of

[5]Let A be the event $e^\alpha < \hat{e}_-^\alpha$ and B be the event $e^{1-\alpha} > \hat{e}_+^{1-\alpha}$, then $p(A \cup B) = p(A) + p(B) - p(A)p(B|A) = (1 - \beta) - \frac{1-\beta}{2} p(B|A) \leq 1 - \beta$

the confidence in the estimated single-sample confidence interval. For the example in Figure 4-8, the estimated 95% single-sample confidence interval is [-10.0%,13.5%] with $\beta = 0.95$. The skew of the sampled error data in Figure 4-7 is reflected in the single-sample confidence interval, which is not symmetric about the mean error and skewed towards more positive values.

An assumption of the non-parametric bootstrap is that the distribution of the original sampled data well represents the underlying distribution. If this is not true, the bootstrap sampling distribution will not well represent the true statistic sampling distribution and, consequently, confidence intervals derived from the bootstrap sampling distribution will be of poor accuracy. As the percentile points near the tails are sought, the underlying error distribution must be sufficiently sampled to ensure the tails are well represented, in other words, sufficient virtual experiments must be conducted to probe the tails of the error distribution. To ensure the error distribution was sufficiently sampled, a convergence study was performed to examine the variation in the single-sample confidence interval with the number of virtual experiments performed. It was found that different nodal diameters converged at different rates, e.g. the 1^{st} forward nodal diameter converged quickly whereas the 3^{rd} backward nodal diameter showed the most variation. Figure 4-9 shows the variation of the 95%, 90%, 85%, and 80% single-sample confidence intervals as a function of the number of virtual experiments performed, all with $\beta = 0.95$, for the 3^{rd} backward nodal diameter mode.

The limits of the lower confidence single-sample confidence intervals converge more quickly as less data from the tails is needed. 300 virtual experiments are required to reduce the variation of the 80% single-sample confidence interval below two percentage points, whereas 1,000 virtual experiments are needed for the 95% single-sample confidence interval. Each experiment requires multiple dynamic simulations per nodal diameter due to ensemble averaging. For reference, 1,000 virtual experiments required approximately 6.5 hours wall-time per nodal diameter with typical amounts of ensemble averaging. 95% single-sample confidence intervals are thus computed only for the most important studies, e.g. quantifying error throughout the fan operating range,

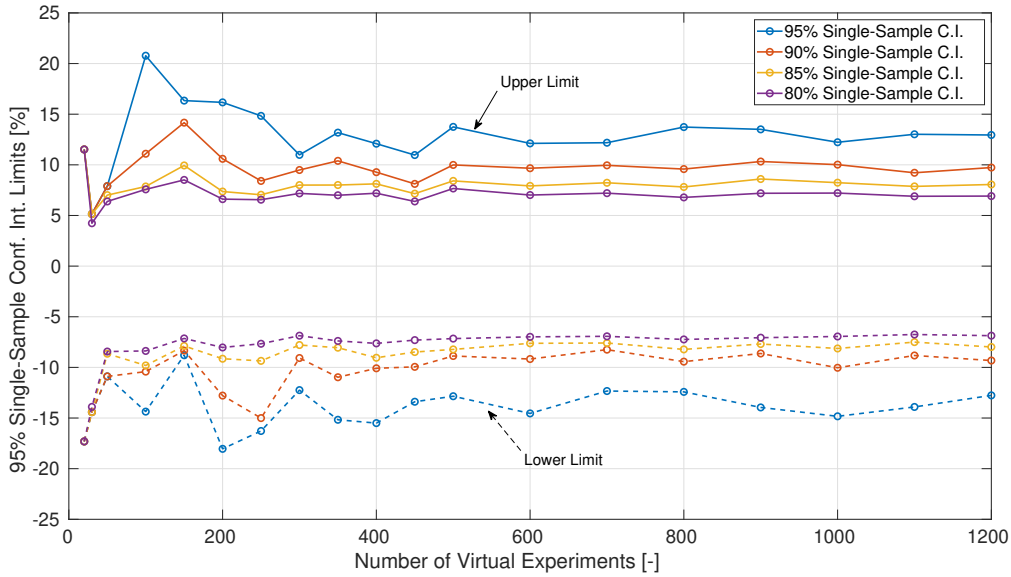


Figure 4-9: Dependence of 80% - 95% single-sample confidence intervals on number of virtual experiments performed. 300 and 1000 experiments needed for 80% and 95% single-sample confidence intervals to converge respectively.

and 80% single-sample confidence intervals used for studies where trends are more significant than specific values, e.g. sensitivity studies. For all cases, the single-sample confidence intervals are constructed with $\beta = 0.95$.

Nevertheless, the relatively low computational cost demonstrates a strength of the reduced order model in experimental design; in the time required for a single-passage unsteady CFD computation, sufficient virtual experiments were performed for a statistical analysis. This framework is general and applicable to other forced response system identification experimental design problems where reduced order models can reasonably represent the system dynamics.

The remainder of this chapter focuses on the results of virtual experiments with expected noise levels and nominal experimental conditions. The impact of varying noise levels and the establishment of the nominal experimental procedure, as well as other sensitivity studies, will be discussed in Chapter 5. 95% single-sample confidence intervals derived from 1,000 virtual experiments are used for all results in the remainder of this chapter.

4.4 Results at Design Point with Noise

Results with noise are first examined for operation at the design flow coefficient and at takeoff speed, the same condition as for Section 4.1. Figure 4-10 demonstrates the impact of noise on the measured transfer function for 1st forward nodal diameter forcing. The variance in the transfer function magnitude and phase is greatly increased, especially in regions where the coherence is near zero (e.g. between frequencies of 1E - 2E), indicating the response in those regions is driven nearly entirely by noise. Near the frequency of the 1st forward nodal diameter mode, however, the coherence is near unity and the variance in the transfer function is substantially less. The useful frequency range is reduced compared to Figure 4-1 and the coherence is used to choose the frequency limits for system identification. A heuristic was to place the limits where the coherence drops to 80% of its peak value[6] as in Figure 4-10 where the limits were 2.5E and 3.1E.

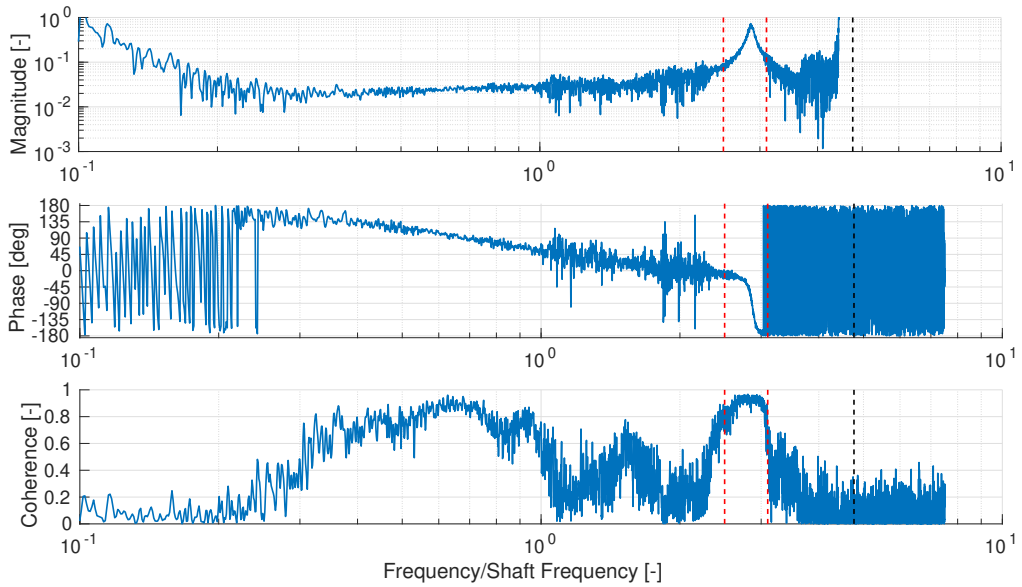
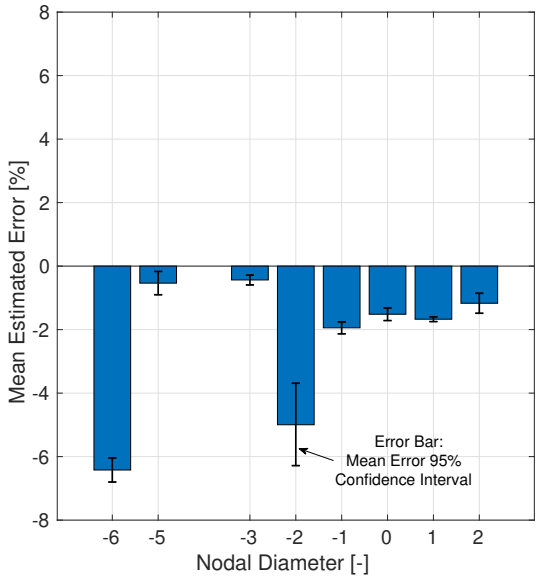


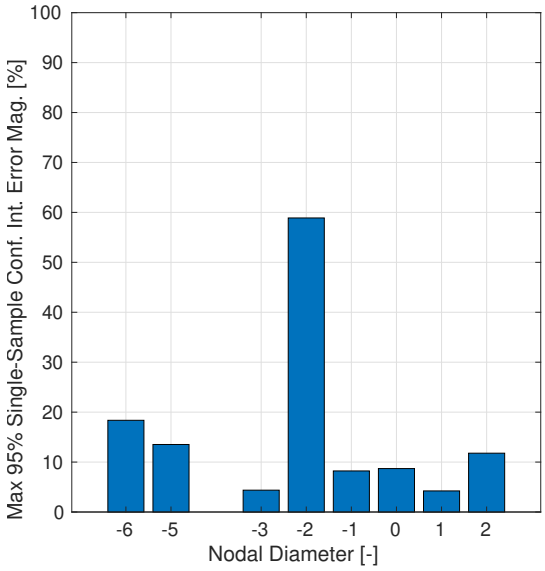
Figure 4-10: Transfer function from 1st forward nodal diameter forcing with expected noise levels. Coherence values around resonance used to guide system identification frequency limits.

The statistical methodology of Section 4.3.2 was applied to all nodal diameters

[6]the 80% criterion was selected from trial and error



(a) Mean Error with 95% confidence interval



(b) Maximum 95% single-sample confidence interval magnitude

Figure 4-11: Error metrics from statistical analysis for operation at design point and expected noise levels. Mean error less than 2% and 95% single-sample confidence interval magnitude less than 15% except for 2$^{\text{nd}}$ and 6$^{\text{th}}$ backward nodal diameters.

within the actuator temporal and spatial frequency range for the design point. Figure 4-11a show the mean error for all excitable nodal diameters[7] with the 95% mean-error confidence interval in error bars. For this condition, the experiment has low bias, with the mean error $< 2\%$ and the confidence interval $< \pm 0.4\%$ for all nodal diameters except the 2$^{\text{nd}}$ and 6$^{\text{th}}$ backward for reasons that will be shortly discussed. Figure 4-11b gives the maximum magnitude of the 95% single-sample confidence interval, i.e. $\max(|\hat{e}_{-}^{0.025}|, |\hat{e}_{+}^{0.975}|)$, corresponding to the maximum error magnitude at least 95% of the time. The maximum error is less than 15% for all nodal diameters, except for the 6$^{\text{th}}$ backward nodal diameter at above with 18% and the 2$^{\text{nd}}$ backward nodal diameter at near 60%. Such a large single-sample confidence interval renders the 2$^{\text{nd}}$ backward nodal diameter un-identifiable for practical purposes.

The plots of Figure 4-11 are useful for quantifying the accuracy of the experiment for each nodal diameter, but the relative change in damping ratio between nodal

[7] positive abscissa values correspond to forward nodal diameters and negative values to backward nodal diameters

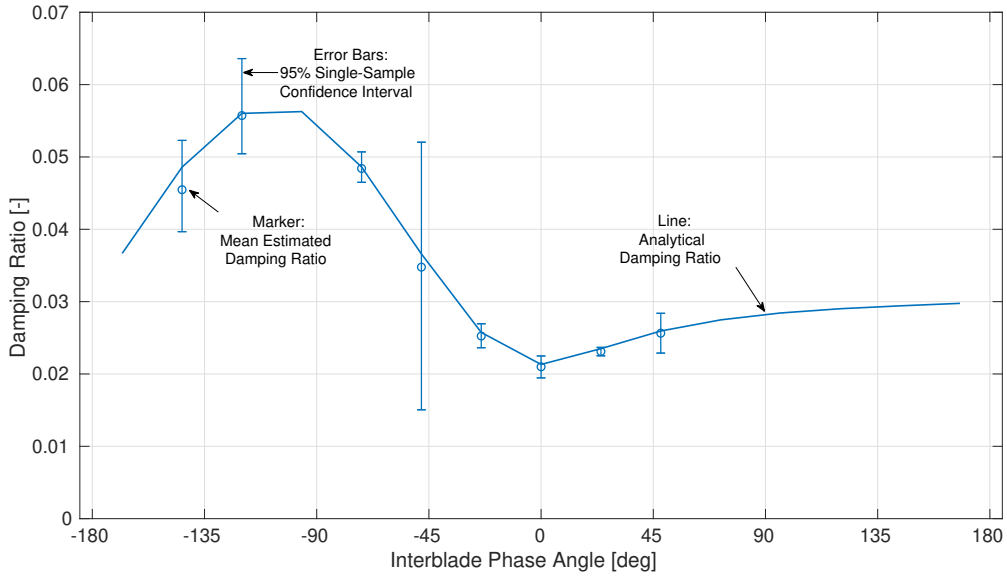


Figure 4-12: Mean damping ratio with 95% single-sample confidence interval error bars as a function of interblade phase angle. Mean error and confidence intervals are small relative to changes in analytical damping ratio with interblade phase angle.

diameters is not apparent. To bring context to the error quantification, Figure 4-12 shows the mean estimated damping ratio as a function of interblade phase angle with the 95% single-sample confidence interval as error bars. The solid line indicates the analytical, or "true," damping ratio from the flutter model. The mean error and confidence intervals are shown to be small compared to the change in damping ratio from mode to mode, except for the 2^{nd} backward nodal diameter (IBPA $\approx -45°$). This type of plot will be used extensively when comparing results across conditions which change the analytical damping ratio (e.g. engine speed or fan performance parameters) whereas the bar charts in Figure 4-11 are more useful for when the analytical damping ratio is constant (e.g. increasing sensor noise magnitude).

We now consider the cause of the increased error of the 2^{nd} and 6^{th} backward nodal diameter modes. As noted before, the 6^{th} backward nodal diameter is close in frequency to the 2^{nd} forward nodal diameter mode. With a noise-free transfer function, as in Figure 4-2, the system identification succeeds despite this complication. Noise, however, largely overpowers the response from the 6^{th} backward mode as shown in the view of the transfer function in Figure 4-13. While the 2^{nd} forward nodal

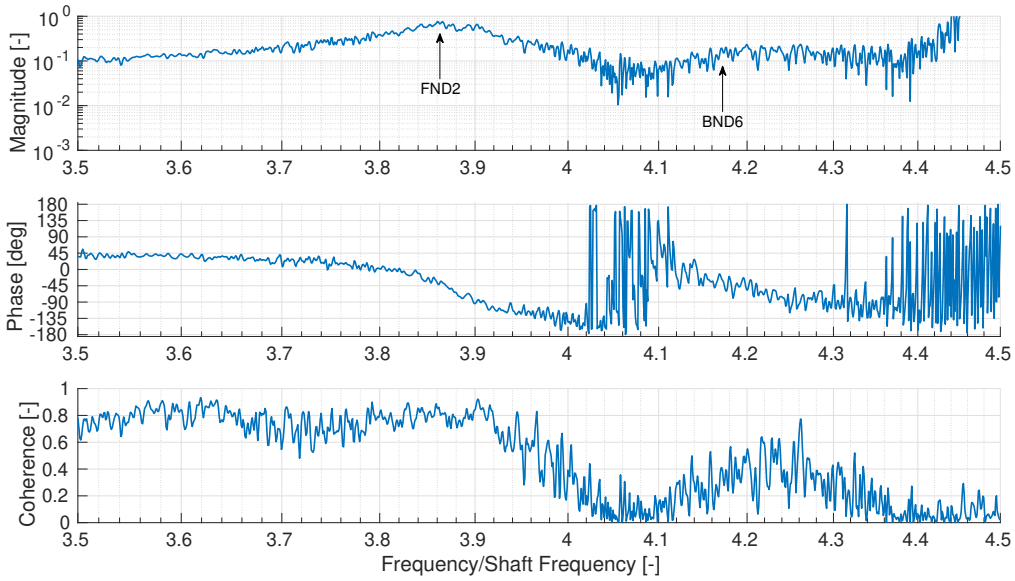


Figure 4-13: Low coherence and proximity of 6$^{\text{th}}$ backward nodal diameter mode to 2$^{\text{nd}}$ forward nodal diameter results in greater error than other modes.

diameter is distinguishable and has a coherence of approximately 0.8, the 6$^{\text{th}}$ backward nodal diameter is obscured and has a coherence of only 0.4. A combination of the high frequency of the mode, placing it near the actuator bandwidth limit, and the fact that the mode is excited through spatial aliasing, reducing the effective power of the actuator even further, results in the observed low signal-to-noise ratio and coherence. The proximity to the higher response and less damped 2$^{\text{nd}}$ forward nodal diameter is even more problematic for identification of the 6$^{\text{th}}$ backward nodal diameter at lower speeds. This is due to a general limitation of identifying modes with similar absolute frame frequencies when using a single tip-timing sensor, as will be discussed further in Section 4.5.2.

The 2$^{\text{nd}}$ backward nodal diameter faces the opposite challenge as it is near the low frequency limit of the actuator. Even for the ideal transfer function, Figure 4-2, only a small portion of the transfer function at frequencies below the mode frequency is measurable. As shown in Figure 4-14, however, response at these frequencies is dominated by noise. The increased power of inlet turbulence noise at low frequencies[8] further obscures the response from low frequency modes. Using the system identifica-

[8]as discussed in Section 4.3.1, the turbulence power spectrum varies inversely with frequency

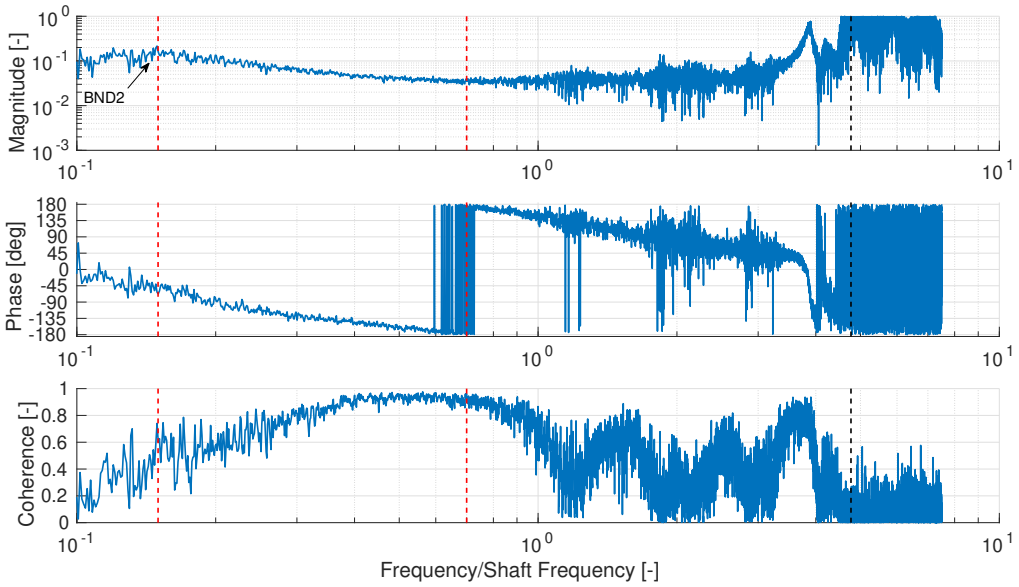


Figure 4-14: 2nd backwards nodal diameter mode near low frequency limit of actuator rendering it un-identifiable with noise.

tion frequency limit heuristic would eliminate the response near the mode frequency, as the lower limit would be placed near 0.3E. Relaxing the heuristic and expanding the lower limit, as in Figure 4-14, produced little improvement in the error metrics.

Modes near zero frequency are potentially un-identifiable, a limitation imposed by actuators operating in the absolute frame because no actuator can operate at arbitrarily low frequencies. Whether a mode is sufficiently low frequency as to be un-identifiable is dependent on the combination of mode frequency and actuator performance characteristics. For the PW615 specifically, the 2nd backward nodal diameter mode is sufficiently low-frequency at takeoff speed to be un-identifiable, as are the 3rd and 5th backward nodal diameter modes at lower engine speed. Which, if any, modes are un-identifiable will change for different fans and actuator designs, but can be determined with *a-priori* knowledge of the fan blade natural frequency and actuator performance characteristics.

4.5 Effect of Operating Point on System Identification

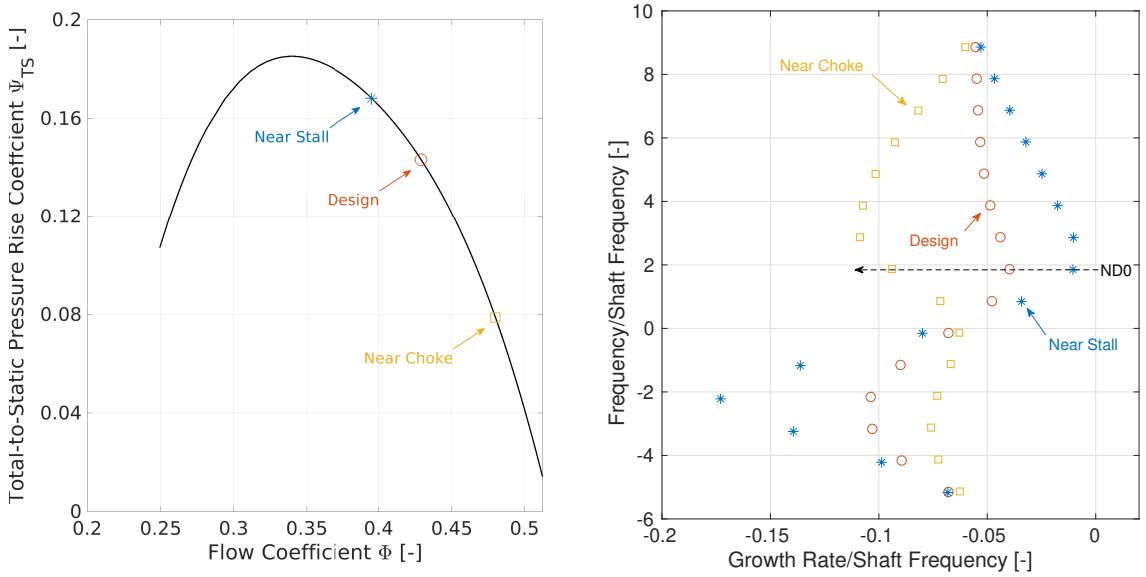
4.5.1 Flow Coefficient Variation

We now examine multiple fan operating points to determine the expected error throughout the operating range. The aerodynamic operating point can be changed by changing the inlet corrected mass flow, the fan speed, or some combination of both. Within the incompressible flutter model, fan performance is characterized by the flow coefficient and pressure-rise coefficient. Moving up and down the fan pressure-rise characteristic at different fan speeds defines a fan operating map.[9].

Figure 4-15a shows a lower flow coefficient operating point near stall and a higher flow coefficient operating point near choke on the fan pressure-rise characteristic and resultant bending mode eigenvalues are plotted in Figure 4-15b. The mode frequencies are constant as they are dominated by the blade natural frequency, but the growth rate changes by as much as 250% with changing flow coefficient. Moving towards stall reduces damping for the forward nodal diameter modes and increases it for the backward nodal diameters. Moving from design towards choke has the opposite effect.

The resultant mean estimated damping ratios and 95% single-sample confidence intervals for the three operating conditions are compared to the analytical damping ratios in Figure 4-16. As the mode frequencies do not change, the 2^{nd} backward nodal diameter mode remains effectively un-identifiable and the 6^{th} backward nodal diameter damping is under-predicted as before. The remaining nodal diameters, however, follow the analytical variation in damping ratio well. The least damped modes are the most accurately measured, with both the mean error and the single-sample confidence interval size decreasing as a mode becomes less damped. The opposite is also true with the error metrics worsening as a mode's damping ratio

[9]The pressure rise characteristic changes slightly with speed due to the change in the effective stiffness of the blade and the associated change in steady twist, but this effect is neglected as the pressure rise coefficient varied by at most 5% with speed



(a) Total-to-static characteristic

(b) Bending mode eigenvalues

Figure 4-15: Approaching stall on total-to-static characteristic reduces damping for forward nodal diameters and increases damping for backward nodal diameters

increases. The dependence of error on damping ratio is due to the amount of response from the mode for a given forcing level. Less damped modes produce greater response, and therefore a higher signal-to-noise ratio, reducing error.

Furthermore, the damping ratio is not changing in isolation as the steady inlet coefficient also changes. At higher flow coefficient, the actuator-to-engine massflow ratio decreases, resulting in a lower effective forcing level. The magnitude of the inlet turbulence fluctuations increase with the flow coefficient as well. Both effects act to reduce the signal-to-noise ratio more than just the increase in damping ratio. The opposite is true for decreases in flow coefficient, with the signal-to-noise ratio improving due to an increase in effective forcing level and a reduction in the process noise level.

The error data of Figure 4-16 is quantified in Table 4.2. The mean error is generally seen to be within $\pm 3\%$ and the 95% single-sample confidence interval within $\pm 15\%$. The exceptions are the 0^{th}, 1^{st} forward and backward, and 2^{nd} forward nodal diameters near choke for which the maximum error was as much as 25% due to the increase in analytical damping ratio. The 2^{nd} forward nodal diameter error grew especially as it

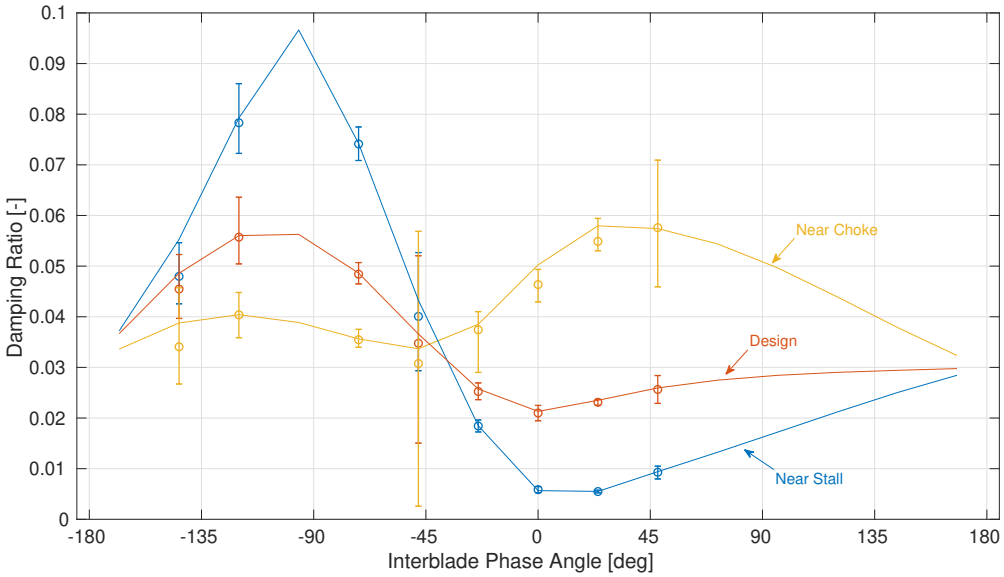


Figure 4-16: Mean damping ratios and 95% single-sample confidence intervals for multiple steady flow coefficients. Error metrics improve for modes with reduced damping.

is also near the actuator bandwidth limit where the actuation power is lowest. The 6^{th} backward nodal diameter has a mean error as great as -13.2% and a maximum error as great as 31.1% due to the combined negative effects discussed previously.

ND	Near Stall	Design	Near Choke
2	-1.2%	-1.2%	0.3%
1	-0.5%	-1.7%	-5.3%
0	3.4%	-1.5%	-7.7%
-1	-0.3%	-2.0%	-2.8%
-2	U.I.	U.I.	U.I.
-3	-0.2%	-0.4%	-0.5%
-4	-	-	-
-5	-1.2%	-0.5%	-0.1%
-6	-13.2%	-6.4%	-12.1%

(a) Mean Error

ND	Near Stall	Design	Near Choke
2	15.3%	11.8%	23.5%
1	5.3%	4.2%	8.5%
0	14.1%	8.7%	14.5%
-1	6.7%	8.2%	24.7%
-2	U.I.	U.I.	U.I.
-3	4.5%	4.4%	5.3%
-4	-	-	-
-5	8.8%	13.5%	11.3%
-6	23.0%	18.4%	31.1%

(b) Max. 95% single-sample confidence interval magnitude

Table 4.2: Mean error generally ±3% and maximum 95% single-sample confidence interval magnitude ±15% across multiple operating points at takeoff speed.[10]

[10]U.I. meaning "Un-identifiable."

Estimating Flutter Margin from Damping Ratio Measurements

We have thus far assessed the error bounds on the flutter damping ratio for different operating points on the fan characteristic, but the fan designer is typically interested in the *flutter margin*[11] as well, not the damping ratio alone. The flutter margin is estimated by measuring the damping ratio at multiple, stable points along the fan characteristic and fitting a curve to estimate the neutral stability flow coefficient ϕ_{NS} where the damping ratio is zero. Measuring flutter margin is useful not only during engine testing and certification, to ensure there is sufficient margin to begin with, but also enables investigations into how the flutter margin changes as the engine deteriorates. Deterioration effects have been shown to have reduce dynamical stability in other engine systems, such as a decrease in stall margin of the high-pressure compressor [64]. Characterizing these effects could enable new prognostic and diagnostic techniques to improve engine maintenance procedures and reduce costs.

An example of this procedure for the PW615 is given in Figure 4-17 which shows the analytical damping ratio and the estimated mean damping ratio with the 95% single-sample confidence interval as a function of flow coefficient for the critical flutter mode, the 1$^{\text{st}}$ forward nodal diameter. Also plotted are best fit lines through the maximum and minimum values of the single-sample confidence interval, producing the bounds of the flutter margin estimate. The flutter margin is under-estimated for both curves with a maximum error of 1.5 points of flutter margin, or 14% of the total.

[11] the flutter margin here is defined as $\frac{\phi_{op}-\phi_{NS}}{\phi_{op}}$ where ϕ_{op} is the flow coefficient at the operating line or design and ϕ_{NS} is the neutral-stability flow coefficient where $\zeta = 0$

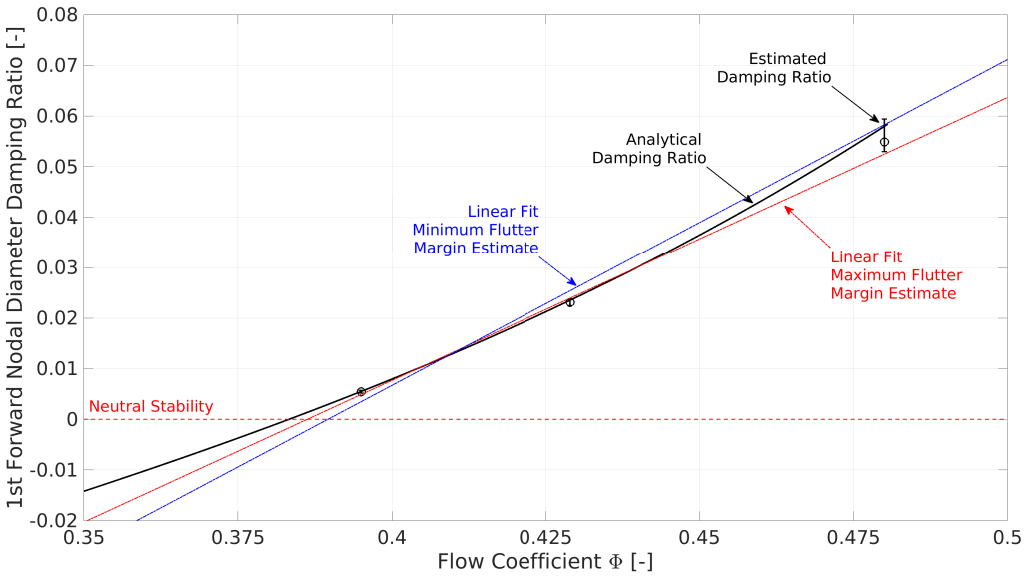


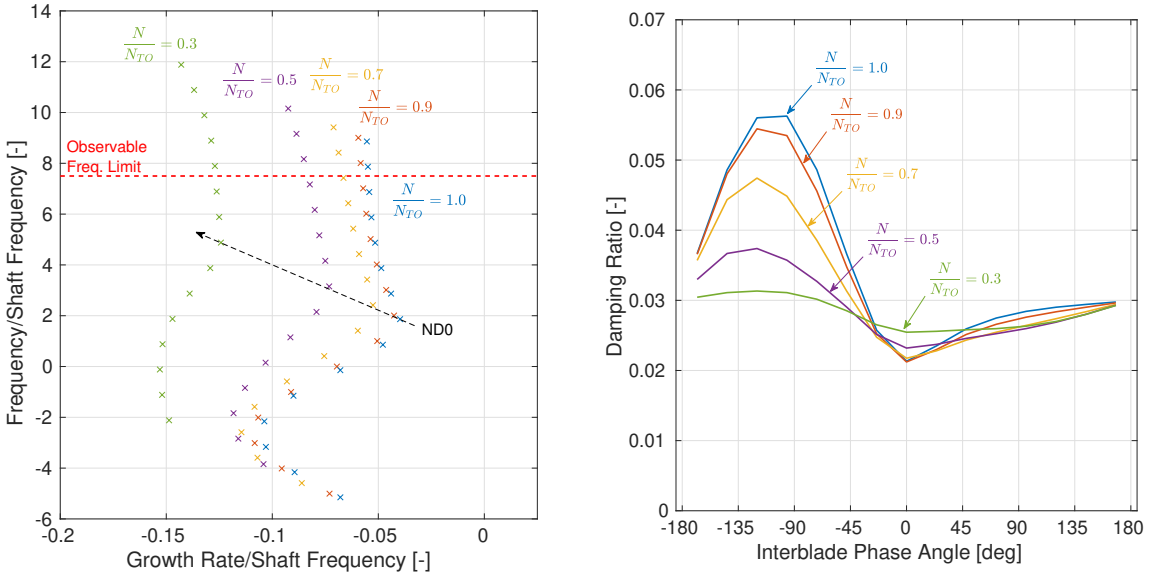
Figure 4-17: Multiple damping measurements along fan characteristic enables flutter margin estimate. Flutter margin estimated within 1.5 points or 14% for critical flutter mode of PW615, the 1st forward nodal diameter.

4.5.2 Fan Speed Variation

As fan speed is reduced from takeoff to idle, approximately 30% of takeoff speed, the dimensional blade natural frequency decreases due to a reduction in centrifugal stiffening. The shaft frequency, however, decreases faster than the blade natural frequency resulting in an increase in non-dimensional frequency of the flutter modes as in Figure 4-18a which shows the eigenvalues for multiple fan speeds. The blade non-dimensional natural frequency, Q_b in Section 2.2, is a measure of effective blade stiffness and thus while the absolute stiffness is decreasing, dynamically the blade grows stiffer. This is seen in the reduced variation of mode damping ratio with interblade phase angle at lower speeds in Figure 4-18b, with all modes converging to the mechanical damping ratio $\zeta_b = 0.03$.

There are several competing effects when reducing fan speed. Positively impacting the error, reducing fan speed also reduces the engine massflow, thus the ratio of actuator massflow to engine massflow increases and the effective forcing level increases[12]. Furthermore, the effective sensor resolution increases with the reduction

[12]this effect is captured in the model at constant inlet flow coefficient through the actuator flow



(a) Eigenvalues

(b) Analytical Damping Ratio

Figure 4-18: Reducing fan speed increases mode non-dimensional frequency and effective stiffness, reducing the variation of damping ratio with interblade phase angle.

in shaft frequency as per Equation 2.5. Finally, the reduction of the dimensional blade natural frequency due to reduced centrifugal stiffening improves the effective bandwidth of the actuator. Negatively impacting the error, the effective stiffness of the blade increases, reducing the magnitude of the forced response and signal-to-noise ratio. The dimensional frequency separation between the modes also decreases as the shaft frequency decreases, increasing the opportunity for associated errors from the system identification.

Reducing the fan speed by only 10% produces a small change in the analytical damping ratio but, as in Figure 4-19, the mean estimated damping ratios follow the analytical trend. The exceptions are, as at takeoff speed, the 2$^{\text{nd}}$ and 6$^{\text{th}}$ backward nodal diameters and now also the 2$^{\text{nd}}$ forward nodal diameter. At this speed, the 2$^{\text{nd}}$ backward nodal diameter frequency is zero (within two decimal places), resulting in essentially a stationary wave in the absolute frame. This is both un-excitable due to the actuator lower frequency limit and un-observable with a single sensor, resulting in

coefficient $\Phi_{act} = u_{avg}/U_{tip}$ where u_{avg} is constant and U_{tip} decreases with fan speed

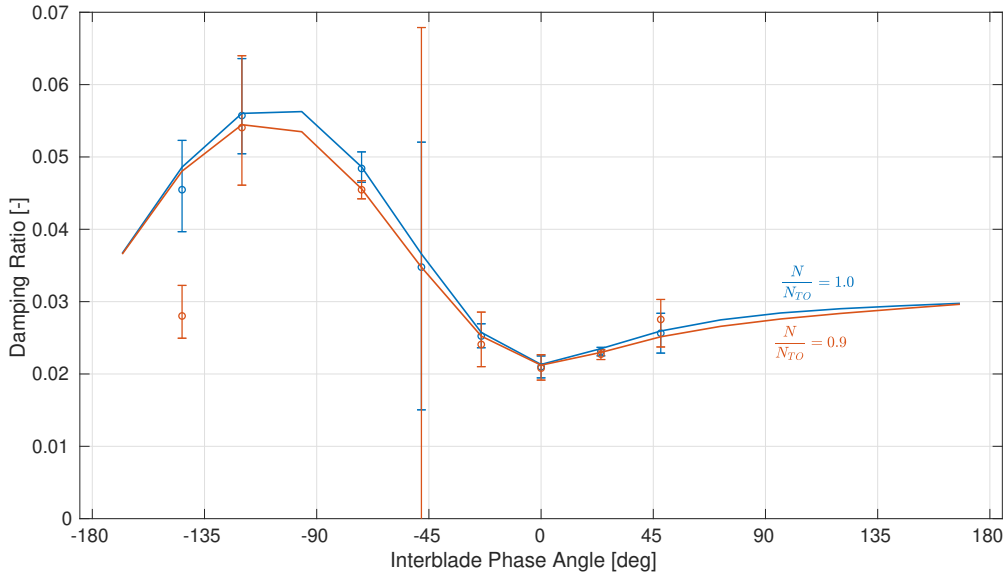
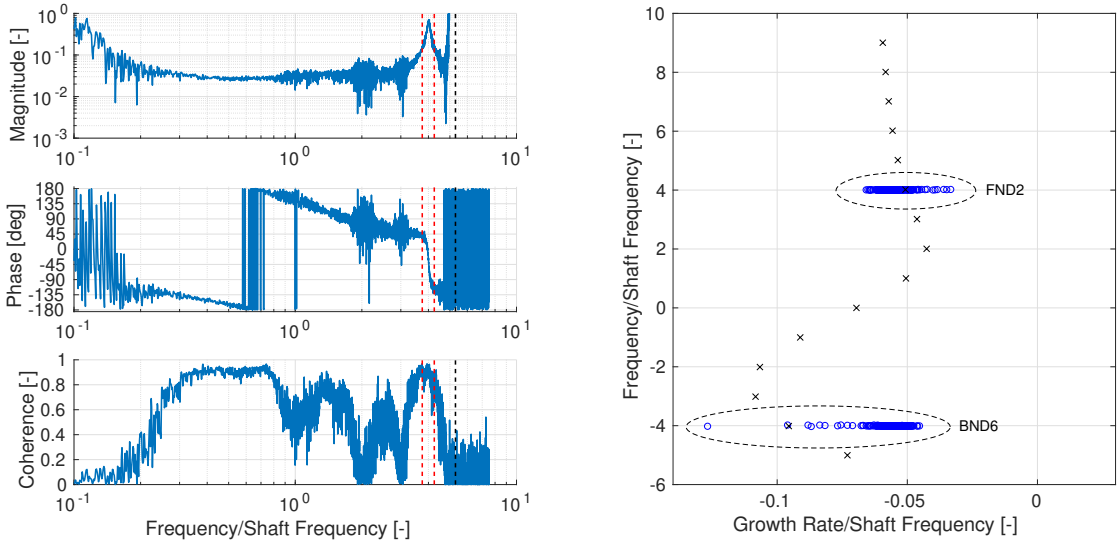


Figure 4-19: Mean estimated damping ratio and 95% single-sample confidence intervals for $\frac{N}{N_{TO}} = 1.0, 0.9$. Mean damping ratio follows trend except for 6^{th} backward and 2^{nd} forward nodal diameters.

the large error bar and mean damping ratio of zero[13]. The mean estimated damping for the 2^{nd} forward nodal diameter does not follow the analytical damping ratio for this small reduction in fan speed. Simultaneously the damping of 6^{th} backward nodal diameter is significantly underestimated, with the mean estimated damping ratio of these two modes separated by only 1.5%.

As in Figure 4-18a, the frequencies of the 6^{th} backward and the 2^{nd} forward nodal diameters for $\frac{N}{N_{TO}} = 0.9$ are -4.0 and 4.0 respectively, with the magnitudes differing by only 0.075%. Both of these modes are excited by the same forcing pattern and at the same frequency, resulting in their responses merging into a single peak in the transfer function shown in Figure 4-20a. The system identification algorithm essentially is faced with a response representative of a single mode of intermediate damping, resulting in a distribution of identified eigenvalues centered around the same growth rate as in Figure 4-20b. This is a limitation, however, imposed by the use of a single sensor. With a sufficient sensor count the response of the two modes can

[13]a failure mode of the system identification algorithm when presented with no useful response is to estimate the growth rate at zero



(a) Transfer Function

(b) Identified Eigenvalues

Figure 4-20: Merging of 2nd forward and 6th backward nodal diameter modes in transfer function due to equal absolute frame frequency results in identified eigenvalues at intermediate growth rate.

be separated by determining the unsteady spatial Fourier coefficients. As the 2nd forward nodal diameter is of greater interest due to its lower damping ratio, only 5 sensors would be needed to isolate its response. This is more feasible and economical than the 13 needed to isolate the 6th backward nodal diameter mode.

Reducing the fan speed further, Figure 4-18a shows the frequency of the 2nd backward nodal diameter mode increases and correspondingly it moves above the actuator lower frequency limit and becomes identifiable for $\frac{N}{N_{TO}} = 0.7$ and slower, as in Figure 4-21. The 3rd backward nodal diameter mode, previously at sufficiently negative frequencies as to be identifiable, is near zero frequency for $\frac{N}{N_{TO}} = 0.5$. Correspondingly, its single-sample confidence interval magnitude is greater than 80%, rendering that mode effectively un-identifiable for this speed. At the speed $\frac{N}{N_{TO}} = 0.3$ the mode frequency increases and it becomes identifiable once again. The 5th backward nodal diameter mode frequency, however, is now near zero and it too becomes un-identifiable (it is not shown on Figure 4-21 at this speed). The inability to excite and identify certain modes is an inherent limitation to absolute frame frequency excitation and identification as modes cross the zero-frequency axis. This is a trade-off made for the

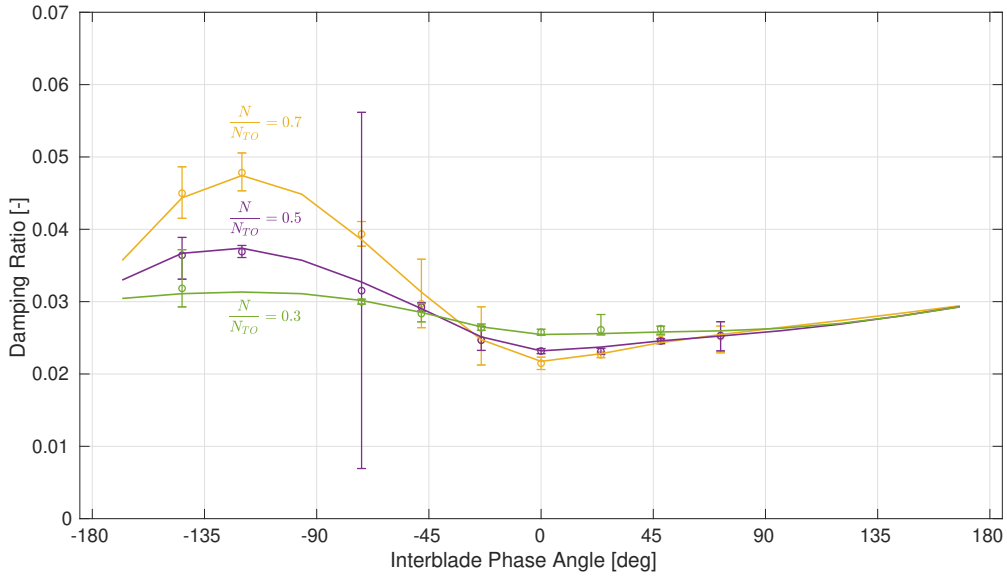
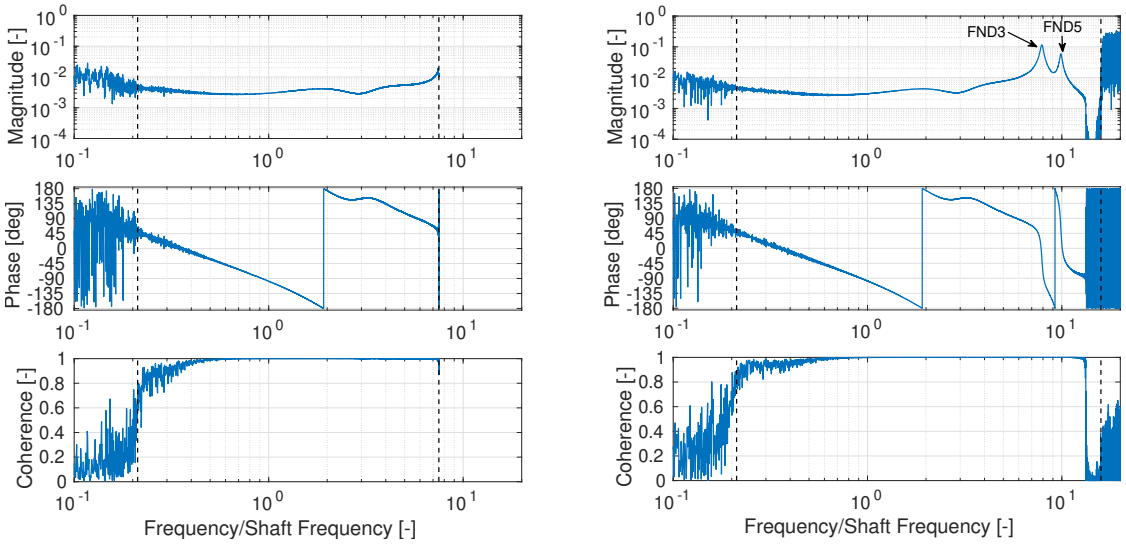


Figure 4-21: Mean estimated damping ratio and 95% single-sample confidence intervals for $\frac{N}{N_{TO}} = 0.7, 0.5, 0.3$. Analytical trends captured but 3$^{\text{rd}}$ and 5$^{\text{th}}$ backward nodal diameters becomes un-identifiable for certain speeds.

benefits of absolute frame excitation and measurement, namely simpler actuator and sensing design and the spectral separation for system identification. This trade-off is made less undesirable as the only modes that can have a near-zero frequency are the higher order backward nodal diameter which are typically more damped and of less interest.

The 3$^{\text{rd}}$ forward nodal diameter mode (IBPA $\approx 75°$) becomes identifiable for $\frac{N}{N_{TO}} = 0.7$ and 0.5. While the non-dimensional frequency for this mode increases at lower speeds, its dimensional frequency decreases and falls within the bandwidth limitation of the actuator. At $\frac{N}{N_{TO}} = 0.3$, however, the mode frequency exceeds the observable frequency limit. The transfer function for 3$^{\text{rd}}$ forward nodal diameter forcing in Figure 4-22a confirms the absence of any dynamics in the accessible frequencies, which are limited by the Nyquist frequency of 7.5E. The chirp in this case was terminated at 7.5E despite the upper frequency limit of the actuator being greater If the actuator is operated at frequencies greater than the observable frequency limit, response at the higher frequencies alias into lower frequencies and corrupt the transfer function. Artificially increasing the sampling rate, as in Figure 4-22b, demonstrates



(a) Nominal Sampling Rate

(b) 3x Nominal Sampling Rate

Figure 4-22: Transfer functions for 3rd forward nodal diameter forcing at $\frac{N}{N_{TO}} = 0.3$. 3rd and 5th forward nodal diameter modes excitable by actuator but un-observable due to limited sampling rate from tip-timing.

that the 3rd and 5th forward nodal diameter modes are excitable but simply not observable. Unlike before, this limitation is inherent to the mechanism of tip-timing and cannot be mitigated by adding more sensors.

Table 4.3 quantifies the error metrics across the fan speed range. As with the variation along the fan characteristic, the mean error is generally ±3% and the maximum confidence interval limits ±15%, with the 5th and 6th backward nodal diameters reaching as high as ±20% due to the reasons stated previously. The 1st backward nodal diameter also has a larger confidence interval at intermediate speed. At these two speeds the response magnitude fell below the sensor resolution at frequencies just above the mode frequency, limiting the useful response for system identification.

ND \ $\frac{N}{N_{TO}}$	1.0	0.9	0.7	0.5	0.3
3	U.I.	U.I.	-1.2%	0.3%	U.I.
2	-1.2%	U.I.	1.8%	-0.1%	1.8%
1	-1.7%	-1.1%	-0.6%	-2.5%	2.0%
0	-1.5%	-1.9%	-1.2%	-0.1%	1.2%
-1	-1.9%	-4.6%	0.0%	-1.9%	-0.6%
-2	U.I.	U.I.	-5.2%	0.7%	-0.6%
-3	-0.5%	-0.3%	2.1%	U.I.	-0.6%
-4	-	-	-	-	-
-5	-0.6%	-0.6%	1.0%	-1.3%	U.I.
-6	-6.0%	U.I.	1.4%	-0.7%	2.6%

(a) Mean Error

ND \ $\frac{N}{N_{TO}}$	1.0	0.9	0.7	0.5	0.3
3	U.I.	U.I.	10.0%	8.1%	U.I.
2	11.8%	U.I.	4.1%	1.5%	3.1%
1	4.2%	4.3%	2.4%	4.3%	10.3%
0	8.7%	9.7%	5.2%	1.7%	2.9%
-1	8.2%	16.7%	18.4%	7.5%	1.8%
-2	U.I.	U.I.	15.7%	2.7%	4.6%
-3	4.4%	3.1%	6.7%	U.I.	1.7%
-4	-	-	-	-	-
-5	13.5%	17.2%	6.6%	3.5%	U.I.
-6	18.4%	U.I.	9.6%	9.8%	20.4%

(b) Max. 95% single-sample confidence interval magnitude

Table 4.3: Mean error generally ±3% and maximum 95% single-sample confidence interval magnitude ±15% across fan speed range.

4.5.3 New Capability: Quantification of Damping Across Fan Map

With this experiment, we can develop a picture of how the damping varies across the entire operating envelope. For example, a result of this experiment could be contours of constant damping ratio on the fan map, as done in Figure 4-23 for the 1st forward nodal diameter with data from the virtual experiments in this chapter. This represents an evolution of Figure 1-3, with not only the flutter boundary identified by the contour of zero damping ratio, but also how much the damping varies across a speedline or operating line. This new map can be created for each nodal diameter measured to discover not only regions of the fan map which have low damping or instability, but also which flutter mode is responsible.

Although flutter or low damping is not expected to be limiting for the PW615, as evidenced by the "well-behaved" contours of damping ratio in Figure 4-23, Figure 4-24 shows an example map of a fan for which flutter and low damping *are* problematic. Such a map identifying problematic operating points can be produced using the experiment developed in this thesis.

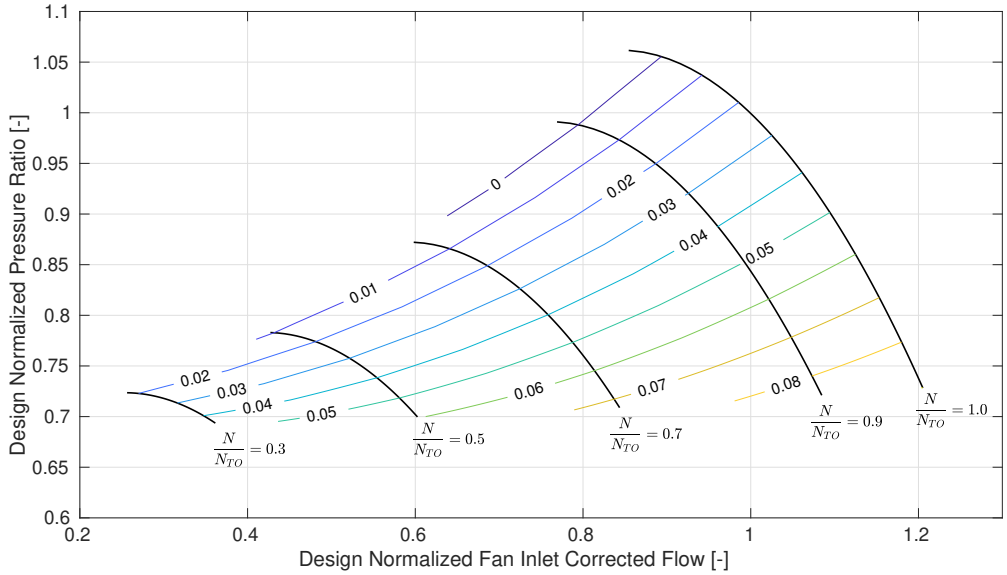


Figure 4-23: Fan map with contours of constant 1st forward nodal diameter damping ratio produced from virtual experiment data. Experiment provides new capability to identify regions of low damping or instability.

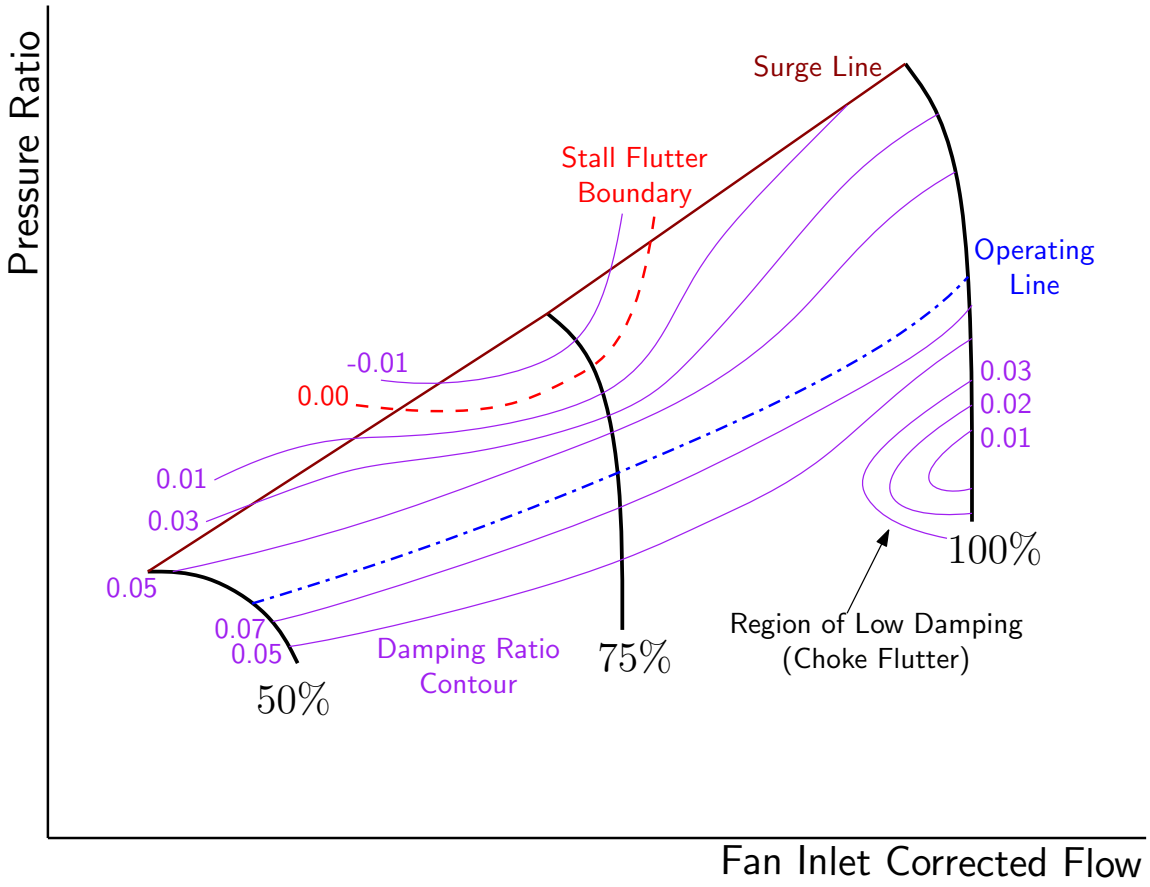


Figure 4-24: Example fan map with flutter instability limiting fan operation and regions of low damping in operating range. Experiment enables identification of problematic operating points.

4.6 General Limitations of Experimental Design

The results and discussion in Sections 4.4 and 4.5 have identified three general limitations of the current experimental design which are summarized below:

1. The inability of a single tip-timing sensor to distinguish the response from separate modes close in absolute frame frequency, resulting in inaccurate system identification. For the PW615, this increased the error of the 6^{th} backward nodal diameter mode throughout the operating range and rendered it and the 2^{nd} forward nodal diameter mode un-identifiable at 90% of takeoff speed. This limitation, however, can be mitigated by increasing the number of sensors to permit a spatial Fourier decomposition, thereby isolating each mode's response.

2. The inability to excite backward nodal diameter modes with absolute frame frequency below the lower frequency limit of the actuator. This is a consequence of actuators operating in the absolute frame, in which the frequency of backward nodal diameters can grow arbitrarily close to zero and become a standing wave. No actuator can operate at arbitrarily low frequencies, rendering such low frequency modes un-excitable. For the PW615 specifically, this effect prevents identification of the 2^{nd} backward nodal diameter mode at takeoff speed and the 3^{rd} and 5^{th} backward nodal diameter modes to lower engine speeds. Which modes, if any, modes are un-identifiable due to this phenomena can be estimated prior to conducting the experiment as it is dependent the blade natural frequency, operating speed, and actuator bandwidth which are typically known *a-priori*.

3. The inability of tip-timing systems to measure modes with absolute frame frequencies greater than half of blade passing frequency. This limitation is inherent to the mechanism of tip-timing which produces an effective sampling rate of the blade passing frequency, thereby restricting measurement of modes with modes above half blade passing frequency due to the Nyquist sampling theorem. This limitation grows more restrictive and prevents measurements of a greater num-

ber of modes as the engine speed decreases, even if the actuator is capable of exciting these modes. It was demonstrated that this restriction prevents identification of the 3rd and 5th forward nodal diameter modes for the PW615 at idle despite the actuator having sufficient bandwidth to excite these modes.

4.7 Summary of Virtual Experiment Results

In this chapter, virtual experiments using the experimentally measured actuator frequency response were used to assess expected error in the forced response experiment. Virtual experiments without noise sources were first used to assess the error in the system identification process and to evaluate the importance of characterizing actuator dynamics for damping estimation. These experiments showed the system identification process itself introduced little error, on the order of 0-2%. If state-space models of sufficient degrees of freedom are used for system identification, characterization of the actuator dynamics is not necessary. The extra degrees of freedom are able to compensate for the presence of actuator dynamics in the measured transfer function and isolate the underlying flutter dynamics, although this is likely untrue for actuators with non-linear dynamics.

Random process and sensor noise were implemented into the virtual experiments to simulate the physical experiment. A statistical framework was developed to quantify experimental error, with the mean and percentile statistics of the error distribution from multiple virtual experiments quantifying the systematic bias of the experiment and confidence of a single damping measurement. The statistical framework is general and can be applied to the experimental design of other forced response experiments. For the PW615 specifically, the mean error was found to be within $\pm 3\%$ and a single damping measurement within $\pm 15\%$ of the true value (with 95% confidence) for most flutter modes throughout the engine operating range. Fitting a curve to multiple measurements along the fan pressure-rise characteristic enabled estimation of the flutter margin. Flutter margin was estimated within 1.5 points or 14% for the PW615.

Greater error was found for certain modes at specific operating points and revealed some general limitations of the experimental design, but these exceptions were for the more highly damped backward nodal diameter modes which do not limit engine operation. The least damped modes, and therefore modes of greatest interest, had the lowest error due to increased signal-to-noise-ratio, demonstrating the utility of the experiment.

Chapter 5

Error Sensitivity Studies

The error estimation in Sections 4.4 and 4.5 are useful in characterizing the performance of a single experiment, but they do not address how the error may change for different experiment designs or conditions. A natural question for the experimentalist to ask is what is the impact of a change in experimental setup and what improvements would be most useful. This chapter utilizes the statistical error framework to perform sensitivity studies to the experimental parameters in Table 5.1. For all sensitivity studies in this Chapter, an 80% single-sample confidence interval is used based on 300 virtual experiments with $\beta = 0.95$. The parameters are broken into three general categories and ranked from most easily controlled by the experimentalist to least as below. General recommendations are provided at the end of the chapter in Section 5.4.

Signal Processing*	**Experimental Conditions**	**Fan Design***
Window Length	Ensemble Averaging*	Mechanical Damping
Windowing Function	Forcing Magnitude*	Blade Mass
Window Overlap Fraction	Sensor Noise Magnitude	Rotor Loss
	Inlet Turbulence Intensity	Blade Axial Locations

Table 5.1: Parameters for sensitivity study from most controllable (signal processing) to least controllable (fan design). *means at nominal noise levels and/or experimental setup.

1. **Signal Processing**: These parameters, which control the analysis of the data

after the experiment has been completed, are associated with the windowing procedure necessary for the derivation of power spectral densities by Welch's method. While the topic of windowing and the performance of windowing functions has been studied extensively, e.g. Refs. [65, 66], these discussions are often couched in the language of theoretical signal processing. It can be difficult to translate these abstract results into the effect windowing choices have for a specific application. In quantifying the impact of windowing choices on the damping ratio error, guidelines specific to the application of flutter forced response system identification are developed.

2. **Experimental Conditions**: These parameters are related to the setup and execution of the experiment itself and represent a trade-off between reduction in experimental error and increased cost, complexity, or time. Increasing the amount of ensemble averaging, for example, reduces the impact of noise but increases the experiment duration. By quantifying the sensitivity of error to these parameters, an informed decision of these trade-offs can be made. Furthermore, the studies quantify the amount of margin available to compensate for uncertainty in parameters which may not be known a-priori (e.g. noise levels).

3. **Fan Design**: The parameters in this section correspond to the performance or design of the fan to be tested. The reduced order model has 20+ parameters used to describe the fan and the parameters selected represent those with the largest influence on flutter damping ratio. These sensitivity studies address how extensible the current experiment is to fans of other design.

5.1 Signal Processing

In this section sensitivity studies are performed to windowing parameters that define the operation of Welch's method to derive the estimated transfer functions. The nominal windowing configuration consists of Hann windows of length 9,375 samples with 50% overlap. When one of these parameters is varied in the sections below, the

others are held constant. Particular attention is paid to some of the potential pitfalls that can come from windowing choices.

5.1.1 Windowing Function

Perhaps the most immediate decision with respect to windowing is the choice of windowing function. The goal of windowing is to reduce the spectral leakage from performing a discrete Fourier transform on signals with non-integer periods. The performance of window functions has been studied and characterized extensively [65, 67, 68], but the advice for window selection is often limited to "it depends heavily on the user's application." In this section we thus characterize the effect of windowing function on the damping ratio error, and discuss impacts of windowing function on the estimated transfer functions using a selection of windows with varying performance characteristics, including the Rectangular, Hamming, Hann, Blackman, and $\alpha = 3.5$ Kaiser windows.

One large trade-off in window design is that of main-lobe width to side-lobe suppression. A narrower main lobe improves frequency resolution and the ability to distinguish separate tones close in frequency. Reduced side-lobe levels and higher side-lobe decay rates reduce the leakage of spectral energy from a tone to nearby frequencies in the spectrum. The need for precise frequency resolution in this application is reduced due to the frequency separation of the flutter modes with measurements in the absolute frame. For typical window lengths in this application, the discrete Fourier transform bin size is 0.001E - 0.025E and main lobe half-widths of windows are typically on the order of 1-5 DFT bins. Even the most closely coupled modes, the 2^{nd} forward and 6^{th} backward nodal diameters, are separated by 0.3E at takeoff, much more than the frequency resolution limitations imposed by the window choice. This is in contrast to the case when measuring in the relative frame where the flutter modes are very close in frequency. For example, the 0^{th} and 1^{st} backward nodal diameters are separated by only 0.003E, well within the range where window frequency resolution becomes relevant. Side-lobe suppression, however, may be more relevant as the leakage of energy from the flutter mode frequency distorts the transfer function

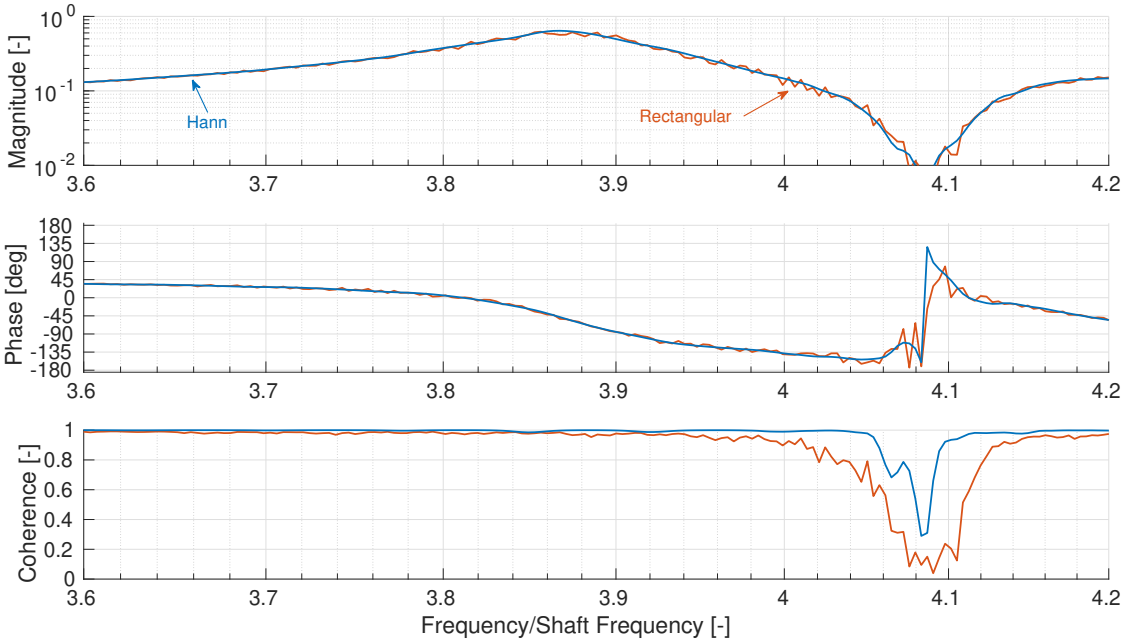


Figure 5-1: Example result of window function choice: increased side-lobes of Rectangular window manifests as ringing in transfer function as compared to Hann window.

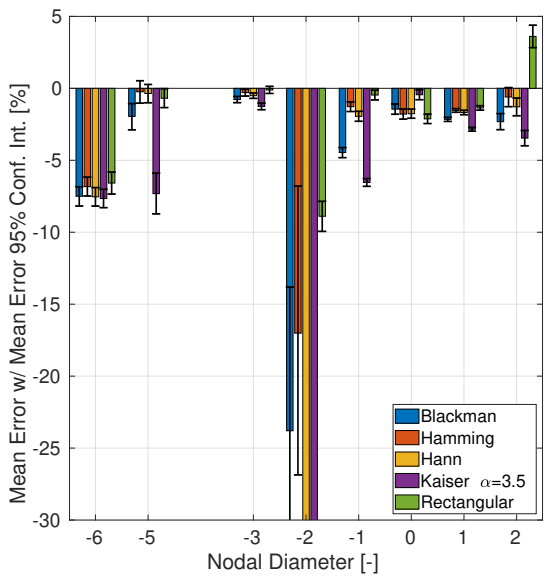
in nearby frequencies which is important for damping estimation. The effect of the greater side-lobes of the Rectangular window is seen in the zero-noise transfer function in Figure 5-1, which compares transfer functions for the 2$^{\text{nd}}$ forward nodal diameter using both windows, as "ringing" when compared to that of the Hann window.

Figure 5-2 compares windowing functions with respect to their impact on the error metrics for the experiment with noise. On the basis of mean error, the Hamming and Hann windows perform statistically equivalent[1] to, or better than, the other window choices.[2] The Hamming and Hann windows perform well on the basis of the 80% single-sample confidence interval, performing as well or better than the other windows across the range of nodal diameters considered. These results are perhaps not unexpected given the reputation of the Hamming and Hann windows as good general purpose windows.

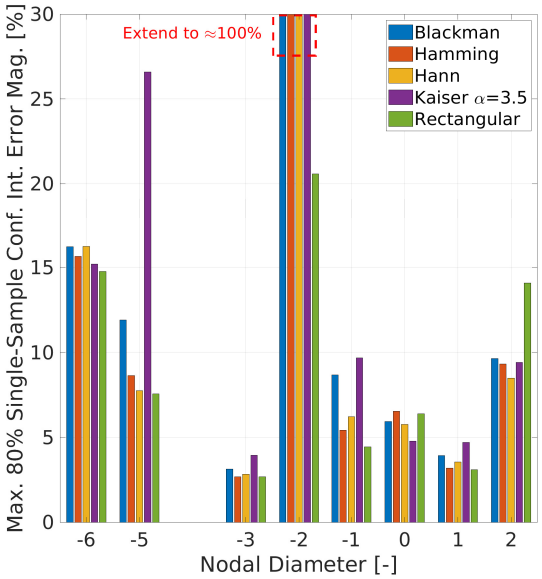
[1] as indicated by the 95% confidence interval of the mean error

[2] An exception is the 0$^{\text{th}}$ nodal diameter where the Kaiser window performs statistically better than the others, however, the Kaiser window performs significantly worse for other modes such as the 2$^{\text{nd}}$ forward and 5$^{\text{th}}$ backwards nodal diameter.

The 2nd backward nodal diameter is included in Figure 5-2 as it demonstrates a particularly strong sensitivity to the window function. The maximum single-sample confidence interval magnitude is approximately 100% for all windows except the Rectangular. This is not due to the specific performance characteristics of the Rectangular window but rather because of the input signal non-stationarity. All windows except the Rectangular window feature tapering to near zero in the time domain at the window edges. As demonstrated schematically in Figure 5-3a, where the time-domain window is overlaid with the chirp instantaneous frequency, using tapered windows discards the information from low frequency excitation. Due to the overlap of the windows, there is at least one window in which all other frequencies are well captured. As a result, the transfer function using tapered windows has low coherence and does not capture the transfer function shape at low frequencies, as in Figure 5-3b with the Hann window. Using the Rectangular window, however, results in improved coherence and agreement with the ideal transfer function. The Hann window is thus recommended overall, and is used for all studies in this work, except for low frequency modes. Despite the improvement from the Rectangular window, however, low frequency modes were largely un-identifiable for the PW615 as discussed in Section 4.5.

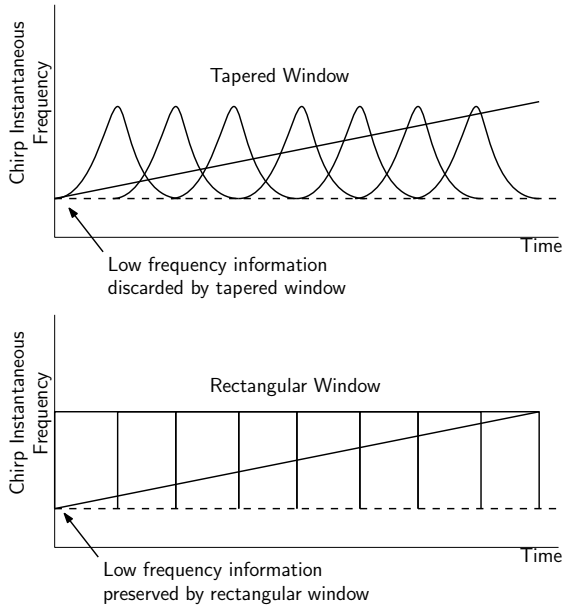


(a) Mean Error with 95% Confidence Interval

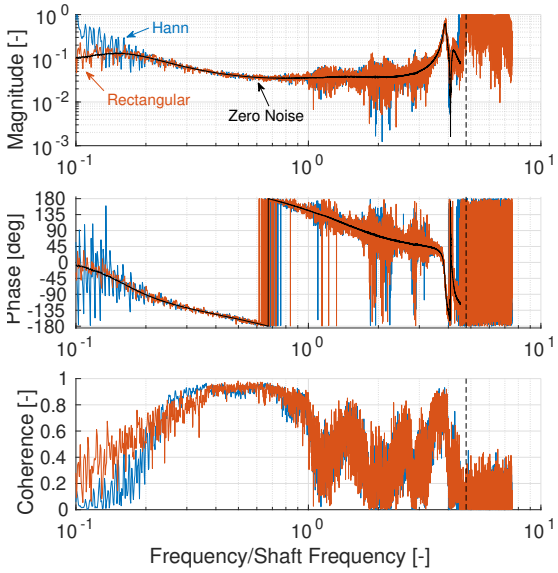


(b) Maximum 80% single-sample confidence interval magnitude

Figure 5-2: Impact of window function on error metrics. Hann and Hamming windows perform best overall except for 2nd backward nodal diameter with Rectangular window.



(a) Windows & chirp in time domain

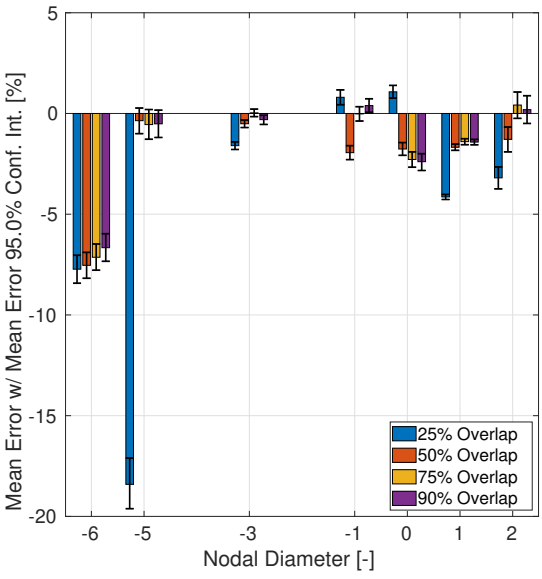


(b) Transfer Function (FND2 Forcing)

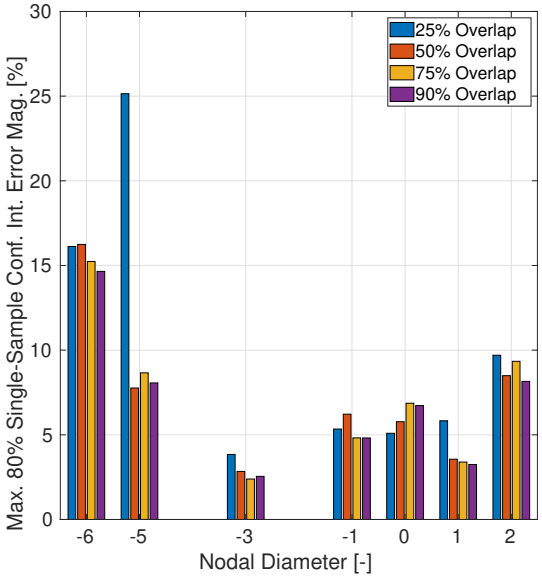
Figure 5-3: Rectangular window preserves low-frequency information discarded by tapered windows due to input signal non-stationarity.

5.1.2 Window Overlap

Inherent to Welch's method is the concept of averaging multiple spectra taken from windowing the signal under analysis. These windows overlap in the time domain and the extent to which a window is overlapped by the preceding window is dictated by the overlap fraction. The overlap fraction can vary from 0%, at which point the windows are independent, to 100%, which is simply the discrete Fourier transform of the entire signal. Overlap fractions from 0% to 60% are typical, with 50% being a common starting point [66]. Increasing the overlap fraction reduces noise in the resultant spectrum at the cost of increased computational cost (due to the increased number of windows needed at a fixed window length).



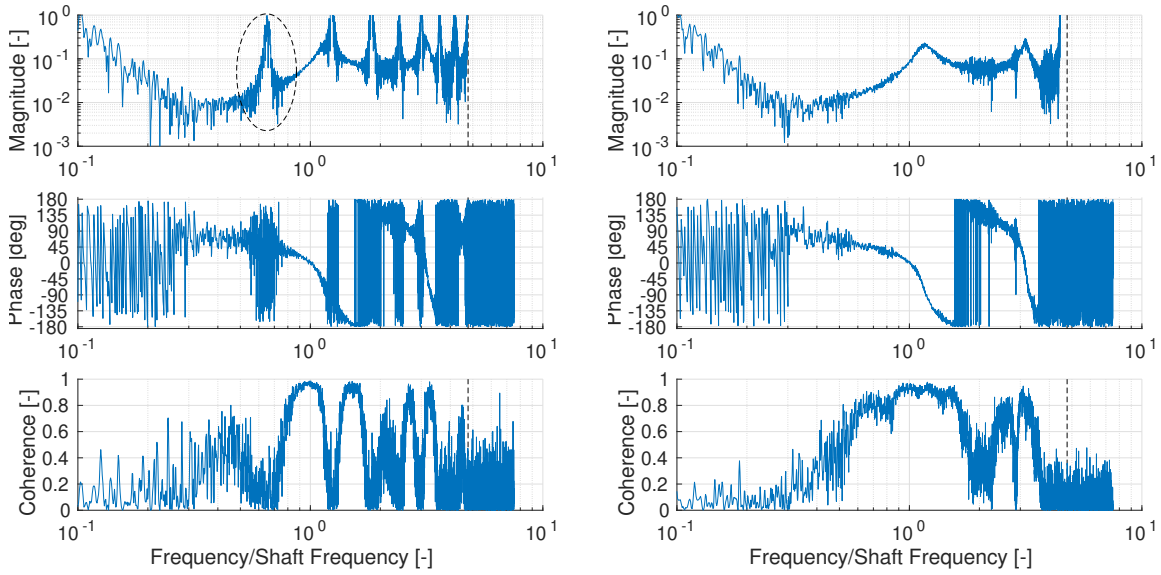
(a) Mean Error with 95% Confidence Interval



(b) Maximum 80% single-sample confidence interval magnitude

Figure 5-4: Impact of window overlap fraction on error metrics. Little impact on error metrics with 50% overlap or greater.

For overlap fractions of 50% and above, there is little impact on the error metrics as in Figure 5-4, which shows the error metrics for Hann windows with varying overlap fraction. There is no statistically significant change in the mean error and while variation in the single-sample confidence interval magnitude occurs, there is no discernible trend with increasing overlap fraction. 25% overlap fraction, however,



(a) 0% Overlap Fraction

(b) 50% Overlap Fraction

Figure 5-5: Low overlap fraction corrupts estimated transfer function with regions of high noise.

shows significant increases in the error metrics, especially for the 5^{th} backward and 1^{st} forward nodal diameters, indicating a complication with low overlap fractions. The 0% overlap fraction case is not presented as the transfer functions proved unusable, as shown in Figure 5-5 which compares the transfer functions for 50% and 0% overlap fraction. As circled in Figure 5-5a, regions of noise centered at discrete frequencies corrupt the transfer function with 0% overlap, but these regions are absent at 50% overlap. The 25% overlap case showed similar behavior, although not as extreme as that in Figure 5-5a. One of these regions occurred near the frequency of the 5^{th} backward nodal diameter, resulting in the high error for that mode with 25% overlap fraction.

This noise is numerical in nature and also related to the non-stationarity of the chirp signal, as shown schematically in Figure 5-6. The transfer function at any frequency is the ratio of the cross-power spectral density of the input and output signals and the power spectral density of the input signal. The moment in time corresponding to the window's edge corresponds to an instantaneous frequency in the chirp signal, t_0 and f_0 in Figure 5-6.

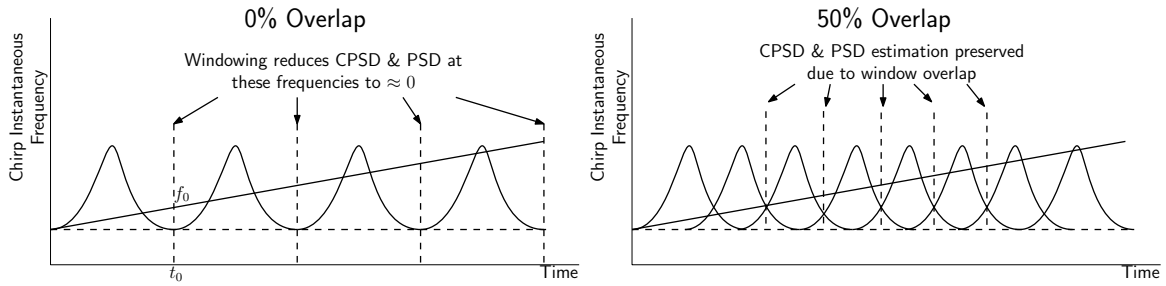
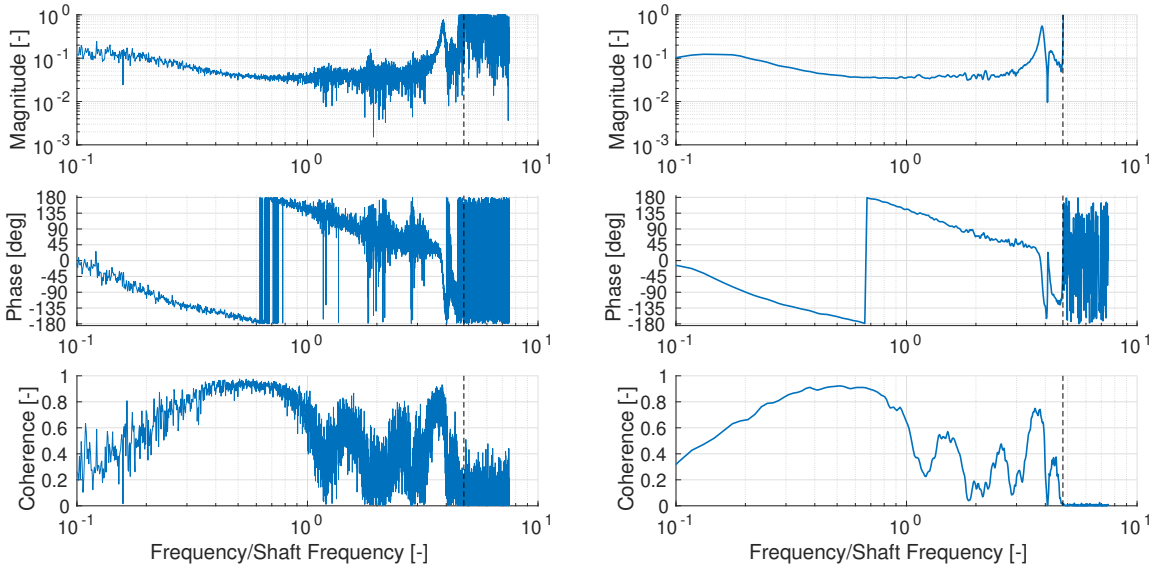


Figure 5-6: Reduction in cross-power spectral density and power spectral density at discrete frequencies due to non-overlaping, tapered windows

Most of the spectral energy at the frequency f_0 in both the input and output signals is produced at that moment in time t_0 (all of the energy in the absence of noise). A non-overlapping, tapered window, however, reduces that energy to near zero because the samples near t_0 are nearly eliminated. As the same windowing function is applied to both the auto-correlation and cross-correlation functions, the magnitudes of the cross-power spectral density and power spectral density are ideally reduced equally, with the ratio remaining constant at the true transfer function value. Numerically, however, this is prone to erratic behavior due to the division of small floating point numbers. Using the non-tapered Rectangular window with 0% overlap fraction eliminated this effect, providing evidence for this explanation. As discussed prior, however, the Hann window performs better than the Rectangular window for most modes. Because there is no advantage in using 0% overlap fraction, the Hann window with 50% overlap remained as the best configuration for this experiment. It is therefore recommended that overlap fractions below 50% be avoided when utilizing non-stationary excitation to avoid these numerical issues.

5.1.3 Window Length

The window length in samples controls the amount of averaging done in Welch's method for a given length input or output signal. Decreasing the window length reduces the noise in the resultant spectrum as more averaging is performed, but as each window has fewer samples, this comes at the cost of a reduction in frequency resolution. For simplicity the window length henceforth will be referred to in terms



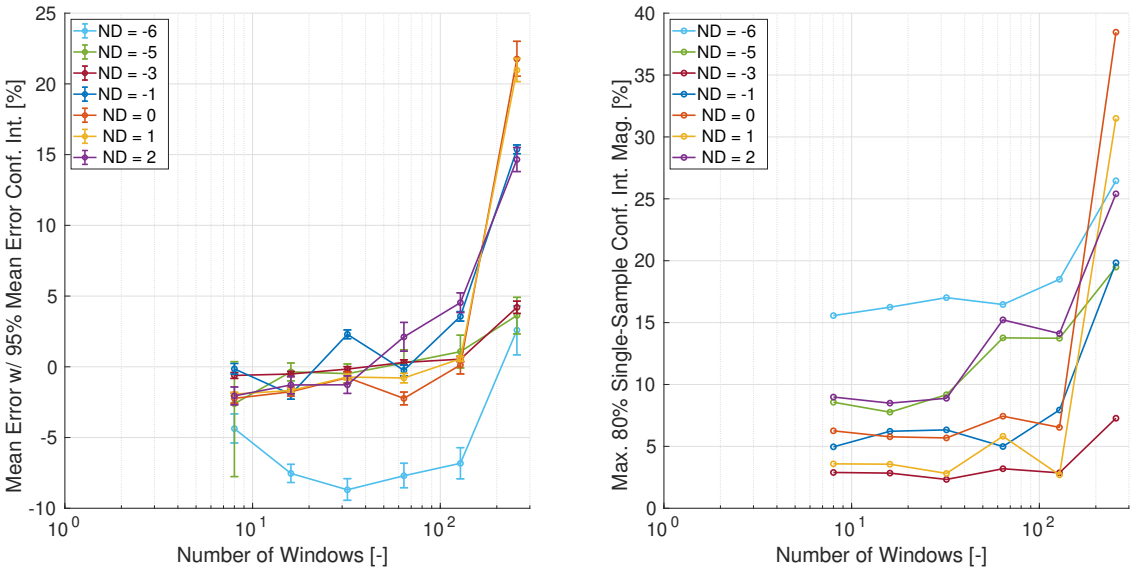
(a) 16 Windows (b) 256 Windows

Figure 5-7: Decreasing window length/increasing number of window reduces noise in estimated transfer function making dynamics more recognizable.

of the number of windows utilized. The input and output signal both consisted of 75,000 samples, producing a window length of floor$(75,000/N_{win})$ samples.[3] Figure 5-7 compares the transfer functions for 2$^{\text{nd}}$ forward nodal diameter forcing for window lengths of 16 and 256 windows. The increased averaging with the shorter window significantly reduces the variance in the transfer function, aiding in the visual recognition of the dynamics by the user.

While the greater window count improves visual recognition of the dynamics, taken to high numbers of windows it increases the quantitative error. The error metrics, Figure 5-8, show little variation when approximately 8-32 windows are used. Above that, however, the error metrics begin to increase, especially when more than 128 windows are used. Increasing the window count cannot change the signal-to-noise ratio of the underlying signal, only the variance in the resultant spectrum through increased averaging. The system identification algorithm, however, has far too few degrees of freedom to capture this variance, so it is essentially fitting the transfer

[3]when the overlap fraction was varied in Section 5.1.2 it was the length, not the number of windows, held constant to ensure the frequency resolution did not simultaneously change with the overlap fraction.



(a) Mean Error with 95% Confidence Interval

(b) Maximum 80% single-sample confidence interval magnitude

Figure 5-8: Impact of window length on error metrics. Error insensitive to window length in 8-32 window range but increases above 32 windows, with damping over-predicted.

function on an average basis. As a result, the small decrease in transfer function variance in the range of 8-32 windows has little effect on the fitting procedure.

High levels of averaging, however, smooth the transfer function even on an average basis, discarding useful information and increasing the apparent damping of the mode. This effect is greatest on the least damped modes as in Figure 5-8a where the mean error for the 0^{th} nodal diameter, the least damped mode, increases from 0.1% to 22% when increasing from 128 to 256 windows whereas the 5^{th} backward nodal diameter, the least damped mode, increases only from 1% to 4%. The apparent increase in damping due to excessive smoothing is perceptible in the transfer function, as in Figure 5-9 which compares the estimated 1^{st} forward nodal diameter transfer function for 8 and 256 windows (the ends of the range tested). While visually the effect is subtle, it has a significant impact on the quantitative result of the system identification algorithm.

As the amount of averaging is dependent both on the window length and the length of the signal being analyzed, it is not possible to give a specific value for the window

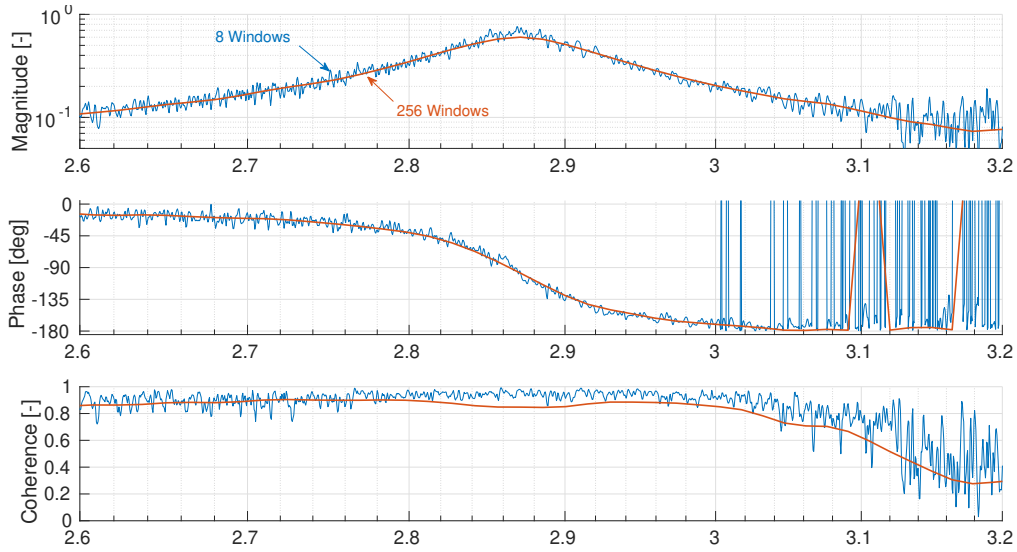


Figure 5-9: Estimated 1st forward nodal diameter transfer function with 8 and 256 windows. Increased averaging from high window counts excessively smooths transfer function, erroneously increasing apparent damping.

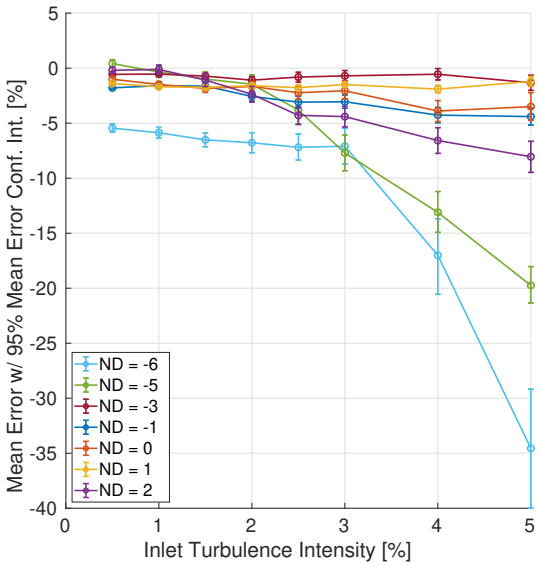
length that is appropriate in all cases. In general, however, it is not recommended that shorter windows and increased averaging be used to obtain a "cleaner" transfer function with less variance because this over-smooths the transfer function and results in over-prediction of the damping ratio. Multiple window lengths should be tried until the estimated damping ratio converges to a single value[4].

5.2 Experimental Conditions

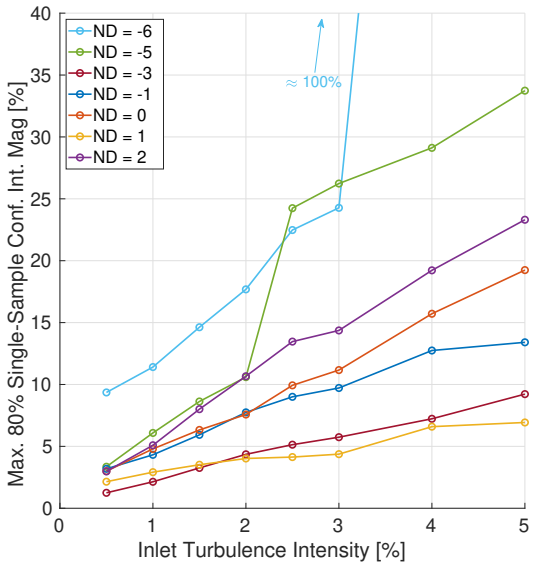
5.2.1 Noise Magnitude

It is difficult to know a-priori what the noise levels in the physical experiment will be, motivating the quantification of the error metrics to these magnitudes. The two sources of noise modeled in this framework are sensor noise and inlet turbulence as process noise. Inlet turbulence intensities in engine tests are typically of the order of 0.1% to 3% for well designed inlets [69, 70]. Turbulence intensity in tests of Rotor 67 was measured to be 1.5% [43] and this was taken as a baseline value for the PW615 experiment. It is especially relevant to quantify the sensitivity to turbulence intensity

[4]as is the case in Figure 5-4b for 32 windows and below.



(a) Mean Error with 95% Confidence Interval



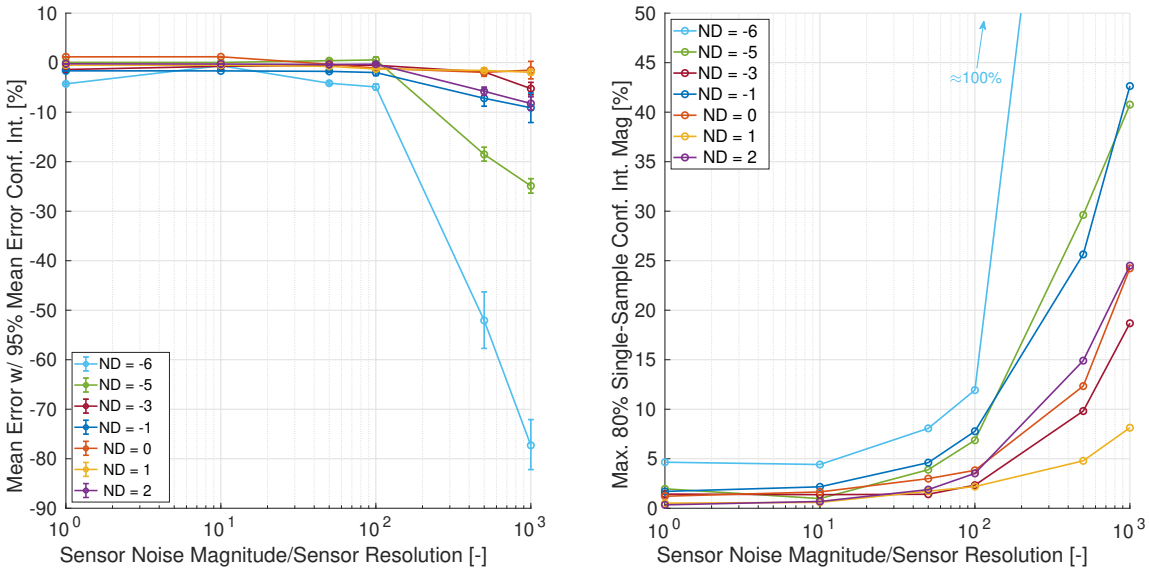
(b) Maximum 80% single-sample confidence interval magnitude

Figure 5-10: Error metrics increase with turbulence intensity and 6$^{\text{th}}$ backward nodal diameter un-identifiable above 3%.

as the the turbulence levels for the PW615 operating in the MIT test cell have yet to be assessed.

The error metrics were computed in the absence of sensor noise for turbulence intensities in the range of 0.5% to 5%, Figure 5-10. The error behavior is similar across all nodal diameters. The maximum single-sample confidence interval magnitude increases roughly linearly with turbulence intensity and the mean bias grows more uncertain (larger confidence intervals) and more negative. The exceptions are the 5$^{\text{th}}$ and 6$^{\text{th}}$ backwards nodal diameters which are the most sensitive to noise levels due to the reduced forcing levels previously discussed. Above 3% turbulence intensity the 6$^{\text{th}}$ backward nodal diameter is un-identifiable, with the maximum error near 100%.

For the PW615 experiment specifically, inlet turbulence intensity should be kept below 3% to ensure all nodal diameters in Figure 5-10 are identifiable. In general, any reduction in inlet turbulence would be effective in reducing error because the single-sample confidence interval magnitude increases monotonically with inlet turbulence



(a) Mean Error with 95% Confidence Interval

(b) Maximum 80% single-sample confidence interval magnitude

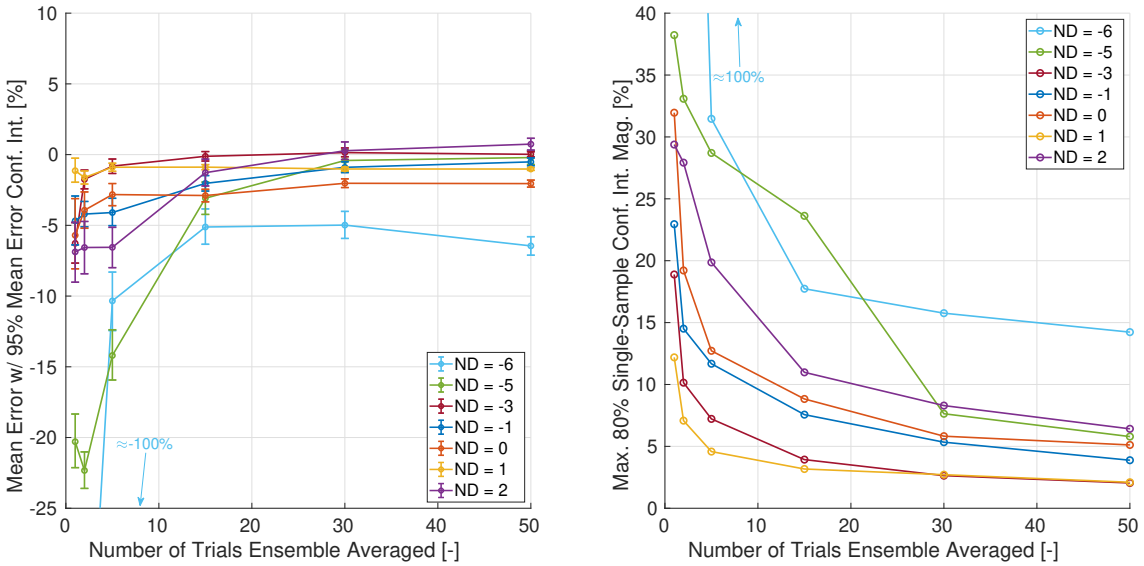
Figure 5-11: No change in error metrics for sensor noise below 10x sensor resolution with error growing rapidly above 50x sensor resolution.

intensity.

The sensitivity of the 5$^{\text{th}}$ and 6$^{\text{th}}$ backward nodal diameter error metrics holds for sensor noise as well, as in Figure 5-11. The error metrics are largely insensitive to noise below a level of 50x the sensor resolution. Above that, the error begins to grow rapidly, with the 6$^{\text{th}}$ backward nodal diameter becoming un-identifiable above a magnitude of 100x sensor resolution. A baseline level of sensor noise of 1x sensor resolution was used for the computations in this work, but that level could be increased to 10x with an increase of only 1-2% in the error metrics.

5.2.2 Ensemble Averaging

Ensemble averaging consists of averaging multiple, phase-locked time sequences measured by the sensor, thus improving the signal-to-noise ratio of the final signal by averaging out the random noise perturbations. It is only effective, however, for noise sources that are uncorrelated with the excitation from the actuator, such as inlet turbulence and sensor electrical noise. If a given noise source is correlated with exci-



(a) Mean Error with 95% Confidence Interval

(b) Maximum 80% single-sample confidence interval magnitude

Figure 5-12: Ensemble averaging effective in reducing error from noise, but has diminishing returns above 30 trial averaging.

tation, its contributions are the same for each trial to be averaged and thus cannot be reduced by the averaging process. Examples of correlated noise sources are electrical cross-talk between the actuator and sensor wiring or aerodynamic separation triggered by actuator operation.

Even small amounts of ensemble averaging is effective in improving the error metrics for the baseline noise levels established in the previous section. As in Figure 5-12, the greatest improvement occurs for ensemble averaging in the range of 2-15 trials, with diminishing returns for increased averaging. The 6^{th} nodal diameter is un-identifiable without some amount of ensemble averaging and it shows the greatest sensitivity. 30 trial averaging was chosen as nominal seeing as there is at most a 2% improvement in either error metric for greater averaging. Increasing ensemble averaging comes at the cost of a longer experimental duration and for the 20 second chirp needed at take-off conditions, 30 trial ensemble averaging requires approximately 10 minutes per nodal diameter forcing pattern, or approximately 40 minutes overall.

At least 5 to 15 trial ensemble averaging is generally recommended, but averaging

as many trials as possible within the allowable experiment duration is preferable. If needed, the frequency range of the chirp can be limited to reduce the length of a single trial. Initial exploratory experiments with fewer trials can be used to determine the needed frequency range for system identification and later experiments run with more trials for quantitative measurement of the mode damping. For example, the frequency range could be limited to 2.5E to 3.1E for the 1st forward nodal diameter in Figure 4-10, rather than the 0.1E to 4E shown.

5.2.3 Forcing Magnitude

Thus far all studies have been performed with the actuator operating at maximum capability. Of interest, however, is how much actuator margin exists within the system, i.e. whether the actuator can be operated at reduced levels to reduce blade and actuator stress. The actuator flow is controlled by reducing the input voltage to the actuator. Under the assumption of small, linear perturbations to a steady state, reducing the actuator flow shifts the bending response curve down in magnitude, as in Figure 5-13 which shows the effect of reducing actuator flow on the bending transfer function schematically. For a given sensor resolution, less of the flutter transfer function is measurable due to the reduced response. In the absence of noise or in a low noise environment[5], margin in actuator flow can be traded for sensor resolution, i.e. operation at reduced actuator flow with fixed sensor resolution is equivalent to reducing sensor resolution at maximum actuator flow. When noise levels exceed the sensor resolution, however, reducing the actuator flow reduces the resultant signal-to-noise ratio due to the reduction in bending response relative to the fixed noise level. This is the case expected for the PW615 and thus the actuator flow was varied with a fixed sensor resolution and noise magnitude.

There is little change in the error metrics in Figure 5-14 as the flow is reduced from 100% of maximum to 75%. At 50% maximum flow, the 6th backward nodal diameter becomes un-identifiable and the mean error for the 5th backward nodal diameter increases significantly. Both error metrics increase rapidly below 35% maximum forcing

[5]low here meaning the noise level is below the sensor resolution

until 15% maximum forcing where most modes become un-identifiable due to the high single-sample confidence interval magnitude.

The current actuator design has at least 50% flow margin to identify all the modes and as much as 85% margin for the least damped modes, the 0^{th} nodal diameter and the 1^{st} and 2^{nd} forward nodal diameters. This permits identification at reduced actuator flow to decrease the imposed stress on the blades[6] or to compensate for a higher noise environment. Measurements should be conducted at the highest possible forcing level, however, to improve the signal-to-noise ratio and reduce the error from noise.

[6]although it will be shown in Section 6.4 that even maximum flow does not impose excessive stress on the blades

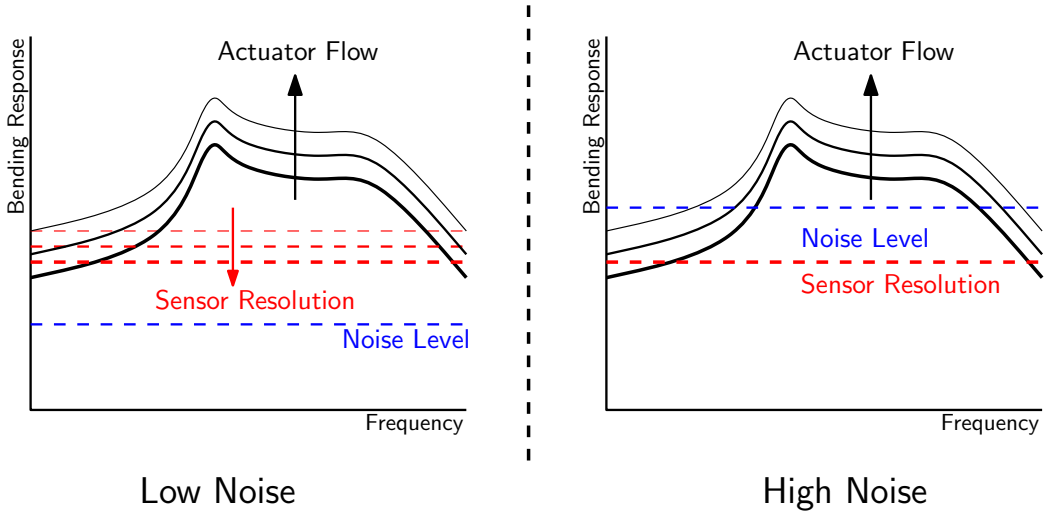
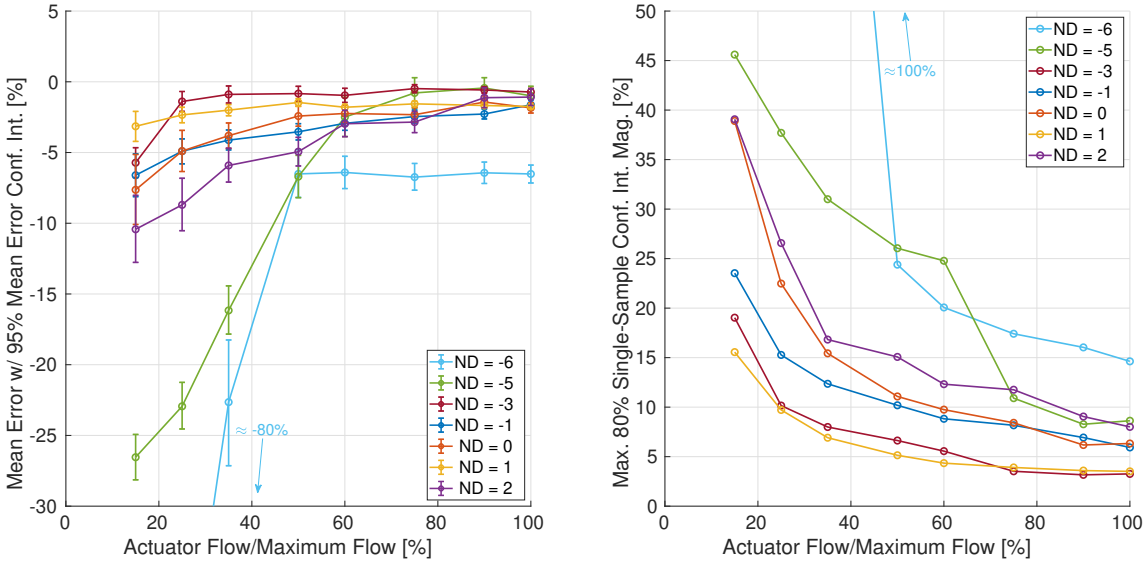


Figure 5-13: Schematic representation of reducing actuator flow. Margin in actuator flow equivalent to margin in sensor resolution for low noise environments, but not in high noise environments where noise level dominates.



(a) Mean Error with 95% Confidence Interval

(b) Maximum 80% single-sample confidence interval magnitude

Figure 5-14: Error increases with reduced forcing magnitude due to reduced signal-to-noise ratio, but least damped modes identifiable with up to 85% reduction in actuator flow.

5.3 Fan Design

We now assess how sensitive the experimental design and error metrics are to changes in the fan performance. This is not only to assess the robustness of the experimental design and applicability to other fans, but also to assess the assumption of utilizing Rotor 67 as a representation of the PW615 fan. Of the 20+ model parameters that represent the fan design those that most influence the flutter modes and were likely to vary between Rotor 67 and the PW615 fan were chosen to be assessed. Copeland et al. [22] assessed the sensitivity of the 1st forward nodal diameter damping ratio to model parameters as reproduced in Figure 5-15.

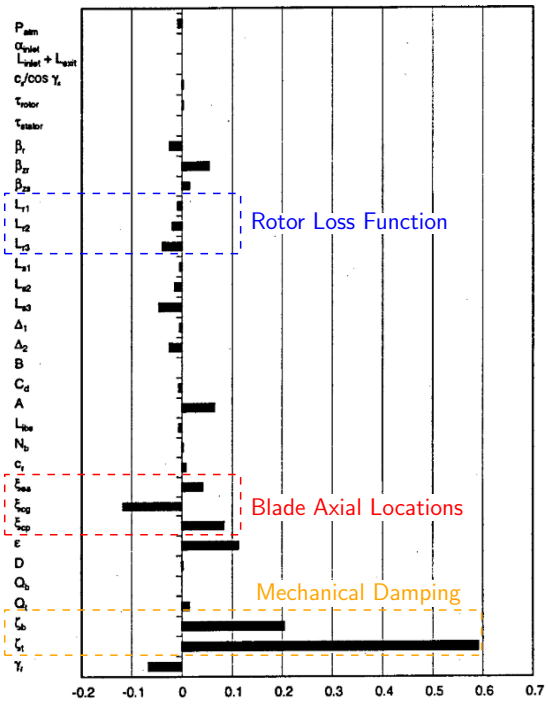


Figure 5-15: Sensitivity of 1st forward nodal diameter damping ratio to fan parameters (reproduced from [22]). Studies performed for parameters with high sensitivity and that are likely to vary between Rotor 67 and the PW615 fan.

The most influential parameters are those relating to the mechanical damping. This is also the parameter which is most likely to vary in the current experimental design, especially as the blisk rotor of the PW615 fan may have reduced mechanical damping compared to traditional rotors with separate blades and disks often discussed

in the literature. Aerodynamic parameters of the PW615 fan such as the rotor loss function and center of pressure location are also more uncertain and deserve particular attention.

The mechanical damping is investigated first as it provides the clearest picture of the impact of varying fan design parameters on the error metrics. Table 5.2 compares the mechanical damping ratio used in similar flutter models throughout the literature, including that by Copeland [23] which was adjusted to match experimental results. The mechanical damping was varied from its nominal value of $\zeta_b = 0.30 \pm 50\%$ to cover the range of values in the literature. Varying the mechanical damping does not change the shape of the damping ratio vs interblade phase angle curve, as in Figure 5-16, but results in each mode increasing or decreasing in stability by the same amount.

Source	**Year**	ζ_b
Gysling [20]	1996	0.020
Wong [21]	1997	0.030
Copeland [22]	1998	0.035
Copeland [23]	2004	0.021

Table 5.2: Survey of mechanical damping values across literature. Assessed range $\zeta_b = 0.30 \pm 50\%$ covers values from literature.

Figure 5-16 demonstrates the overall trend with varying fan design parameters. Changes which result in a particular mode's damping to be decreased also improve the error metrics, reducing the mean error and the single-sample confidence interval size. This is seen in the 2^{nd} forward nodal diameter, as well as the 6^{th} backward nodal diameter. This is due to the increased response resulting in higher coherence and clearer transfer function, as in Figure 5-17 which compares transfer functions with 50% and 150% of the nominal mechanical damping. The coherence for the 6^{th} backward nodal diameter mode increases by approximately 20% with the reduction in mechanical damping and the phase portion is especially clearer when compared to the increased damping case, providing the system identification algorithm more information and improving the damping estimate.

The same relationship in mode damping and the resultant error metrics was ob-

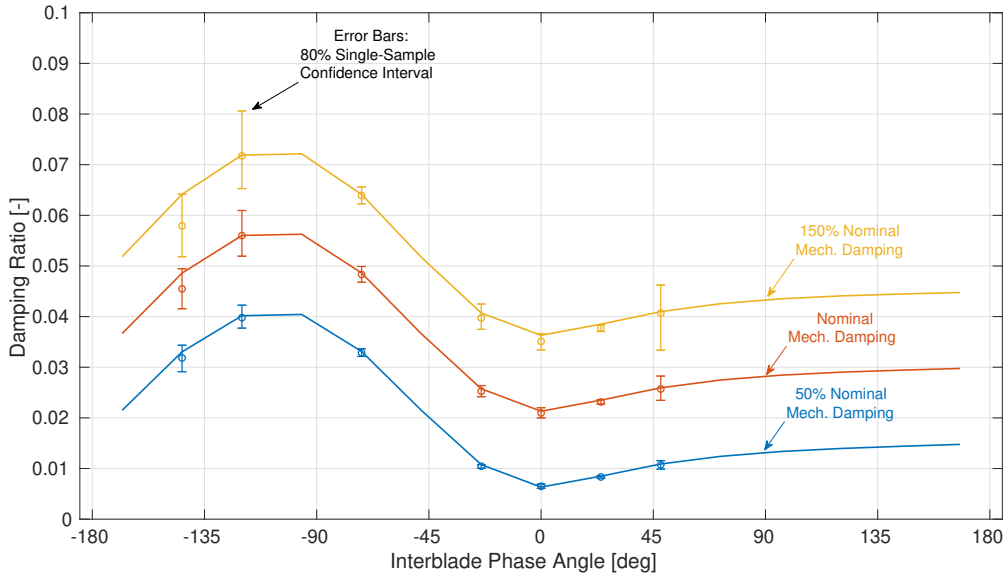
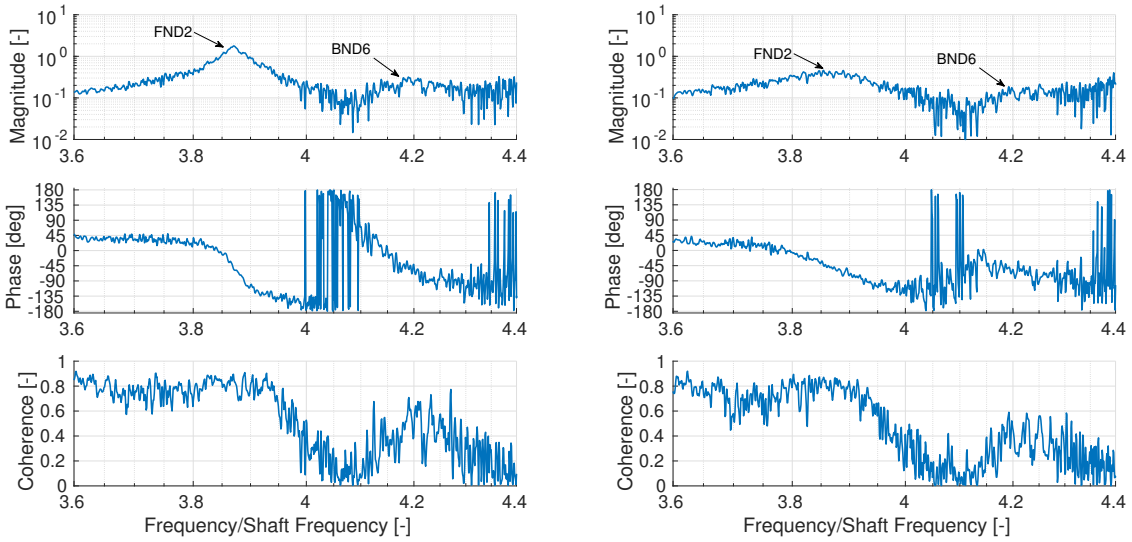


Figure 5-16: Varying mechanical damping demonstrates improved error metrics for fan designs that reduce mode damping.



(a) 50% Nominal Mechanical Damping

(b) 150% Nominal Mechanical Damping

Figure 5-17: Transfer functions with varying mechanical damping. Decreased damping improves 6$^{\text{th}}$ backward nodal diameter coherence, improving identification.

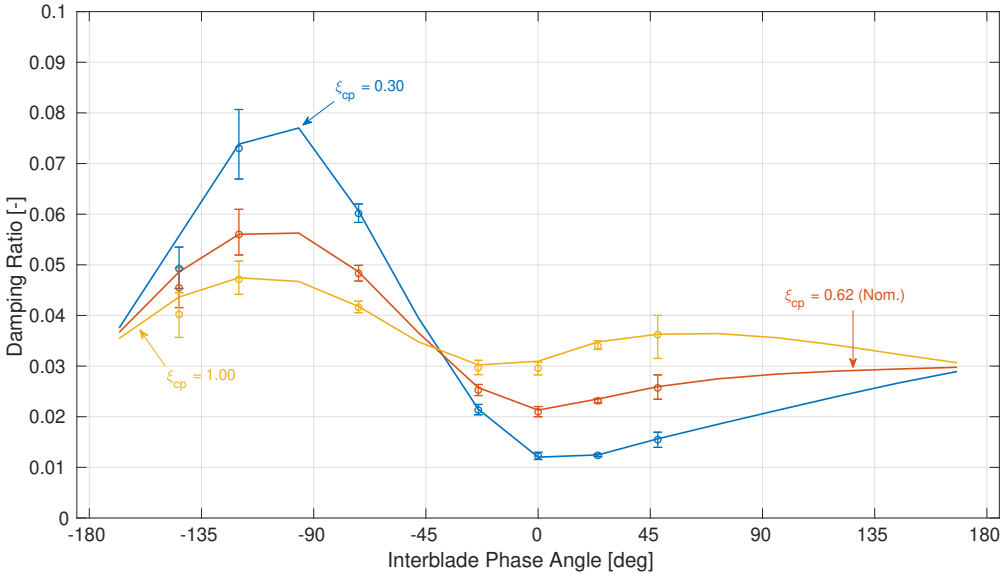


Figure 5-18: Changes in damping ratio due to center of pressure location captured with same dependence of error metrics on mode damping ratio.

served for all parameters varied in the fan design study. For example, the location of the center of pressure (normalized by the chord) was varied[7] from its nominal value of 0.62 to 0.3 and 1.0 in Figure 5-18. The resultant changes in the damping ratio are well identified by the experiment with the error metrics improving for reductions in damping as before. As similar trends were found for the remaining fan design studies, these results are not shown here but are included in Appendix C.

5.3.1 Applicability of Experimental Design to Larger Engines

These fan design studies focused on aerodynamic and mechanical characteristics of the fan that are independent of scale, but it is also useful to consider how applicable the experimental design is as the engine increases in size. There are three considerations as the fan diameter grows:

1. The primary consideration is actuator authority, i.e. whether the actuator can produce a sufficient mass perturbation as to excite the flutter modes. The

[7] moving the center of pressure towards the leading edge further than 0.3 resulted in the destabilization of the torsional modes and could not be simulated

question is thus how does the ratio of actuator mass flow, $\dot{m}_a$, to engine mass flow, $\dot{m}_e$, scale with fan radius, r_{fan}?

The engine mass flow scales as the *inlet* area, or the square of the fan radius, $\dot{m}_e \sim r_{fan}^2$, whereas the actuator mass flow scales as the *speaker* area, or the square of the speaker radius, $\dot{m}_a \sim r_{speak}^2$. The speaker radius is constrained only by packing considerations around the fan casing and thus scales with the fan circumference, $r_{speak} \sim r_{fan}$. The mass flow ratio is therefore independent of the fan radius, $\dot{m}_a/\dot{m}_e \sim r_{speak}^2/r_{fan}^2 \sim const$, and the actuator authority constrained only by the availability of sufficiently large speakers as the fan diameter increases. For reference, a 60" diameter fan would require approximately a 20" diameter speaker.

2. The blade natural frequency will generally decrease as the length of the blade increases, reducing the bandwidth requirement of the actuator. This is particularly important as the larger diameter speakers required for larger fans are designed for operation at lower frequencies than the speaker considered in this thesis.

3. The shaft rotational speed decreases as the fan diameter grows as to maintain acceptable relative Mach numbers at the fan tip. As shown in Equation 2.5, a reduction in shaft frequency will improve the non-dimensional sensor resolution for a fixed sensor sampling frequency.

The conclusion from these considerations is that the experimental design is generally applicable and can be scaled up to larger diameter fans.

5.4 General Recommendations and Guidelines

The results of this chapter have resulted in general recommendations for the future experimentalist performing a forced response system identification experiment for flutter and they are summarized below.

1. Transfer function estimation should be performed for all modes with a Hann window function except low frequency modes which should use Rectangular windows to preserve low frequency content due to the non-stationarity of the chirp signal.

2. Overlap fractions below 50% should not be used as this results in numerical noise in the transfer functions at the window edges due to the non-stationarity of the chirp signal.

3. Short window lengths with increased averaging to reduce transfer function variance should be avoided to prevent over-smoothing the transfer function, resulting in erroneously high damping values. Multiple window lengths should be tried until the estimated damping converges to a single value.

4. Inlet turbulence intensity should be reduced whenever possible as the error increases monotonically with turbulence levels.

5. At least 5-15 trial ensemble averaging should be used, with more trials whenever possible. The frequency range of the chirp signal can be restricted to reduce the experiment duration needed to achieve the desired level of ensemble averaging.

6. The maximum forcing magnitude should be used to maximize the signal-to-noise ratio and reduce error due to noise.

5.5 Summary of Error Sensitivity Studies

This chapter assessed the robustness of the experimental design and the sensitivity of the experimental error to design choices, noise levels, and fan performance with the statistical error metrics from Chapter 4. The choice of window parameters was shown to be significant with a Hann window of 9,375 samples and 50% overlap performing best overall. The non-stationarity of the chirp excitation signal was shown to introduce significant error for certain windowing parameters, further emphasizing the importance of assessing the choice in window parameters.

The experimental design was found to be robust to sensor noise, with little increase in error for noise levels up to 10x sensor resolution, but grew more rapidly above 50x sensor resolution. Identification succeeded for noise levels up to 1000x sensor noise, albeit with error as great as 40%. Error was found to scale linearly with inlet turbulence intensity, with identification succeeding with inlet turbulence intensities up to 5%, again albeit with error as great as 35%. Reducing the actuator flow increased error metrics for all modes, due to the decrease in signal-to-noise ratio of the measured response, but identification for most modes was possible with up to a 50% reduction in actuator flow and up to a 85% reduction for the least damped modes. Finally, the experimental design was shown to be applicable to other fan designs, producing similar levels of error as compared to the PW615 when design parameters that are most influential on flutter mode damping were varied. The results of this section have demonstrated the experimental design to be robust and were used to produce general guidelines for future forced response system identification experiments of flutter.

Chapter 6

Detailed Experimental Design

6.1 Functional Requirements of Experimental Design

With preliminary design and a rigorous assessment of the experimental design completed, the actuation and sensing scheme must now be designed in detail to be implemented on the PW615 engine. The design must satisfy the following functional requirements:

1. Reduce the impact of the actuator and sensor implementation on the engine steady-state performance and actuator performance.

2. Maintain flexibility in actuator geometry to tailor actuator performance and permit the experiment to adapt to initial data and findings.

3. Ensure that no engine or blade limitations are exceeded.

This chapter outlines the results of the detailed design process to meet these functional requirements. First, the inlet is modified to incorporate the actuators and is guided by an acoustic flutter model to minimize the impact of the modified inlet on the flutter modes. The inlet has also been designed to reduce aerodynamic effects from the actuator implementation which impact fan performance. Second, an

actuator design has been developed that maintains actuator performance and allows multiple actuator geometries characterized in Section 3.4 be implemented as needed. Finally, a blade stress analysis has been performed based on the deflection levels at takeoff power in Section 4.4 and the peak stress is estimated to be below blade limits.

6.2 Inlet Duct Acoustic Flutter Model

The ZNMF actuators are to be mounted circumferentially upstream of the fan face via an additional mounting duct placed between the bellmouth and the engine inlet duct in Figure 6-1. This provides the opportunity to impact the inlet duct acoustics by selecting a net inlet length. Inlet duct acoustics have been shown to be an additional source of flutter damping (both positive and negative) for speed ranges where the upstream acoustic field is cut-on and the downstream field is cut-off. Flutter damping due to inlet acoustics and the unsteady pressure field interaction with the blade vibratory mode shape were found to be independent [71], motivating the characterization of the "blade-only" flutter damping on top of which the contributions of the inlet acoustics for a given inlet are added. A model by Zhao [72] was found to capture the impact of inlet acoustics on flutter damping and provides a tool for inlet design. A brief overview of the model is provided below and the reader is referred to Refs. [72, 73] for further details.

Acoustic flutter is driven by the interaction of an upstream propagating pressure wave emitted from the vibrating fan and the reflection of that pressure wave from the inlet highlight. The maximum impact occurs when these two pressure waves are 90° out of phase at the fan face. Flutter damping decreases when the reflected wave lags the upstream propagating wave by 90° and increases when the reflected wave leads the upstream propagating wave [12].

As in Figure 6-2, Zhao determined the phases of these two pressure waves by considering the phase change of the upstream propagating wave as it traverses the inlet duct $\delta\phi_-$, the phase change due to the reflection of the inlet highlight $\delta\phi_R$, and the phase change of the reflected wave as it travels back to the fan face $\delta\phi_+$. The phase

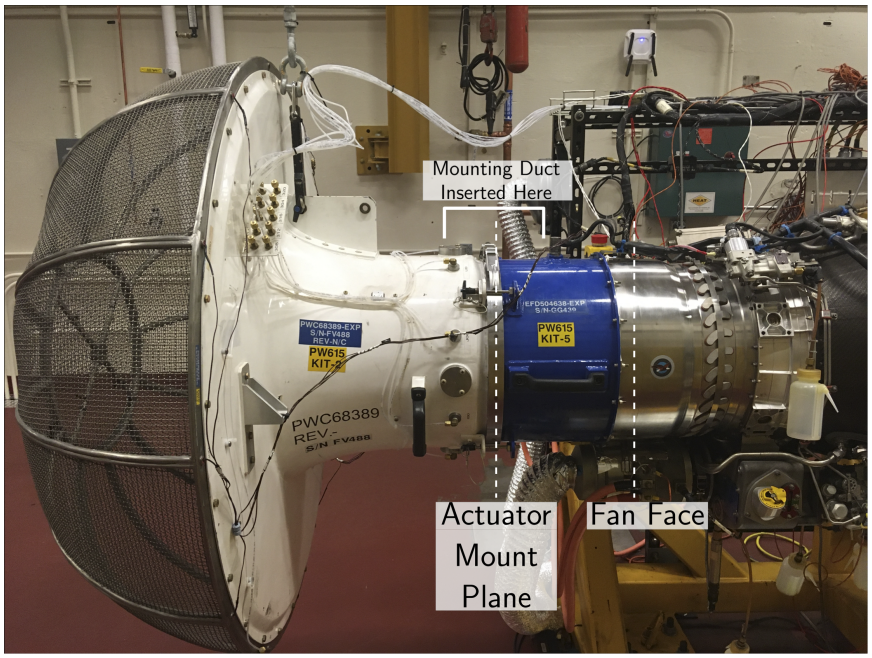


Figure 6-1: Actuator mounting duct to be placed between engine inlet duct and bellmouth. Ability to set total inlet length provides opportunity to influence inlet duct acoustics.

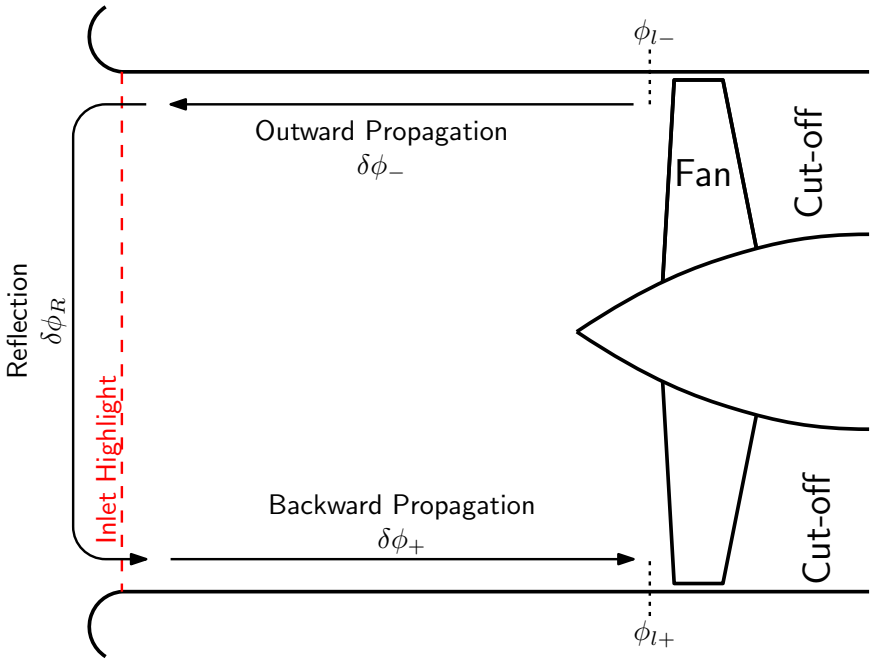


Figure 6-2: Acoustic model for determining pressure wave phase difference at fan face which drives acoustic flutter (reproduced from [72])

change for the propagating pressure waves is determined by solving the convective wave equation for a hard-walled, constant radius cylindrical duct with axial mean flow. By assuming the solution to be harmonic in time, axial position, and circumferential position, the axial wavenumber for each wave k_x can be determined and integrated over the inlet duct length L to determine the phase change for each propagating pressure wave.

$$\delta\phi_{\pm} = \int_0^L \Re(k_x^{\pm})dx$$

The phase change due to reflection at the intake highlight was determined using the model of Rienstra [74] who derived an analytical procedure for determining the reflection coefficient for a semi-infinite circular duct submersed in an axial mean flow. The argument of the complex reflection coefficient represents the phase shift due to reflection and the magnitude represents the ratio of the reflected wave amplitude to the upstream propagating wave amplitude. The reflection coefficient model implementation was validated using the results published by Rienstra [74, 75].

With the phase change for each component, the net phase difference between the outgoing and reflected wave is

$$\phi_+ - \phi_- = \delta\phi_- + \delta\phi_R + \delta\phi_+.$$

Zhao introduced the flutter index β

$$\beta = |R| \sin(\phi_+ - \phi_-),$$

where $|R|$ is the magnitude of the reflected wave (the magnitude of the complex reflection coefficient R). The flutter index varies between 1 and -1, with -1 being the most de-stabilizing condition. $\beta = 0$ corresponds to a condition where the inlet acoustics have no influence, i.e. the measured damping is equal to the blade-only damping. The flutter index was shown to capture the impact of fan speed, inlet length, and mean flow velocity on acoustic flutter for multiple nodal diameters.

Contours of the flutter index are plotted as a function of fan speed and inlet length

(non-dimensionalized by the speed at take-off power and the inlet diameter respectively) in Figure 6-3 for the 0^{th} to the 3^{rd} forward nodal diameter. At lower speeds the upstream acoustic field is cut-off for the 2^{nd} and 3^{rd} forward nodal diameters and the flutter index is not meaningful. The backward nodal diameters are cut-off for all speeds as their absolute frame frequency is reduced by multiples of the shaft frequency, driving it below the cut-on frequency for their respective spatial harmonic.

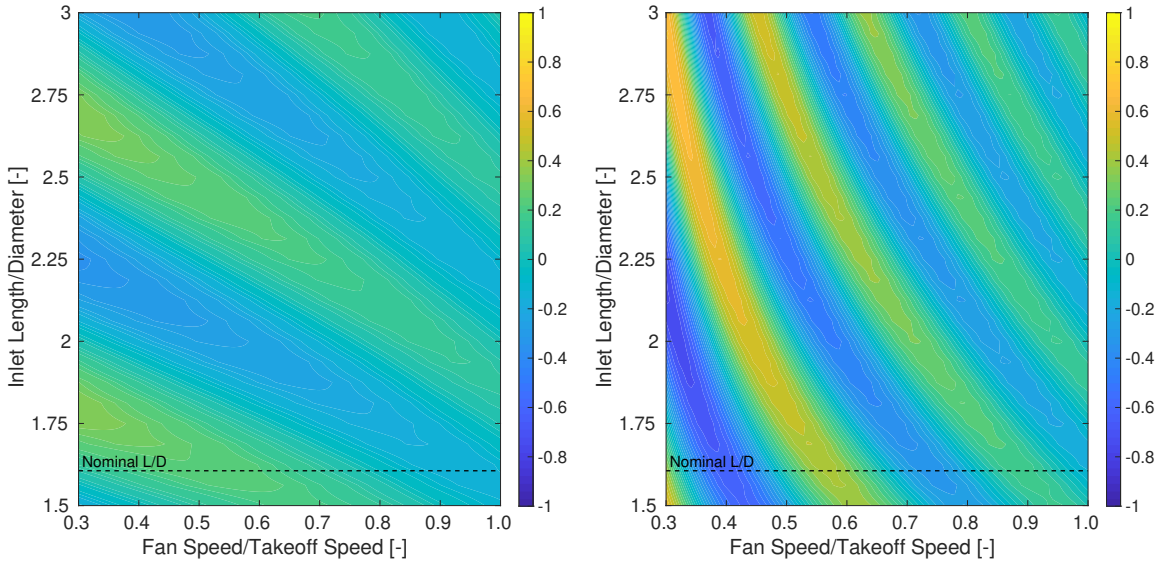
The flutter index is a stronger function of fan speed for higher nodal diameters. The flutter index for the 2^{nd} and 3^{rd} forward nodal diameters vary as much as ± 0.8 across the speed range while that for the 0^{th} nodal diameter varies only ± 0.2. For constant fan speed, however, the flutter index varies less with inlet length for higher nodal diameters as indicated by the steepening of the lines of constant flutter index in Figure 6-3.

While the goal would be to measure the blade-only damping for all nodal diameters and fan speeds, there is no single inlet length for which $\beta = 0$ across all speeds. A single inlet length can at best provide the blade-only damping on an average basis. The fan speed averaged flutter index $\beta_{\bar{N}}$ is thus defined as

$$\beta_{\bar{N}}(\text{L/D}, \text{ND}) = \frac{1}{N_{T/O} - N_{Idle}} \int_{N_{Idle}}^{N_{T/O}} \beta(N, \text{L/D}, \text{ND}) dN \tag{6.1}$$

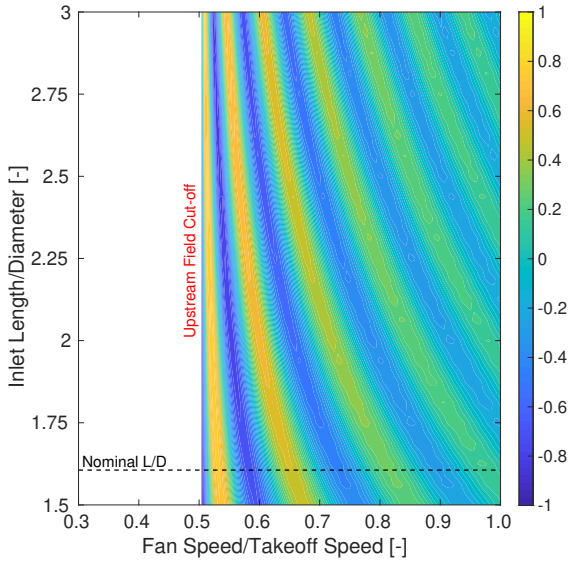
where N is the fan speed. $\beta_{\bar{N}}$ is plotted as a function of inlet length for all four nodal diameters in Figure 6-4.[1] Because the flutter index for the 2^{nd} and 3^{rd} forward nodal diameters is rapidly varying with speed, the speed-averaged flutter index magnitude is close to zero (similar to averaging a sinusoid over many periods). The flutter index for the 1^{st} forward and 0^{th} nodal diameters varies slowly with speed, so the magnitude of the speed-averaged flutter index is greater. Even on a speed-averaged basis, however, there is no inlet length for which $\beta_{\bar{N}} = 0$ for all nodal diameters. The inlet length-to-diameter ratio of 2.35 was selected as it was a value for which $\beta_{\bar{N}} \approx 0$ for the 2^{nd} and 3^{rd} forward nodal diameters and similar magnitudes of $\beta_{\bar{N}}$ for the 0^{th} and 1^{st} forward nodal diameters.

[1] For speeds where the upstream field is cut-off, $\beta(N) = 0$ as the inlet acoustics impose no additional flutter damping.

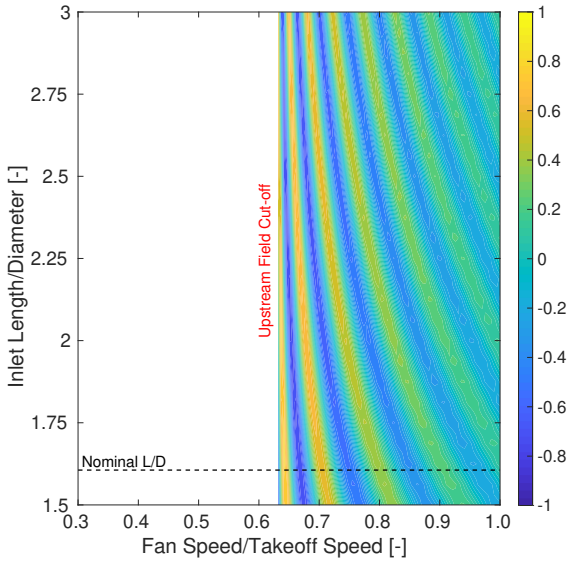


(a) ND0

(b) FND1



(c) FND2



(d) FND3

Figure 6-3: Flutter index as a function of fan speed and inlet length for PW615 for 0^{th} to 3^{rd} forward nodal diameters. At constant inlet length, flutter index varies more rapidly with speed for higher nodal diameters, reducing speed-averaged flutter index.

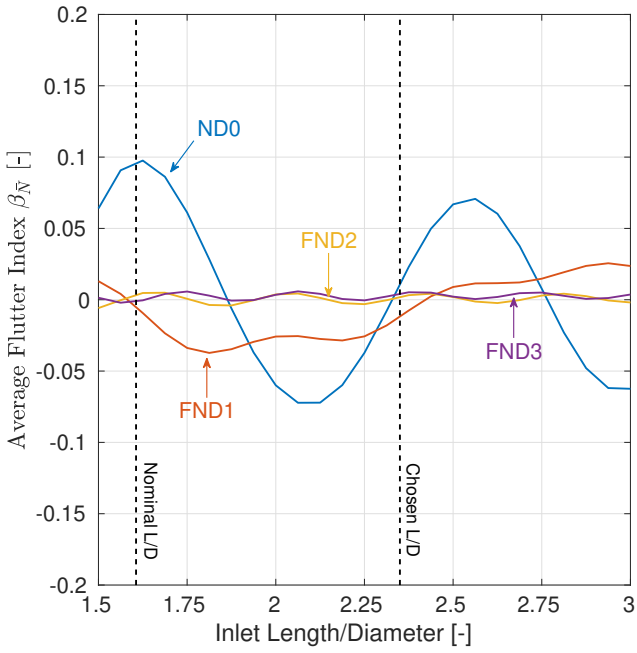


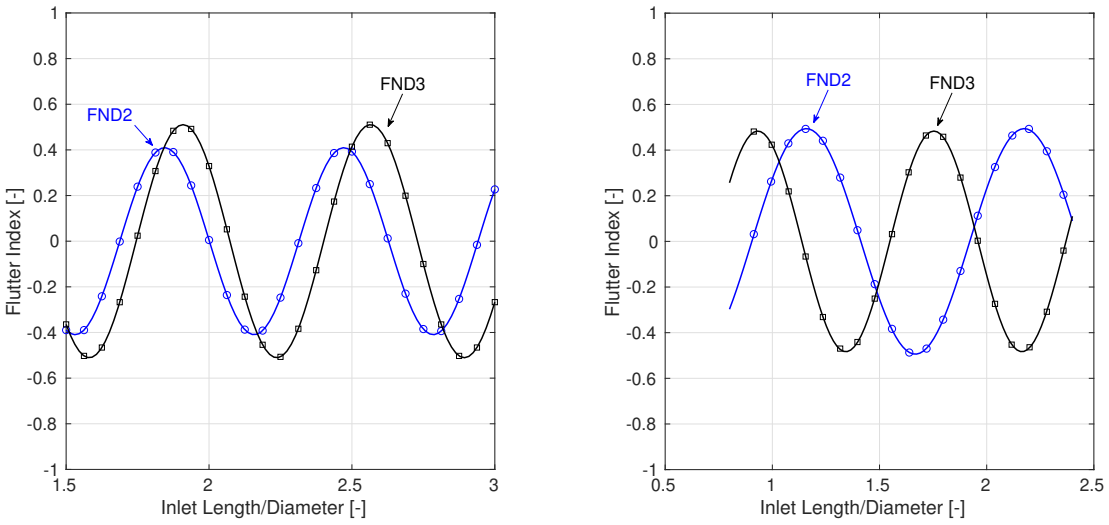
Figure 6-4: Fan speed averaged flutter index $\beta_{\bar{N}}$ as a function of inlet length. No inlet length produces $\beta_{\bar{N}} = 0$ for all nodal diameters, L/D = 2.35 chosen as compromise between 0^{th} and 1^{st} forward nodal diameters.

Measurements with the selected inlet L/D of 2.35 represents the closest possible to blade-only damping on an averaged basis, but for any given speed and nodal diameter there is still a non-zero impact of inlet acoustics. An estimate of the damping's dependence on inlet length for a given nodal diameter and fan speed, however, can be derived from measurements at two different inlet lengths.

At constant fan speed[2], the flutter index has a sinusoidal dependence on inlet length. The reflection coefficient, and thus the phase change due to reflection, is constant with inlet length for a fixed fan speed. The overall phase difference therefore varies only due to the product of the axial wavenumber, also constant for a fixed fan speed, and the inlet length. This results in the observed sinusoidal dependence for both the PW615 and the fan in Ref. [72] in Figure 6-5, which shows the flutter index for two modes as a function of inlet length for a constant fan speed.

It is thus proposed that the damping follows the same sinusoidal dependence as

[2]and thus a constant absolute frame mode frequency and mean flow axial Mach number



(a) PW615, $N/N_{T/O} = 0.75$

(b) Ref. [72] data

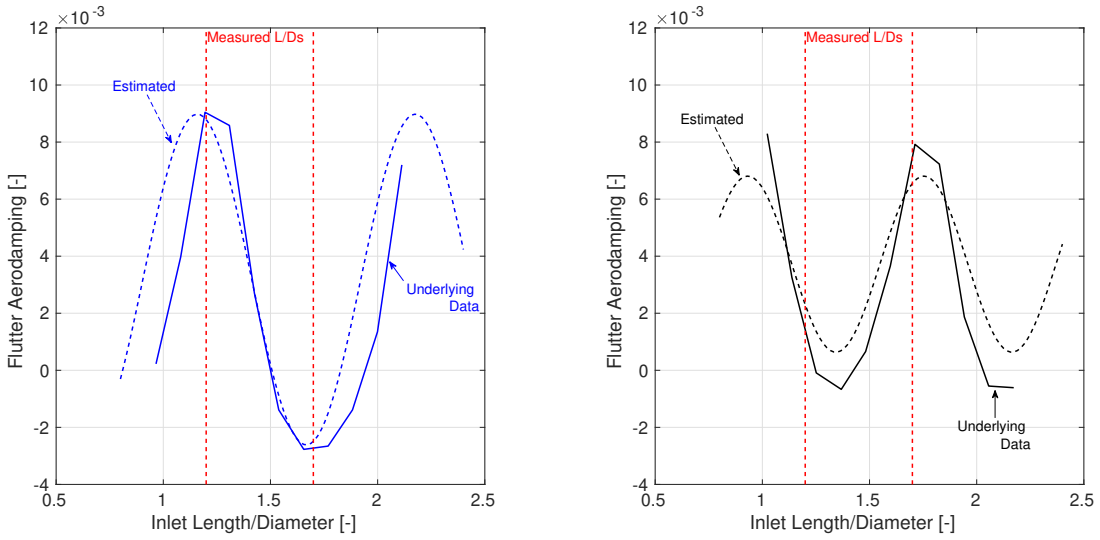
Figure 6-5: Sinusoidal dependence of flutter index on inlet length at constant fan speed.

the flutter index (Eqn. 6.2). Assuming the spatial frequency k and phase ϕ for the damping is the same as that for the flutter index, the amplitude A and mean damping $\bar{\sigma}$ can be estimated via a least-squares fit of Eqn. 6.2 with measurements of flutter damping at two inlet lengths.

$$\sigma\left(\frac{L}{D}\right)\Big|_N = A\sin\left(k\frac{L}{D} + \phi\right) + \bar{\sigma} \tag{6.2}$$

Figure 6-6 demonstrates the results of this estimation procedure utilizing the data from Ref. [72]. The dashed estimated damping distribution is determined using the damping values from the two inlet lengths marked with vertical red lines and is in reasonable agreement with the true distribution. Repeating this procedure for a variety of fan speeds, problematic speeds where flutter damping is reduced can be estimated for shorter flight inlets ($\frac{L}{D} < 1$) utilizing data from longer inlets ($\frac{L}{D} > 1$) that are common in engine tests.

[3]Underlying data reproduced from Ref. [72].



(a) FND2 (b) FND3

Figure 6-6: Estimation of flutter aerodamping dependence on inlet length using flutter damping measurements for inlet lengths marked by red dashed lines.[3]

6.3 Actuator Detailed Design

The design of the actuator mounting duct to be installed at the actuator mount plane in Figure 6-1 is shown in Figure 6-7. Eight ZNMF actuators are mounted radially and are equi-spaced about the duct circumference. The axial length of the actuator mount duct is set such that the inlet duct length, from bellmouth highlight to the fan face, matches the desired $L/D = 2.35$ from the acoustic flutter model. A modular mounting system for the actuator audio speaker was designed such that multiple neck lengths could be accommodated. The mounting system consists of two plates which are fastened to the audio speaker and the mounting duct, separated by the neck tube which can be of arbitrary length, as in Figure 6-8 for $\frac{L_{neck}}{r_{speak}} = 0.33$ and $\frac{L_{neck}}{r_{speak}} = 1.0$.

The actuator design in Figure 6-8 is different to that seen in Chapter 3 due to the different environment the actuator must operate in during an engine test. When the engine is running, the static pressure in the inlet duct is sub-ambient. Were the speaker unprotected, with the backside exposed to the ambient pressure of the test cell, a net load would be imposed on the speaker cone. At takeoff speed, this load would be upwards of 45lbf. At minimum this would alter the actuator performance

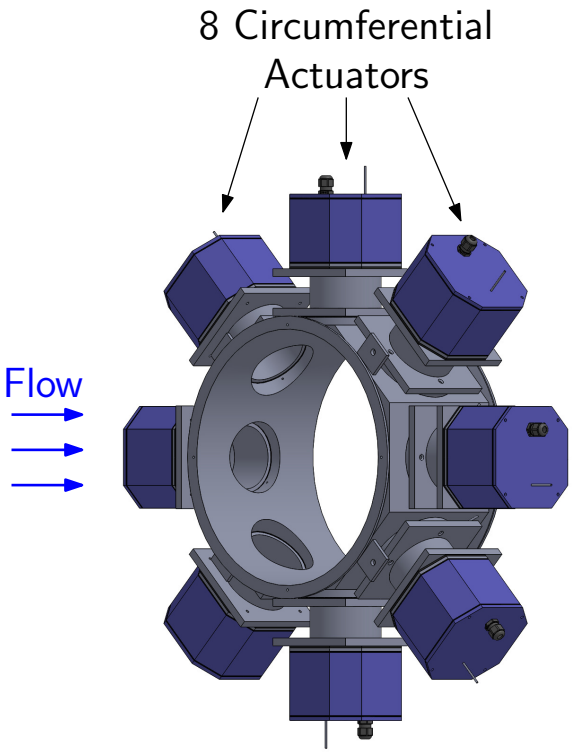
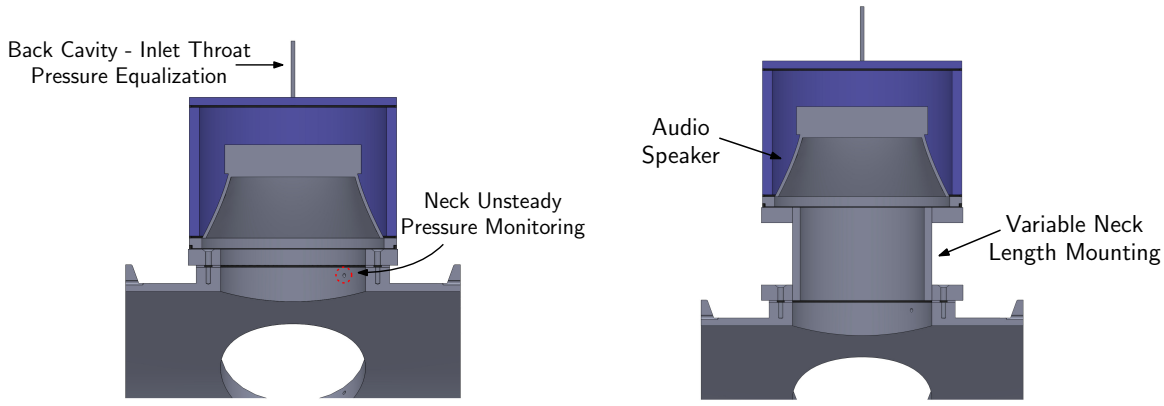


Figure 6-7: Mounting duct with eight circumferential actuators to be installed between bellmouth and engine inlet duct.



(a) $\frac{L_{neck}}{r_{speak}} = 0.33$ (b) $\frac{L_{neck}}{r_{speak}} = 1.0$

Figure 6-8: Modular actuator mounting system which allows multiple neck lengths to be used to tailor actuator performance to the flutter mode of interest.

from that measured in Section 3.4, but also possibly damage or destroy the speaker diaphragm. To mitigate this, the speaker is enveloped in a sealed back-cavity, as in Figure 6-9, such that the static pressure on the back side of the speaker cone can be controlled. The speaker back-cavity is pneumatically connected to an upstream bellmouth throat static pressure port to equalize the pressure across the speaker diaphragm[4] . A pressure tap is installed in the neck for a flush mounted fast-response pressure transducer to enable in-situ actuator performance monitoring during the experiment. To ensure fan tip clearances are not impacted by the addition of the actuator mounting duct, a ground support structure is used to eliminate any vertical load or bending torque on the fan case.

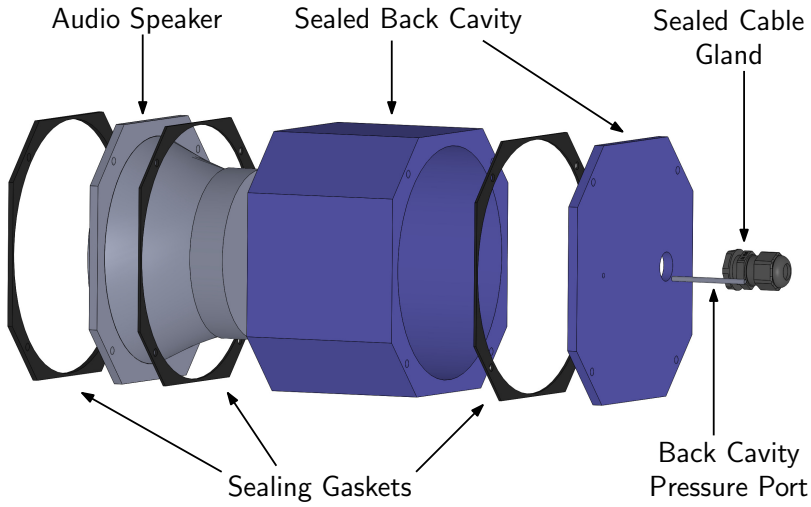


Figure 6-9: Static pressure in sealed back cavity equalized with bellmouth throat to eliminate steady force on speaker diaphragm.

The large diameter cavity formed by the actuator neck is subject to a grazing flow from the primary flow in the inlet duct, producing the potential for an unsteady lip-separation or cavity resonance. Such a separation would convect downstream into the fan, producing a new source of process noise. If the unsteady component of separation was correlated with actuator operation, the resultant noise could not be mitigated by ensemble averaging. Furthermore, the steady component of the separation would result in a total pressure distortion, altering the fan's performance and possibly de-

[4]at least 3m of 0.50mm diameter tubing should be used to damp perturbations in the frequency range of interest and ensure the actuator dynamics are unchanged [76].

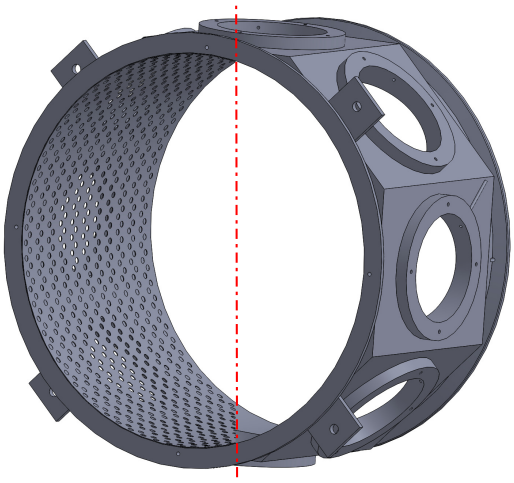


Figure 6-10: Mesh lining of actuator duct to reduce lip-separation from actuator neck cavity prevents additional process noise and changes in fan steady performance.

stabilizing it. To reduce the lip-separation the actuator mounting duct is lined with a 58% open area mesh screen as in Figure 6-10[5]. The actuator performance was measured with the screen installed to determine what, if any, impact the screen has on actuator performance.

The traverse system was modified to incorporate a sample of the mesh screen as in Figure 6-11. The mesh screen was attached to the traverse system such that it would move with the hotwire, which was placed through a hole into the neck. The entire assembly was traversed at increments of the hole center-to-center spacing such that the hole pattern across the actuator orifice was the same for each measurement. The hotwire was located axially upstream of the mesh 1.3 times the center-to-center spacing to minimize non-axial velocities due to the induced pressure field. The presence of the screen has a negligible impact on the measured volume flow frequency response as in Figure 6-12, reducing the peak volume flow by only 5%. Such a reduction is well within the actuator flow margin demonstrated in Section 5.2.3.

[5]the mesh in Figure 6-10 is of lower open area due to rendering capability

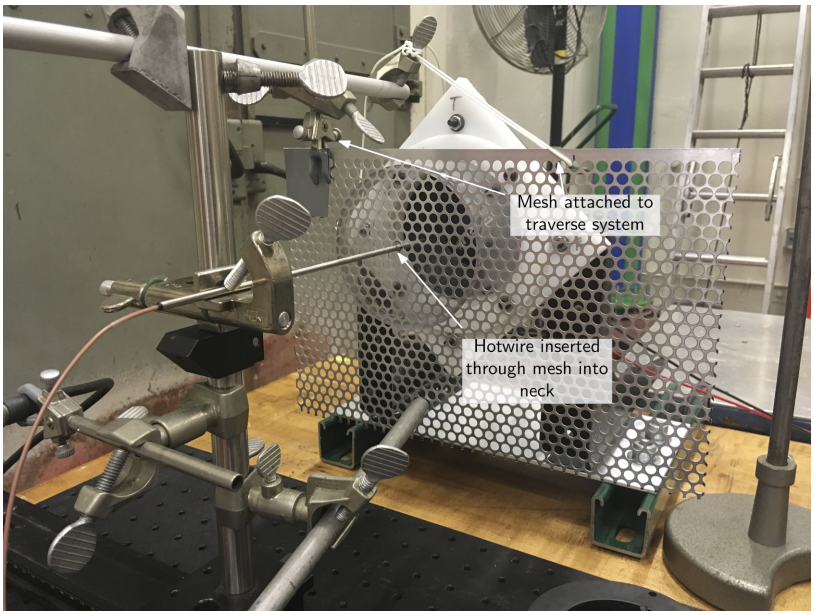


Figure 6-11: Traverse system modified with mesh screen sample to assess impact of mesh on actuator volume flow frequency response.

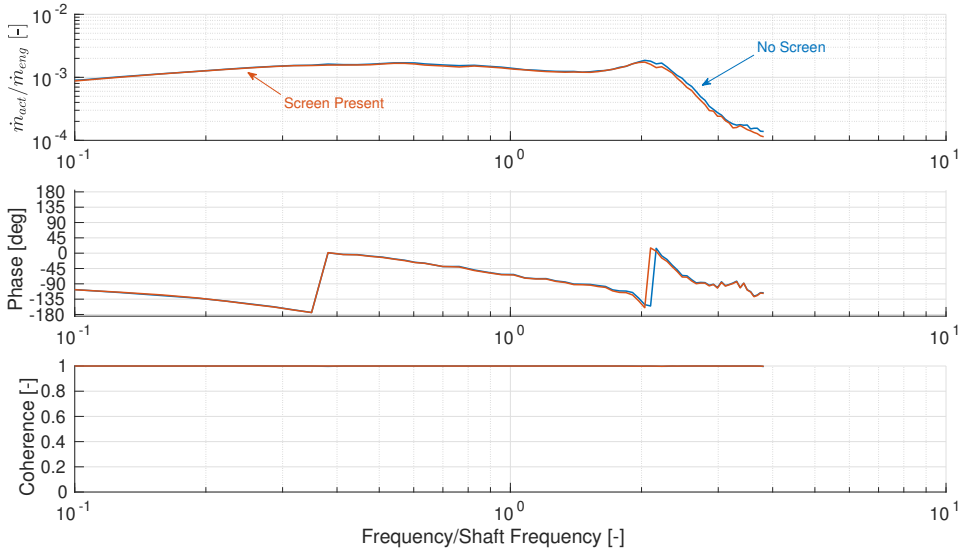


Figure 6-12: Volume flow frequency response with and without mesh screen present. Mesh screen has negligible impact on actuator performance

6.4 Blade Stress Analysis

A blade stress analysis was performed to estimate the peak alternating stress encountered by the blade during the experiment and ensure that blade limitations are not exceeded and the experiment could be safely conducted. The analysis in this section shows that the stress imposed by the forcing is approximately 30% of the limitation with respect to high-cycle fatigue. Rotor 67 geometry was used as the detailed blade geometry for the PW615 was not available, but the stress results from Rotor 67 are in good agreement with what data is available for the PW615 from engine testing by the manufacturer.

A finite element analysis of the Rotor 67 geometry was performed using the Solidworks structural solver. The estimated first bending mode frequency at design conditions (incorporating centrifugal stiffening) was within 0.5% of that in the literature which utilized an alternative FEA solver ABAQUS [19]. The first bending mode shape and stress distribution were also in good agreement with that in the literature [19, 77]. A dynamic computation was performed in which the blade root was oscillated at the first bending mode frequency in order to excite the blade entirely in the first bending mode. The magnitude of the oscillation was such that the tip displacement was $\frac{q}{r_{tip}} = 2 \times 10^{-3}$, the maximum predicted by the flutter modeling framework for any nodal diameter at takeoff speed in Section 4.4. The alternating stress for Rotor 67 is compared to that of the PW615 fan experimentally measured by the manufacturer with strain gauges at the first bending mode Campbell diagram crossing at 80% take-off speed, shown in Figure 6-13.

Figure 6-14 compares the computed Rotor 67 stress distribution with the measurements from the PW615 fan for both the pressure and suction sides of the blades.[6] For both datasets the stress values are normalized by the peak stress in the Rotor 67 computation. On the pressure side of both blades, regions of high stress occur at mid-span and the leading-edge root and a small region of low stress occurs near the trailing-edge root. Fewer PW615 measurements are available for the suction side, but

[6] the PW615 fan profile has been stretched axially and radially by arbitrary constants but the relative position of strain gauges has been maintained

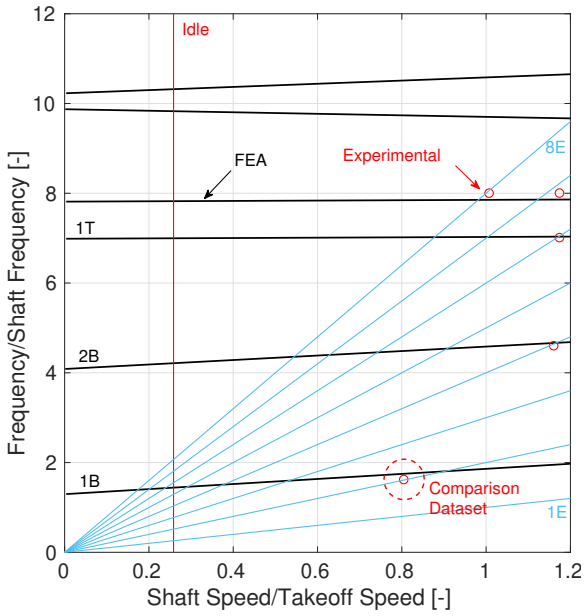


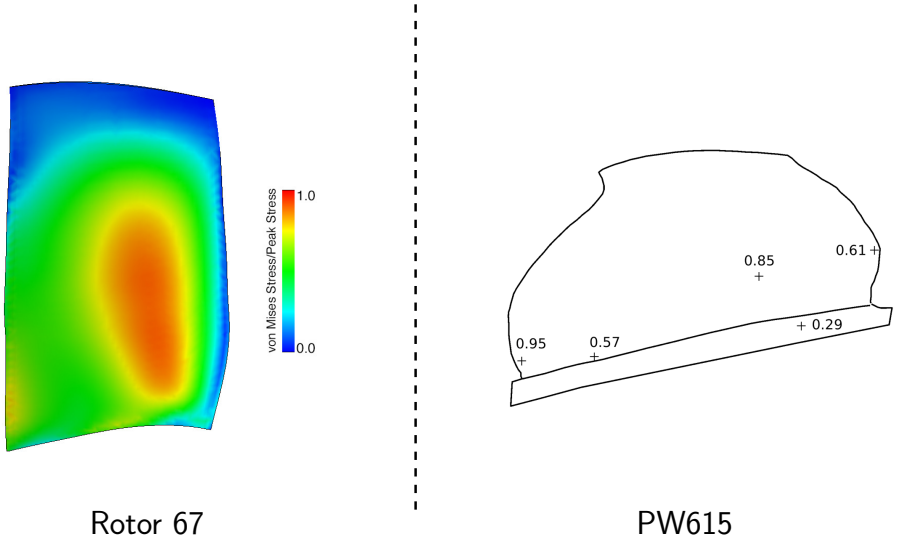
Figure 6-13: Experimentally measured alternating stress for PW615 from first bending mode Campbell diagram crossing provides comparison dataset for blade stress analysis of Rotor 67 blade geometry (measurements by manufacturer).

the two available are also consistent with that of Rotor 67 with a region of high stress spanning from the root to mid-span at mid-chord.

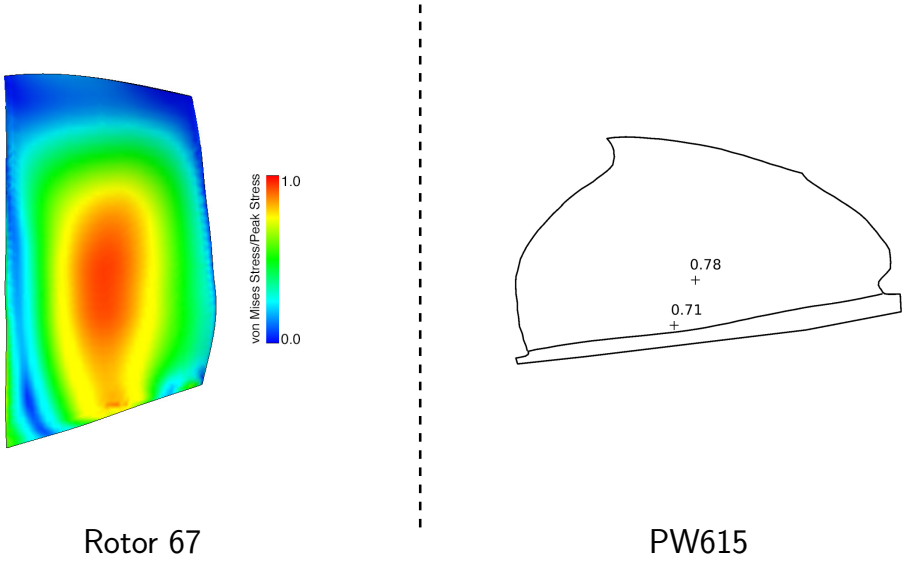
The peak alternating stress from the Rotor 67 computation is of similar magnitude to that measured on the PW615 fan, as seen in the Goodman diagram in Figure 6-15, and approximately 30% of the Goodman line value for the steady operating points of interest. The only measurements for which the steady loading would not permit the imposed alternating stress, points to the right of the intersection of the Goodman line and the alternating stress level of the Rotor 67 computation, are from operations above take-off speed. The forced response experiment is not designed for these conditions and this does not impose any restriction on the experiment.

The above analysis is not intended to be the final effort for ensuring experimental safety, but rather is an initial estimate of experimental viability given structural constraints from the available data. Further analyses with the PW615 fan blade geometry[7] should be performed in cooperation with the manufacturer to establish

[7] the "hot" geometry, the geometry under load with centrifugal stretching and aerodynamic loads, should be used for such analyses



(a) Pressure Side



(b) Suction Side

Figure 6-14: Comparison of Rotor 67 first bending stress distribution to measured PW615 fan stress. Rotor 67 analysis representative of PW615 with good agreement in modeshape and stress magnitude

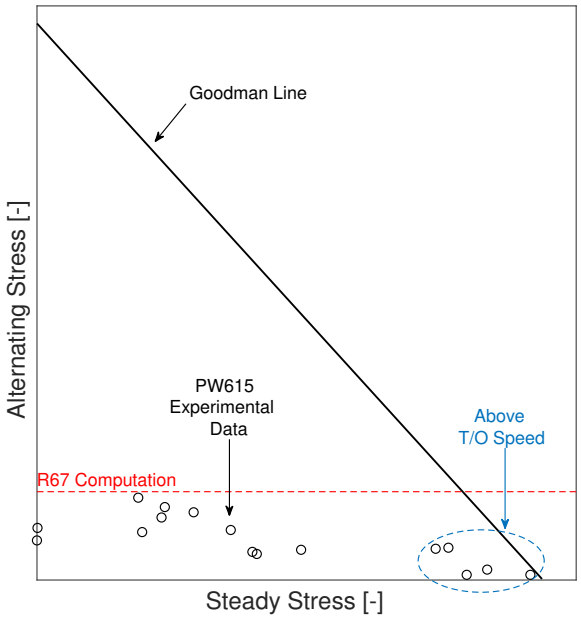


Figure 6-15: Blade stress limitations not exceeded as estimated peak alternating stress from forced response experiment below Goodman line for all speeds to be tested.

maximum limits of blade displacement. Real-time measurements from the tip-timing system should be monitored to ensure these limits are not exceeded while conducting the experiment and the tip-timing system integrated with test cell, actuator, and engine control systems to automatically shut down the engine if the limits are exceeded.

The above analysis also represents the most taxing case expected to be encountered, i.e. the peak response due to maximum forcing from the actuators. As there is sufficient actuator power margin for identification at reduced forcing levels, early experiments should be conducted to assess the minimum forcing, and thus alternating stress, needed to produce a blade response sufficient for system identification.

6.5 Summary of Detailed Design

A modular design of the ZNMF actuator was developed to implement the actuator geometries characterized in Chapter 3 and ensure engine operation did not negatively impact actuator performance. The inlet mounting duct for the ZNMF actuators was

designed with a mesh screen to minimize the impact on the fan steady performance from possible flow separation due to the presence of the actuators. The mesh screen was shown to reduce actuator peak volume flow by 5% with further experimental measurements. An acoustic flutter model was used to size the inlet mounting duct such that the extra inlet length minimized the impact on flutter damping. Furthermore, a procedure was proposed to use two different length inlet mounting duct to identify problematic speeds where flutter damping is reduced for shorter flight inlets. Finally, an unsteady blade stress analysis was performed and indicated that the imposed stress due to forcing does not exceed blade limitations for the operating speeds of interest, but an analysis with the PW615 fan geometry is needed given the safety implications of blade failure. Once this analysis is performed, the forced response experiment is ready for implementation on the PW615 engine with the detailed design of this chapter.

Chapter 7

Summary, Conclusions, & Future Work

7.1 Summary

An engine scale forced response system identification experiment to measure flutter damping throughout the engine operating range has been developed and demonstrated to be feasible. A reduced order modeling framework for fan flutter has been developed to estimate forced response with upstream zero-net mass flux (ZNMF) actuators. Reduced order modelling of the actuators indicated they had sufficient bandwidth and authority to excite the flutter modes of interest. The modeling framework is capable of simulating the full forced response experiment and enabled a rigorous assessment of the experimental design. It can be further expanded with models for other relevant engine system dynamics for complete engine system dynamics modeling.

The unprecedented physical scale of the actuator, and the violation of several assumptions of the reduced order model, motivated an experimental characterization of its performance. A novel methodology to measure ZNMF actuator performance using hotwire anemometry has been developed and used to characterize the effect of actuator geometry on performance. A study of the actuator design space revealed a trade-off between peak actuator flow and actuator bandwidth with actuator neck length, precluding a single optimal actuator geometry. Instead multiple geometries

can be used to tailor the actuator performance to the flutter mode to be identified. The actuator reduced order model did not capture the measured trends in performance metrics with the actuator geometry and over-predicted actuator performance by as much as an order of magnitude. This finding establishes the need for experimental characterization of ZNMF actuators at this scale for future forced response experiments.

The measured actuator performance was incorporated into the flutter modeling framework to perform "virtual" experiments and assess the experimental error. Characterization of the actuator dynamics was found to be unnecessary as the system identification procedure was capable of isolating the underlying flutter dynamics even in transfer functions containing actuator dynamics. A statistical framework was developed to quantify experimental error with the inclusion of random process and sensor noise. The mean error was found to be within $\pm 3\%$ and a single damping measurement within $\pm 15\%$ of the true value (with 95% confidence) for most flutter modes throughout the PW615 operating range. The least damped modes had the lowest error because of their higher forced response levels, increasing the signal-to-noise ratio and improving system identification. Measurement of the flutter damping at stable operating points along the pressure-rise characteristic enables estimation of the flutter margin of the fan. The flutter margin was under-estimated by at most 1.5 points for the PW615, or 14% of total flutter margin estimated by the model.

The sensitivity of the error metrics to experimental design choices was characterized with a variety of sensitivity studies. Best practices for spectral windowing used in transfer function estimation were established, especially to prevent large errors which occur for certain windowing parameters due to the non-stationary excitation signal. The experimental design was shown to be robust to sensor noise and inlet turbulence process noise, with successful identification of the least damped modes for noise levels as high as 1000x the sensor resolution and 5% inlet turbulence intensity. The actuator was demonstrated to have substantial flow margin, permitting the least damped modes to be identified with an 85% reduction in actuator flow. General recommendations for future forced response system identifications experiments are provided based

on the results of these studies. A sensitivity study to fan design parameters that are most influential on flutter damping demonstrated that the experimental design is applicable to other engine fans with comparable error levels to the PW615. Changes in fan design that reduced flutter damping also reduced error, again demonstrating that the experiment best measures the least damped, and therefore most problematic, flutter modes.

Finally, detailed design of the forced response experiment was performed. The ZNMF actuator was designed to implement multiple actuator geometries to tailor the actuator response to the flutter mode of interest, minimize the impact of the actuator on the steady state performance of the fan, and ensure engine operation did not impact actuator performance. An acoustic flutter model was used to guide the actuator inlet mounting duct design and a procedure was proposed to estimate problematic speeds for flight inlets due to acoustic flutter with damping measurements from engine tests. A preliminary dynamic blade stress analysis was performed and indicated the load imposed by the actuators was 30% of the blade limitation, but further analyses in coordination with the manufacturer must be conducted to establish safety limits for conducting the experiment. Once such limits have been established, the forced response experiment is ready to be implemented and conducted on the PW615 engine.

7.2 Conclusions

Conclusions that are applicable to general forced response system identification experiments for flutter, as well as the PW615 experiment specifically are provided below.

7.2.1 General Conclusions

1. Measurement of flutter damping via forced response system identification is feasible for gas turbine engine fans.

2. Current reduced order models in the literature cannot capture zero-net mass

flux (ZNMF) actuator performance for actuators of the physical scale needed for flutter experiments. Future experiments utilizing ZNMF actuators should experimentally characterize actuator performance to ensure sufficient bandwidth and authority for the experiment.

3. Characterization of actuator dynamics is unnecessary and flutter dynamics can be identified from transfer functions containing actuator dynamics by the system identification algorithm. This finding, however, is likely limited to actuators with dynamics that can be well represented by the sum of linear modes.

4. The least damped, and therefore most limiting, flutter modes have the least measurement error due to their greater forced response, which improves signal-to-noise ratio and system identification.

5. Backward nodal diameter modes can have absolute frame frequencies arbitrarily close to zero and such modes may not be excitable by actuators operating in the absolute frame if the mode frequency falls below the lower limit of the actuator.

6. Tip-timing sensors cannot be used to identify modes with absolute frame frequency greater than half the blade passing frequency, even if such modes are excitable by the actuator. This prevents damping measurements of a greater of number of modes as fan speed decreases because blade passing frequency decreases more quickly than flutter mode absolute frame frequencies.

7.2.2 PW615 Specific Conclusions

1. The ZNMF actuator as designed has sufficient bandwidth and authority to excite flutter modes between the 6^{th} backward nodal diameter and the 2^{nd} forward nodal diameter at takeoff speed. More flutter modes can be excited at lower engine speeds.

2. The damping of most flutter modes can be measured within $\pm 15\%$ (with 95% confidence) throughout the engine operating range. Flutter margin can be es-

timated within 1.5 points, or 14%, with only three damping measurements at stable operating points along the pressure-rise characteristic.

3. The 2nd backward nodal diameter mode cannot be identified at takeoff speed because of its near zero absolute frame frequency and the bandwidth of the ZNMF actuator. This prevents identification of the 3rd and 5th backward nodal diameter modes at 50% and 30% of takeoff speed as well.

4. The 3rd and 5th forward nodal diameter modes are excitable by the ZNMF actuator at idle speed but cannot be identified with the tip-timing system as their absolute frame frequency is above half of blade passing frequency.

7.3 Recommendations for Future Work

7.3.1 Flutter Reduced Order Modeling

A reduced order model of the flutter dynamics was the core enabling component for this work, but there are opportunities to make the model more representative of the real gas turbine environment and increase its utility in experimental design. The most important improvement would be to incorporate the effects of compressibility, which are relevant for two reasons. First, is the effect of shocks or choking on the blade passage flow as such flow features change the unsteady pressure distribution on the blade and the resultant aerodamping. They are also a driving mechanism of certain types of flutter [9]. Second, is to capture the effect of actuator operation on the acoustics upstream and downstream of the fan. As discussed in [72] and Section 6.2, inlet acoustics impact the onset of flutter and the flutter damping. During operation, the actuator will produce a pressure wave that propagates through the inlet and fan, and potentially reflects off of downstream geometry. It is unclear how this pressure wave from the actuator will interact with the inlet acoustics and alter the flutter behavior. Capturing this interaction would be valuable to quantify any changes in flutter damping due to actuator operation and assess how representative the experiment is of normal engine operation. The refined model could also be used

to modify the experimental design in order to minimize any changes in damping. Reduced order models of stall dynamics with a similar structure to the current flutter model have also been expanded to incorporate compressibility [78], demonstrating the feasibility of such an expansion of the model.

Another useful expansion of the model would be to include the effects of mistuning and a non-uniform background flow. The framework developed by Gordon [61] to include stationary and rotating frame non-uniformity for stall modeling could be adopted for structural and aerodynamic mistuning in the flutter model. The benefit for such a model to the experimental design is twofold. First, it would identify any modifications to the experimental design needed to perform an intentional mistuning experiment in an engine environment. Second, the ability to simulate inlet flow non-uniformity enables incorporation of this source of process noise. This can serve as a framework for the development of signal processing and system identification techniques tailored to the experiment at hand. Although high-fidelity methods can capture all the effects discussed in this section, this thesis has shown the utility of a computationally inexpensive dynamical model for experimental design.

7.3.2 Signal Processing & System Identification

The signal processing and system identification methodology in this work, while shown to be effective, is somewhat basic and "black-box" in nature. There exists more advanced processing techniques for time-frequency analysis such as wavelet methods [79] and Wigner-Ville Distribution methods [80] which have proven useful for the estimation of transfer functions for system identification. The virtual experiment and statistical framework developed in this thesis serves as a useful means of assessing the efficacy of such methods for flutter applications specifically.

7.3.3 PW615 Experiment

A list of future work and recommendations specifically for the PW615 experiment is provided below in priority order:

1. Establishing safe limits on blade displacement with the manufacturer. This is the highest priority item and the only one that absolutely must be completed prior to running the experiment due to its safety implications. The experiment should be conducted with real-time monitoring of blade displacement to prevent exceeding these limits and the tip-timing system should be integrated with test cell, actuator, and engine control systems to automate shutdown of the engine should blade limits be exceeded.

2. Measuring true noise levels in the MIT test cell and the sensor system. Surveys of the PW615 inlet total pressure and temperature non-uniformity and turbulence levels are recommended to estimate the process noise levels within the experiment. These levels can be used to refine the expected error from the experiment using the results of Section 5.2.1and inform what, if any, more advanced filtering or system identification techniques mentioned in Section 7.3.2 could reduce the error further.

3. Improving the characterization of the actuator performance and dynamics. Higher fidelity methods are available to resolve the spatially and temporally non-uniform flow field such as particle image velocimetry (PIV) or laser doppler velocimetry (LDV). PIV has been historically of limited use for the characterization of synthetic jet actuators due to the small size of typical devices requiring high resolution [53], but such restrictions may not apply to actuators at this physical scale. Such higher fidelity methods would mitigate the need to calibrate the hotwire anemometer at low velocities as in this work. Furthermore, characterization of the actuator operating at crossflow conditions and distances from the fan face representative of the PW615 would also be of great utility. This refined characterization would better estimate the true forcing level and spatial pattern experienced by the fan.

4. Deriving all flutter model inputs for the PW615 fan specifically rather than relying on some Rotor 67 data. This is the lowest priority item given the similarity of Rotor 67 and the PW615 fan discussed in Section 2.2.1 and the

feasibility of the experiment for a wide range of input parameters as shown in Section 5.3.

Appendix A

Flutter Reduced Order Model Inputs

The required inputs to the flutter reduced order model that describe the fan system are summarized in Table A.1. Further details on how these inputs are used and defined can be found in Ref. [21].

Aerodynamic	Structural
Rotor & stator loss functions	Rotor & stator bending & torsion mode frequencies
Rotor flow angle deviation function	Mechanical damping coefficients
Chordwise center of pressure	Chordwise center of gravity
Greitzer B Parameter	Chordwise elastic axis

Geometric
Rotor & stator stagger angles
Rotor & stator metal angles
Rotor & stator chord lengths
Rotor blade mass & radius of gyration

Table A.1: Required fan system inputs to flutter reduced order model

Appendix B

Actuator Volume Flow Estimation from Centerline Velocity

Of interest is the extent to which the measured axial velocity profile across the orifice is represented by analytical solutions such that the volume flow can be estimated with fewer measurements than that required for a full traverse. The analytical profile of axial velocity for unsteady flow in a circular orifice for an oscillating pressure gradient with a Stokes number $St = 2r_{orif}\sqrt{\frac{\omega}{\nu}}$ is given by

$$\frac{U}{U_{CL}}\Big(\frac{r}{r_{orif}}, St\Big) = 1 - \frac{J_0[\frac{St}{2}\sqrt{-j(r/r_{orif})^2)}]}{J_0[\frac{St}{2}\sqrt{-j}]}, \tag{B.1}$$

where J_0 is a Bessel function of order zero [81]. For the Stokes numbers of interest, the velocity profile is nearly uniform across the actuator with higher velocities near the orifice edge. Figure B-1 compares the measured velocity profile to the analytical expression for a Stokes number of 170. The measured velocity profile is in relatively good agreement with the analytical expression. The non-zero velocities beyond the orifice edge are due to jet vortex roll-up during expulsion and the large capture area during ingestion. Such phenomena are in agreement with higher fidelity measurements by Gallas [53]. Equation B.1 can be used to define the ratio of the average velocity, defined as the volume flow per unit area $u_{avg} = \frac{\dot{V}}{A}$, to the centerline velocity u_{cl} as a function of the Stokes number. This ratio is very near unity for the range of

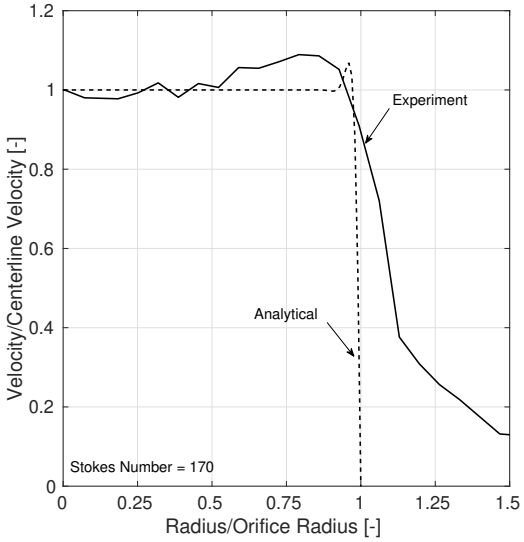


Figure B-1: Measured velocity profile is in qualitative agreement with analytical results.

Stokes numbers of the actuator, as shown in Figure B-2, suggesting the volume flow magnitude could be well predicted by the centerline velocity and orifice area.

Direct comparisons between the volume flow frequency response as determined by a full traverse of the orifice and by the centerline velocity in conjunction with the relationship in Figure B-2 were performed for a variety of actuator geometries. As in Figure B-3 for $\frac{L_{neck}}{r_{speaker}} = 2$, the two methods are in good agreement, with the centerline velocity method under-predicting the volume flow magnitude by at most 20%. The centerline velocity method thus represents a conservative estimate of the actuator volume flow frequency response.

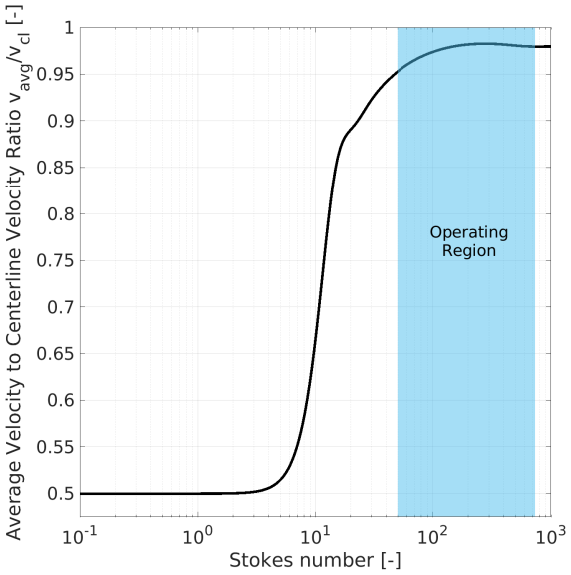


Figure B-2: Ratio of average velocity to centerline velocity for unsteady flow expected to be near unity for actuator operation, enabling volume flow estimation from centerline velocity.

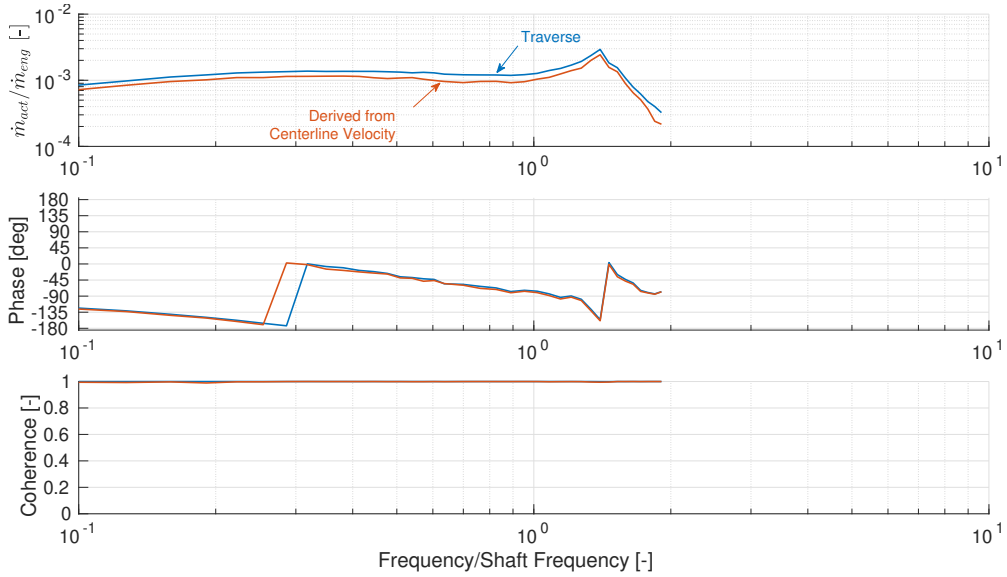


Figure B-3: Good agreement of volume flow frequency responses from traverse measurement and centerline velocity methods with centerline velocity method producing a conservative estimate.

Appendix C

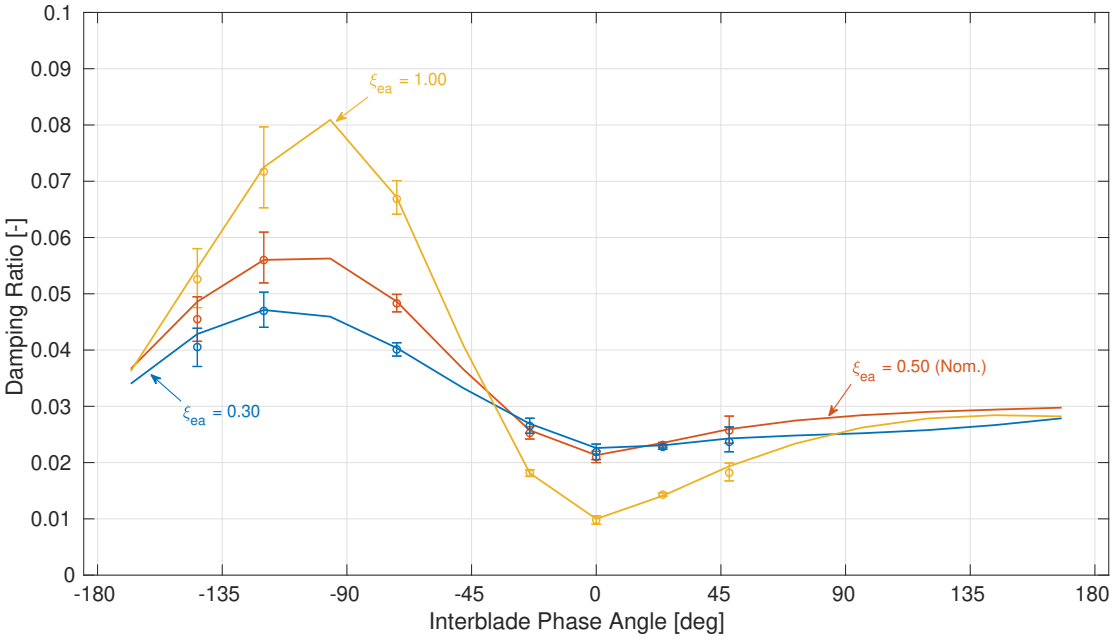
Fan Design Sensitivity Studies

The remaining results from the sensitivity studies of the experimental design to fan performance and design parameters are presented in this section. In all cases the flutter damping ratio was well captured and the trends in the error metrics discussed in Section 5.3 apply. The variation in error metrics for changes in the elastic axis and center of gravity chordwise positions is presented in Figures C-1a and C-1b respectively. As with the center of pressure, the elastic axis is limited to 30% chord as moving it further upstream de-stabilized the torsional modes.

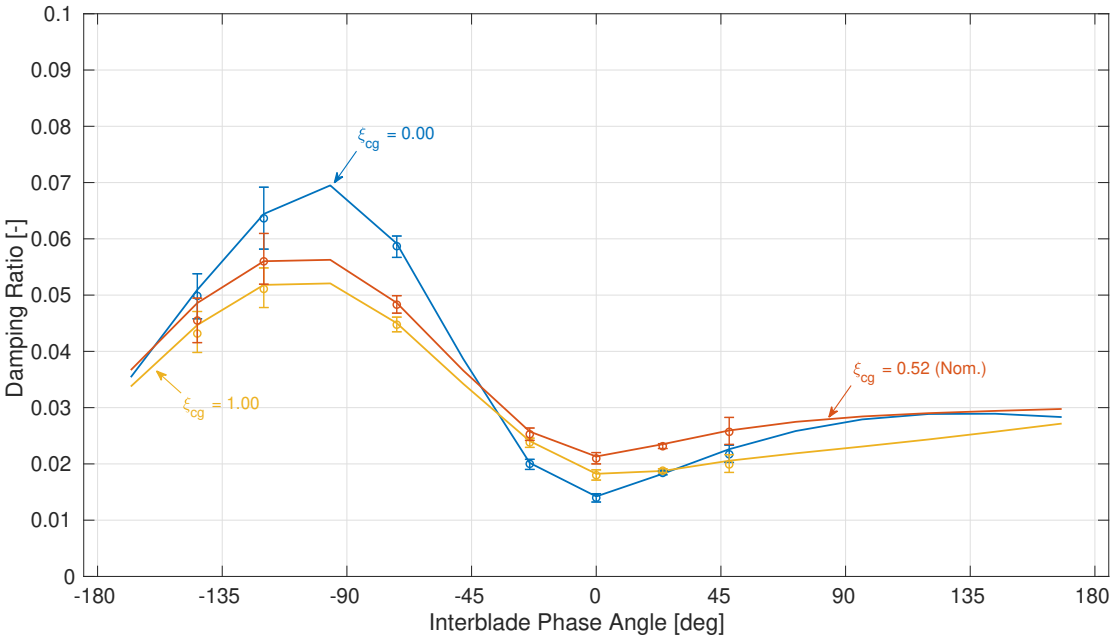
A critical parameter that governs the rotor performance is the rotor stagnation pressure loss function. The rotor loss ω_r is modelled as a parabolic function of the blade incidence i_r as below:

$$\omega_r(i_r) = a_r(i_r - i_{r,min})^2 + \omega_{r,min}$$

It was found that the flutter damping ratio was insensitive to the minimum loss value $\omega_{r,min}$ but sensitive to the steepness parameter a_r, which was varied by a factor of 2 and 0.5 in Figure C-2a, which shows the modified and nominal rotor loss functions are shown with the underlying Rotor 67 data. While all previous fan design studies were performed at the design flow coefficient, this resulted in operation at the minimum loss incidence where the steepness parameter has little influence. The rotor was instead operated at the near stall flow coefficient where the incidence was greater, marked

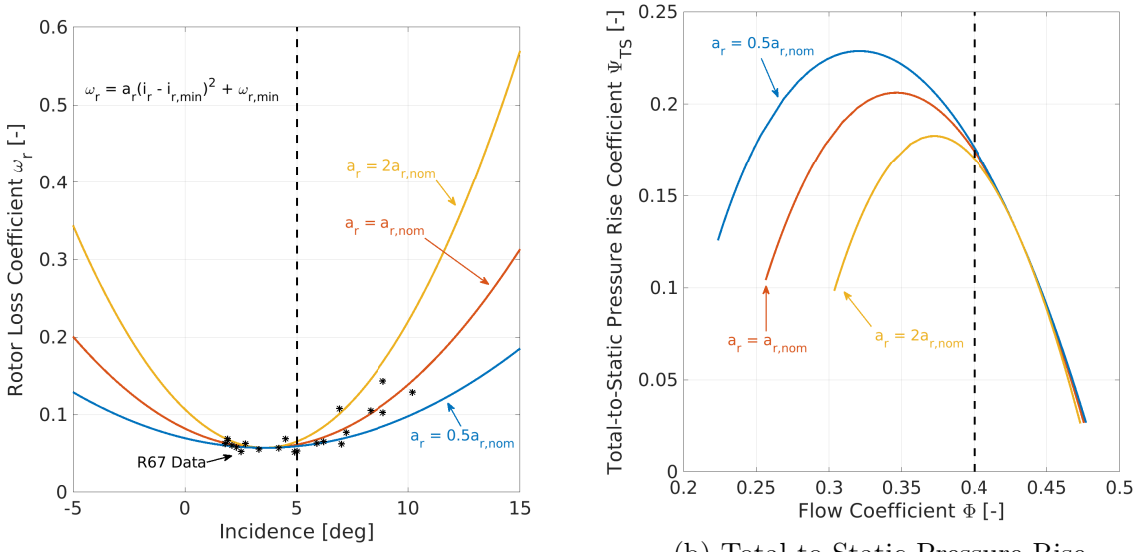


(a) Elastic Axis



(b) Center of Gravity

Figure C-1: Error metrics for variation of elastic axis and center of gravity location. Change in damping ratio well captured by experimental design.



(a) Rotor Loss Functions

(b) Total-to-Static Pressure Rise Characteristics

Figure C-2: Rotor loss functions with modified steepness parameter and resultant total-to-static pressure rise characteristics. Damping measured off-design to increase impact of loss function.

with a dashed line in Figure C-2a, and the loss function steepness had an influence on the flutter damping. The resultant total-to-static pressure rise characteristics with the operating point marked with a dashed line are shown in Figure C-2b. The identified damping ratios in Figure C-3 show that the variation in analytical damping ratio is well captured.

Finally the blade mass was varied by a factor of 0.5 and 2 with the change in analytical damping ratio well captured as in Figure C-4. Note that the non-dimensional blade frequency parameter Q_b was held constant, thus the dimensional blade stiffness increased simultaneously with the mass such that the frequency was constant. As the blade mass to air mass ratio increases, the aerodamping contribution lessens as compared to the mechanical damping and the flutter damping ratio converges to the mechanical damping ratio of $\zeta_b = 0.03$.

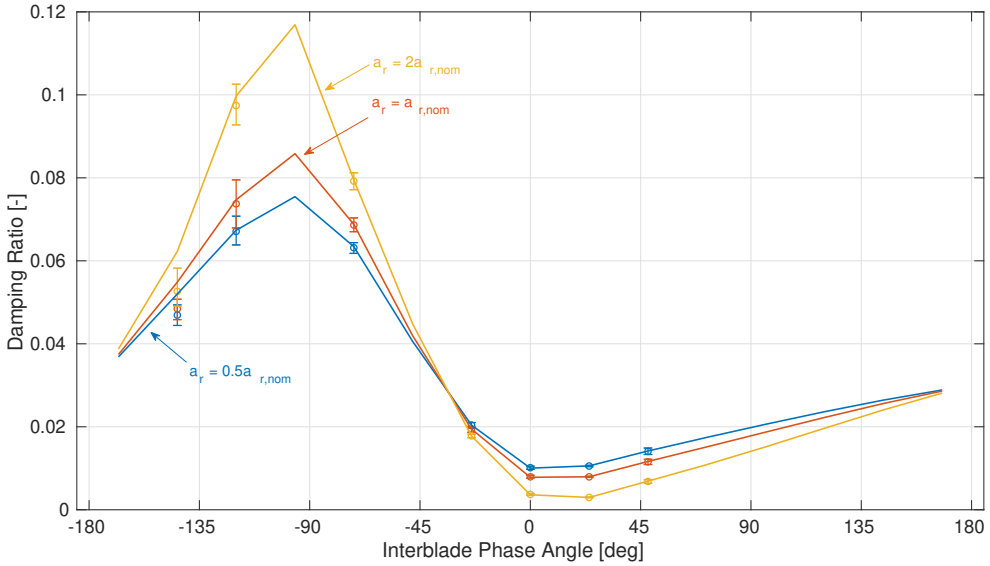


Figure C-3: Experiment captures changes in flutter damping with loss function steepness parameter.

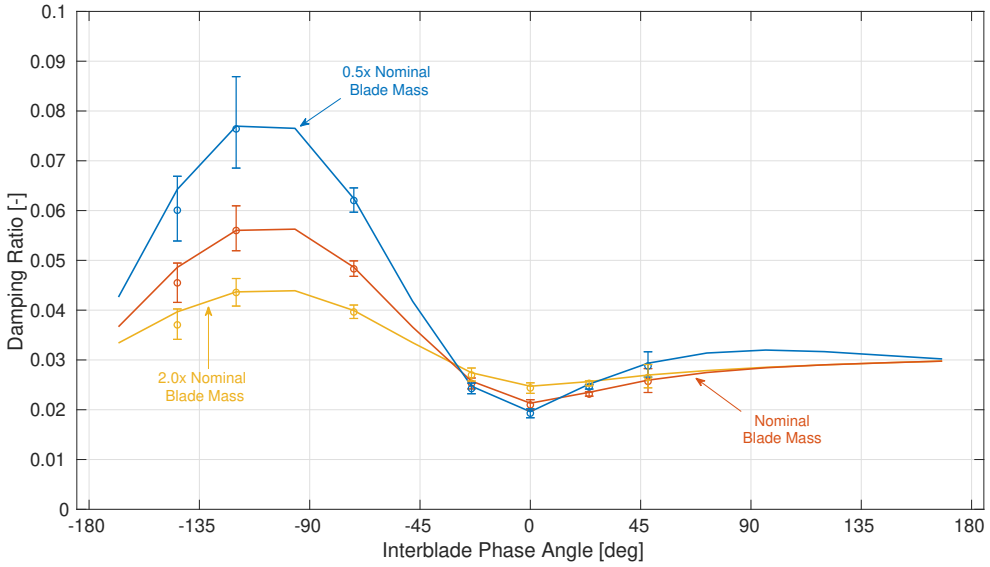


Figure C-4: Experiment capture variation of flutter damping ratio with blade mass.

Appendix D

Reduced Order Modeling in Test Cell Design

A common theme in this thesis is the power and utility of reduced order modeling. This was further demonstrated in the complex task of designing the test cell for the PW615 engine at MIT. Reduced order modeling was utilized as a tool throughout the design process of many sub-systems in order to explore the design space, evaluate solutions, and assess trade-offs. One such system was the exhaust system to remove engine exhaust from the test cell and vent it to atmosphere. As shown in Figure D-1, traditional engine test cells have large diameter augmentor tube, several times that of the engine exhaust, to collect exhaust gasses and induce a secondary flow into an even larger exhaust stack which vents to atmosphere. Such a design, however, was not possible given the constraints of operating within an existing building on MIT's campus. The building housing the test cell was built around an existing 18" diameter, approximately 1.3 times the exhaust diameter, piping system that was used for turboshaft engines previously run at MIT with approximately a quarter of the massflow of the PW615. Enlarging this piping system was not feasible as it would require extensive building modifications and only the exhaust piping immediately within the test cell and exterior to the building could be specified. Given this, two questions drove the exhaust design process:

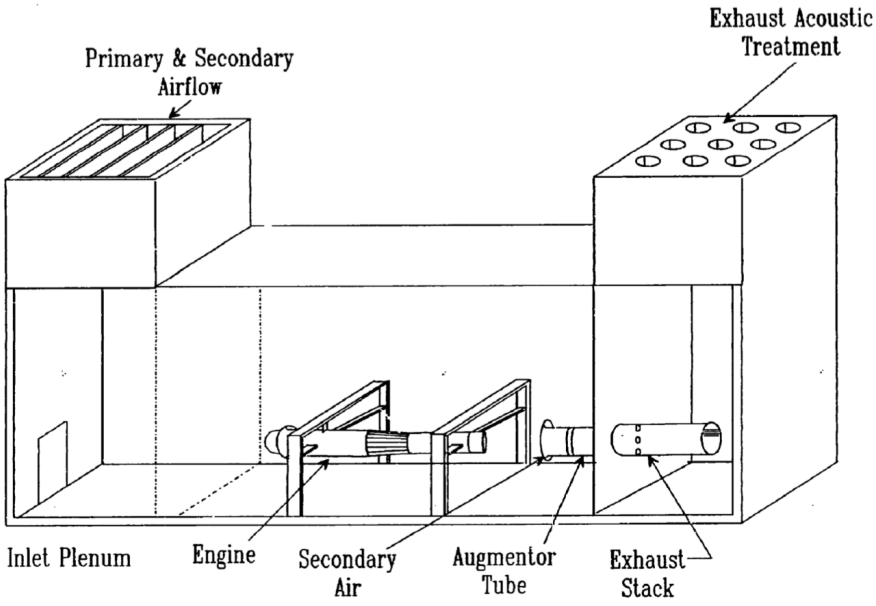


Figure D-1: Typical engine test cell design with large diameter augmentor tube and exhaust stack not feasible for MIT test cell (reproduced from [82])

.

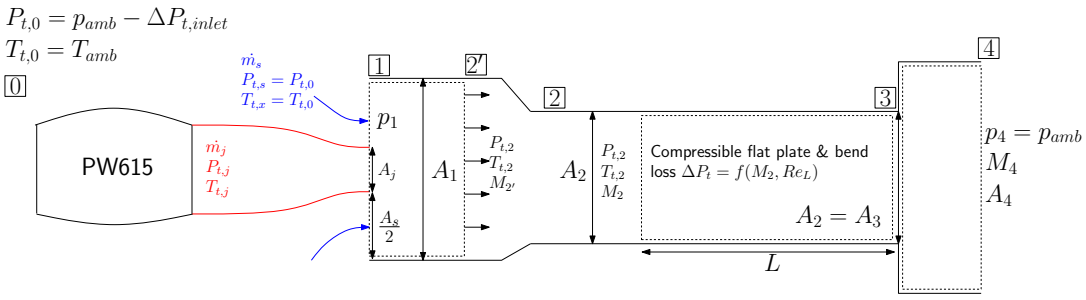


Figure D-2: Exhaust system reduced order model consisting of linked compressible flow and control volume analyses enabled assessment of design concepts and design space exploration.

1. Is it feasible to run the engine in the test cell? In other words, can the existing piping pass the required flow set by the PW615 exhaust mass flow and stagnation pressure and temperature? If so, what is needed to enable this?

2. If the exhaust can be sufficiently removed, what can be done to reduce the noise associated with engine operation?[1]

To address these questions, a reduced order model was developed to estimate the steady state performance of the exhaust system. The model evolved with various early configuration ideas, but the final model consists of a series of linked compressible flow analyses, shown schematically in Figure D-2. Following the flow from the inlet to the test cell, left to right in Figure D-2, the model is described below:

- **Inlet Loss:** Outside ambient air is drawn through an inlet system, incurring a total pressure loss $\Delta P_{t,inlet}$ which is derived from empirical data on the inlet system and sudden expansion loss. This sets the test cell ambient conditions $P_{t,0}$ and $T_{t,0}$.

- **Secondary Flow and Mixing:** The engine exhaust jet massflow $\dot{m}_j$ and stagnation state $P_{t,j}, T_{t,j}$ is known *a-priori* from manufacturer data. The exhaust jet entrains test cell air and induces a secondary flow (shown in blue). Both are captured by the exhaust system bellmouth at station 1 with a controllable area A_1. The exhaust jet area is assumed to contract isentropically due to the static pressure gradient as $p_1 < P_{t,0}$, setting the secondary flow area in the bellmouth A_s and the associated massflow $\dot{m}_s$. A control volume analysis is used to determine the mixed out properties at station 2'. The mixed out flow is brought to area A_2 at station 2, which could be larger or smaller than A_1. The area A_2 is fixed by the 18" diameter piping through the building.

- **Friction Loss:** Station 2 to station 3 represents a large length (approximately 100') of constant 18" diameter piping with several bends. The flow is assumed adiabatic and total pressure loss due to friction is estimated using turbulent

[1]The test cell is located near the center of MIT's campus and is in a noise sensitive area.

flat plate correlations for the skin friction coefficient [83] and 1D compressible flow theory [54]. Loss from the bends is treated as secondary loss and estimated with empirical correlations for compressible flow in circular ducts [84]. Station 3 is located outside the building nearly at the end of the exhaust system.

- **Diffusion:** The exhaust flow is vented to outside ambient air via a dump diffuser of controllable area ratio A_4/A_3. This was introduced to reduce the jet Mach number and hence noise. The total pressure loss in the sudden expansion is computed using another control volume analysis.

The two design parameters are the bellmouth and diffuser area ratios, A_1/A_2 and A_4/A_3 respectively. With those specified, the static pressure p_1 required to meet the matching condition $p_4 = p_{amb}$ is determined with an iterative numerical method. With p_1 determined, the total flow through the system and the fluid properties at each station are calculated. The simple reduced order model proved invaluable during the design and commissioning process of the exhaust system, providing many contributions:

1. Demonstration that engine operation was feasible in that there were configurations where the engine exhaust could be passed by the system.

2. Valuable insight and learning as to how the pressure evolved through the system as a function of the design parameters as summarized in Figure D-3. This was useful in assessing different configuration during the structural design where pressure throughout the system was of great concern.

3. Quantitative estimates across the design space for parameters of interest such as the diffuser exit Mach number, Figure D-4a, or the maximum pressure in the piping, Figure D-4b. These estimates identified trade-offs in the design, such as increasing the diffuser area ratio $A_4/A_3 > 2$ reduced exit Mach number and noise but produced a greater maximum system pressure. The noise impact on the surrounding area was also estimated by coupling the exhaust model with a jet noise model [85], as in Figure D-5. A configuration that satisfied the

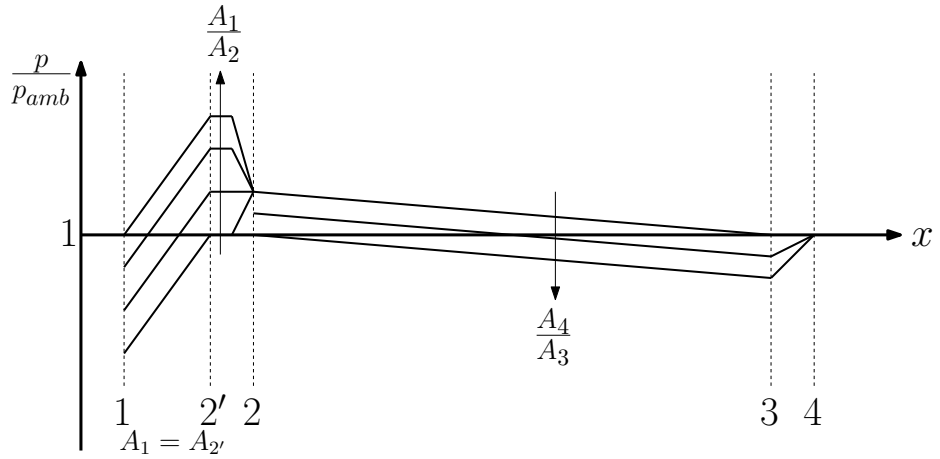
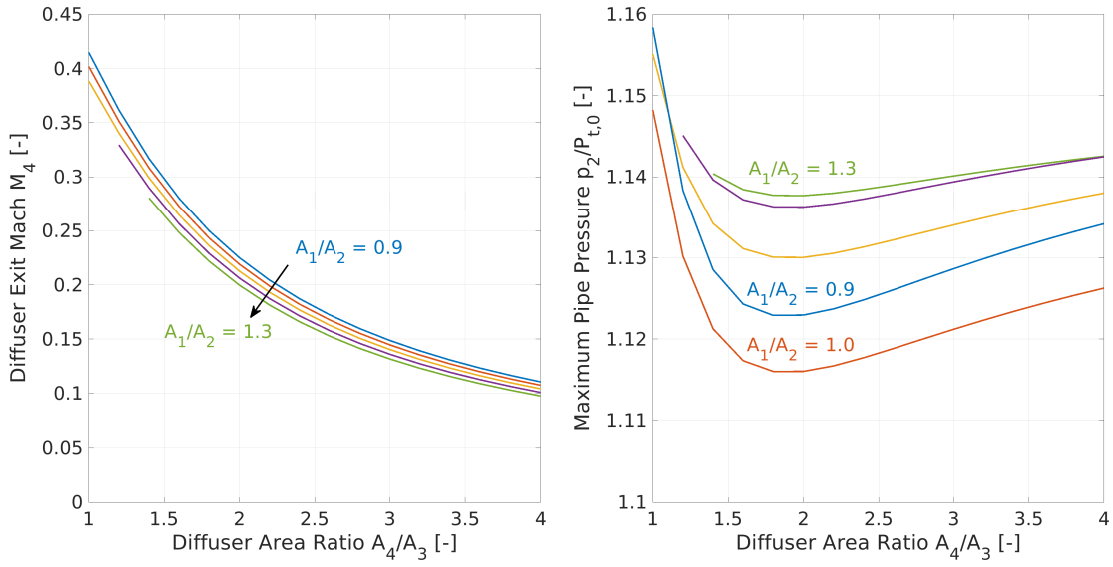


Figure D-3: Structural design of exhaust system enabled by insight into relationship of design parameters A_1/A_2 and A_4/A_3 and system pressure levels provided by model.

aerodynamic, structural, and noise requirements was identified using the model. Furthermore, the identified the limits of the design space where the flow could no longer be passed. For example, bellmouth area ratios $A_1/A_2 > 1.3$ were not feasible as this drove the static pressure at station 1 p_1 above cell ambient pressure $P_{t,0}$, resulting in exhaust spillage into the test cell.

4. A means to assess hypothetical scenarios. For example, an assumption of the model is that the exhaust jet and secondary flow fully mix out prior to the area change from station 2' to 2. Assuming the other extreme, that no mixing occurs and treating the two streams as a compound flow, revealed the secondary flow stream would choke for even very small reductions in area. This indicated the need for complete mixing if an area reduction were employed, mandating longer piping at the larger area to allow full mixing or the inclusion of a lobed mixer. As another example, an early proposal was to cool the exhaust flow and increase its density by injecting liquid into the exhaust piping in case the system could not otherwise pass the flow. It was straightforward to modify the model to include evaporative cooling due to an injected fluid (e.g. liquid CO2) in the mixing process from 1 to 2. The analysis from the model revealed that such a scheme was not effective and had little effect on the system performance.



(a) Diffuser Exit Mach Number (b) Maximum Pipe Pressure

Figure D-4: Model provides estimates of quantities of interest across design space and identified trade-offs that informed final design configuration.

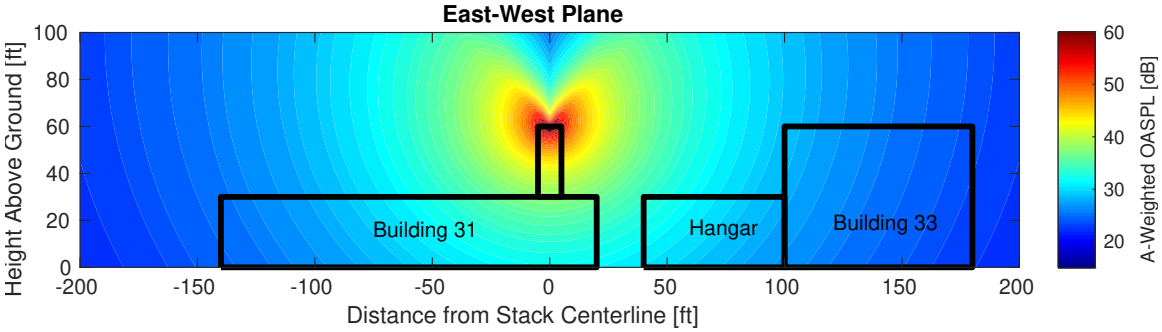


Figure D-5: Noise impact on surrounding buildings deemed acceptable due to estimates from reduced order model.

5. A point of comparison to understand the experimentally measured exhaust system performance while commissioning the test cell and engine. As an example, early data from commissioning tests indicated the measured static pressure after mixing p_2 and at the diffuser inlet p_3 were higher than expected from the model. Deeper investigation into the experimental data suggested mixing in the diffuser was incomplete, reducing the static pressure rise across the diffuser. Correcting the experimental data for incomplete diffusion brought the experimental and model data into good agreement, as in Figure D-6, further supporting this hypothesis. Without the model predictions to provide insight into the exhaust system behavior and expected performance, this may never have been discovered.

The design and commissioning of the exhaust system has provided a perfect example of the power and utility of reduced order modeling. More complex and higher fidelity computations could have been performed in the design process, but such a relatively simple model permitted a much more thorough exploration of the design space. More importantly, it provided key insights into the parameters and physics that govern system performance; insights that may have been difficult to extract or otherwise been lost in the details of high fidelity models. The reduced order model played a critical role in the successful commissioning of the PW615 engine at MIT.

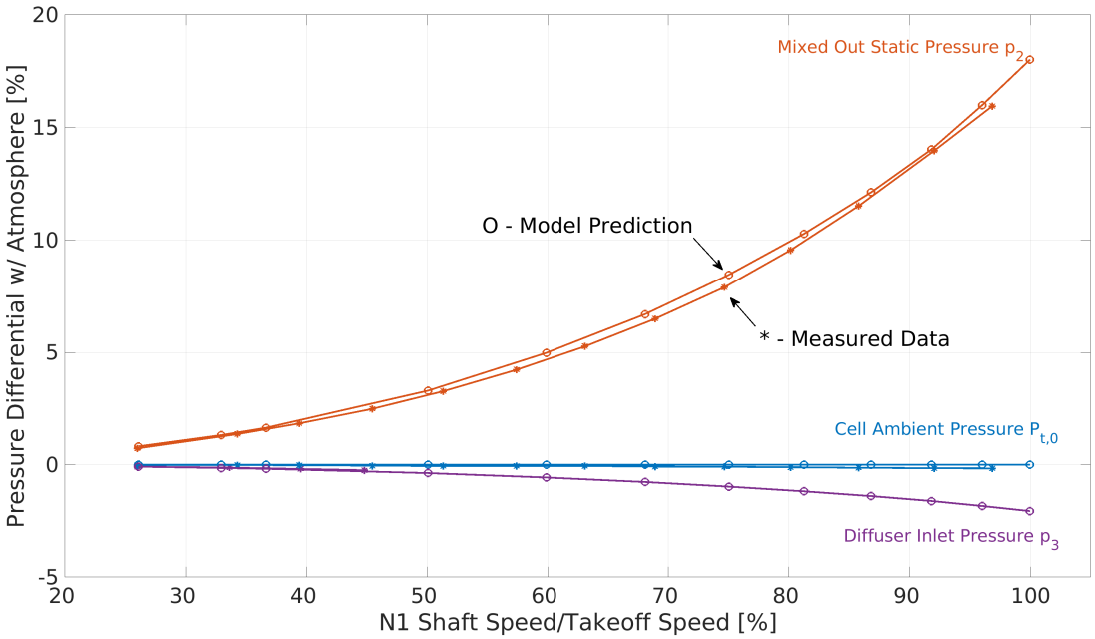


Figure D-6: Reduced order model provided insight to diagnose observed system behavior as incomplete diffusion. Experimentally measured data in good agreement with model when corrected for incomplete diffusion.

Bibliography

[1] F. Lane. System Mode Shapes in the Flutter of Compressor Blade Rows. *Journal of the Aeronautical Sciences*, 23(1):54–66, 1956.

[2] P. Dhopade and A. J. Neely. Aeromechanical modeling of rotating fan blades to investigate high-cycle and low-cycle fatigue interaction. *Journal of Engineering for Gas Turbines and Power*, 137(5):1–12, 2015.

[3] National Transportation Safety Board. Left Engine Failure and Subsequent Depressurization, Southwest Airlines Flight 1380, Boeing 737-7H4, N772SW. Accident Report PB2019-101439, 2018.

[4] T. M. Bartsch. High Cycle Fatigue (HCF) Science and Technology Program. Technical Report AFRL-PR-WP-TR-2002-2060, 2002.

[5] A. V. Srinivasan, D. G. Cutts, and S. Sridhar. Turbojet Engine Blade Damping. Technical report, NASA CR 165406, 1981.

[6] A. V. Srinivasan and D. G. Cutts. Dry friction damping mechanisms in engine blades. In *Proceedings of ASME Turbo Expo*, 1982.

[7] J. Dugundji. Flutter Analysis of a Tuned Rotor with Rigid and Flexible Disks. Technical Report 146, Gas Turbine Laboratory, Massachusetts Institute of Technology, 1979.

[8] E. F. Crawley. Aerodynamic Damping Measurements in a Transonic Compressor. *Journal of Engineering for Power*, 105(July), 1983.

[9] A. V. Srinivasan. Flutter and resonant vibration characteristics of engine blades. *Proceedings of the ASME Turbo Expo*, 4(October), 1997.

[10] J. G. Marshall and M. Imregun. A review of aeroelasticity methods with emphasis on turbomachinery applications. *Journal of Fluids and Structures*, 10(3):237–267, 1996.

[11] R. E. Bartels and A. L. Sayma. Computational aeroelastic modelling of airframes and turbomachinery: Progress and challenges. *Philosophical Transactions of the Royal Society A: Mathematical, Physical and Engineering Sciences*, 365(1859):2469–2499, 2007.

[12] M. Vahdati, G. Simpson, and M. Imregun. Mechanisms for Wide-Chord Fan Blade Flutter. *Journal of Turbomachinery*, 133(4):041029, 2011.

[13] M. Vahdati and N. A. Cumpsty. Aeroelastic Instability in Transonic Fans. *Journal of Engineering for Gas Turbines and Power*, 138(2):022604, 2016.

[14] K. Lee, M. Wilson, and M. Vahdati. Numerical Study on Aeroelastic Instability for a Low-Speed Fan. *Journal of Turbomachinery*, 139(7):071004, 2017.

[15] S. Stapelfeldt and M. Vahdati. Improving the flutter margin of an unstable fan blade. *Journal of Turbomachinery*, 141(July):1, 2019.

[16] S. C. Stapelfeldt and M. Vahdati. On the importance of engine-representative models for fan flutter predictions. *Journal of Turbomachinery*, 140(8), 2018.

[17] M. P. Castanier and C. Pierre. Modeling and analysis of mistuned bladed disk vibration: Status and emerging directions. *Journal of Propulsion and Power*, 22(2):384–396, 2006.

[18] E. F. Crawley, E. H. Ducharme, and D. R. Mokadam. Analytical and experimental investigation of the coupled bladed disk/shaft whirl of a cantilevered turbofan. *Journal of Engineering for Gas Turbines and Power*, 108(4):567–575, 1986.

[19] I M Hongsik, X Chen, and G Zha. Detached eddy simulation of transonic rotor stall flutter using a fully coupled fluid-structure interaction. In *Proceedings of ASME Turbo Expo*, number GT2011-45437, pages 1217–1230, 2011.

[20] D. L. Gysling and M.R. Myers. A Framework for Analyzing the Dynamics of Flexibly-Bladed Turbomachines. In *International Gas Turbine and Aeroengines Congress & Exhibition*, pages 28–45, 1996.

[21] M.T. Wong. System Modeling and Control Studies of Flutter in Turbomachinery. Master's thesis, Massachusetts Institute of Technology, 1997.

[22] G. S. Copeland and G. Rey. Nonlinear Modeling Analysis and Control of Turbomachinery Stall Flutter. Technical Report AFRL-SR-BL-TR-98-0694, Air Force Office of Scientific Research, 1998.

[23] G. S. Copeland and G. Rey. Comparison of experiments and reduced-order models for turbomachinery high-incidence flutter. *Journal of Fluids and Structures*, 19(5):713–727, 2004.

[24] G. Rey, A. Banaszuk, and D. L. Gysling. Active Control of Flutter in Turbomachinery Using Off Blade Actuators Sensors: Experimental Results. In *41st Aerospace Sciences Meeting and Exhibit*, number AIAA 2003-1258, 2003.

[25] L. E. Snyder and G. L. Commerford. Supersonic Unstalled Flutter in Fan Rotors; Analytical and Experimental Results. *Journal of Engineering for Power*, (October):379–386, 1974.

[26] S. Fleeter, A. S. Novick, R. E. Riffel, and J. E. Caruthers. Experimental Determination of the Unsteady Aerodynamics in a Controlled Oscillating Cascade. *Journal of Engineering for Power*, (January):88–96, 1977.

[27] F. O. Carta and A. O. St. Hilaire. Experimentally Determined Stability Parameters of a Subsonic Cascade Oscillating Near Stall. *Journal of Engineering for Power1*, 100(January):111–120, 1978.

[28] J. Lepicovsky, E. R. McFarland, V. R. Capece, and J. Hayden. Unsteady pressures in a transonic fan cascade due to a single oscillating airfoil. In *Proceedings of ASME Turbo Expo*, 2002.

[29] T. Watanabe, S. Uzawa, J. Kazawa, and B. Keim. Numerical and Experimental Study of Active Flutter Suppression with Piezoelectric Device for Transonic Cascade. In *Proceedings of the ASME Turbo Expo*, 2008.

[30] M. C. Keerthi and A. Kushari. Experimental study of aerodynamic damping of an annular compressor cascade with large mean incidences. *Journal of Turbomachinery*, 141(6), 2019.

[31] L. Malzacher, S. Geist, V. Motta, D. Peitsch, and H. Hennings. A low-speed compressor test rig for flutter investigations. *Journal of Turbomachinery*, 141(5):1–12, 2019.

[32] A. Bölcs and T. Fransson. Aeroelasticity in Turbomachines: Comparison of Theoretical and Experimental Cascade Results. Technical Report AFOSR 84-0105, Air Force Office of Scientific Research, 1993.

[33] I. McBean, K. Hourigan, M. Thompson, and F. Liu. Prediction of Flutter of Turbine Blades in a Transonic Annular Cascade. *Journal of Fluids Engineering*, 127(November):1053–1058, 2005.

[34] A. Vega and R. Corral. The low reduced frequency limit of vibrating airfoils-Part II: Numerical experiments. *Journal of Turbomachinery*, 138(February):1–9, 2016.

[35] Jack L. Kerrebrock. Flow in transonic compressors. *AIAA Journal*, 19(1):4–19, 1981.

[36] T. R. Jeffers, J. J. Kielb, and R. S. Abhari. A Novel Technique for the Measurement of Blade Damping Using Piezoelectric Actuators. In *Proceedings of ASME Turbo Expo*, pages 2000–GT–0359, 2000.

[37] J. J. Kielb and R. S. Abhari. Experimental Study of Aerodynamic and Structural Damping in a Full-Scale Rotating Turbine. *Journal of Engineering for Gas Turbines and Power*, 125(1):102–112, 2003.

[38] W. L. Murray and N. L. Key. Experimental investigation of a forced-response condition in a multistage compressor. *Journal of Guidance, Control, and Dynamics*, 38(6):1320–1329, 2015.

[39] A. Kammerer and R. S. Abhari. Experimental Study on Impeller Blade Vibration During Resonance—Part II: Blade Damping. *Journal of Engineering for Gas Turbines and Power*, 131(2):022509, 2009.

[40] H. D. Vo. Active Control of Rotating Stall in a Three-Stage Axial Compressor with Jet Actuators. Master's thesis, 1997.

[41] J. D. Paduano. *Active Control of Rotating Stall in Axial Compressors*. PhD thesis, Massachusetts Institute of Technology, 1992.

[42] D. C. Urasek, W. T. Gorrell, and W. S. Cunnan. Performance of Two-Stage Fan Having Low-Aspect Ratio, First-Stage Rotor Blading. Technical Report 1493, NASA, 1979.

[43] A. J. Strazisar, J. R. Wood, M. D. Hathaway, and K. L. Suder. Laser Anemometer Measurements in a Transonic Axial-Flow Fan Rotor. Technical Report 2879, 1989.

[44] F. O. Carta and A. O. St. Hilaire. Effect of Interblade Phase Angle and Incidence Angle on Cascade Pitching Stability. *Journal of Engineering for Power*, 102(April):391–396, 1980.

[45] Z. S. Spakovszky, J. D. Paduano, R. Larsonneur, A. Traxler, and M. M. Bright. Tip clearance actuation with magnetic bearings for high-speed compressor stall control. *Journal of Turbomachinery*, 123(3):464–472, 2001.

[46] R.G. Berndt. *Actuation for Rotating Stall Control of High Speed Axial Compressors*. PhD thesis, Massachusetts Institute of Technology, 1995.

[47] Q. Gallas, B. Carroll, L. N. Cattafesta, R. Holman, T. Nishida, and M. Sheplak. Lumped Element Modeling of Piezoelectric-Driven Synthetic Jet Actuators. *AIAA Journal*, 41(2):240–247, 2003.

[48] J. S. Agashe. *Modeling, Design, and Optimization of Electrodynamic Zero-Net Mass-Flux (ZNMF) Actuators*. PhD thesis, University of Florida, 2009.

[49] PRV Audio. 6mb500ft data sheet. `https://prvaudio.com/wp-content/uploads/2019/02/PRV-Audio-6MB500FT-Datasheet.pdf`. Last Accessed: May 04 2020.

[50] R. H. Small. Direct-Radiator Loudspeaker System Analysis. *AES: Journal of the Audio Engineering Society*, 20(5):383–395, 1972.

[51] Prime Photonics. Data capture unit datasheet. `http://www.primephotonics.com/images/pdfs/Data_Capture_Unit_10-19.pdf`. Last Accessed: May 04 2020.

[52] L. Ljung. *System Identification Toolbox: User's Guide*. The Mathworks, 2020.

[53] Q. Gallas. *On the Modeling and Design of Zero-Net Mass Flux Actuators*. PhD thesis, University of Florida, 2005.

[54] E.M. Greitzer, C.S. Tan, and M.B. Graf. *Internal Flow: Concepts and Applications*. Cambridge University Press, 2004.

[55] S. S. Sattarzadeh, A. Kalpakli, and R. Örlü. Hot-wire calibration at low velocities: Revisiting the vortex shedding method. *Advances in Mechanical Engineering*, 2013, 2013.

[56] M. S. Guellouz and S. Tavoularis. A simple pendulum technique for the calibration of hot-wire anemometers over low-velocity ranges. *Experiments in Fluids*, 18(3):199–203, 1995.

[57] E. Özahi, M. O. Çarpinlioğlu, and M. Y. Gündoğdu. Simple methods for low speed calibration of hot-wire anemometers. *Flow Measurement and Instrumentation*, 21(2):166–170, 2010.

[58] F.E. Jorgensen. How to measure turbulence with hot-wire anemometers. Technical report, 2005.

[59] H. P. Hackenberg and A. Hartung. An Approach for Estimating the Effect of Transient Sweep Through a Resonance. *Journal of Engineering for Gas Turbines and Power*, 138(8):1–12, 2016.

[60] C.M. Van Schalkwyk, J.D. Paduano, E.M. Greitzer, and A.H. Epstein. Active stabilization of axial compressors with circumferential inlet distortion. *Proceedings of the ASME Turbo Expo*, 4(July), 1997.

[61] K. A. Gordon. *Three-dimensional Rotating Stall Inception and Effects of Rotating Tip Clearance Asymmetry in Axial Compressors*. PhD thesis, Massachusetts Institute of Technology, 1999.

[62] N. E. Goodzeit and M. Q. Phan. System Identification in the Presence of Completely Unknown Periodic Disturbances. *Journal of Guidance Control and Dynamics*, 23(2), 2000.

[63] B. Efron and R.J. Tibshirani. *An Introduction to the Bootstrap*. Chapman & Hall/CRC, Boca Raton, FL, 1994.

[64] Z.S. Spakovszky, J.B. Gertz, O.P. Sharma, J.D. Paduano, A.H. Epstein, and E.M. Greitzer. Influence of compressor deterioration on engine dynamic behavior and transient stall-margin. *Journal of Turbomachinery*, 122(3), 2000.

[65] A. H. Nuttall. Some Windows with Very Good Sidelobe Behavior. *IEEE Transactions on Acoustics, Speech, and Signal Processing*, 29(1):84–91, 1981.

[66] M. O. Solomon. PSD Computations Using Welch's Method. Technical Report SAND91-1533, Sandia National Laboratories, 1991.

[67] K. M. M. Prabhu. *Window Functions and Their Applications in Signal Processing*. Taylor & Francis Group, Boca Raton, FL., 2014.

[68] F. J. Harris. On the Use of Windows for Harmonic Analysis with the Discrete Fourier Transform. *Proceedings of the IEEE*, 66(1):51–83, 1978.

[69] J. Takado, T. Sonoda, and S. Nakamura. The effect of the inlet boundary layer on the tip flow field in a transonic fan rotor. In *Proceedings of ASME Turbo Expo*, number 98-GT-130, 1998.

[70] J. Lee. *Characterization and Mitigation of Blade Waviness Effects on Fan Performance*. PhD thesis, Massachusetts Institute of Technology, 2019.

[71] M. Vahdati, N. Smith, and F. Zhao. Influence of Intake on Fan Blade Flutter. *Journal of Turbomachinery*, 137(8):081002, 2015.

[72] Z. Zhao, N. Smith, and M. Vahdati. A simple model for identifying the flutter bite of fan blades. *Journal of Turbomachinery*, 139(7), 2017.

[73] F. Zhao. *Embedded Blade Row Flutter*. PhD thesis, Imperial College London, 2016.

[74] S. W. Rienstra. Acoustic radiation from a semi-infinite annular duct in a uniform subsonic mean flow. *Journal of Sound and Vibration*, 94(2):267–288, 1984.

[75] S. W. Rienstra. Fundamentals of Duct Acoustics. In *Von Karman Institute Lecture Notes*, 2015.

[76] H. Bergh and H. Tijdeman. Theoretical and experimental results for the dynamic response of pressure measuring systems. Technical Report NLR-TR.F238, National Aeronautical and Astronautical Research Institute - Amsterdam, 1965.

[77] K. Ni, X. Q. Wang, and M. Mignolet. Blade stress estimation during multiple vibratory modes. *54th AIAA/ASME/ASCE/AHS/ASC Structures, Structural Dynamics, and Materials Conference*, pages 1–21, 2013.

[78] L.P. Bonnaure. Modelling High Speed Multistage Compressor Stability. Master's thesis, Massachusetts Institute of Technology, 1991.

[79] E. Feron, M. Brenner, J. D. Paduano, and A. Turevskiy. Time-Frequency Analysis for Transfer Function Estimation and Application to Flutter Clearance. *Journal of Guidance, Control, and Dynamics*, 21(3):375–382, 1998.

[80] S. C. Bradford. *Time-Frequency Analysis of Systems with Changing Dynamic Properties*. PhD thesis, California Institute of Technology, 2006.

[81] S. G. Sawant, M. Oyarzun, M. Sheplak, L. N. Cattafesta, and D. P. Arnold. Modeling of Electrodynamic Zero-Net Mass-Flux Actuators. *AIAA Journal*, 50(6):1347–1359, 2012.

[82] B. Milatovic. Portable Static Test Facility for Small, Expendable, Turbojet Engines. Technical Report AD-A286 337, United States Missile Command, Department of the Army, 1994.

[83] Hermann Schlichting. *Boundary-layer theory.* McGraw-Hill series in mechanical engineering. New York : McGraw-Hill, c1979., 1979.

[84] J.T Higginbotham, C.C. Wood, and E.F. Valentine. A study of the high-speed performance characteristics of 90 ° degree bends in circular ducts. Technical Report Technical Note 3696, National Advisory Committee for Aeronautics, 1956.

[85] J.R. Stone, D.E. Groesbeck, and C.L. Zola. Conventional profile coaxial jet noise prediction. *AIAA Journal*, 21(3):336–342, 1983.